Magnetohydrodynamic and Hydrodynamic studies of relativistic accretion flows around black holes

A Thesis Submitted in Partial Fulfillment of the Requirements

for the Degree of

Doctor *of* **Philosophy** *in Physics*

By

Mr. Samik Mitra

Thesis Supervisor

Prof. Santabrata Das

Department of Physics

Indian Institute of Technology Guwahati

Guwahati, Assam, 781039, India

October, 2024

Declaration

This is to certify that the thesis entitled "**Magnetohydrodynamic and Hydrodynamic studies of relativistic accretion flows around black holes**", submitted by me to the *Indian Institute of Technology Guwahati*, for the award of the degree of Doctor of Philosophy, is a bonafide work carried out by me under the supervision of Prof. Santabrata Das. The content of this thesis, in full or in parts, have not been submitted to any other University or Institute for the award of any degree or diploma. I also wish to state that to the best of my knowledge and understanding nothing in this report amounts to plagiarism.

Signed: Samik Mitra

Samik Mitra
Prime Minister's Research Fellow,
Department of Physics,
Indian Institute of Technology Guwahati,
Guwahati-781039, Assam, India.

Date: 30/9/24

Disclaimer

The bibliography included in this thesis is by no means complete, but it contains the ones that I consulted thoroughly. I apologize for inadvertently missing out on some of the research papers, review articles, and other scientific documents pertaining to the focus of this thesis, which should also have been cited.

Signed: Samik Mitra

Samik Mitra
Prime Minister's Research Fellow,
Department of Physics,
Indian Institute of Technology Guwahati,
Guwahati-781039, Assam, India.

Date: 30/9/24

Certificate

This is to certify that the thesis entitled "**Magnetohydrodynamic and Hydrodynamic studies of relativistic accretion flows around black holes**", submitted by Samik Mitra (196121026), a Prime Minister's Research Fellow in the *Department of Physics*, *Indian Institute of Technology Guwahati*, for the award of the degree of Doctor of Philosophy, is a record of an original research work carried out by him under my supervision and guidance. The thesis has fulfilled all requirements as per the regulations of the institute and in my opinion has reached the standard needed for submission. The results embodied in this thesis have not been submitted to any other University or Institute for the award of any degree or diploma.

Signed: 

Supervisor: Prof. Santabrata Das
Department of Physics,
Indian Institute of Technology Guwahati,
Guwahati-781039, Assam, India.

Date: 30/09/2024

This thesis is dedicated to my parents, grandparents, family members, and friends who were always there for my support. To all my teachers who inspired me to walk beyond the horizon. And to my beloved wife, Srimona, for her unwavering support.

Acknowledgements

Reaching this significant milestone in the journey of life has been a source of great joy, accompanied by a spectrum of emotions, including sadness, fear, and excitement. I hereby wish to convey my profound respect and gratitude to all those who have offered their support and encouragement throughout this endeavour.

First and foremost, I am expressing my sincere gratitude to my Ph.D. advisor, Prof. Santabrata Das, for his tireless guidance. His patience and strong work ethic have always been an inspiration to me. I am also thankful to him for emphasizing the importance of focus and time management to me. His practical way of thinking has helped me understand how to think critically in research. Working closely with him has enriched my understanding of the mysteries of '*accretion physics*'.

Next, I would like to acknowledge my doctoral committee members – Dr. Debaprasad Maity, Dr. Sayan Chakrabarti, and Dr. Sovan Chakraborty – for constantly motivating me and for their constructive feedback and insights on various intricacies. I thank Dr. Maity for the timeless discussions we had on the blackboards, which inspired me to ask questions at every point. Also, my interactions with Sayan da have always been exciting and extremely supportive, which has motivated me to continue my research. His lucid way of teaching the General Theory of Relativity took us out of boredom even during the pandemic. I thank Sovan Sir for all the detailed comments about improving the quality of the presentation during each progress seminars. I offer special thanks to Dr. Bibhas Ranjan Majhi for his valuable comments and suggestions on various aspects that pushed me to think deeper. My special acknowledgment goes to the prestigious *Prime Minister's Research Fellowship* for providing me the financial support to attend many seminars and conferences, which gave me a broad view of the subject.

During my Ph.D. I have met some amazing collaborators, and I would like to thank all of them, Prof. Shahram Abbassi, Dr. Bhupendra Mishra, Dr. Amin Mosallanezhad, Dr. Elham Nazari, Dr. S. M. Ghoreyshi, and finally, Dr. Indu Kalpa Dihingia. Special thanks to Prof. Abbassi for always discussing new ideas and opportunities, which opened up my mind toward broader areas of physics. I also would like to express my heartfelt gratitude to Indu da, who was always there for me from the beginning of my Ph.D. journey. His simple and confident way of dealing with research problems has always captivated my attention. Additionally, I would like to acknowledge Prof. Luciano Rezzolla, Dr. Anuj Nandi, Dr. Indranil Chattopadhyay, Prof. Banibrata Mukhopadhyay, Dr. Bhargav Vaidya, Dr. Biplob Sarkar, Dr. Ramiz Aktar, Dr. Deepika Bollimpalli, Dr. Maciek Wielgus, Dr. Jiri Horak, Dr. Javlon Rayimbaev, Dr. Eduardo M. Gutiérrez, Dr. Shilpa Sarkar, Dr. Parth Bambhaniya, Dr. Rahul Kumar Walia, and Dr. Raj Kishor Joshi. It was really a great experience for me to interact with them on multiple occasions, and their valuable suggestions helped me to improve my research.

My initial fascination with Physics was sparked by Mr. Sabyasachi Kundu, whose extraordinary insights and captivating teaching methods truly captured my imagination. Then, I was introduced to the Late Prof. Timir Baran Chakrabarty, who unveiled the wonders of Physics to me. I want to extend my special acknowledgment to Prof. Patrick Das Gupta, Prof. Debajyoti Choudhury, Prof. T. R. Seshadri, and Dr. Swarnendu Sarkar, whose invaluable teaching and guidance furthered my passion for physics. I am especially grateful to Prof. Patrick Das Gupta for introducing me to the vast area of Astrophysics during my Master's at Delhi University.

Now, I acknowledge all the help, guidance, and advice I obtained from the Heads of the Department of Physics and all the faculty and staff members of the department during my doctoral period. I especially thank Prof. Arunansu Sil and Prof. Pamda K. Padmanabhan for teaching us the Quantum Field Theory and Computational Methods. Also, I want to thank Dr. Subhaditya Bhattacharya and Prof. Saurabh Basu for some good memories and interesting discussions. I further thank Mr. Basab Bijoy Purkayastha, Mr. Himanku Dutta, Mr. Ambarish Biswas, Mr. Nishit Chowdhury, Mr. Sajal Mani Pathak, Mr. Chandan Sharma, Mr. Hirak Jyoti Das, and Mr. Riju Mahato for their prompt support. I also want to thank Ranjit da and Nayan of Core-4 Tea Shop.

I consider myself fortunate to have had productive interactions with extremely talented group members, Dr. Pradeep, Dr. Aneesha, Monu da, Gargi, Seshadri, Amit, Camelia, Subhankar, Abhilash, Sreetama, and Pratiksha. Their enthusiastic responses, queries, constructive criticism, and lively discussions motivated me to produce quality work. I am especially thankful to Amit, who was always there to offer assistance. His help is uncountable. Amit and I have been friends since our time at Delhi University, where we both decided to pursue careers in Astrophysics. I am thrilled that we have both reached this point. I would also like to express my gratitude to our extended '*accretion*' family members, Anupama Ma'am, Sagnik, and Adi.

During the doctoral journey, I was fortunate to have brilliant batchmates Aastha, Alolika, Amalika, Ashirbad, Banashree, Chinmoy, Dipankar (Dipu), Debabrata, Esha, Gourav, Koushik, Kakali, Lipika, Madhav, Maruthi, Rupresha, Shantanu, Saraswati, Sagar, Swarup, Soumen, Sourav, and Tripti. I thank the RS3 lab, where Dipu and I sat throughout our entire doctoral tenure. Also, I have shared some great moments with seniors like Sourav da, Arghya da, Rajesh da, Dipti di, Suresh da, Surojit da, Sumit da, Sovan da, Jyotirmoy, Sahabub, Subhangi, Devender, Samprit, and Rajnandan. I also remember enjoyable moments with enthusiastic juniors like Indrajit, Murrari, Sanu, Madan, Shawan, Nayan, Dipankar, Mijanur, Mouli, Rakshanda, Sayak, Rupam, Shivam, Shoaib, Niloy, Aritra, Sourav, Utsab, Ayan, Subhasis, Disha, Surendra, Joya, Srijata, Tandrima, Urmi, Vaibhab, and Vishal. I am also indebted to Manas Hostel, our '*close*' Manas group, Achyuta, Atul, Ayushman, Nedup, Madhav, Sachin, Sugata, and Vivek. I would also like to thank Akhil, Arijit, Ashish, and Rittick for the quality *discussion* time we spent together during their stay at IIT Guwahati. Most importantly, I want to extend

my heartfelt thanks to Bhoomika and Shailesh for always being there to listen to me. I will cherish many discussions we had on a wide range of topics, including physics, politics, cricket, food, and philosophy. I would also like to thank my dearest friends Doyel, Kajal, Sumanta, Suvam, Shantanu, Swarnendu, Sayantan, Tupai, and lastly, Biswajit. I am especially grateful to Biswa for being a constant source of motivation and calmness.

It might seem odd, but I would like to offer special thanks to some movies and series that have kept my mind fresh, '*Jamalaye Jibanta Manush* (1958)', '*Deya Neya* (1963)', '*Subhas Chandra* (1966)', '*Mouchaak* (1974)', '*Sonar Kella* (1974)', '*Gol Maal* (1979)', '*Goopy Bagha Phire Elo* (1991)', '*The Truman Show* (1998)', '*Hera Pheri* (2000)', '*Friends* (1994-2004)', '*Rush Hour Trilogy* (1998-2007)', '*Big Bang Theory* (2007-2019)', '*The Intern* (2015)', '*Young Sheldon* (2017-2024)' and '*Chander Pahar* (Sunday Suspense)'. Also, my sincere thanks to the '*GOAT*' Christiano Ronaldo for inspiring and motivating the whole world with his dedication and discipline.

Now, I wish to convey my heartfelt appreciation and profound affection to my wife, Srimona, my lifelong confidante and soulmate. Her unwavering encouragement and belief in my potential have been the winds beneath my wings, propelling me toward the successful completion of my endeavours.

Lastly, it may seem obvious, but my heart is filled with gratitude for my parents and family members, my brother Arka. The daily phone calls from '*Baba & Ma*' to check whether I have taken my food or not often made me divert the topic. But they caught me every single time. I am nowhere near as hard-working as my father, who still manages to make time for everything. Hopefully, I will learn his work ethic someday. I, eventually thank them and Srimona for all the sacrifices they made for me. In this list, I would like to add my parents-in-law, my aunt, Arpita di and Munmun di, for their invaluable contribution to my life. Their support and relentless efforts have been my guiding stars, leading me to the completion of my work.

To all the above, and to many I have missed (though unintentionally), thank you for being a part of my journey.

Sincerely
Samik Mitra

Abstract

One of the most efficient energy sources in the universe is the matter accretion onto compact objects, such as black holes (BHs) and neutron stars (NSs). With the presence of an ample amount of angular momentum, this convergent matter cannot fall radially onto the central object. Instead, it forms a swirling disk-like structure widely known as the accretion disk. During the course of accretion onto BHs, the inflowing material begins its journey from the outer edge of the disk with negligible flow velocity (subsonic). In the absence of any dissipative processes, the matter circularizes along the Keplerian orbits, forming a differentially rotating disk. Subsequently, viscous stress develops within the disk and the convergent flow loses angular momentum as it moves to the lower orbits. However, the Keplerian flow terminates at the marginally stable orbit and fails to reach the event horizon of the BH. On the contrary, the sub-Keplerian (low angular momentum) matter is able to enter the horizon with the speed of light (supersonic), suggesting the transonic nature of accretion flows around BHs. Therefore, the low angular momentum (λ) transonic accretion flow has become an active area of research due to its ability to explain the high energy radiations emanating from the innermost parts of the disk in BH X-ray binaries (BH-XRBs) and active galactic nucleii (AGNs).

Indeed, the viscous stress potentially transports the angular momentum within the astrophysical disks. However, the actual source of viscosity remains inconclusive. In this regard, several numerical simulations propose that the viscous stress in accretion disks is plausibly turbulence driven via the magneto-rotational instability (MRI). Since magnetic fields are ubiquitous everywhere, the accretion flow is expected to be magnetized in nature where the large-scale magnetic fields inside the disks are commonly rooted either from the companion star or the interstellar medium.

Being motivated by this, in the first part of the thesis, we investigate the structure of low angular momentum magnetohydrodynamic (MHD) accretion flows around a Schwarzschild BH using a general relativistic (GR) framework. To begin with, we adopt a steady, axisymmetric, advective accretion disk, which is threaded by the radial and toroidal components of magnetic fields. These magnetic field lines are frozen in the accreting plasmas following the ideal GRMHD approximation. In an accretion disk, the convergent flow is assumed to be thermally relativistic close to the BH and remains non-relativistic far away from the horizon. Hence, the ideal equation of state (IEoS) with a constant adiabatic index (Γ) is not suitable to describe the thermodynamics of the relativistic disk. We, therefore, choose a relativistic EoS (REoS) where Γ is determined self-consistently from the thermal properties of the inflowing matter. With these assumptions, we obtain the family of smooth global trans-magnetosonic accretion solutions for the first time in the GRMHD framework. In this theoretical model, both radial and toroidal components of the magnetic field play a crucial role in regulating the accreting matter, and Maxwell's

stress developed by them successfully transports the flow angular momentum outwards. Towards this, we compute the viscosity parameter (α) due to the turbulent Maxwell stress, and it appears to be radially varying. Notably, the toroidal magnetic field remains more dominant in the disk mid-plane than the radial component. Although the flow remains gas pressure ($p_{\rm gas}$) dominated (plasma-$\beta = p_{\rm gas}/p_{\rm mag} > 1$, where $p_{\rm mag}$ is the magnetic pressure), the effect of magnetic fields becomes predominantly important near the horizon ($\sim 10^6$ G for a stellar-mass BH). Moreover, we examine the correlation between α and plasma-β, and identify two distinct accretion domains along the radial extent of the disk. Finally, we discuss the utility of the present steady state formalism in providing potential seed solutions for the global GRMHD simulations in higher dimensions.

Depending on the model parameters (such as energy, angular momentum, magnetic fields), these low angular momentum flows often possess multiple critical points, *i.e.,* inner ($r_{\rm in}$) and outer ($r_{\rm out}$). While accreting onto a BH, the supersonic matter containing $r_{\rm out}$ experiences centrifugal repulsion and slows down. Consequently, matter piles up in the vicinity of the BH and a centrifugal pressure supported boundary layer forms. This centrifugal barrier can not clench the accumulation of matter indefinitely and as a result, the flow variables undergo a discontinuous shock transition to the subsonic branch. After the transition, the subsonic flow eventually gains more radial velocity and becomes supersonic upon passing through $r_{\rm in}$. Ultimately, this supersonic flow enters into the BH and we obtain a global shock-induced accretion solution. We must point out that shock solutions are thermodynamically favourable due to their higher entropy content than shock-free solutions. With this motivation, in Chapter 3, we study the shock-induced steady GRMHD flows around Kerr BHs following the MHD shock conditions. In this work, we characterize the shock-induced flow with energy ($\mathcal{E}$) and angular momentum ($\mathcal{L}$) flux, radial magnetic flux (Φ), and iso-rotation parameter (F), respectively. Due to shock compression, there is a significant jump in the flow density, temperature, and toroidal magnetic fields across the shock front. This evidently leads to a hot, dense, strongly magnetized post-shock corona (PSC). The presence of such corona is essential in explaining the hard X-ray radiations coming from the inner parts of the accretion disk. Since the characteristics of PSC (size, density, and temperature) are determined by the shock properties, namely shock location ($r_{\rm sh}$), compression ratio (R), and shock strength (Ψ), we extensively study their dependence on the magnetic fields. We notice that Φ and F strongly determine $(r_{\rm sh}, R, \Psi)$, which reflects the importance of magnetic fields in deciding the spectral properties of BH-XRBs. Further, we identify the effective domain of shock parameter space, which is largely altered as the BH spin ($a_{\rm k}$) and Φ are changed. Meanwhile, we estimate the critical magnetic flux ($\Phi^{\rm cri}$) that admits shocks in GRMHD flows and obtain a positive correlation between $a_{\rm k}$ and $\Phi^{\rm cri}$. Finally, we conclude that the present GRMHD shocked accretion flow fails to meet the Magnetically Arrested Disk (MAD) limit.

In the subsequent part of the thesis, we concentrate on systems with extremely low mass accretion rate, *i.e.,* BH-XRBs in hard/quiescence states and low-luminous AGNs

(LLAGNs), where the hot plasma surrounding the BHs is collisionless. Therefore, thermal conduction plays a decisive role in governing the disk dynamics and effectively transports energy via heat flux from the inner to the outer regions of the disk. To understand such an effect, we begin with a steady, axisymmetric, viscous, hot accretion flow (HAF) around a non-rotating BH, where pseudo-Newtonian potential (Paczyński & Wiita, 1980) describes the space-time geometry. We neglect the influence of magnetic fields and solve the governing hydrodynamic equations incorporating the saturated thermal conduction flux. With these considerations, we present the global transonic accretion solutions incorporating thermal conduction ($\Phi_{\rm s}$) for the first time and compare the global solutions with the self-similar results. In the global accretion solutions, we notice that thermal conduction is effective in the outer parts of the disk. Further, we investigate the correlation between the viscosity parameter (α) and maximum saturation constant ($\Phi_{\rm s}^{\rm max}$), where we notice a disagreement between the global and self-similar solutions. Moreover, we compute the Bernoulli parameter (Be) for the global and self-similar solutions, and it comes out to be positive $Be > 0$. Therefore, the present formalism indicates that thermal conduction in HAFs causes the accreting gas to become gravitationally unbound, which is relevant in explaining the mass-loss from the disk.

It is noteworthy that the pseudo-Newtonian approach bears limitations in describing the accretion flows around BHs, and GR treatment is desired. However, due to a high degree of non-linearity, studying relativistic accretion flow in a full GR framework involving all physical processes is numerically challenging. It is, therefore, important to find the bridge between Newtonian and GR formalism of accretion flows, where post-Newtonian (PN) theory comes out as the potential alternative. This theory consists of the Newtonian hydrodynamics and gravity (0PN), and their higher order relativistic corrections (*i.e.,* 1PN, 2PN and so on). With this motivation, in Chapter 5 of the thesis, we put effort into formulating the post-Newtonian hydrodynamic equations around a spinning compact object upto the first post-Newtonian order (1PN). At first, we estimate the domain of validity of the present formalism, which is outside the post-Newtonian radius, $r_{\rm PN} \sim 10$ gravitational radius. Next, we identify the effective potential ($\Phi_{\rm eff}^{\rm PN}$) from the governing post-Newtonian equations. Interestingly, $\Phi_{\rm eff}^{\rm PN}$ continues to mimic the general relativistic effective potential ($\Phi_{\rm eff}^{\rm GR}$, Dihingia et al. (2018a)) even at $r < r_{\rm PN}$ for a wide range of spin parameter. Since the present formalism is valid way beyond $r_{\rm PN}$, IEoS suitably describes the thermodynamics of the inflowing matter. With this, for the first time in literature, we discuss the steady, inviscid, advective global transonic accretion flows around a spinning compact object in 1PN regime. Finally, using the PN approach, we compute the energy flux emitted from the disk and find that it varies as $\sim 1/r^5$.

In Chapter 6, we draw the conclusions of the thesis and discuss the future directions.

List of Publications

Peer Reviewed Journals

- **Mitra S.**, Das S., **Low angular momentum general relativistic magnetohydrodynamic accretion flow around rotating black holes with shocks**, ApJ, 971, 1, 2024, doi: https://iopscience.iop.org/article/10.3847/1538-4357/ad55cb.* [1]
- Narazi, E., **Mitra S.**, Abbassi S., Das S., **Accretion flows around spinning compact objects in the post-Newtonian gravity**, *JCAP*, 117, 2024, doi: https://iopscience.iop.org/article/10.1088/1475-7516/2024/05/117. *
- **Mitra S.**, Ghoreyshi S. M., Mosallanezhad A., Abbassi S., Das S., **Global transonic hot accretion flow with thermal conduction**, *MNRAS*, 523, 2023, 4431-4440, doi: https://doi.org/10.1093/mnras/stad1682. *
- **Mitra S.**, Maity D., Dihingia I. K., Das S., **Study of general relativistic magnetohydrodynamic accretion flow around black holes**, *MNRAS*, 516, 2022, 5091-5109, doi: https://doi.org/10.1093/mnras/stac2431.*
- Das S., Nandi A., Stalin C. S., Rakshit S., Dihingia I. K., Singh S., Aktar R., **Mitra S.**, **On the origin of core radio emissions from black hole sources in the realm of relativistic shocked accretion flow**, *MNRAS*, 514, 2022, 1940-1951, doi: https://doi.org/10.1093/mnras/stac1398.

National and International Conferences

- International workshop on *NUMERICAL ASTROPHYSICS*, organized by Ferdowsi University of Mashhad, Iran, July 2020 (Online).
- Hosted/organized *North East Meet of Astronomers (NEMA -VI)*, November 2020, IIT Guwahati (Online).

[1] Publications marked with * is included in the thesis.

- Online workshop on HPC in Astrophysics and Astronomy, September 2021, NCRA-TIFR and IIT Kharagpur (Online).
- International Online Conference on Black Holes Inside and Out (BHIO 2021), September 2021 (Online).
- Prime Minister's Research Fellow (PMRF) symposium at IIT Guwahati, November 2021 (Online).
- XII Biennial National conference of PANE: Physics Academy of North East, December 2021. Received *PANE Young Researcher Award in Astrophysics & Cosmology* category (Online).
- *School on Black Holes and Gravitational Waves*, January 2022, IIT Madras, India (Online).
- *Research and Industrial Conclave 2022 (RIC 2022)*, January 2022, IIT Guwahati (Online).
- *North-East Meet of Astronomers (NEMA-VII)*, January 2022, Rajiv Gandhi University, Arunachal Pradesh (Online).
- *Black Hole Astrophysics with VLBI*, February 2022, Institute of Cosmic Ray Research, University of Tokyo (Online).
- 40^{th} meeting of the *Astronomical Society of India (ASI) 2022*, March 2022, Jointly hosted by IIT Roorkee and ARIES (Online).
- *IAGRG School*, May 2022, IIT Gandhinagar (Online).
- 44^{th} COSPAR Assembly, Greece, Athens, July 2022 (In-person).
- *Young Astronomers Meet 2022*, November 2022, ARIES, Nainital, India (In-person).
- *Challenges and Innovations in Computational Astrophysics IV*, November 2022 (Online).
- National conference on *REcent Trends in the study of Compact Objects: Theory and Observation (RETCO-V)*, IIA, Kodaikanal Solar Observatory, India, April 2023 (In-person).

- *Challenges and Innovations in Computational Astrophysics V*, November 2023 (Online).
- 25$^{\text{th}}$ Relativistic Astrophysics Group Meeting *RAGTIME*, November 2023 (Online).
- Hosted/organized 10$^{\text{th}}$ *International Conference on Gravitation and Cosmology (ICGC 2023)*, IIT Guwahati, India, December 2023 (In-person).
- Seventeenth Marcel Grossmann Meeting, Pescara, Italy, July 7-12, 2024 (Online).
- Galactic and extragalactic X-ray transients, theory and observational perspectives, Warsaw, Poland, September 9-11, 2024 (In-person).

Awards/Honor/Talks

- During my Ph.D. I received the prestigious Prime Minister's Research Fellowship (PMRF) from the Government of India to fulfill my research. PMRF Tenure: September 2020 - July 2024.
- Qualified for the 2019 Graduate Aptitude Test in Engineering (GATE) funded by MHRD, Govt. of India.
- Received *PANE Young Researcher Award in Astrophysics & Cosmology* category.
- Securing 2$^{\text{nd}}$ place in *Three Minute Thesis Presentation: Scientifique* during RIC 2022, IIT Guwahati.
- Delivered a talk '*Magnetohydrodynamic flows around black holes in strong gravity regime: an analytical and numerical study*' on the *National Science Day 2022*, in Department of Physics, IIT Guwahati.
- Delivered a talk '*How A Black Hole Lights Up Its Surroundings*' of the *National Science Day 2023*, in Department of Physics, IIT Guwahati.
- Showcased as the Commendable Research by PMRFs on the webpage of Ministry of Education, PMRF, Govt. of India.

Contents

List of Figures

Chapter 1

Introduction

"Though my soul may set in darkness, it will rise in perfect light; I have loved the stars too fondly to be fearful of the night"

Sarah Williams 'The Old Astronomers'

1.1 Background

Astrophysics, a realm where the infinitely vast cosmos meets the infinitesimally small world of particles, beckons with unparalleled allure. The study of astrophysics generously provides environments inaccessible in the laboratory, yet essential for testing and advancing modern physical theories. From deciphering the cosmic symphony of gravitational waves to unraveling the '*silhouette*' of super-massive black holes (SMBHs), astrophysicists stand at the forefront of scientific exploration. The breakthrough discovery by the Event Horizon Telescope Collaboration et al. (2019a) (EHTC; see Fig. 1.1) has laid the groundwork for delving deeper into the physics of compact objects like BHs and rigorously testing general relativity in the strong gravity regime. Towards this, one of the prime interests in high energy astrophysics is the study of accretion onto BHs.

FIGURE 1.1: The very first image of a BH, at the center of the galaxy M87. Image courtesy: EHT/April 10, 2019 press release.

1.1.1 Accretion onto compact objects

BHs are grouped into a class of compact objects, with white dwarfs (WDs) and neutron stars (NS). They are the dense remnants of massive stars that have exhausted their nuclear fuel and undergone gravitational collapse. These objects are classified by the *compactness parameter* $\mathcal{C}_{\rm R}$ (Shapiro & Teukolsky, 1983; Abramowicz & Fragile, 2013), a dimensionless quantity that characterizes the density and gravitational field strength of the massive objects as,

$$\mathcal{C}_{\rm R} = \frac{2GM_*/c^2}{R_*}, \tag{1.1}$$

where, G is the Gravitational constant, c is the speed of light, and M_* and R_* represent the mass and radius[1] of the central object. For WDs, $\mathcal{C}_{\rm R}$ is approximately $\sim 10^{-4}$, for NS it ranges from about $\sim 0.3 - 0.9$, whereas for BHs, $\mathcal{C}_{\rm R}$ becomes high as $1 - 2$ depending on its spin angular momentum $0 \leq a_{\rm k} < 1$. Note that, $\mathcal{C}_{\rm R}$ values are expressed in units of $2G/c^2$. It is worth mentioning that NS and WD have hard outer surfaces, whereas BHs are covered by an imaginary mathematical surface called the event horizon (EH). The presence of such a null hypersurface around BHs cuts off the external world from the interior of the EH. Moreover, due to the strong gravitational potential of the BH,

[1]For BHs, the radius $R_*\big(=1+\sqrt{1-a_{\rm k}^2}\,GM_*/c^2\big)$ is the event horizon (EH), a null hypersurface which causally disconnects the interior of the BH from the external world.

even light can not escape. This unique feature isolates BHs as the most distinctive and mysterious member of the family of compact objects. Since light cannot escape from the strong gravity of the BH, we need to rely on indirect detection by studying the surrounding matter, which is trapped under the immense gravitational potential.

According to observations, BHs exist across a wide range of mass-spectrum, spanning from stellar-mass BHs with mass $\sim 3 - 33 M_\odot$[2] (Gaia Collaboration et al., 2024) to the super-massive BHs (SMBHs) with mass $\sim 10^6 - 10^{10} M_\odot$ (Dullo et al., 2021). However, the gravitational wave observations show a much broader mass range of the BHs compared to the mass range obtained from the electromagnetic (EM) observations. This is because the merging of less massive objects often leads to the formation of BHs (Abbott et al., 2016). Despite the enormous mass range, both stellar-mass BHs and SMBHs feed on surrounding matter either from the companion binary star, stellar winds as observed in X-ray binaries (XRBs, Chen & Taam (1994)), or from encompassing gas cloud, orbiting stars, interstellar medium as in Active Galactic Nuclei (AGN, Zel'dovich & Novikov (1964); Salpeter (1964)).

1.1.2 Energy budget of accretion

During the accretion process, the gravitational potential energy of the accreted matter is extracted, releasing an enormous amount of energy. Consider a blob of mass m that falls onto a compact star of mass M_* and radius R_* from infinity. The amount of released energy due to the central object is $\sim GM_*m/R_*$. If the central star is a Schwarzschild BH with $a_{\rm k} = 0$, then $R_* = 2GM_*/c^2$, and energy liberated from the system is roughly the rest-mass energy, *i.e.,* mc^2. In reality, only a fraction of the rest-mass energy can be released as $\sim \eta_{\rm A} GM_*m/R_*$, where $\eta_{\rm A}$ is the efficiency factor. Accretion efficiency depends on several factors, such as the central object, flow structure, the inner boundary conditions, flow angular momentum, magnetic fields, and radiative processes (Yuan & Narayan, 2014, for review). Following the general relativistic calculation of the equatorial motion of particles in circular orbits around BHs (Hobson et al., 2006), one obtains $\eta_{\rm A} \sim 5.7\%$ for Schwarzschild BH, whereas for maximally co-rotating BH ($a_{\rm k} = 1$),

[2] $M_\odot$ denotes the solar mass.

$\eta_{\rm A} \sim 42\%$ of the rest-mass energy from the accreting material. Consequently, the accretion process becomes the powerhouse in most astrophysical objects, such as XRBs, AGNs and gamma-ray bursts (GRBs), with the emitted radiation spanning the entire EM spectrum from high energy gamma rays to low-frequency radio waves.

With the increase in $\eta_{\rm A}$, the observed luminosity from the system would increase too, $L = \eta_{\rm A}\dot{M}c^2$ ($\dot{M}$ is the matter accretion rate onto the compact object). The luminosity of an astrophysical system is often expressed in terms of the Eddington luminosity ($L_{\rm Edd}$) where $L_{\rm Edd} \simeq 1.3 \times 10^{38}\,(M_*/M_\odot)$ erg s^{-1}.

1.2 Foundations of accretion theory and its developments

Previously, we discussed that a BH alone possesses no astrophysically significant means to produce energy. However, a black hole, coupled with the accreting matter, is by far the most efficient generator of huge energies in XRBs, AGNs, GRBs, and quasars, surpassing the output generated by nuclear fusion processes (the efficiency is $\sim 0.7\%$ (Frank et al., 2002)). Among all these sources, BH-XRBs stand as the most ideal cosmic laboratory to probe the effect of strong gravity due to a broad distribution in their variability timescales $\sim$ from milliseconds to several days (Remillard & McClintock, 2006, see for review). Therefore, the foundation of accretion theory needs to be visited in the most rigorous way.

1.2.1 Spherical 'Bondi' flows

The theoretical expedition to model the accretion flows started by Hoyle & Lyttleton (1939) (hereafter HL39), way before the detection of the first BH X-ray sources (Giacconi et al., 1962, 1971). HL39, for the first time, introduced the concept of accretion and formulated the rate of accumulation of matter coming from the interstellar medium on the star's surface. However, they did not obtain satisfactory results as the pressure of the gas cloud was neglected. Later, Bondi & Hoyle (1944); Bondi (1952) developed the 'classic' spherical accretion model by considering pressure effects but assuming a zero gas angular momentum flow (better known as '*Bondi flows*') around an isolated,

gravitating star at rest in an infinite gas cloud. Towards this, the gaseous matter, originating subsonically[3] at a large distance, often exceeds the local sound speed[4] before hitting the surface of the star. Therefore, the matter has to pass through one sonic point where the flow velocity exactly matches the local sound speed (C_s) of the gas. Later, Michel (1972) introduced the general relativistic version of Bondi flows and considered Schwarzschild BH as the accretor. Even though the 'transonic' spherically symmetric model was successful in various aspects (Armitage, 2020, see for review), it failed to explain the observed luminosities of quasars and XRBs due to the low radiative efficiency (Shapiro, 1973; Shapiro & Salpeter, 1975; Shapiro & Teukolsky, 1983, see for review). To resolve this problem, astrophysicists argued that the accreted material around the compact object must have a large angular momentum (Prendergast & Burbidge, 1968). As a consequence, the inflowing matter fails to retain its spherical symmetry (particularly in XRBs). Hence, a temporary disk-like depositary forms around the compact object.

1.2.2 Disk accretion

Previously, we discussed the properties of spherically symmetric 'Bondi' flows. Since the inflowing matter had zero angular momentum, the corresponding radial infall velocity became very high, and for a given accretion rate, the density turned out to be very small. Hence, this spherical flow model seemed to be inefficient in converting the rest mass energy of the infalling matter into radiation. On the contrary, the presence of angular momentum prevents the inflowing matter from radially falling onto the central object. Instead, the fluid revolves around the compact body, which lowers the infall velocity, and matter begins to accumulate, forming a spiraling disk-shaped structure commonly known as accretion disk.

The quest for accretion disk physics began with the accretion in a binary system, where the primary companion was chosen to be a compact object (BHs or NSs), and the secondary companion was a binary star with sufficient angular momentum. In this thesis, we are interested in the accretion process onto a BH. Subsequently, the strong gravitational potential of BH would strip out the matter either from the tidally locked

[3]Flow velocity (v) is much less than the sound speed C_s.
[4]Flow velocity exceeds the local sound speed $v > C_s$.

binary companion through Roche lobe overflow or from the winds of the surrounding stars (Frank et al., 2002). Therefore, the inflowing matter would possess an ample amount of intrinsic angular momentum (nearly Keplerian). Because of this, the accreting matter has a longer infall timescale yielding higher density than the Bondi flow. This increase in infall timescale allows the viscosity to dissipate energy and angular momentum within the disk. Note that, in a differentially rotating disk, viscosity naturally comes into the picture due to the continuous generation of frictional force between the consecutive fluid layers. As the matter loses angular momentum, it drifts more toward the BH with a larger infall velocity (v) and ultimately falls into the BH with the speed comparable to c. With time, a large amount of accreting matter sinks deeper into the potential well of the BH and radiates more efficiently for a longer duration, which potentially resolves the mystery of high luminous X-ray sources (Prendergast & Burbidge, 1968; Lynden-Bell, 1969).

BH-XRBs are embedded in the disk of inwardly spiraling accreted matter that is a known source of the X-ray emissions with energy ranging from sub-KeV to a few hundred KeV (Remillard & McClintock, 2006). These X-ray photons are the ideal messenger to decode the tale-tell signature of the strong gravity around BHs. Motivated by this, we focus on modeling the accretion flow around BHs to explain their observational findings. Over the years, several analytic models of accretion disks (Shakura, 1973; Shakura & Sunyaev, 1973; Shapiro et al., 1976; Fukue, 1987; Abramowicz et al., 1988; Chakrabarti, 1989, 1996; Narayan & Yi, 1994, 1995a; Narayan et al., 1997) have been proposed to explain the high energy EM radiations from various astrophysical sources. These models are one-dimensional (1D), steady (time-evolution is neglected), axisymmetric, and vertically averaged. In general, the semi-analytic models are characterized by the mass accretion rate ($\dot{M}$), and the final outcome shows a broad class of accreting models with different aspect ratios (the ratio between disk half-thickness (H) to radius r), optical depths, and radiative efficiency. In the subsequent section, we briefly summarize various accretion disk models.

1.2.3 Standard 'thin' disk model

One of the founding pillars in the accretion disk theory is the standard disk model proposed by Shakura and Sunyaev (Shakura & Sunyaev, 1973, SSD), which was later extended to the general relativistic version by Novikov & Thorne (1973); Page & Thorne (1974). The standard disk applies when $\dot{M} \sim 0.1\dot{M}_{\rm Edd}$, or disk luminosity is just below the Eddington limit, resulting in a luminous disk model. In their seminal work, Shakura & Sunyaev introduced a form of anomalous viscosity (α), which approximates the vertically integrated radial stress ($T_{r\phi}$) proportional to the pressure ($p_{\rm tot}$, including gas or radiation pressure or both). The α-viscosity assumes that the angular momentum transport is driven by turbulence in the disks, which could possibly be related to the magnetic fields. In the standard disks, the flow angular momentum remains locally Keplerian ($\lambda \propto r^{1/2}$) at all radii (r), and therefore, most of the inflowing matter settles down in the disk mid-plane. Eventually, a geometrically 'thin' disk forms. During accretion, the energy produced by the viscous dissipation is largely radiated away (about one-tenth of the rest mass energy, Narayan & McClintock (2008)) due to the high radiative efficiency of the thin disks. Consequently, the SSD is classified as *cold accretion flow* with a temperature range of $T \sim 10^4 - 10^7$ K, and it obeys a simple power-law profile $T \propto r^{-3/4}$. With this, the optically thick disk produces a *multicolored blackbody spectrum*, but could not explain the high energy non-thermal components (Mitsuda et al., 1984; Zimmerman et al., 2005). However, the Shakura Sunyaev disk can explain the high/soft states in BH-XRBs.

Thin disk model can be divided into three broad regions based on the dominant pressure effects along the radial extent of the disk. The inner region of the disk is supported by radiation pressure ($p_{\rm rad}$), with disk opacity determined by scattering. While in the intermediate and outermost regions, gas pressure dominates $p_{\rm gas} > p_{\rm rad}$. Here, electron scattering ($\kappa_{\rm es}$) and free-free absorption ($\kappa_{\rm ff}$) control the opacity in the intermediate and outer regions, respectively. The condition $\kappa_{\rm ff} \sim \kappa_{\rm es}$ identifies the separation between these two regions. Overall, the model was very successful in drawing the attention of the astrophysical community. Soon after this, Lightman & Eardley (1974) reported the viscously unstable (known as the L-E instability) nature in the radiation pressure-dominated inner disk and later, Shakura & Sunyaev (1976); Piran (1978) found the

thermal instability in this region. Meanwhile, Thorne & Price (1975), argued that the L-E instability could force the inner region of SSD to thicken until it becomes optically so thin that it results, $p_{\rm rad} < p_{\rm gas}$. Hence, the concept of geometrically *thick* disk has opened up with new avenues in the field of accretion domain.

Another drawback of the Keplerian disk model is that the inner edge of the disk is terminated at the innermost stable circular orbit (ISCO). Therefore, the flow is unable to enter beyond ISCO, and the inner boundary conditions imposed by the event horizon (EH) can not be fulfilled. Hence, there is a need to develop a more realistic model with a sub-Keplerian distribution of angular momentum incorporating the advection process.

1.2.4 SLE disk model

With the early hint of Thorne & Price (1975), the optically thin, puffy (geometrically thick) inner disk model has garnered much interest as it could explain the 1971 transition in the Cygnus-X1 spectrum spanning over a wide energy range (Tananbaum et al., 1972). Later, Eardley et al. (1975); Shapiro et al. (1976) (hereafter SLE) considered the puffed-up region to be fully ionized with electrons and ions, where ions remain much hotter than the electrons. This key feature introduced the 'two-temperature' accretion flow model in the sub-Eddington regime ($\dot{M} \ll \dot{M}_{\rm Edd}$). In contrast to the standard thin disks, the SLE model is much hotter, with ions reaching the virial temperature ($\sim 10^{12}$ K). Because of the high thermal pressure supported by ions, the disk remains geometrically thick. The puffed-up region, being optically thin, allows the hot electrons ($\sim 10^{9}$ K) to radiate away via the non-thermal processes, *i.e.,* bremsstrahlung, synchrotron, and Comptonization. Even though the SLE model was successful in explaining the hard X-ray emissions from XRBs and AGN (Kusunose & Takahara, 1985; Wandel & Liang, 1991; Melia & Misra, 1993), the model turned out as thermally unstable. Consequently, the rapid growth of instability in the SLE model often breaks the thermal equilibrium of the accretion disk (Pringle, 1976; Piran, 1978).

The models discussed so far have not addressed advection, which is going to be the main focus in the subsequent sections.

1.2.5 Slim disk model

When matter is fed onto a BH with moderately super-Eddington rate, *i.e.,* $\dot{M} \gtrsim \dot{M}_{\rm Edd}$, accreting plasma becomes way too optically thick to radiate the dissipated heat energy. With such an accretion rate, the flow remains radiation pressure dominated. In this case, the radiation escape (or photon diffusion) time, $t_{\rm diff} = 3H\tau/c$ (Mihalas & Mihalas, 1984, where τ is the optical depth) exceeds the infall timescale, $t_{\rm acc} = r/|v|$. Radiation is thereby trapped (photon trapping) within the disk and advected inwards along with the convergent flow. This evidently lowers the radiative efficiency, and *slim* disk model was discovered (Abramowicz et al., 1988). The accretion solutions in the slim disk model are transonic and the flow passes through an inner critical point with a sub-Keplerian angular momentum. The disk thickness of this model remains intermediate between the standard thin and thick disks. Finally, the significant role of advection leads to a thermally and viscously stable accretion model. The general relativistic (GR) version of the slim disk was studied by Beloborodov (1998); Sądowski (2009) which are often used to model some phases of gamma-ray bursts (with dominant neutrino cooling, Liu et al. (2017)), Tidal Disruption Events (TDE, Curd & Narayan, 2019) and Ultra Luminous X-ray (ULX) sources (Watarai et al., 2001; Narayan et al., 2017).

Notably, the slim disk and standard disk belong to the same category of solutions *i.e., optically thick, cold accretion flows* (Yuan & Narayan, 2014, for review). It is worth mentioning that when the accretion rate is well below the Eddington limit, the slim disk model converges into the SSD model (Czerny, 2019, and references therein). However, such a transition between an optically thick and optically thin disk remains elusive.

1.2.6 Advection dominated accretion flow (ADAF)

Advection dominated accretion flow has garnered significant attention from astrophysicists due to its ability to elucidate the dynamics of the inner regions of the accretion disk. In low-accreting ($\dot{M} \ll \dot{M}_{\rm Edd}$) systems [namely, SMBHs, low-luminous AGNs (LLAGNs), BH-XRBs in their hard and quiescent states[5]], the heat generated by viscous dissipation

[5]Since the discovery of XRBs, they show several states during their outbursting cycle. The most notable among these are the bright, high-temperature state (thermal or high soft state), the slightly less luminous, low-hard state, and the very dim, quiescent state.

can directly contribute to heating the accretion flow through a dominant advection process, rather than being radiated away. For the first time, Ichimaru (1977) introduced the analytic solution of the ADAF model. Almost after a decade, in the mid-1990s, ADAF models were rediscovered by Narayan & Popham (1993); Narayan & Yi (1994, 1995a,b); Abramowicz et al. (1995); Chen (1995) and finally become established to study accretion flows around BHs. These studies described the flow structure by assuming *self-similarity* of flow variables, meaning that the variables are simple functions of radial distance r. The self-similar solutions described the ADAF model in a lucid manner with the following key properties, *i.e.,* the disk is hot with nearly virial temperature $T \sim 10^{12}/r$ and a geometrically thick nature $H/r \sim 0.5$ (Narayan & McClintock, 2008). The hot accretion flow has a much larger radial velocity (v) compared to the thin disk model and possesses a sub-Keplerian angular velocity. With a large v and low-$\dot{M}$, the hot accretion flow (HAF) is optically 'too' thin (Yuan & Narayan, 2014). Hence, the emitted radiation is never a blackbody, but is dominant by the non-thermal emission processes, namely bremsstrahlung, synchrotron (if magnetic field is present), and Compton. However, these ADAF solutions hardly exist beyond the luminosity $L > 10\%L_{\rm Edd}$. Therefore, in the optically thin ADAFs, radiative cooling is inefficient ($\eta_{\rm A} \sim 0.1$) and hereby known as the radiatively inefficient accretion flow (RIAF).

Importance of thermal conduction in RIAF models

By analyzing the density and temperature profiles of RIAF models with sufficiently low-$\dot{M}$, it is observed that the electrons have much larger collisional mean free paths compared to the typical lengthscale of accretion flows (Mahadevan & Quataert, 1997; Tanaka & Menou, 2006; Johnson & Quataert, 2007). Therefore, the plasma in HAFs is expected to be collisionless, with thermal conduction flux playing a crucial role in transporting energy in the disk (Shadmehri, 2008; Abbassi et al., 2010; Faghei, 2012; Ghasemnezhad et al., 2012; Khajenabi & Shadmehri, 2013; Bu et al., 2016; Mosallanezhad et al., 2021, and references therein). Furthermore, Menou (2005); Tanaka & Menou (2006) reported that the presence of thermal conduction in HAFs is potentially viable in launching thermal outflows from the disk. This will be discussed elaborately in Chapter 4 of the thesis.

Even with the tremendous success of the self-similar model, the scale-invariant approach prevents it from describing the flow near the inner or outer boundary of the disk. As most of the radiation originates from the innermost part of the accretion disk, the global solutions of ADAF models are required to study. Fukue (1987); Chakrabarti (1989); Abramowicz & Chakrabarti (1990); Chakrabarti (1996), presented the global picture of advective accretion flows. The global ADAF solutions are necessarily transonic in nature to satisfy the inner boundary conditions imposed by the horizon. Further, Narayan et al. (1997), implemented the 'no-torque condition' to self-consistently estimate the sonic radius and specific angular momentum accreted by the BH. However, Becker & Le (2003) identified the limitation of the 'no-torque condition' and modified it with a new condition where '*the radial derivative of the torque vanishes at the horizon*'. With these modifications, Chakrabarti & Das (2004); Das & Chakrabarti (2004); Das (2007); Becker et al. (2008); Das et al. (2009) identified the multi-transonic nature of the flow, possessing inner, and outer critical points, while Narayan et al. (1997) obtained the ADAF solutions only with single critical points. With this, in Chapter 4 of the thesis, we have shown a comparative study between the self-similar and global ADAF solutions.

1.2.7 Two Component Advective Flow (TCAF)

The detailed overview of the existing theoretical models suggests that accretion flows may not be Keplerian everywhere but can also have a sub-Keplerian component. This sub-Keplerian matter is necessary to explain the dynamics of the inner hot accretion disk and therefore, the low angular momentum ADAF models have become a growing area of research. Keeping this in mind, Chakrabarti (1990a); Chakrabarti & Titarchuk (1995) introduced a lucrative two component advective accretion flow (TCAF) model, which comprises the sub-Keplerian and Keplerian distribution of matter. In this model, a highly viscous Keplerian disk resides in the mid-plane of the disk. This thin accretion disk is further sandwiched by a low viscous, sub-Keplerian halo component. With this theoretical model, Chakrabarti & Titarchuk (1995) analyzed the existence of shock waves in the advective disk, which was absent in the ADAF model proposed by Narayan et al. (1997). In the following, we describe the shock waves and their importance in explaining the spectral and temporal behaviours of BH-XRBs (Chakrabarti, 1990a).

Shock-induced advective flow

In the TCAF model, the sub-Keplerian matter spirals in and experiences a centrifugal repulsion, resulting in the accumulation of matter in the vicinity of the BH. As the rotating matter piles up, a centrifugal barrier forms, which eventually prevents additional matter to enter the inner regions of the disk. However, the centrifugal barrier can not hold the excess inflowing matter indefinitely and triggers a discontinuous shock transition of the flow variables. To execute such a discontinuous shock transition, the convergent flow must satisfy certain jump conditions, which are known as the Rankine-Hugonoit shock (RHC) conditions (Landau & Lifshitz, 1959; Fukue, 1987; Chakrabarti, 1989, 1990b; Frank et al., 2002). During shock, the low entropy supersonic solution makes a transition to the subsonic branch that possesses higher entropy. Such an increase in entropy across shock is indeed thermodynamically favourable (Sponholz & Molteni, 1994; Becker & Kazanas, 2001; Gu & Lu, 2004, 2006; Le & Becker, 2007; Fukumura & Kazanas, 2007). Depending on the flow parameters, when the shock forms, it remains steady at a specific radius and is known as the standing shock solution. At the shock, the convergent flow gets compressed, resulting in a hot and dense post-shock corona (PSC). The puffed-up corona is a perfect reservoir for hot electrons. These hot electrons intercept the soft (low energy) photons originating from the Keplerian disk and reprocess them via inverse Comptonization. Consequently, hard X-rays emerge from the PSC, which explains the high energy non-thermal tail. Notably, the emitted radiation spectra carry the imprints of both the thin Keplerian disk and halo. Therefore, with the combined effect of Keplerian and sub-Keplerian accretion rates, the TCAF model characterizes the overall spectrum (Mandal & Chakrabarti, 2005, 2008; Chakrabarti & Mandal, 2006; Debnath et al., 2013).

On the contrary, if the infall timescale of the accretion flow roughly matches the PSC cooling timescale, the PSC modulates. This fact has been scrutinized with rigorous numerical simulations (Molteni et al., 1996a,b; Suková & Janiuk, 2015; Suková et al., 2017; Kim et al., 2017, 2019; Debnath et al., 2024), where they reported this oscillation to be quasi-periodic in nature. Therefore, the observed Quasi-Periodic Oscillations (QPOs) in galactic BH sources can be related to the oscillatory shock waves (Chakrabarti &

Manickam, 2000; Nandi et al., 2001a,b, 2012). Overall, the shock-induced accretion flow is useful for the spectrotemporal modeling of GBH sources.

It is noteworthy that the astrophysical environment surrounding compact objects is characterized by an abundance of magnetic fields. In this regard, the aforementioned models remain incomplete without adding the magnetic fields into their analysis.

1.3 Impact of Magnetic Fields on Accretion Processes

From the Earth's own magnetic field, which shields us from harmful solar radiation to the vast galactic magnetic fields that shape the formation and evolution of stars, galaxies justify the importance of magnetic fields in our universe (Davidson, 2001, for review). In the case of accretion around BHs, these magnetic fields play a crucial role, exhibiting a wide range of fascinating characteristics that offer profound insights into these enigmatic cosmic beasts (Moffatt, 1978; Schekochihin & Cowley, 2007; Longair, 2011; Davis & Tchekhovskoy, 2020; Shukurov & Subramanian, 2021, and references therein).

It was Shvartsman (1971) who first showed that the radiative efficiency increases enormously in the presence of magnetic fields when matter is spherically accreting onto a central object. In reality, disk accretion is more relevant than the spherical inflows in most of the astrophysical sources (for details Sec. 1.2.2). Soon after the conventional $\alpha-$disk model (Shakura & Sunyaev, 1973) was discovered, it raised an important question about the possible origin of viscosity that transports the angular momentum. In their seminal work, Shakura & Sunyaev (1973) predicted that magnetohydrodynamic (MHD) turbulence could potentially account for the viscosity. Towards this, Eardley & Lightman (1975) and Ichimaru (1976) independently developed a theory of hydromagnetic turbulence, where magnetic stress accounts for the viscosity that arises from the fluctuating magnetic fields. Later, Balbus & Hawley (1991) pointed out that a weak poloidal magnetic field threading the disk taps the shear energy from the differential rotation and leads toward a shearing instability, widely known as magneto-rotational instability (MRI). This linear instability indeed generates fluctuating magnetic fields and powers the disk turbulence (Hawley et al., 1995).

MRI can be qualitatively explained by analyzing the behavior of a magnetized ideal fluid element in a differentially rotating disk (Balbus & Hawley, 1998, see for review). In the ideal MHD limit, the fluid is considered as a perfect conductor, where magnetic field lines are frozen into the fluids. Let us consider two fluid elements that are attached by a poloidal magnetic field line at radius r_m. With a small radial disturbance in the differentially rotating disk, the blob positions are displaced in such a way that one stays in a smaller orbit than the other. This initial perturbation eventually bends the field line and the fluid element at $r < r_m$ gains rotational velocity (Ω) due to the conservation of angular momentum. While the fluid element at larger radii ($r > r_m$) loses Ω for the same reason. When the magnetic field strength is strong enough, the field line simply flexes back and resists the separation between these two fluid blobs. However, if the field strength is relatively low, the field line exerts a slight pull on the fluid elements, reducing the angular momentum of the inner one, while the angular momentum of the fluid element at $r > r_m$ increases. The continuous occurrence of such a process throughout the disk eventually transports the angular momentum outwards and accretion begins. The astrophysical observations suggest the value of α to be in the range of $\sim 0.01 - 0.1$ (Gou et al., 2011, and references therein). Similar results were obtained in numerical simulations based on MRI (Penna et al., 2010), although they revealed that the value of α is not constant in the disk (Penna et al., 2013). Hence, the inclusion of magnetic fields (or the MRI) in the accretion disk model resolves the question of "α" in standard disk theory. This is obvious since the interaction between the magnetic field and the plasma generates turbulence, which develops the magnetic viscosity, $\alpha_{\rm mag} = \delta B_r\, \delta B_\phi / p_{\rm tot}$[6]. Once the MRI is triggered with an initial poloidal magnetic field, it self-consistently produces radial and toroidal magnetic fields within the disk.

Meanwhile, Pariev et al. (2003); Pessah & Psaltis (2005); Blaes et al. (2006) suggested that MRI-driven turbulence strongly amplifies the toroidal magnetic fields to a maximum value, which subsequently dominates the disk structure even in the region where radiation pressure exceeds the gas pressure. Following these works, Begelman & Pringle (2007) showed that an optically thick and geometrically thin accretion disk threaded by a strong toroidal magnetic field is thermally and viscously stable (unlike the standard 'thin'

[6]Here, δ represents the fluctuations of the radial B_r and toroidal B_ϕ field, and $p_{\rm tot}$ is the total pressure.

disk), although they did not discuss the optically thin disk. Notably, the magnetic fields often play an important role in transitioning between optically thin 'hot' and optically thick 'cold' disk (Ichimaru, 1977), where $p_{\rm mag}$ limits itself below the $p_{\rm gas}$. Otherwise, magnetic flux can buoyantly escape from the disk via Parker instability (Parker, 1966). However, Shibata et al. (1990); Mineshige et al. (1995) showed that a strongly magnetic pressure-supported (low-β disk with strong magnetic tension) disk suppresses the growth of Parker instability and disk stays in a quasi-equilibrium state.

Later, Machida et al. (2006) performed a global 3D MHD simulation considering a radiatively inefficient equilibrium torus threaded by weak toroidal magnetic fields. As the MRI develops in the torus, it leads to an optically thin, hot, $p_{\rm gas}$ dominated (high$-\beta$ disk) accretion flow, which describes the low/hard state of Galactic BHs. Once the density of the flow surpasses the critical threshold corresponding to the cooling instability, the disk cools down. It lowers the thermal pressure and eventually contracts the disk vertically. As the cooling timescale is much smaller than the buoyant escape timescale of the magnetic fluxes, the toroidal flux remains conserved (Machida et al., 2006). This enhanced magnetic pressure within the disks, and when $p_{\rm mag} > p_{\rm gas}$, the disk no longer shrinks vertically but is supported by the toroidal magnetic pressure. Consequently, Machida et al. (2006) noticed a transition of a high$-\beta$ disk into a radiatively efficient, cool, low-β disk. The magnetically supported low-β disk sustains for a timescale comparable to the accretion timescale, which is way more than the thermal timescale. Meanwhile, in a series of works, Oda et al. (2007, 2009, 2010, 2012) discussed the relevance of magnetically supported optically thin and thick disks on the thermal stability, which is dominated by the toroidal field component. However, they claimed that the interplay between radial and toroidal fields can not be neglected in a turbulent accretion disk *i.e.,* $< B_r\, B_\phi >$[7]. With this, in the present thesis, we focus on a vertically integrated, axisymmetric accretion disk threaded by both radial and toroidal magnetic fields. Moreover, Oda et al. (2012) revealed that low-β disks work satisfactorily over the ADAF/RIAF models at higher mass accretion rates, providing a robust explanation for the bright/hard state through the dynamics of optically thin low-β disks. Later, Li & Begelman (2014) revealed that magnetically driven outflows also help in stabilizing the accretion disk by lowering the disk

[7]Here, <> refers to the azimuthal averaging of the physical quantity.

temperature. Overall, the above-mentioned facts on stabilizing the disks via magnetic pressure support are broadly verified by several global GRMHD simulations (Sądowski, 2016a; Lančová et al., 2019; Mishra et al., 2022; Huang et al., 2023).

On the other hand, numerous efforts have been made to reveal the structure of the magnetic fields inside the accreting plasmas around BHs using 2D/3D GRMHD simulations (Hawley, 2001; De Villiers et al., 2003; Hirose et al., 2004; Kato et al., 2004; Dihingia et al., 2021; Mizuno, 2022). It is shown that the plunging region is mostly governed by the poloidal magnetic fields, although ordered toroidal fields play a significant role in regulating the dynamics at the inner parts of the disk. So far, we have realized that the accretion disk around a BH is expected to be threaded by large-scale magnetic fields. But, what is the origin of such fields? or how do these strong fields reach near the BHs? Bisnovatyi-Kogan & Ruzmaikin (1974, 1976); Bisnovatyi-Kogan & Lovelace (2000) suggested that the fields can arise from either the low-mass companion star or the interstellar medium. In this regard, Sądowski (2016a,b) argued that in a tidally locked XRB, the companion star could provide such strong magnetic flux ($\sim 10^{22} - 10^{24}$ G cm^2) that eventually stabilizes the inner regions of the thin disk. Furthermore, Sądowski (2016a,b) questioned the accumulation of large-scale fields since SSD is unable to drag such strong magnetic fields onto the BH (Lubow et al., 1994; Ghosh & Abramowicz, 1997). Meanwhile, Guilet & Ogilvie (2012, 2013) proposed that by considering the vertical structure of the disk, the advection of magnetic fluxes would be much faster. This eventually leads to surface accretion, which is commonly observed in strongly magnetized disks (Mishra et al., 2020, 2022; Begelman et al., 2022). Also, the conservation of toroidal flux (Machida et al., 2006), often plays an important role in gathering large-scale magnetic fields near the BHs. On the contrary, Avara et al. (2016), with their radiatively efficient thin disk simulation, showed that large-scale magnetic fields accrete through the disk naturally while enhancing disk's radiative efficiency. Meanwhile, MHD simulations of large-scale dynamics (Ressler et al., 2020a,b) showed that initially weak magnetic fields from stellar winds are passively advected towards the BH. As the field lines accumulate at horizon scales, they become dynamically important and begin to regulate accretion, similar to magnetically arrested disks (MADs; Igumenshchev et al., 2003; Narayan et al., 2003; Chael et al., 2019; Chatterjee & Narayan, 2022, Bisnovatyi-Kogan, 2019, see for

review). In MAD, the outward pressure exerted by the accumulated magnetic flux is balanced by the inward gravitational pull of the BH. There exists another class of accretion solutions with relatively weak magnetic flux, *i.e.,* SANE (Standard And Normal Evolution; Narayan et al. (2012); Sądowski et al. (2013); Ryan et al. (2018)) model, where the plasma motion guides the field lines in the disks (Ricarte et al., 2021).

One of the most intriguing features of magnetic fields is that they help in launching jets or outflows around BHs (Davis & Tchekhovskoy, 2020, for review). When large-scale magnetic fields thread the ergosphere, the field lines can extract energy from a rotating BH via Blandford-Znajek mechanism (Blandford & Znajek, 1977, hereafter BZ77) and eventually produce magnetically driven powerful jets. On the other hand, the convergent matter can leave the surface of the accretion disk with the help of magneto-centrifugal wind popularly known as Blandford-Payne (BP) wind (Blandford & Payne, 1982). Following these two mechanisms, several MHD simulations confirmed that jets/outflows are mainly produced from the accretion disk with the help of magnetic fields (Shibata & Uchida, 1985; Koide et al., 1999; De Villiers et al., 2005; Hawley & Krolik, 2006; Ohsuga & Mineshige, 2011; Tchekhovskoy et al., 2011; Dihingia et al., 2021; Kwan et al., 2023; Aktar et al., 2024a,b). However, it is important to note that all of these studies are reliant on specific models. Hence, an exact configuration of the magnetic fields within the disk remains unresolved. In this thesis, as a first step, we plan to take up this challenge and discuss the global structure of a steady, axisymmetric, MHD accretion flow using full GR framework.

Finally, the major breakthrough came with the recent findings of dynamically important large-scale fields (Event Horizon Telescope Collaboration et al., 2021, 2024) around SMBHs, *i.e.,* M87 and Sgr A*, confirming the direct influence of magnetic fields on the accretion-ejection mechanisms. Therefore, magnetic fields are inevitable in accretion disks and need to be studied with great detail.

1.4 Overview: Relativistic stationary accretion flow

The majority of matter in the universe exists in some form of fluids, and in many astrophysical scenarios (such as supernova explosions, jets, and accretion onto black holes/neutron stars), it undergoes relativistic motion. This highlights the significance of studying relativistic fluid dynamics, including both hydrodynamics and magnetohydrodynamics (Lichnerowicz, 1970; Anile, 1990; Font, 2008; Rezzolla & Zanotti, 2013). In this thesis, we focus on analyzing the hydrodynamics and magnetohydrodynamics nature of steady accretion flows onto BHs.

1.4.1 Newtonian hydrodynamics

Hydrodynamics is a model-independent approach that helps in examining the low energy dynamics of any generic field theory which is based on the underlying symmetry and conservation laws. In general, the space-time around the BHs happens to be extremely curved, and relativistic effects become dominant. Therefore, with Newtonian hydrodynamics (HD), one can not describe the real scenario occurring to the fluid close to the BH. Indeed, the relativistic/general relativistic (GR) formalism of hydrodynamics is required. Before delving into the complex details of GRHD, astrophysicists simplified the problem with the pseudo-Newtonian framework, where the Newtonian potential in the Newtonian HD equations is being replaced with the Paczyński & Wiita (1980) potential. Using PW80 potential, numerous studies have been performed so far, both semi-analytically as well as with numerical simulations (Liang & Thompson, 1980; Abramowicz & Zurek, 1981; Muchotrzeb & Paczynski, 1982; Matsumoto et al., 1984; Muchotrzeb-Czerny, 1986; Fukue, 1987; Chakrabarti, 1989; Narayan et al., 1997; Das et al., 2001b; Takahashi et al., 2002; Das & Chakrabarti, 2004; Machida et al., 2006; Das, 2007; Das & Chakrabarti, 2007; Oda et al., 2007; Das & Chakrabarti, 2008; Das et al., 2009, 2010, 2014; Mukhopadhyay & Chatterjee, 2015). This effective pseudo-Newtonian potential satisfactorily mimics the space-time around a Schwarzschild BH. However, the pseudo-Newtonian potential fails to satisfy the inner boundary condition as the free-fall velocity exceeds the speed of light near the horizon (Becker & Le, 2003; Das et al., 2009).

On the other hand, most of the astrophysical objects are envisioned to be rotating in nature (Reynolds, 2021). The space-time around a Kerr BH is very complex as the BH has one extra 'hair', *i.e.,* spin angular momentum ($a_{\rm k}$). Due to the spinning nature of the central BH, the frame-dragging effect drags the nearby space-time and the BH horizon is shifted even further inwards, $r_{\rm h} = 1 + \sqrt{1 - a_{\rm k}^2}$. Several attempts have been made to obtain the effective potentials that satisfactorily describe the space-time around Kerr BH (Artemova et al., 1996 (ABN96), Mukhopadhyay, 2002 (MU02), Chakrabarti & Mondal, 2006 (CM06)). These pseudo-Kerr potentials were formulated based on certain physical constraints and aimed to address specific problems. Hence, all the above-mentioned potentials have limitations on their own. For instance, the CM06 potential is unable to describe the space-time around a Kerr BH with spin $a_{\rm k} > 0.8$. Hence, this potential can not be used to study the accretion flows around rapidly rotating BHs (*i.e.,* Cyg X-1, LMC X-1, GRS-1915+105, Sgr A*, M87, etc.). Recently, Aktar et al. (2019) examined the shocked accretion solutions involving all three pseudo-Kerr potentials. The authors noticed that the results significantly differ from each other when the BH spin is higher and shock ceases to exist beyond $a_{\rm k} > 0.84$ for MU02 and $a_{\rm k} > 0.92$ for ABN96 potentials. It is, therefore, difficult to rely on these pseudo-Kerr potentials, and general relativistic treatment is required to obtain an effective potential without any restrictions.

1.4.2 Relativistic hydrodynamics

The quest for the accretion flows around Kerr BH with GR formalism started with Page & Thorne (1974); Fukue (1987); Riffert & Herold (1995); Abramowicz et al. (1996, 1997); Peitz & Appl (1997), although they have assumed a polytropic equation of state. Meanwhile, Gammie & Popham (1998); Popham & Gammie (1998) showcased the importance of a relativistic equation of state (REoS) onto the accretion flows. Later, Chattopadhyay & Chakrabarti (2011) investigated the effect of fluid composition on the accretion solutions with another REoS (Chattopadhyay & Ryu, 2009). Further, Dihingia et al. (2018a) solved the GRHD equations around the general stationary axisymmetric background and identified the form of GR effective potential from the momentum equations. Clearly, the spin effect is manifested in the effective potential as *spin-orbit*

coupling with the specific angular momentum (λ) of the flow. Unlike the previous pseudo-Kerr potential, the GR effective potential does not suffer any limitations and even works seamlessly for $a_{\rm k} \to 1$. Dihingia et al. (2018a) further tested the transonic accretion flow model in the semi-relativistic (SR, where the Lorentz factor $\gamma \sim 1$) regime and found good agreement with the GR results. Soon after the development of such effective potential, several semi-analytic works have been performed around various axisymmetric non-Kerr space-times (Dihingia et al., 2020b; Sen et al., 2022; Patra et al., 2022, 2024) in full GR, and also using SR equations (Dihingia et al., 2020a; Singh & Das, 2024; Jana & Das, 2024).

1.4.3 GR + Magnetohydrodynamics (MHD)

When large-scale magnetic stress becomes dynamically important, magnetohydrodynamics (MHD) becomes a relevant theoretical tool to explain the fluid motion around BHs. In this context, we consider the perfect fluids with EM induction, but having an infinite conductivity, *i.e.,* ideal MHD. The study of magnetized accretion/winds is not new; it started way back in the late 1960s with the pioneering works led by Weber & Davis (1967); Mestel (1968) in the context of solar winds. Meanwhile, Camenzind (1986a,b, 1987) formulated the relativistic version of MHD wind, which could be applicable to any stationary and axisymmetric rapid rotating compact object with a surrounding magnetosphere. Later, it was extended to Kerr background by Camenzind (1989). Following this approach, Takahashi et al. (1990) analyzed the Alfvén point[8] of the poloidal flow equations[9] within the BH magnetosphere. Here, a BH magnetosphere was assumed in relation to the AGN activity. Overall, this work focussed on the poloidal flow equation for smooth trans-Alfvénic solutions that carry negative energy along the poloidal field lines inside the event horizon. This, in turn, helps extract energy from the rotating BH. In this context, Gammie (1999) reported that relativistic magnetized disks in steady state possess higher accretion efficiency compared to thin disks due to non-vanishing magnetic torques in the plunging region. Surprisingly, GRMHD simulations show similar efficiency for both thick and thin disks (McKinney & Gammie, 2004). Meanwhile, Takahashi (2002)

[8]Unlike hydrodynamics, the magnetized flow is generally characterized by three sonic points, namely, the fast and slow magnetosonic points and the Alfvén point.

[9]These equations correspond to the poloidal velocity.

reported the necessary conditions for a trans-magnetosonic accretion to occur around a BH magnetosphere. Takahashi (2002) further showed that hot, magnetized flow originating from a stagnant plasma source (e.g., disk surface) could enter into the horizon after passing sequentially through the slow magnetosonic, the Alfvén, and fast magnetosonic point, following the magnetic flux tube. Such poynting flux-dominated (PFD) flow is useful near the BHs to model two-dimensional steady inflow-outflow GRMHD solutions (Pu et al., 2015).

In several works, it has been demonstrated that the formation of shock waves in MHD accretion flows around BHs is a physically plausible mechanism for creating very hot and strongly magnetized coronal regions. These regions could possibly be associated with subsequent thermal or nonthermal high energy emissions. Meanwhile, Koide et al. (1999) and Nishikawa et al. (2005) discovered from their MHD simulations that the creation of a jet originates from the high-temperature areas due to shock compression. Hence, the magnetized post-shock corona may act as the base of the magnetized outflows. Takahashi et al. (2002) extend the work by Appl & Camenzind (1988) for special relativistic MHD jets to the GR framework while studying the standing shock formation for accreting MHD plasma around a rotating, stationary, and axisymmetric BH magnetosphere. Later, (Rilett, 2004) reported that the slow-MHD shocks are considered to be ineffective particle accelerators, so examining the fast-MHD shock is important. Furthermore, Fukumura et al. (2007) performed an off-equatorial shock study where they observed that the poloidal magnetic field and BH spin largely alter the shock properties.

In all the above studies, authors considered a stationary and axisymmetric BH magnetosphere and solved the poloidal field equations close to the horizon. However, these works have not discussed the details of the plasma source, which can be a torus or a thin disk. The plasma begins its journey from the surface of the disk and connects to the ergosphere or the BH horizon via loop-like field lines. On the contrary, in the present thesis, we are interested in studying the vertically integrated magnetized disk structure, which extends upto ~ 1000 gravitational radius. With this, we investigate the trans-magnetosonic accretion solution around BHs using a REoS.

1.4.4 Post-Newtonian Hydrodynamics

As discussed earlier, GR effects are prominent near the compact object, while the space-time far from the central object can be described by the Newtonian gravity. However, there is a need to bridge between Newtonian and GR formalism of accretion flows, particularly in regions where Newtonian gravity deviates from the exact GR results. In this regard, the slow-motion condition and weak field limit of general relativity play a crucial role, which is the post-Newtonian (PN) theory. The PN theory is a method of successive approximations in $1/c^2$ for the solution of Einstein's field equations, which was introduced by Einstein et al. (1938). Based on this idea, the post-Newtonian hydrodynamics was formulated in several works (Fock, 1964; Chandrasekhar, 1965, 1967, 1969; Chandrasekhar & Nutku, 1969; Chandrasekhar & Esposito, 1970; Will, 1993, 2011; Poisson & Will, 2014). These equations include Newtonian hydrodynamics and gravity (0PN), the first-order relativistic corrections to those (1PN) or successive higher order terms. The PN framework is largely discussed in the context of gravitational waves (Abbott et al., 2017) and binary systems (Blanchet & Damour, 1989; Damour & Taylor, 1991; Blanchet et al., 1995; Lai & Wiseman, 1996; Faber & Rasio, 2000). However, in the context of accretion flows, post-Newtonian gravity has not been thoroughly explored except for a few cases around spherically symmetric accretion by Kremer & Mehret (2021) and twisted accretion model with self-gravity (Demianski & Ivanov, 1997; Ivanov & Illarionov, 1997; Jaranowski et al., 2015). Therefore, we plan to investigate the properties of transonic accretion flows in post-Newtonian gravity.

1.4.5 Need for semi-analytic modeling

With the state-of-the-art GRMHD simulations, the EHT collaboration (Porth et al., 2019; Event Horizon Telescope Collaboration et al., 2019b, 2022) successfully interprets the horizon-scale observations of Sgr A* and M87. This opens up new possibilities to examine the behaviour of accreting (outflowing) plasmas in the immediate vicinity of the BHs. However, the numerical studies to investigate the horizon-scale structure of the accretion flow that results from a large-scale feeding (*i.e.,* Bondi radius $\sim 10^6$ gravitational radius (Frank et al., 2002)) pose a significant computational threat. This

challenge arises for the required simulation length and timescales spanning approximately six orders of magnitude (Olivares S. et al., 2023). Therefore, it is highly desirable to acquire deeper insights into the properties of the accretion flow through the semi-analytic transonic accretion solutions that connect the event horizon to infinity.

These analytical solutions are derived based on simple conservation principles, which shall be discussed in this thesis. Semi-analytic models of transonic accretion flows are useful as one can achieve various topological structures (*i.e.,* smooth, Bondi-like flows, standing accretion shocks, or the formation of circularized tori) with different choices of flow parameters, namely angular momentum, energy, plasma$-\beta$ or the local magnetic field strength. Over the years, several successive attempts were made to examine the steady state hydrodynamic and magnetohydrodynamic accretion solutions semi-analytically in the non-relativistic (Aktar et al., 2015, 2017; Sarkar & Das, 2016, 2018; Sarkar et al., 2018; Dihingia et al., 2018b, references therein), and general relativistic frameworks (Fukumura & Kazanas, 2007; Kumar et al., 2013; Dihingia et al., 2018a, 2020b, 2019; Sarkar et al., 2020; Das et al., 2022; Patra et al., 2022; Sen et al., 2022, and references therein). We emphasize that these semi-analytic solutions are potentially viable to provide the steady state seed solutions that would be useful to carry out the more realistic global hydrodynamic and magnetohydrodynamic simulation studies.

However, semi-analytic multi-transonic accretion solutions in the GRMHD framework have yet to be explored. Earlier semi-analytical GRMHD studies by Fukumura et al. (2007) limit themselves only to the polytropic EoS. Hence, a full GR based analysis with appropriate REoS is essential. Further, the study of the energy transport process with thermal conduction in viscous hot, transonic accretion flows is yet to be discussed. Apart from this, the utility of semi-analytic solutions in examining various gravitational backgrounds (modified gravity, non-Kerr space-time, post-Newtonian background) needs to be studied in detail. Being motivated by this, in this thesis, we present the relativistic, advective, and transonic accretion flows around black holes in the magneto-hydrodynamic, hydrodynamic, and post-Newtonian hydrodynamic frameworks.

1.5 Outline of the thesis

The purpose of this thesis is to delve into the intricacies of astrophysical fluid dynamics, with a specific focus on accretion processes around BHs. In the first part of this thesis, we carry out an extensive study of the properties of low angular momentum magnetized accretion flows around BHs in a steady state regime. In doing so, we adopt a single-temperature, advective accretion flow model that incorporates a complete general relativistic (GR) treatment. The accretion flow is considered to be highly conductive in nature and is threaded by radial and toroidal magnetic field components within the disk midplane. Using this vertically integrated flow model, we provide a detailed discussion on the interplay between the radial and toroidal magnetic fields, and we analyze the family of global, trans-magnetosonic accretion solutions. Interestingly, the present low angular momentum GRMHD flow exhibits a multi-transonic behaviour, transitioning between subsonic-to-supersonic velocities at multiple radii within the disk. This multi-transonic nature leads us to explore the shock-induced GRMHD accretion solutions around both the rotating and non-rotating BHs. With the GRMHD shock solutions, we find the upper limit of allowed magnetic flux, which remains within the SANE limit. The second part of the thesis focuses on the hydrodynamic aspects of the hot accretion flow (HAF), with a particular emphasis on the mechanisms of energy transport. In this regard, we investigate the role of saturated thermal conduction in facilitating energy exchange within the accretion flow. Subsequently, we study the influence of thermal conduction on the transonic solutions and the corresponding flow variables. Finally, we discuss the global accretion solutions around a rotating compact object following the post-Newtonian hydrodynamics up to the leading-order corrections.

Overall, this thesis consists of four working chapters, each providing a comprehensive and in-depth discussion of the various aspects investigated.

1.5.1 Chapter 2

Chapter 2 presents a novel approach to analyze the global structure of steady, axisymmetric, advective, magnetohydrodynamic (MHD) accretion flows around Schwarzschild

BH in a general relativistic regime. Considering ideal MHD conditions, the convergent flow is threaded by radial (b^r) and toroidal (b^ϕ) magnetic fields in the disk mid-plane. In such relativistic flows, thermodynamics is aptly governed by the REoS, where the adiabatic index is a function of temperature. With this, we solve the governing GRMHD equations, and for the first time, we obtain the global trans-magnetosonic steady accretion solution. We examine the properties of trans-magnetosonic accretion flow in terms of the flow parameters, namely the conserved energy ($\mathcal{E}$) and angular momentum flux ($\mathcal{L}$), and local magnetic fields (b^r, b^ϕ). Depending on several combinations of these model parameters, we showcase a wide class of smooth trans-magnetosonic accretion solutions passing through the inner ($r_{\rm in}$) and outer ($r_{\rm out}$) critical points. However, not all ($\mathcal{E}, \mathcal{L}, b^r, b^\phi$) combinations result in global accretion solutions, as the flow often fails to reach the outer edge of the disk. Accretion solutions, passing through $r_{\rm in}$, presumably be more magnetically active than the other solutions. In the present axisymmetric flow, we observe that the toroidal component (b^ϕ) of the magnetic fields usually dominates over the radial component (b^r) all over the mid-plane. However, the radial component overcomes the toroidal field near the BH, $r \leq 3$ (Begelman et al., 2022). Overall, the vertically averaged disk remains mostly gas pressure ($p_{\rm gas}$) dominated ($\beta = p_{\rm gas}/p_{\rm mag} > 1$, $p_{\rm mag}$ refers magnetic pressure) except at the near horizon region, where magnetic fields become stronger $\beta \sim 1$. Meanwhile, the continuous interplay between b^r and b^ϕ develops the Maxwell stress ($T^{\rm MAX}_{r\phi}$), which eventually yields angular momentum transport to sustain the accretion process. Towards this, we calculate the viscosity parameter (α) due to Maxwell's stress, and it appears to be radially varying, suggesting the importance of magnetic fields on the disk dynamics.

1.5.2 Chapter 3

During accretion, the low angular momentum sub-Keplerian matter often piles up in the vicinity of the BH due to centrifugal repulsion, which eventually triggers a discontinuous shock transition of the flow variables. Shock solutions are of utmost importance due to their ability to explain the spectro-temporal behaviours of BH-XRBs. However, in the GRMHD framework, such centrifugally supported shock is yet to be explored. As discussed in Chapter 2, low-λ GRMHD flows often display a multi-transonic nature.

Keeping this in mind, in Chapter 3, we investigate the shock-induced steady GRMHD solutions around a Kerr BH by implying appropriate jump conditions. We observe that shock solutions are not isolated solutions, as they continue to exist for a wide range of model parameters, namely $\mathcal{E}, \mathcal{L}$, conserved radial magnetic flux (Φ), and iso-rotation parameter (F). Towards this, we identify the shock parameter space in $\mathcal{L} - \mathcal{E}$ plane. Further, we explore the modifications of $\mathcal{L} - \mathcal{E}$ space and identify that it alters with BH spin ($a_{\rm k}$) and Φ. While comparing the shock solutions around weakly and rapidly spinning BHs, we notice that shock forms at a relatively smaller radius for BHs with $a_{\rm k} = 0.99$ compared to the results of $a_{\rm k} = 0$ case. Due to shock compression, the toroidal magnetic field gets amplified enormously in the post-shock regime. Hence, the post-shock flow is mainly governed by b^{ϕ}. Moreover, with different combinations of $(\mathcal{E}, \mathcal{L}, \Phi, F)$, we obtain ranges of shock location ($r_{\rm sh}$), compression ratio (R), and shock strength (Ψ), which are responsible to determine the nature of post-shock flow or corona (PSC). Since Φ significantly influences the shock properties, $(r_{\rm sh}, R, \Psi)$, therefore the magnetic fields essentially affect the spectral state transitions in BH-XRBs. Meanwhile, we estimate the maximum allowed magnetic flux ($\Phi^{\rm cri}$) for which the shock solution persists, and, find that $\Phi^{\rm cri}$ fails to achieve the Magnetically Arrested Disk (MAD) flux. We also observe that $\Phi^{\rm cri}$ strongly depends on the BH spin. Finally, we discuss the astrophysical importance of shock waves in the context of GRMHD flow.

1.5.3 Chapter 4

In Chapter 4, we focus on hot advective accretion flows, which are common in the SMBHs and LLAGNs. In these systems, central BH engulfs matter at a low accretion rate, and the surrounding hot plasma happens to be collisionless. Consequently, thermal conduction becomes important in governing the accretion disk dynamics and allows the accreting matter to transport energy via heat flux. To this end, we employ the saturated form of conductive heat flux and numerically solve the set of dynamical equations corresponding to a steady, axisymmetric, viscous, advective accretion flow. We analyze the accretion dynamics in terms of the input parameters, namely energy (ε_0) and angular momentum at the horizon (λ_0), viscosity parameter (α), and the saturation constant ($\Phi_{\rm s}$) that regulates the effect of thermal conduction. Our findings suggest that the saturation constant ($\Phi_{\rm s}$),

plays a pivotal role in determining the transonic characteristics of the global accretion solutions. When Φ_s is increased, the critical point (r_c) recedes away from the BH, and flow variables are altered, especially in the outer part of the disk. Further, we put effort into estimating the maximum saturation constant (Φ_s^{max}) for which global transonic solutions exist. On the contrary, Φ_s^{max} obtained from the global transonic solutions exceeds the value predicted by the self-similar approach. Overall, thermal conduction provides an extra degree of freedom to the system (latitudinal energy transport, Tanaka & Menou (2006)), which is necessary for launching outflows from the disk. Towards this, we compute the Bernoulli parameter (Be), which remains positive throughout the disk, suggesting the unbound nature of the convergent flow. In the end, we highlight the relevance of this work in the astrophysical context, as thermal conduction sheds light on the mass loss from the unbound disk.

1.5.4 Chapter 5

In reality, when the convergent flow approaches the horizon (or surface of NS), GR effects become dominant, and due to a high degree of non-linearity, it is generally difficult to solve the problem by including all necessary physical processes. To avoid such complexity, most of the analysis of the accretion flow invokes the Newtonian or pseudo-Newtonian equations, as we did in Chapter 4. However, the Newtonian potential is not suitable to explain gravity around BHs, and the pseudo-Newtonian potentials (Paczyński & Wiita, 1980) have several limitations, particularly around a maximally rotating BH (Dihingia et al., 2018a). Therefore, in Chapter 5, we seek an alternative approach to deal with the complex phenomenon of accretion physics around spinning compact bodies. Towards this, we follow the post-Newtonian (PN) theory, which is based on the slow-motion condition and weak field limit of GR. Applying the weak field limit, we estimate the PN radius ($r_{PN} \sim 10$ gravitational radii), which is considered as the radius upto which the PN theory works perfectly. In the next, we develop the most general formalism of PN hydrodynamics equations (Poisson & Will, 2014, see for details) around a spinning compact object up to the leading PN order $\mathcal{O}(c^{-2})$, *i.e.,* 1_{PN} . We further identify the PN effective potential (Φ_{eff}^{PN}) from the Euler equations and observe that Φ_{eff}^{PN} mimics the exact GR effective potential even beyond the PN regime, *i.e.,* $r \leq r_{PN}$ (Will, 2011).

However, to study the transonic accretion solutions, we consider the flow to be stationary, axisymmetric, and inviscid. Considering the IEoS, we analyze the vertically integrated accretion flows and obtain a global transonic accretion solution for the first time to the best of our knowledge. It is worth mentioning that we restrict ourselves only to the accretion solutions passing through $r_{\rm out}$, since $r_{\rm in} \ll r_{\rm PN}$. Furthermore, we provide a qualitative estimate of the amount of radiative flux emitted from the disk, and the PN correction contributes as $\sim 1/r^5$. Finally, we suggest that the present theoretical formalism might be useful in providing the missing link between the Newtonian and GR descriptions of accretion flows.

Following these chapters, in Chapter 6, we provide the overall conclusion of the thesis with a summary of possible future studies.

Chapter 2

Study of general relativistic magnetohydrodynamic accretion flow around black holes

The content of this chapter has been published in Mitra S., Maity D., Dihingia I. K., Das S., 2022, MNRAS, 516, 5092.

In this Chapter, we present a novel approach to study the magnetohydrodynamic (MHD) accretion flows around a Schwarzschild BH adopting the general relativistic (GR) framework and provide an insight into the possible magnetic field configuration in the steady state. Based on the disk geometry (*i.e.,* axisymmetry) and plasma dynamics around BHs, the toroidal magnetic fields stand out as the simplest choice in an accretion disk (Machida et al., 2000, 2006; Hirose et al., 2004). Meanwhile, in the series of works, Oda et al. (2007, 2009, 2010, 2012) mentioned that the interplay between radial and toroidal magnetic fields can not be neglected inside a turbulent disk. For an advective flow, the presence of a radial magnetic fields is obvious due to the dominant radial motion of accreting plasmas, particularly in the near horizon region. Therefore, in this work, we consider the disk to be threaded by both the radial (b^r) and toroidal (b^ϕ) components of magnetic fields. To account for the dynamics of the magnetic fields, we use the homogeneous Faraday's law. Additionally, we consider the ideal GRMHD approximation (Koide et al., 1998; Koide, 2004; McKinney & Gammie, 2004) and ignore

the exchange of energies between the plasmas and the radiation field (Anile, 1990; Porth et al., 2019) for simplicity. Here, the thermodynamics of the flow is governed by a simplified relativistic equation of state (REoS) proposed by Chattopadhyay & Ryu (2009) for a multi-component ionized fluid. With this, we solve the governing GRMHD equations for accreting matter to get all the flow variables, namely, density, temperature, velocity, and magnetic fields, using a general relativistic approach (Dihingia et al., 2018a). Further, we examine the dynamical and thermodynamical properties of accreting matter in terms of the flow parameters, namely energy flux ($\mathcal{E}$), angular momentum flux ($\mathcal{L}$), and local magnetic fields (b^r, b^ϕ). By tuning these model parameters, we obtain all the smooth global trans-magnetosonic accretion solutions passing through the inner and outer critical points ($r_{\rm in}$ and $r_{\rm out}$). Here, we wish to emphasize that solutions of these kinds are not isolated solutions; instead they exist for a wide range of flow parameters. While envisaging this fact, we examine the range of flow parameters that admits closed accretion solutions passing through $r_{\rm in}$. This closed type of accretion solution fails to connect the event horizon with the outer edge of the disk. Within the framework of GRMHD, the existence of these wide classes of accretion solutions had not been reported before. Meanwhile, in a vertically integrated GRMHD flow, we observe that the toroidal component (b^ϕ) of the magnetic fields generally dominates over the radial component (b^r) at the disk mid-plane. This evidently suggests that the toroidal magnetic fields indeed play an important role in regulating the disk dynamics. We further notice that the disk remains mostly gas pressure ($p_{\rm gas}$) dominated ($\beta = p_{\rm gas}/p_{\rm mag} > 1$, $p_{\rm mag}$ is the magnetic pressure) except at the near horizon region, where magnetic fields become indispensable ($\beta \sim 1$). With the interplay between b^r and b^ϕ, Maxwell stress is developed, which eventually allows angular momentum transport inside the disk. Towards this, we calculate the viscosity parameter (α) that appears to vary radially and often exceeds unity in the immediate vicinity of the BH. In addition, we examine the underlying scaling relation between α and β, which clearly distinguishes two accretion domains that coexist along the radial extent of the disk. Finally, we discuss the utility of the present formalism in the realm of GRMHD simulation studies.

2.1 GRMHD formalism and underlying assumptions

In order to investigate the magnetohydrodynamic properties of accreting plasma, we consider the GRMHD equations in a stationary axisymmetric space-time. This space-time possesses two commuting killing vectors associated with time (t) and azimuthal coordinate (ϕ) and is given by ξ^t and ξ^ϕ, respectively. The general line element in this space-time is written in Boyer-Lindquist coordinate (t, r, θ, ϕ) (Boyer & Lindquist, 1967) as,

$$ds^2 = g_{tt}dt^2 + 2g_{t\phi}dtd\phi + g_{rr}dr^2 + g_{\theta\theta}d\theta^2 + g_{\phi\phi}d\phi^2. \tag{2.1}$$

The BH is placed at the origin of the coordinate system, and the event horizon is identified as $g^{rr} = 1/g_{rr} = 0$. To express the flow variables, we use a unit system as $M_{\rm BH} = G = c = 1$, where $M_{\rm BH}$ is the black hole mass, G is the gravitational constant and c is the speed of light, respectively. Following this unit system, the radial coordinate, angular momentum, and flow velocity are measured in units of $GM_{\rm BH}/c^2$, $GM_{\rm BH}/c$, and c, respectively. With all these assumptions, in this chapter, we solely focus on studying the accretion dynamics around a Schwarzschild BH, where the metric coefficients are given by $g_{tt} = -(1 - 2/r)$, $g_{rr} = 1/(1 - 2/r)$, $g_{t\phi} = 0$, $g_{\theta\theta} = r^2$, and $g_{\phi\phi} = r^2 \sin^2\theta$.

2.1.1 GRMHD equations

In order to describe the relativistic magnetized accretion processes, the governing GRMHD equations are obtained from the mass conservation, energy-momentum conservation, and the homogeneous Faraday's law (Anile, 1990; De Villiers et al., 2003; Gammie et al., 2003) which are as follows:

$$\nabla_\mu (\rho u^\mu) = 0; \qquad \nabla_\mu T^{\mu\nu} = 0; \qquad \nabla_\mu {}^*\mathcal{F}^{\mu\nu} = 0. \tag{2.2}$$

In these equations, ρ is the mass density, u^μ is the four-velocity of matter, $T^{\mu\nu}$ is the stress energy-momentum tensor and ${}^*\mathcal{F}^{\mu\nu} = \frac{1}{2}(-g)^{-1/2}\eta^{\mu\nu\delta\kappa}\mathcal{F}_{\delta\kappa}$ denotes the Hodge dual of Faraday electromagnetic tensor $\mathcal{F}^{\mu\nu}$, where $g = \det[g_{\mu\nu}]$ is the determinant of the metric. Note that we follow a convention where the four velocities satisfy $u_\mu u^\mu = -1$.

Note: In Einstein's general relativity, the covariant derivative acting on a single rank contravariant tensor is expressed as,

$$\nabla_\mu A^\nu = \partial_\mu A^\nu + \Gamma^\nu_{\mu\alpha} A^\alpha.$$

Here, $\partial_\mu = \frac{\partial}{\partial x^\mu}$ is the partial derivative with respect to the space-time coordinate (x^μ), and $\Gamma^\nu_{\mu\alpha}$ is called the Christoffel connection which is fully determined by the metric, $\Gamma^\nu_{\mu\alpha} = \frac{1}{2} g^{\nu\kappa}(\partial_\mu g_{\kappa\alpha} + \partial_\alpha g_{\kappa\mu} - \partial_\kappa g_{\mu\alpha})$.

Special case: The covariant divergence of A^μ is given by

$$\nabla_\mu A^\mu = \frac{1}{\sqrt{-g}} \partial_\mu (\sqrt{-g} A^\mu),$$

and covariant derivative of an anti-symmetric tensor,

$$\nabla_\mu \mathcal{F}^{\mu\nu} = \frac{1}{\sqrt{-g}} \partial_\mu (\sqrt{-g} \mathcal{F}^{\mu\nu}).$$

Note: All the space-time (Greek) indices (μ, ν, λ) run from $0 \to 3$, whereas the Roman indices (i, j, k) run from $1 \to 3$.

Next, we provide the general form of energy-momentum tensor $(T^{\mu\nu})$ that is relevant in the accretion disk theory as,

$$T^{\mu\nu}_{\rm Gen} = T^{\mu\nu}_{\rm FLU} + T^{\mu\nu}_{\rm VIS} + T^{\mu\nu}_{\rm MAX} + T^{\mu\nu}_{\rm RAD},$$

where $1^{\rm st}$, $2^{\rm nd}$, $3^{\rm rd}$ and $4^{\rm th}$ terms in the right-hand side denote the contributions from the FLU-id, VIS-cous, MAX-well, and the RAD-iations (Abramowicz & Fragile, 2013). For the purpose of simplicity, in this work, we restrict ourselves only to the FLU-id and MAX-well parts. With this, we obtain the simplified energy-momentum tensor as

$$T^{\mu\nu} = (e + p_{\rm gas}) u^\mu u^\nu + p_{\rm gas} g^{\mu\nu} + \mathcal{F}^\mu_{\ \lambda} \mathcal{F}^{\nu\lambda} - \frac{1}{4} \mathcal{F}^2 g^{\mu\nu}, \tag{2.3}$$

where e and $p_{\rm gas}$ are the internal energy density and the gas pressure of the flow. Here, $\mathcal{F}^2 = \mathcal{F}_{\mu\nu}\mathcal{F}^{\mu\nu}$.

In the fluid frame, $\mathcal{F}_{\mu\nu}$ can be decomposed into electric field, $\mathbb{E}^{\mu} = \mathcal{F}^{\mu\nu}u_{\nu}$, and magnetic field $b^{\mu} = {}^{*}\mathcal{F}^{\mu\nu}u_{\nu}$, such that the following relation holds (Misner et al., 1973; Baumgarte & Shapiro, 2003),

$$\mathcal{F}^{\mu\nu} = u^{\mu}\mathbb{E}^{\nu} - u^{\nu}\mathbb{E}^{\mu} - (-g)^{-1/2}\eta^{\mu\nu\lambda\delta}u_{\lambda}b_{\delta}. \tag{2.4}$$

$${}^{*}\mathcal{F}^{\mu\nu} = u^{\mu}b^{\nu} - u^{\nu}b^{\mu} - (-g)^{-1/2}\eta^{\mu\nu\lambda\delta}u_{\lambda}\mathbb{E}_{\delta}. \tag{2.5}$$

In this work, we consider ideal GRMHD approximation where the conductivity of the fluid tends to infinity and, consequently, electric field $\mathbb{E}^{\mu} = 0$. This allows the magnetic field lines to remain frozen into the accreting plasmas, and plasma 'blobs' are forced to move along the field lines. With this approximation, the form of field tensors reduces to,

$$\mathcal{F}^{\mu\nu} = -(-g)^{-1/2}\eta^{\mu\nu\lambda\delta}u_{\lambda}b_{\delta}, {}^{*}\mathcal{F}^{\mu\nu} = u^{\mu}b^{\nu} - u^{\nu}b^{\mu}. \tag{2.6}$$

Using Eq. (2.6), we obtain the energy-momentum tensor as,

$$T^{\mu\nu} = (e + p_{\rm gas})u^{\mu}u^{\nu} + p_{\rm gas}g^{\mu\nu} + \frac{1}{2}g^{\mu\nu}b^2 + b^2u^{\mu}u^{\nu} - b^{\mu}b^{\nu}. \tag{2.7}$$

After some simple algebraic steps, we get,

$$T^{\mu\nu} = \rho h_{\rm tot}u^{\mu}u^{\nu} + p_{\rm tot}g^{\mu\nu} - b^{\mu}b^{\nu}. \tag{2.8}$$

Here, $h_{\rm tot} = h + B^2/\rho$, where the specific enthalpy of the gas is given by $h = (e + p_{\rm gas})/\rho$, and $p_{\rm tot} = p_{\rm gas} + p_{\rm mag}$ with $p_{\rm mag} = B^2/2$, where $1/\sqrt{4\pi}$ factor is absorbed while defining the magnetic fields. Here, the square of the magnetic field strength measured in the fluid frame is computed as $B^2 = b_{\mu}b^{\mu}$.

2.1.2 Conserved quantities in GRMHD flows

In this work, we assume the convergent flow ($u^r < 0$) to be confined in the disk mid-plane ($\theta \simeq \pi/2$). This allows us to ignore the dynamics above the mid-plane and we impose $\partial_{\theta} \to 0$. Hence, the polar component of the four-velocity is chosen as $u^{\theta} \sim 0$ all over the disk and subsequently, the $\theta-$component of the magnetic field is assumed to be zero,

$b^\theta = 0$. Meanwhile, imposing the ideal MHD condition $u_\mu b^\mu = 0$, we are now left with the two independent magnetic field components *i.e.,* the radial (b^r) and toroidal (b^ϕ) fields. With this, we analyze the radial behavior of the advective, axisymmetric ($\partial_\phi \to 0$) flow in the steady state ($\partial_t \to 0$).

From the particle number conservation, the continuity equation boils down to,

$$\sqrt{-g}\rho u^r = \text{const.} = C_{\mathcal{M}}, \tag{2.9}$$

where $C_{\mathcal{M}}$ is the measure of the mass flux and $\sqrt{-g} = r^2$. Additionally, the energy-momentum conservation, supplemented by the killing condition $\nabla_\mu \xi_\nu + \nabla_\nu \xi_\mu = 0$, assumes the following form

$$\nabla_\mu (T^{\mu\nu}\xi_\nu) = 0. \tag{2.10}$$

Equation (2.10) provides two conserved quantities, which are given by,

$$\frac{-\sqrt{-g}\, T^r_t}{C_{\mathcal{M}}} = -h_{\rm tot} u_t + \frac{1}{\rho u^r} g_{tt} b^r b^t = \mathcal{E}, \tag{2.11}$$

and

$$\frac{\sqrt{-g}\, T^r_\phi}{C_{\mathcal{M}}} = h_{\rm tot} u_\phi - \frac{1}{\rho u^r} g_{\phi\phi} b^r b^\phi = \mathcal{L}, \tag{2.12}$$

where $\mathcal{E}$ and $\mathcal{L}$ are the conserved specific energy flux and specific angular momentum flux, respectively. In the absence of magnetic fields ($b^r = b^\phi = 0$), the conserved quantities agree with the (*i.e.,* $\mathcal{E} = -hu_t$ and $\mathcal{L} = hu_\phi$) results reported in Dihingia et al. (2018a).

In addition, the time component of source-free Maxwell's equation implies,

$$\sqrt{-g}\mathcal{B}^r = \sqrt{-g}(u^t b^r - u^r b^t) = \text{const}, \tag{2.13}$$

which expresses the divergence-free constraint, and $\phi-$component equation implies the relativistic iso-rotation equation (McKinney & Gammie, 2004) as,

$$\sqrt{-g}\ {}^*\mathcal{F}^{r\phi} = \sqrt{-g}(u^r b^\phi - u^\phi b^r) = \text{const.} \tag{2.14}$$

Eq. (2.14) is referred to as the induction equation. In these above Eqs. 2.13, 2.14, the fluid frame magnetic field components are expressed in terms of magnetic field 3-vector ($\mathcal{B}^i$) as,

$$b^t = \mathcal{B}^i u^\mu g_{i\mu}, \qquad b^i = (\mathcal{B}^i + b^t u^i)/u^t. \tag{2.15}$$

In the next, we construct the projection operator with respect to the fluid frame as $\gamma^i_\mu = \delta^i_\mu + u^i u_\mu$, which satisfies $\gamma^i_\mu u^\mu = 0$. This allows us to project the Navier-Stokes equation into three vector equations as $\gamma^i_\mu \nabla_\nu T^{\mu\nu} = 0$. By substituting $i = r$, we obtain the radial momentum equation as,

$$\gamma^r_\mu \nabla_\nu T^{\mu\nu} = (g^{r\nu} + u^r u^\nu)\nabla_\nu p_{\rm tot} + \rho h_{\rm tot} u^\nu \nabla_\nu u^\alpha - \nabla_\nu (b^r b^\nu) - u^r u_\mu \nabla_\nu (b^\mu b^\nu) = 0. \tag{2.16}$$

Further, we define the azimuthal velocity $v^2_\phi = \frac{u^\phi u_\phi}{-u^t u_t}$ and the associated bulk azimuthal Lorentz factor as $\gamma^2_\phi = 1/(1-v^2_\phi)$. Subsequently, the radial three-velocity in the corotating frame is defined as, $v^2 = \gamma^2_\phi v^2_r$, where $v^2_r = \frac{u^r u_r}{-u^t u_t}$ and the associated bulk Lorentz factor $\gamma^2_v = 1/(1-v^2)$. Moreover, the specific angular momentum of the fluid is defined as, $\lambda = -u_\phi/u_t$ and the angular velocity is given by,

$$\Omega = u^\phi/u^t = \frac{\lambda(r-2)}{r^3}. \tag{2.17}$$

Upon integrating Eq. (2.9), we obtain the conserved mass accretion rate ($\dot{M}$) in the comoving frame as,

$$\dot{M} = -4\pi\rho v \gamma_v H \sqrt{r(r-2)}. \tag{2.18}$$

In the subsequent analysis, we express the accretion rate in terms of mass Eddington rate as $\dot{m} = \dot{M}/\dot{M}_{\rm Edd}$, where $\dot{M}_{\rm Edd} = 1.44 \times 10^{18} \left(\frac{M_{\rm BH}}{M_\odot}\right)$ g s^{-1} (accretion efficiency is $\eta_{\rm A} = 0.1$). In this work, we choose $M_{\rm BH} = 1 M_\odot$ all throughout.

> **Note:** The Eddington limit is the maximum luminosity beyond which radiation pressure will overcome the gravity of the astrophysical object. On the other hand, the mass Eddington accretion rate is the critical accretion rate for which the BH radiates at the Eddington luminosity.

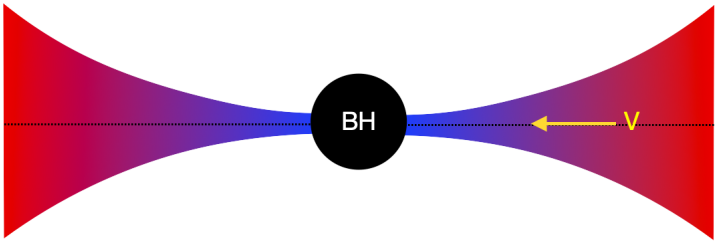

FIGURE 2.1: Cartoon diagram representing accretion disk around a BH. The disk is assumed to be axisymmetric, advective in nature, and maintains hydrostatic equilibrium at all radii.

In equation (2.18), H denotes the local half-thickness of the disk, which is calculated assuming the flow to be in hydrostatic equilibrium in the vertical direction and is given by (Riffert & Herold, 1995; Peitz & Appl, 1997),

$$H^2 = \frac{p_{\rm gas} r^3}{\rho \mathbb{F}}, \tag{2.19}$$

where $\mathbb{F} = \gamma_\phi^2 \frac{(r^2+a_{\rm k}^2)^2+2\Delta a_{\rm k}^2}{(r^2+a_{\rm k}^2)^2-2\Delta a_{\rm k}^2}$, and $\Delta = r^2 - 2r + a_{\rm k}^2$. Here, $a_{\rm k}$ is the BH spin, which is zero for the Schwarzschild case ($a_{\rm k} = 0$), and eventually, $\mathbb{F} = \gamma_\phi^2$.

Relativistic Equation of State

> **Note:** In an accretion disk, the convergent flow is expected to be thermally relativistic (where adiabatic index $\Gamma \to 4/3$, and flow temperature $T \geq 10^{10}$ K) in the inner parts of the disk, whereas the flow remains non-relativistic ($\Gamma \to 5/3$) far away from the central BH. This evidently suggests the need for a variable adiabatic index (Γ) over the radial extent of the disk. In this regard, the REoS (Chattopadhyay & Ryu, 2009) is useful because Γ depends on the temperature of the flow, which is eventually a function of r.

The governing equations are closed with an equation of state (EoS) describing the relation among pressure ($p_{\rm gas}$), density (ρ), and internal energy (e). Following Chattopadhyay & Ryu (2009), we adopt an EoS for relativistic flow as

$$e = \frac{\rho f}{\left(1 + \frac{m_p}{m_e}\right)}, \tag{2.20}$$

with

$$f = \left[1 + \Theta\left(\frac{9\Theta + 3}{3\Theta + 2}\right)\right] + \left[\frac{m_p}{m_e} + \Theta\left(\frac{9\Theta m_e + 3m_p}{3\Theta m_e + 2m_p}\right)\right], \tag{2.21}$$

where Θ ($= k_{\rm B}T/m_e c^2$) is the dimensionless temperature, m_e is the mass of electron, and m_p is the mass of ion. According to the relativistic EoS, we express the adiabatic index and polytropic index of the flow as $\Gamma = (1 + N)/N$ and $N = (1/2)(df/d\Theta)$, respectively (Dihingia et al., 2019).

Following Gammie et al. (2003), the sound speed ($C_{\rm s}$) and the Alfvén velocity ($C_{\rm a}$) for relativistic flow are expressed as $C_{\rm s}^2 = \Gamma p_{\rm gas}/\rho h$ and $C_{\rm a}^2 = B^2/\rho h_{\rm tot}$, respectively. Moreover, Gammie et al. (2003) introduces the dispersion relation for the fast MHD wave $\omega_{\rm d}^2 = \left[C_{\rm s}^2 + C_{\rm a}^2 - C_{\rm s}^2 C_{\rm a}^2\right] k^2$, where $\omega_{\rm d}$ and k denote the frequency and the wavenumber of an MHD wave in the frame comoving with the fluid. Accordingly, we obtain the magenetosonic Mach number $M = v/\sqrt{C_{\rm s}^2 + C_{\rm a}^2 - C_{\rm s}^2 C_{\rm a}^2}$ and the Alfv́enic Mach number $M_A = v/C_{\rm a}$ of the flow.

2.2 Critical point analysis/conditions

Using equations (2.11), (2.12-2.14), (2.16), and (2.18), we obtain the wind equation of the flow (see Appendix A.1), which is given by,

$$\frac{dv}{dr} = \frac{\mathcal{N}(r, v, \Theta, \lambda, b^r, b^\phi)}{\mathcal{D}(r, v, \Theta, \lambda, b^r, b^\phi)}, \tag{2.22}$$

where the numerator $\mathcal{N}$ and the denominator $\mathcal{D}$ are the explicit functions of r, v, Θ, λ, b^r and b^ϕ, and their expressions are given in Appendix A.1. Similarly, the radial derivative of the other flow variables are expressed in terms of (dv/dr) as,

$$\frac{d\lambda}{dr} = \lambda_1 + \lambda_2 \frac{dv}{dr}, \tag{2.23}$$

$$\frac{d\Theta}{dr} = \Theta_1 + \Theta_2 \frac{dv}{dr}, \tag{2.24}$$

$$\frac{db^r}{dr} = b_1^r + b_2^r \frac{dv}{dr}, \tag{2.25}$$

$$\frac{db^\phi}{dr} = b_1^\phi + b_2^\phi \frac{dv}{dr}. \tag{2.26}$$

The explicit expressions of the coefficients, namely λ_1, λ_2, Θ_1, Θ_2, b_1^r, b_2^r, b_1^ϕ, and, b_2^ϕ are given in Appendix A.

2.2.1 Accretion Solution Methodology

During the course of accretion around the black hole, the inflowing matter starts its journey from the disk outer edge ($r_{\rm edge}$) with negligible radial velocity (subsonic) and ultimately enters into the black hole satisfying the inner boundary conditions (Weinberg, 1972; Pringle, 1981; Chakrabarti & Titarchuk, 1995; Narayan et al., 1997; Becker & Le, 2003; Das et al., 2009; Kumar & Chattopadhyay, 2014; Dihingia et al., 2018a, 2019, 2020a; Patra et al., 2022; Sen et al., 2022) at the horizon ($r_{\rm h}$). Because of this, accretion flow around the black hole must change its sonic state at the critical point ($r_{\rm c}$) and become transonic at least once, if not more. Such points are located in between $r_{\rm h}$ and $r_{\rm edge}$. At the critical point, equation (2.22) has the form $(dv/dr)_{r_{\rm c}} = 0/0$ as both numerator ($\mathcal{N}$) and denominator ($\mathcal{D}$) simultaneously vanish there, and we have the critical point conditions $\mathcal{N}_{r_{\rm c}} = \mathcal{D}_{r_{\rm c}} = 0$. Accordingly, we apply the l'Hôpital rule to calculate $(dv/dr)_{r_{\rm c}}$. In general, (dv/dr) owns two distinct values at $r_{\rm c}$: one is for accretion ($(dv/dr)_{r_{\rm c}} < 0$) and the other is for wind ($(dv/dr)_{r_{\rm c}} > 0$). When both the values of $(dv/dr)_c$ are real and of opposite sign, the corresponding $r_{\rm c}$ is called as saddle type critical point (Matsumoto et al., 1984; Chakrabarti, 1989; Kato et al., 1993; Chakrabarti & Das, 2004, and references therein). Similarly, when $(dv/dr)_c$ are real, but of the same sign, $r_{\rm c}$ is called as nodal type, and for imaginary values of $(dv/dr)_c$, the critical point becomes spiral type. In the astrophysical context, saddle type critical points have special importance as the global transonic accretion flow can only pass through it. Depending on the input parameters, GRMHD flow possesses either single or multiple critical points. When the critical point is formed near the horizon, it is referred as the inner critical point ($r_{\rm in}$), and when it forms far away from the horizon, we call them as outer critical point ($r_{\rm out}$) (Chakrabarti & Das, 2004, and references therein).

2.3 Global accretion solutions

In order to obtain the global solution of the GRMHD accretion flow, one requires to solve the coupled differential equations (2.22-2.26) by employing the set of input parameters of the flow. Among these parameters, $\mathcal{E}$, $\mathcal{L}$, $a_{\rm k}$, and $\dot{m}$ are used as global parameters, whereas the critical point ($r_{\rm c}$) and the radial magnetic field $b^r_{\rm c}$ at $r_{\rm c}$ are treated as local parameters. In this work, we consider flows around static black holes with spin parameter $a_{\rm k} = 0$ and also set $\dot{m} = 0.01$ all throughout unless stated otherwise. Using these flow parameters, we simultaneously solve equations $\mathcal{N}_{r_{\rm c}} = 0$ and $\mathcal{D}_{r_{\rm c}} = 0$ to calculate the radial velocity (v_c), temperature (Θ_c), specific angular momentum (λ_c) and toroidal magnetic fields (b^ϕ_c) at $r_{\rm c}$. Employing these parameters, we first integrate equation (2.22) inwards up to the horizon and then outwards up to a large distance, equivalently the outer edge of the disk ($r_{\rm edge} \sim 1000$). Subsequently, we join both segments of the solutions to obtain the global transonic accretion solutions around the black holes. Depending on the input parameters, accretion flow passes through either inner critical point ($r_{\rm in}$) or outer critical point ($r_{\rm out}$) before entering into the black hole.

To this end, we emphasis that in the frame work of GRMHD, the accretion solutions passing through either inner critical point ($r_{\rm in}$) or outer critical point ($r_{\rm out}$) remain largely unexplored and hence, in this work, we intend to study the properties of the magnetized relativistic accretion flow around black holes extensively.

2.3.1 Fluid properties of global accretion solutions containing inner critical point

In Fig. 2.2, we present a typical solution passing through the inner critical point ($r_{\rm in} = 5.1553$) where each panel shows the variation of the flow variables as a function of the radial distance (r). This solution is obtained for $\mathcal{E} = 1.0012$, $\mathcal{L} = 3.10$, and $b^r_{\rm in} = 9.75 \times 10^4$ G that smoothly connects the black hole horizon with the outer edge of the disk $r_{\rm edge} = 1000$. In Fig. 2.2a, we present the Mach number (M) variation of the transonic flow solutions. In this work, our interest is to focus only on the accretion solution (solid curve), however, for the purpose of completeness, we demonstrate its

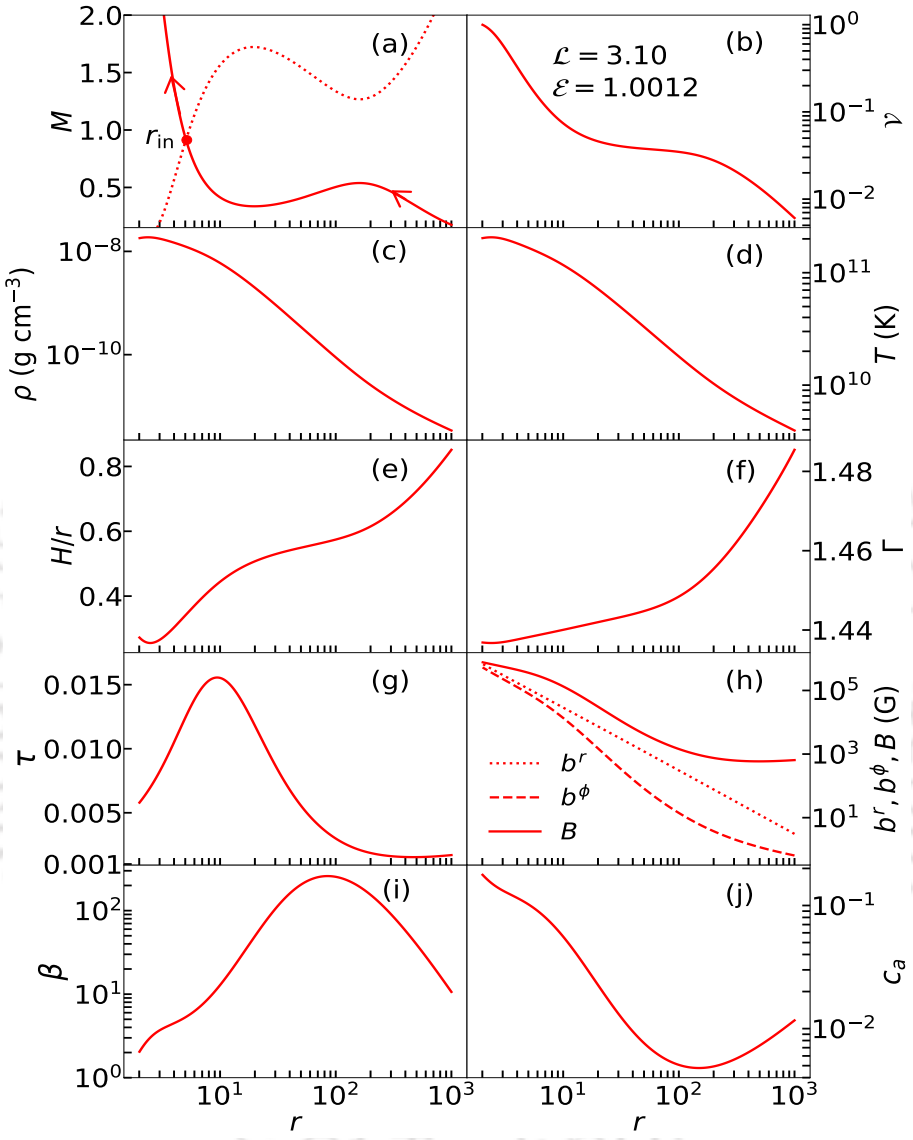

FIGURE 2.2: Example of a complete GRMHD accretion solution that passes through the inner critical point at $r_{\rm in} = 5.1553$. Here, $\mathcal{E} = 1.0012$, $\mathcal{L} = 3.10$, and $b^r_{\rm in} = 9.75 \times 10^4$ G are used. In panels (a)−(j), the profile of Mach number (M), velocity (v), density (ρ), temperature (T), disk aspect ratio (H/r), adiabatic index (Γ), vertical optical depth (τ), magnetic field components (B, b^r, b^ϕ), plasma-β, and Alfv́enic velocity ($C_{\rm a}$) are plotted as function of radial distance (r). Filled circle denotes the location of $r_{\rm in}$ in panel (a). See the text for details.

corresponding wind branch (dotted curve) as well. We observe that subsonic accretion flow from the outer edge of the disk ($r_{\rm edge} = 1000r_g$) gradually gains its radial velocity as it moves inwards and eventually makes smooth transition to become supersonic at the inner critical point ($r_{\rm in} = 5.1553$) before falling into the black hole. At $r_{\rm in}$, we obtain the other flow variables as $v_{\rm in} = 0.1999$, $\Theta_{\rm in} = 27.9544$, $\lambda_{\rm in} = 3.1717$ and $b^{\phi}_{\rm in} = 6.73 \times 10^4$ G. In the figure, arrows indicate the direction of the flow motion and inner critical point ($r_{\rm in}$) is marked using filled circle. In Fig. 2.2b, we show the radial velocity (v) variation of the flow corresponding to the accretion solution depicted in Fig. 2.2a and find that flow enters into the black hole with velocity comparable to the speed of light. We demonstrate the density profile of the accreting flow in Fig. 2.2c, where gradual increase of density is observed as the flow proceeds towards the black hole. This happens mainly due to the geometric compression of the flow, and as a consequence, temperature of the flow is also increased with the decrease of radial distance as shown in Fig. 2.2d. We find that the disk becomes sufficiently hot with temperature as large as $T \geq 10^{11}$ K at the near horizon region with $r < 8r_g$. We display the dependence of the vertical scale height (H/r) on the radial coordinate in Fig. 2.2e, where we find that H/r remains less than unity all the way from the outer edge of the disk to the horizon. In Fig. 2.2f, we depict the profile of adiabatic index (Γ) as function of r. As expected, Γ decreases with the decreasing r and flow tends to become thermally trans-relativistic ($\Gamma \sim 1.4$) as it accretes towards the black hole (Aktar et al., 2015, and references therein). Further, we estimate the scattering optical depth $\tau = \kappa\rho h$, where the electron scattering opacity $\kappa = 0.38$ cm^2 g^{-1} and present the obtained result in Fig. 2.2g. We observe that the flow remains optically thin ($\tau < 1$) even at the inner part of the disk ($r \lesssim 20r_g$) although the density profile remains steeper there. This intuitively indicates that the possibility of escaping the high energy radiations from the inner part of the disk seems to be very much significant. In Fig. 2.2h, we display the variation of b^r (dotted), b^{ϕ} (dashed) and B (solid) with the radial distance. We find that although the strength of the magnetic fields is negligible ($b^r, b^{\phi} \sim 1$ G) at $r_{\rm edge}$, however, it is enhanced to $\sim 10^6$ G at the near horizon region yielding the inner part of the disk to be magnetically active. Next, we display the overall variation of the plasma-β in panel Fig.2.2i, where we find that disk remains mostly gas pressure dominated at all radii except at $r \lesssim 10r_g$. Finally, we show the overall variation

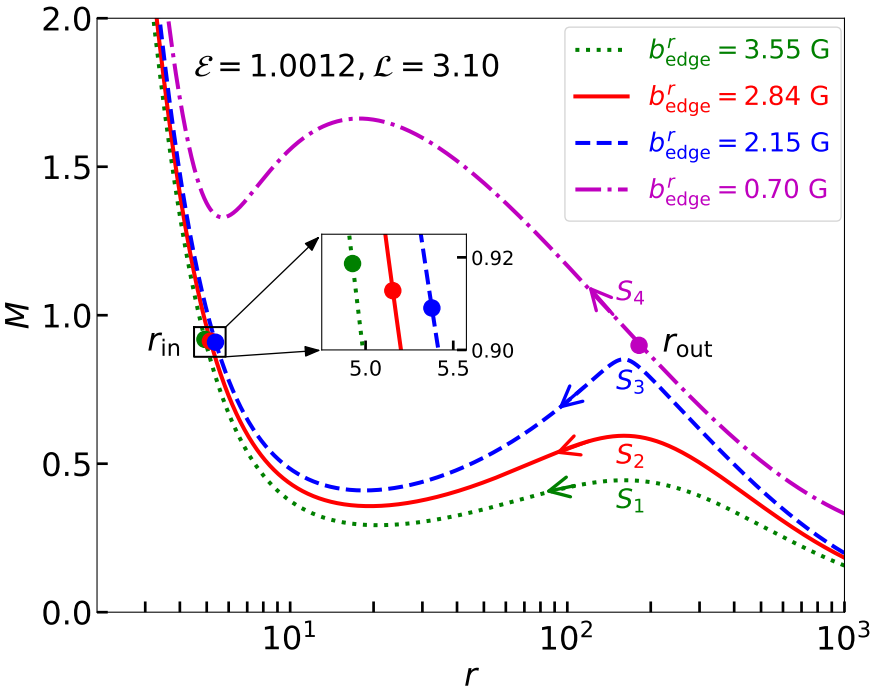

FIGURE 2.3: Variation of global GRMHD accretion solutions around black hole for different values of radial magnetic field ($b^r_{\rm edge}$) at the outer edge of the disk $r_{\rm edge} = 1000$, where $\mathcal{E} = 1.0012$ and $\mathcal{L} = 3.10$. The dotted (S_1, green), solid (S_2, red) and dashed (S_3, blue) curves denote the solutions for $b^r_{\rm edge} = 3.55$ G, 2.84 G, and 2.15 G, respectively that pass through the inner critical points ($r_{\rm in}$). For the same set of the outer edge parameters, when $b^r_{\rm edge} = 0.70$ G is chosen, accretion solution passes through the outer critical point ($r_{\rm out}$) as depicted by dot-dashed (S_4, magenta) curve. In the figure, inner critical points are zoomed, and $r_{\rm in}$ and $r_{\rm out}$ are marked. Arrows indicate the direction of flow motion as it approaches towards the black hole.

of the Alfvénic velocity ($C_{\rm a}$) in panel Fig.2.2j, which initially decreases due to the slow increase of B, however enhances its value as flow moves towards the black hole.

2.3.2 General behaviour of global accretion solutions with fixed outer edge

In Fig. 2.3, we examine the role of magnetic fields in deciding the nature of the accretion solutions having fixed outer boundary. Here, the dotted (green) curve demonstrates a global accretion solutions that starts its journey from $r_{\rm edge} = 1000$ with $b^r_{\rm edge} = 3.55$ G, $\mathcal{E} = 1.0012$, and $\mathcal{L} = 3.10$, and it passes through the inner critical point $r_{\rm in} = 4.9257$ with $b^r_{\rm in} = 1.34 \times 10^5$ G before entering into the black hole. We mark this solution as S_1. Now, we decrease radial magnetic field to $b^r_{\rm edge} = 2.84$ G keeping $\mathcal{E}$ and $\mathcal{L}$ unchanged, and calculate the global accretion solution by suitably tuning $v_{\rm edge} = 0.006356$ and

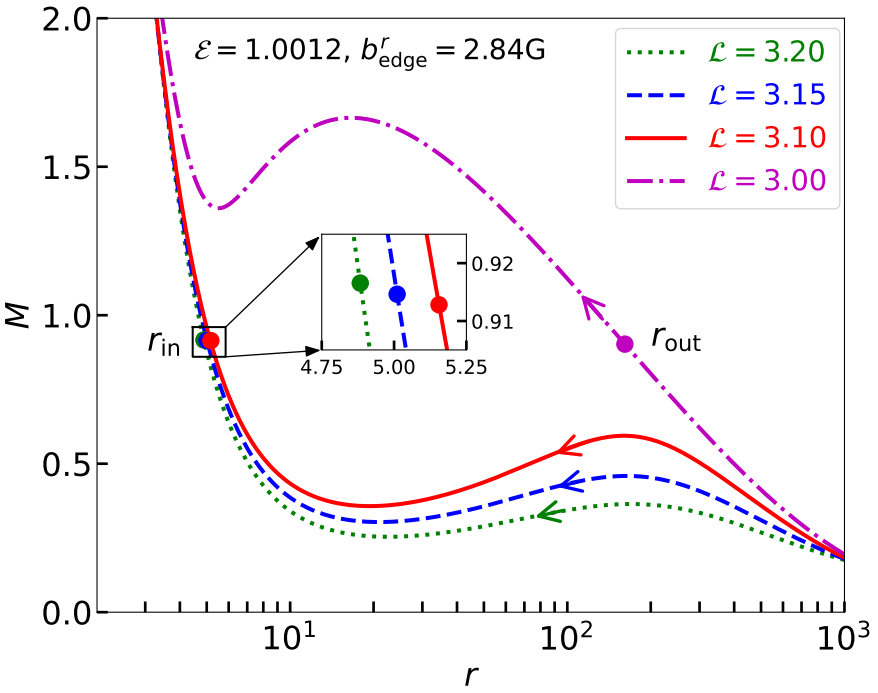

FIGURE 2.4: Similar to Fig. 2.3, showing the variation of accretion solutions, when $\mathcal{E} = 1.0012$ and $b^r_{\rm edge} = 2.84$ G are chosen and $\mathcal{L}$ is varied as marked in the figure. See the text for details.

$\Theta_{\rm edge} = 0.6680$. Here, we need to supply $v_{\rm edge}$ and $\Theta_{\rm edge}$ values additionally to obtain the accretion solution as the critical point is not known a priori. We plot this solution using solid (red) curve and for this solution $r_{\rm in} = 5.1553$, and $b^r_{\rm in} = 9.75 \times 10^4$ G.

This solution is identical to the result presented in Fig. 2.2 and marked as S_2. Upon decreasing $b^r_{\rm edge}$ gradually, we observe that below a minimum value of radial magnetic field at the outer edge $b^{r,\rm min}_{\rm edge} = 2.15$ G, the accretion solution fails to pass through the inner critical point. For $b^{r,\rm min}_{\rm edge} = 2.15$ G, the obtained accretion solution (marked as S_3) is shown by dashed (blue) curve, where $r_{\rm in} = 5.3781$, and $b^r_{\rm in} = 6.78 \times 10^4$ G. When $b^r_{\rm edge} < b^{r,\rm min}_{\rm edge}$, namely 0.70 G, the accretion solution changes its character allowing the flow to pass through the outer critical point ($r_{\rm out} = 181.465$) instead of inner critical point ($r_{\rm in}$) with $b^r_{\rm out} = 21.08$ G, $\mathcal{E} = 1.0012$ and $\mathcal{L} = 3.10$. In the figure, this solution (marked as S_4) is depicted by the dot-dashed (magenta) curve. In the figure, filled circles denote the inner and outer critical points and arrows indicate the overall direction of the flow motion towards the black hole.

Since the nature of the transonic GRMHD accretion solutions also depend on $\mathcal{E}$ and $\mathcal{L}$, in addition to $b^r_{\rm edge}$, it is instructive to study their behavior by tuning these flow

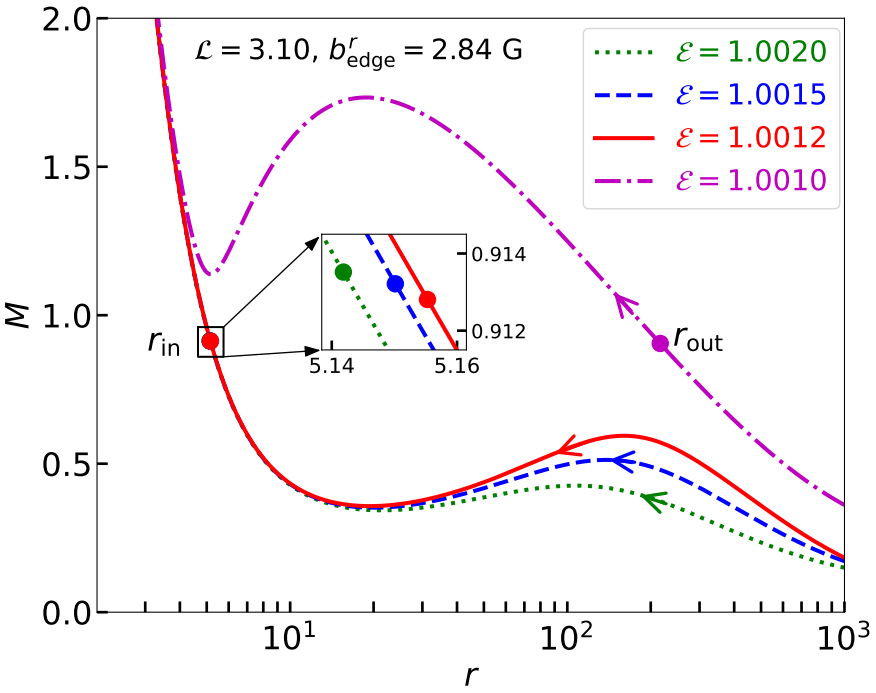

FIGURE 2.5: Similar to Fig. 2.3, showing the variation of accretion solutions, when $\mathcal{L} = 3.10$ and $b^r_{\rm edge} = 2.84$ G, and $\mathcal{E}$ is varied as marked in the figure. See the text for details.

parameters. We find that the behavior of the accretion solutions changes as $\mathcal{L}$ is decreased for flows with $\mathcal{E} = 1.0012$ and $b^r_{\rm edge} = 2.84$ G at $r_{\rm edge} = 1000$. We present the obtained results in Fig. 2.4, where the solutions corresponding to $\mathcal{L} = 3.20$ (dotted, green), 3.15 (dashed, blue), and 3.10 (solid, red) are seen to pass through the inner critical points as $r_{\rm in} = 4.8830$, 5.0105, and 5.1553, respectively, whereas the solution with $\mathcal{L} = 3.0$ becomes transonic after crossing the outer critical point at $r_{\rm out} = 161.3239$ (dot-dashed, magenta). Thus, one arrives at conclusion that the effect of $\mathcal{L}$ is significant in deciding the nature of the accretion solutions around black holes. In the figure, the arrowed paths show the direction of the flow motion towards the black hole.

Similarly, Fig. 2.5 depicts the examples of accretion solutions that change their character due to the variation of $\mathcal{E}$. Here, we fix $\mathcal{L} = 3.10$, and $b^r_{\rm edge} = 2.84$ G at $r_{\rm edge} = 1000$. The results plotted using dotted (green), dashed (blue), and solid (red) curves are for $\mathcal{E} = 1.0020$, 1.0015 and 1.0012, and these solutions cross the inner critical points at $r_{\rm in} = 5.1419$, 5.1502, 5.1553, respectively, before entering into the black hole. As the energy is decreased further, keeping all the remaining flow parameters unchanged, the accretion solution alters its trajectory and pass through the outer critical point at

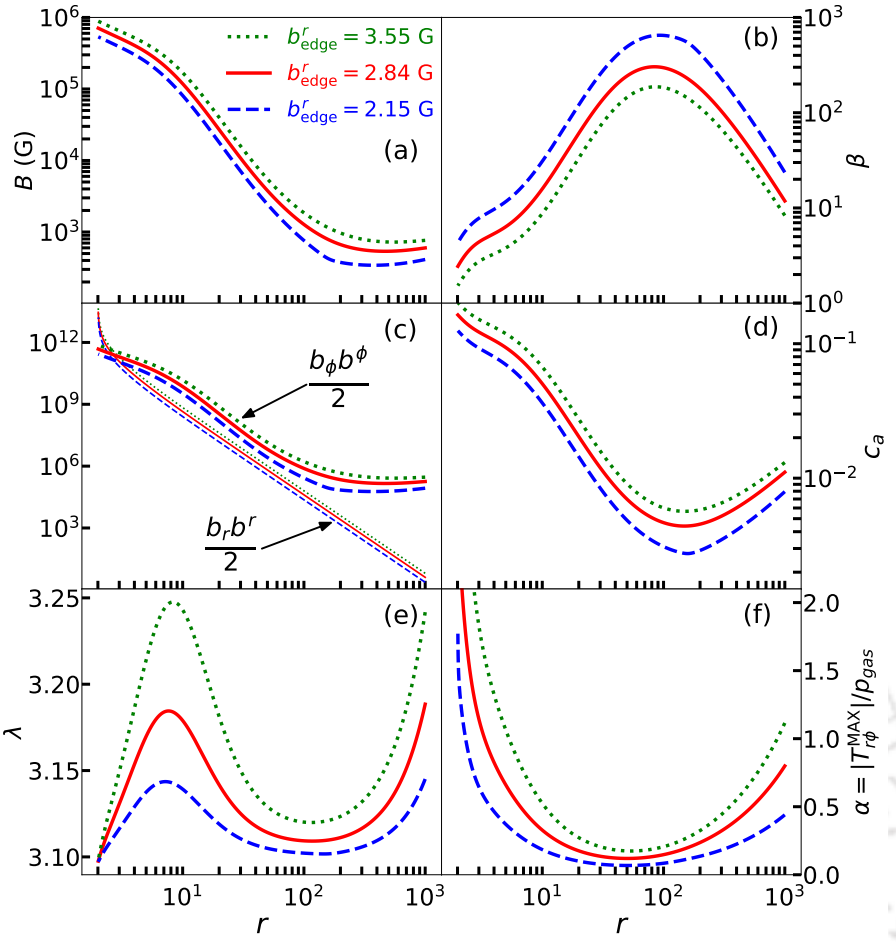

FIGURE 2.6: Parametric dependence of the flow variables for accreting matter around black hole. Various flow variables, namely (a) B, (b) plasma-β, (c) $b_r b^r/2$ and $b_\phi b^\phi/2$, (d) $C_{\rm a}$, (e) λ, and (f) α are plotted as function of r. In each panel, dotted (green), solid (red), and dashed (blue) curves denote the results corresponding to the solutions marked as 'S_1', 'S_2' and 'S_3' in Fig. 2.3. See the text for details.

$r_{\rm out} = 216.4050$ (dot-dashed, magenta) instead of the inner critical point. As before, we assert that $\mathcal{E}$ plays important role in stipulating the nature of the accretion solutions and arrows are used to indicate the direction of the flow motion.

It is customary to examine the effect of magnetic fields on the properties of the disk fluid confined at the disk mid-plane. For the purpose of representation, we consider accretion solutions marked as 'S_1', 'S_2' and 'S_3' in Fig. 2.3 and present the associated fluid variables in Fig. 2.6. While doing so, we show the variation of B (Fig. 2.6a), plasma-β (Fig. 2.6b), $b_r b^r/2$ and $b_\phi b^\phi/2$ (Fig. 2.6c), Alfv́enic velocity (Fig. 2.6d), specific angular momentum λ (Fig. 2.6e), and α (Fig. 2.6f) with radial distance (r). In each panel, dotted (green), solid (red), and dashed (blue) curves are plotted for $b^r_{\rm edge} = 3.55$ G, 2.84 G and 2.15 G, respectively. As expected, we observe in panel (a) that the profile of

B corresponding to higher $b^r_{\rm edge}$ continues to remain higher compared to the cases with smaller $b^r_{\rm edge}$ values. It may be noted that in all cases, the flow starts with a very low radial magnetic fields ($b^r_{\rm edge} \sim 1$ G), however, the strength of the magnetic field tends to attain as high as $\sim 10^6$ G in the near horizon limit of the black hole. In panel (b), it is seen that as flow accretes towards the black hole, the gas pressure ($p_{\rm gas}$) initially increases compared to the magnetic pressure ($p_{\rm mag}$) leading to the increase of plasma-β. But, once the toroidal field component starts growing, plasma-β decreases towards the black hole. Nevertheless, we find that disk is primarily gas pressure ($p_{\rm gas}$) dominated all throughout, although magnetic pressure ($p_{\rm mag}$) tends to become comparable to $p_{\rm gas}$ at the inner part of the disk. Needless to mention that $p_{\rm mag}$ is ascertained by the $b^r_{\rm edge}$ value; for a given r, higher $b^r_{\rm edge}$ renders enhanced $p_{\rm mag}$ as clearly seen in panel (b). Next, we illustrate the magnetic pressure corresponding to r and ϕ components of the magnetic fields which are denoted by thin and thick curves in panel (c). We observe that the magnetic field strength is predominantly dominated by the toroidal component ($b^\phi b_\phi$) all throughout over the radial part ($b^r b_r$) except at the inner edge close to the horizon, $r \lesssim 3r_g$. This finding is in agreement with the recent simulation work of Begelman et al. (2022). As observed before, higher $b^r_{\rm edge}$ yields enhanced magnetic pressure due to both r and ϕ components. In panel (d), we see that relatively higher Alfv́enic velocity ($C_{\rm a}$) is obtained for increasing $b^r_{\rm edge}$ values. Since $C_{\rm a}$ is directly depends on the magnetic field strength, its radial variation in general follows the B profile. In panel (e), we present how the specific angular momentum (λ) is transported in a magnetized accreting plasma. As the flow accrete towards the black hole from the outer edge of the disk, the effect of magnetic fields becomes increasingly important that causes the transport of angular momentum. In reality, the transport of λ is mainly governed by the Maxwell stress ($T^{\rm MAX}_{r\phi} = B^2 u_r u_\phi - b_r b_\phi$), and therefore, it is evident that the profile of λ strongly depends on the interplay among the flow variables. In general, for a given radial distance, λ continues to remain higher for flows with larger B. However, the overall transport of λ appears to be weak resulting the flow to remain sub-Keplerian all throughout the disk. This clearly indicates that MHD flow of this kind seems to remain weakly viscous all throughout the disk domain. Finally, in panel (f), we examine the profile of the viscosity parameter, $\alpha = |T^{\rm MAX}_{r\phi}|/p_{\rm gas}$, which is defined as the ratio of the Maxwell stress to the

gas pressure (Hawley & Krolik, 2001; Pessah et al., 2007; Penna et al., 2012; Mishra et al., 2020, and references therein). We find that α varies with radial distance, unlike the standard viscosity prescription of Shakura & Sunyaev (1973). As the flow proceeds inwards, $p_{\rm gas}$ initially increases over $p_{\rm mag}$ (see panel (b)), leading to the decrease of α, although α eventually enhances its value once the magnetic stress starts to dominate. We notice that α exceeds its outer edge value at the inner part of the disk where magnetic fields are very high (see panel (a)) and because of this, rapid loss of λ is observed at the vicinity of the black hole horizon. Overall, it is evident that α in magnetized disks varies with radial distance as it is computed using magnetic stress, and this finding is in agreement with the results from GRMHD simulation (Avara et al., 2016, and references therein).

Now, we attempt to examine the radial profiles of the quantities, namely density (ρ), gas pressure ($p_{\rm gas}$), magnetic pressure ($p_{\rm mag}$), radial magnetic field (b^r), and toroidal magnetic field (b^ϕ) by means of the power-law fit. For that we consider accretion solutions marked as 'S_1' and 'S_3' in Fig. 2.3, and present the radial variation of the above quantities in Fig. 2.7(a-e). In each panel, thick dotted (green) and thick dashed (blue) curves denote the results obtained from solutions 'S_1' and 'S_3', and the corresponding power-law fits are shown by thin dotted and thin dashed lines, respectively. We find that the best fit for density at all radii gives $\rho \propto r^{-(n+1/2)}$ (panel a) with $n \sim 1$, which seems to be consistent with the results of Narayan & Yi (1995a); Blandford & Begelman (2004) for pure accretion having no outflow. Similarly, the best fits for the remaining quantities are obtained as $p_{\rm gas} \propto r^{-(n+7/6)}$, $p_{\rm mag} \propto r^{-(n+5/2)}$, $b^r \propto r^{-(n+1)}$, and $b^\phi \propto r^{-(n+9/5)}$. Needless to mention that we observe in general poor fits of the accretion solutions in the near horizon limit. This possibly happens due to the fact that the transonic nature of the flow is not taken into account in the power-law fitting.

Next, we make an effort to reconcile our theoretical predictions with previous studies of magnetized accretion flow accomplished by the local shearing box simulations, where tight correlation between the plasma-β and the viscosity parameter α is revealed in two ways, $\alpha\beta \sim 0.5$ and $\alpha \propto \beta^{-0.53}$ (Hawley & Balbus, 1995; Blackman et al., 2008; Sorathia et al., 2012; Salvesen et al., 2016, and references therein). Towards this, in Fig. 2.8, we depict the correlation between α and β for the accretion solutions marked 'S_1' and 'S_3'

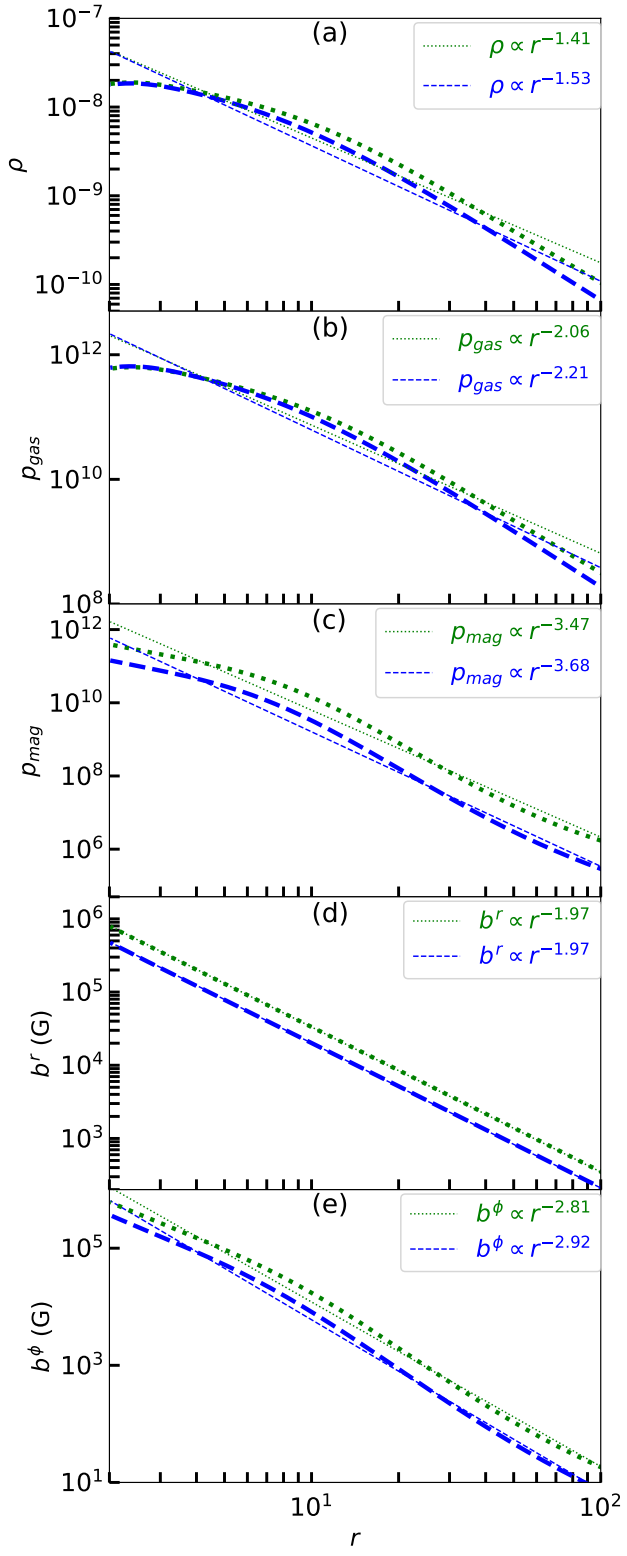

FIGURE 2.7: Best fitted power-law of (a) density ρ, (b) gas pressure $p_{\rm gas}$, (c) magnetic pressure $p_{\rm mag}$, (d) radial component of the magnetic fields b^r and (e) toroidal component of the magnetic fields b^ϕ. In each panel, thick dotted (green) and thick dashed (blue) curves are for solutions marked 'S_1' and 'S_3' in Fig. 2.3, and thin dotted (green) and thin dashed (blue) correspond to the best fit power-law representations. See the text for details.

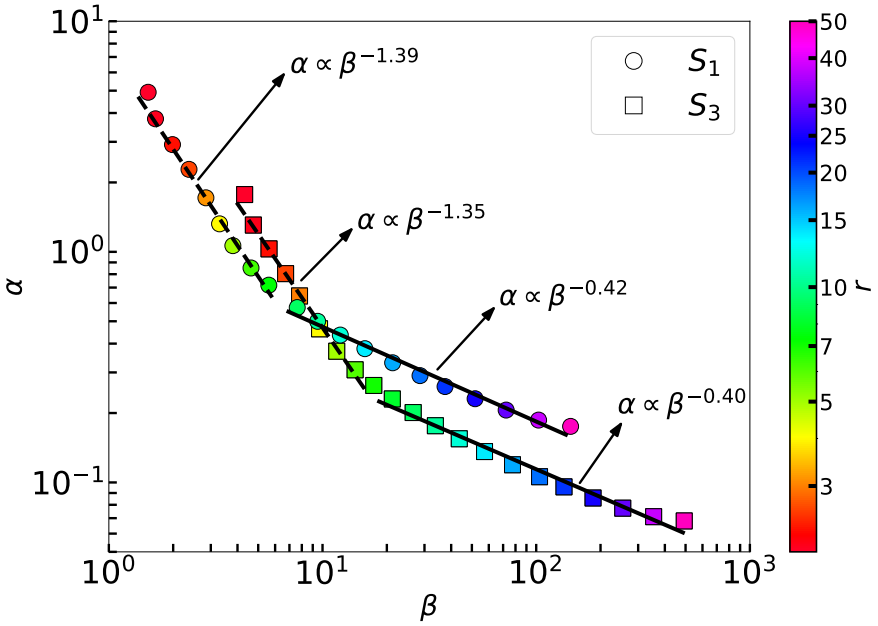

FIGURE 2.8: Viscosity parameter (α) is plotted as a function of plasma-β at all radii between $2 \leq r \leq 50$. Filled circles and filled squares are obtained for the accretion solutions marked 'S_1' and 'S_3' in Fig. 2.3, whereas the solid and dashed lines (black) represent the best fitted power laws, respectively. See the text for details.

in Fig. 2.3. Here, the results are obtained for $r \leq 50r_g$ just to collate with the existing simulation studies. In the figure, 'S_1' and 'S_3' solutions are plotted using filled circles and filled squares, respectively. The color code denotes the radial coordinate and its range is shown using colorbar at the right side of the figure. The best fit generally yields $\alpha \propto \beta^{-q}$, where two distinct domains are ascertained as a result of different exponents (q) values. For $6r_g \lesssim r < 50r_g$, we get the best fit value as $q \sim 0.4$ and ~ 0.42 corresponding to 'S_1' and 'S_3', respectively. This can be expressed approximately as $\alpha \propto \beta^{-2/5}$ which is in close agreement with the value ~ 0.53 as reported in Salvesen et al. (2016). In addition, at the inner part of the disk ($2r_g < r \lesssim 6r_g$) where the magnetic activity is relatively stronger, we obtain $q \sim 1.35$ and ~ 1.39 as depicted by dashed lines. Such stiff scaling relation (approximately $\alpha \propto \beta^{-7/5}$), to the best of our knowledge, has not yet been reported in the literature.

2.3.3 Modification of accretion solutions possessing inner critical point

In this section, we examine how the nature of the accretion solutions alters due to the variation of either magnetic fields or inner critical points for flows with a given set of

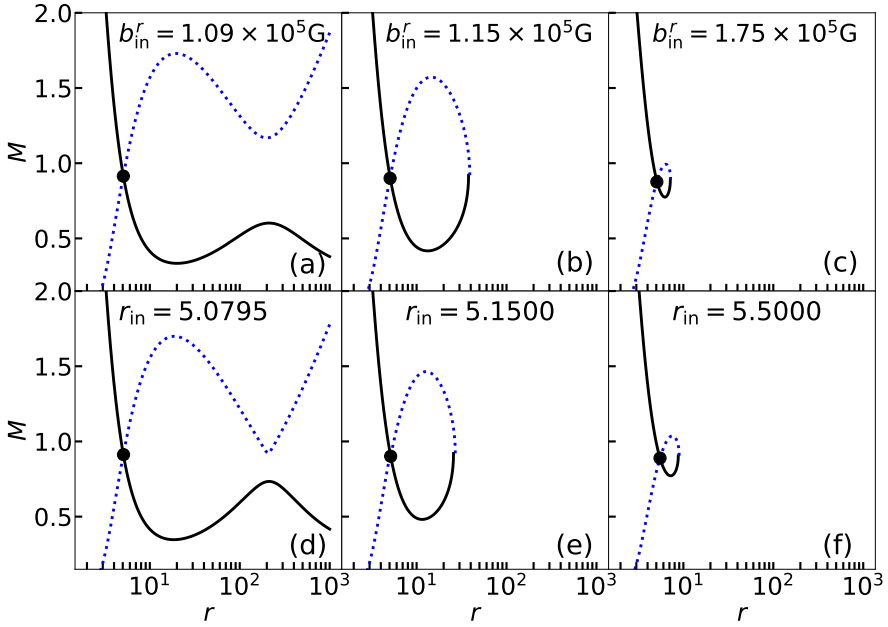

FIGURE 2.9: Plot of Mach number as a function of radial distance (r). Solid (black) curve denotes accretion solution and dotted (blue) curve refers corresponding wind solution. In the upper panels, we choose $r_{\rm in} = 5.0744$, $\mathcal{E} = 1.0012$, and $\mathcal{L} = 3.10$, and increase the local radial magnetic field ($b^r_{\rm in}$) at $r_{\rm in}$ which are marked. In the lower panels, we consider $b^r_{\rm in} = 1.09 \times 10^5$ G, $\mathcal{E} = 1.0012$, and $\mathcal{L} = 3.10$ and vary $r_{\rm in}$ as it is marked. See the text for details.

($\mathcal{E}$, $\mathcal{L}$) values, and plot them in Fig. 2.9. In each panels of the figure, the Mach number (M) is depicted as function of radial distance (r), where solid (black) and dotted (blue) curves represent the accretion and wind solutions, respectively and filled circles denote the inner critical points. In the upper panels, we choose $r_{\rm in} = 5.0744$, $\mathcal{E} = 1.0012$, and $\mathcal{L} = 3.10$, and vary radial component of the magnetic fields as (a) $b^r = 1.09 \times 10^5$ G, (b) 1.15×10^5 G, and (c) 1.75×10^5 G. In panel (a), the flow passes through the inner critical point and smoothly connects the event horizon to the outer edge of the accretion disk ($r_{\rm edge} = 1000$). When the radial magnetic field is increased to $b^r = 1.15 \times 10^5$ G (panel (b)), the flow solution becomes closed in the range $r_{\rm in} < r < r_{\rm out}$ with Mach number $M(r) = M_c$ (Chakrabarti & Das, 2004) and fails to connect the black hole horizon with the outer edge of the disk ($r_{\rm edge}$). However, this solution can join with another transonic solution passing through the outer critical point, if it exists, via shock transition (Fukue, 1987; Chakrabarti, 1989; Das, 2007), and accordingly, the accretion solution can extends up to $r_{\rm edge}$. As the radial magnetic field is increased further, the closed solution gradually shrinks and ultimately disappears as the critical point turns into a nodal type. With this, we indicate that for a given set of flow parameters, there exists two critical values of b^r —

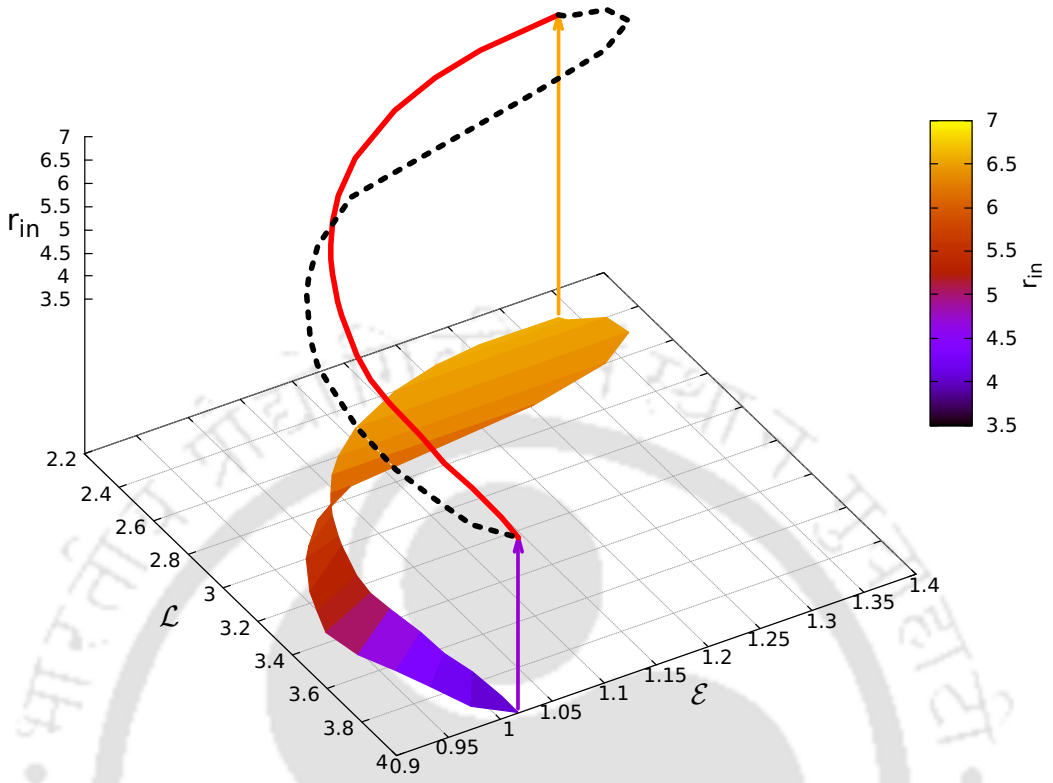

FIGURE 2.10: Plot of three-dimensional parameter space of flow energy ($\mathcal{E}$), angular momentum ($\mathcal{L}$), and inner critical point ($r_{\rm in}$). Here, we fix $b^r_{\rm in} = 1.15 \times 10^5$ G, $b^\phi_{\rm in} = 1.00 \times 10^5$ G. Solid (red) and dashed (black) curves denote the boundary of the parameters surface. The two-dimensional surface projection of the three-dimensional plot is shown in $\mathcal{E} - \mathcal{L}$ plane, where the color code denotes the range of $r_{\rm in}$. See the text for details.

first one is the lower critical value for which the open solution passing through the fixed inner critical point becomes closed, and the other one corresponds to the higher critical value for which saddle type critical points disappear. In the lower panels of Fig. 2.9, we choose flow parameters as $b^r_{\rm in} = 1.09 \times 10^5$ G, $\mathcal{E} = 1.0012$, and $\mathcal{L} = 3.10$, and vary the inner critical point as in panels (d) $r_{\rm in} = 5.0795$, (e) 5.1500, and (f) 5.5000. Similar to the upper panels, we again find that as $r_{\rm in}$ is gradually receded away from the horizon, the flow behaviour changes their character from open type to closed type and ultimately it ceases to exist when $r_{\rm in}$ turns in to nodal type.

So far, we have studied the global accretion solutions that pass through either inner or outer critical points. Here, we wish to emphasize that solutions of these kinds are not isolated solutions, instead they exist for a wide range of flow parameters. While

envisaging this fact, we intend to examine the range of flow parameters that admit closed accretion solutions passing through the inner critical points (see Fig. 2.9). Accordingly, in Fig. 2.10, we separate the effective domain of the parameter space spanned by $\mathcal{E}$, $\mathcal{L}$, and $r_{\rm in}$ that provides closed accretion solutions around black holes. Here, we fix $b^r_{\rm in} = 1.15 \times 10^5$ G and $b^\phi_{\rm in} = 1.00 \times 10^5$ G at $r_{\rm in}$ and plot the parameter space where solid and dotted curves denote its two edges. A wrapping of the the parameter space is clearly visible, which is possibly resulted due to the complex non-linearity involved among the GRMHD flow variables. Moreover, for the purpose of clarity, we present the two-dimensional projection of the three-dimensional parameter space in $(\mathcal{E}, \mathcal{L})$ plane where color code denotes the allowed range of $r_{\rm in}$ as shown using colorbar. From the figure, it is evident that for smaller $\mathcal{L}$, generally higher $r_{\rm in}$ is required to obtain the closed accretion solution for GRMHD flow, and vice versa.

2.3.4 Fluid properties of global accretion solution possessing outer critical point

For completeness, we continue to emphasize the importance of the GRMHD accretion flows that pass through the outer critical point, and study the primitive variables associated with the flow. For that we consider the accretion solution marked as 'S_4' in Fig. 2.3, and plot the profile of the corresponding flow variables, namely M, v, ρ, T, H/r, Γ, τ, B, b^r, b^ϕ, plasma β, and $C_{\rm a}$ as function of radial distance in the respective panels (a)$-$(j) of Fig. 2.11. We observe that the accreting flow attains supersonic speed at a relatively larger radius ($r_{\rm out}$) in comparison to the accretion solutions possessing the inner critical points ($r_{\rm in}$) (see Fig. 2.11(a)). Because of this, the profiles of the primitive variables for 'S_4' differ quantitatively from the solution 'S_1' particularly at lower radii ($r \lesssim 10r_g$), although their qualitative behaviour appear to be similar (see Fig. 2.2). Nevertheless, it is noteworthy to mention that the accreting matter largely remains gas pressure dominated even at the near horizon limit ($r \lesssim 10r_g$) although the strength of the magnetic fields reaches to $B \sim 0.75 \times 10^5$ G at the vicinity of the horizon (see Fig. 2.11(h)). This evidently signifies that the accretion disk presumably becomes magnetically more active for flows passing through $r_{\rm in}$ rather than $r_{\rm out}$ (see Fig. 2.2(h)).

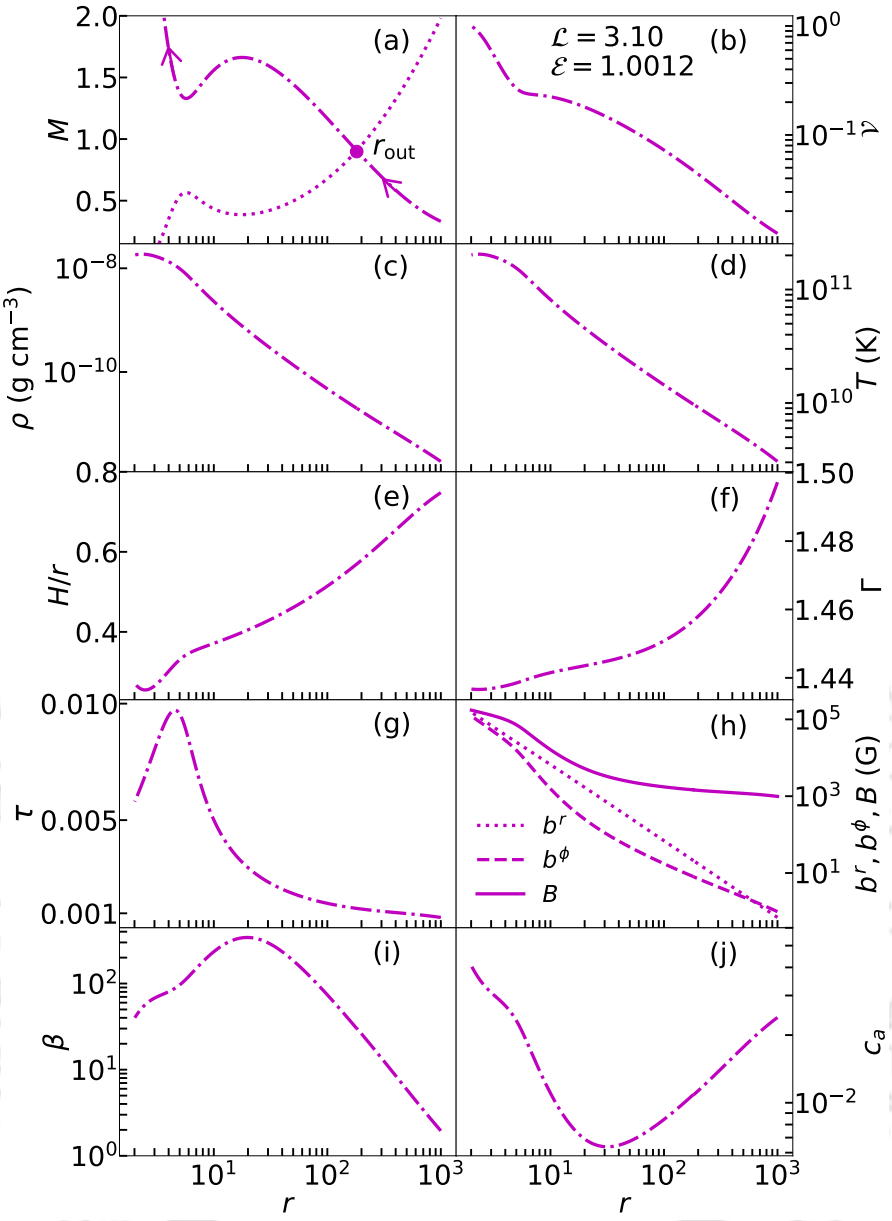

FIGURE 2.11: Same as Fig. 2.2, but the accretion solution eventually pass through the outer critical point $r_{\rm out} = 181.465$ with $\mathcal{E} = 1.0012$, $\mathcal{L} = 3.10$, and $b^r_{\rm edge} = 0.7$ G, respectively. See the text for details.

Next, in Fig. 2.12, we compare the specific entropy function $s \propto p_{\rm tot}/\rho^{\Gamma-1}$ (Das et al., 2009; Porth et al., 2017) corresponding to the accretion solutions passing through $r_{\rm in}$ and $r_{\rm out}$. While doing this, we consider solutions marked as 'S_1' and 'S_4' in Fig. 2.3 and depict the profile of s corresponding to these solutions using dotted (S_1) and dot-dashed (S_4) curves. The inner and outer critical point locations are marked using the filled circles. We find that in both cases, s increases as the flow proceeds towards the black hole. This happens as a result of dissipation yielded in the differentially rotating magnetized

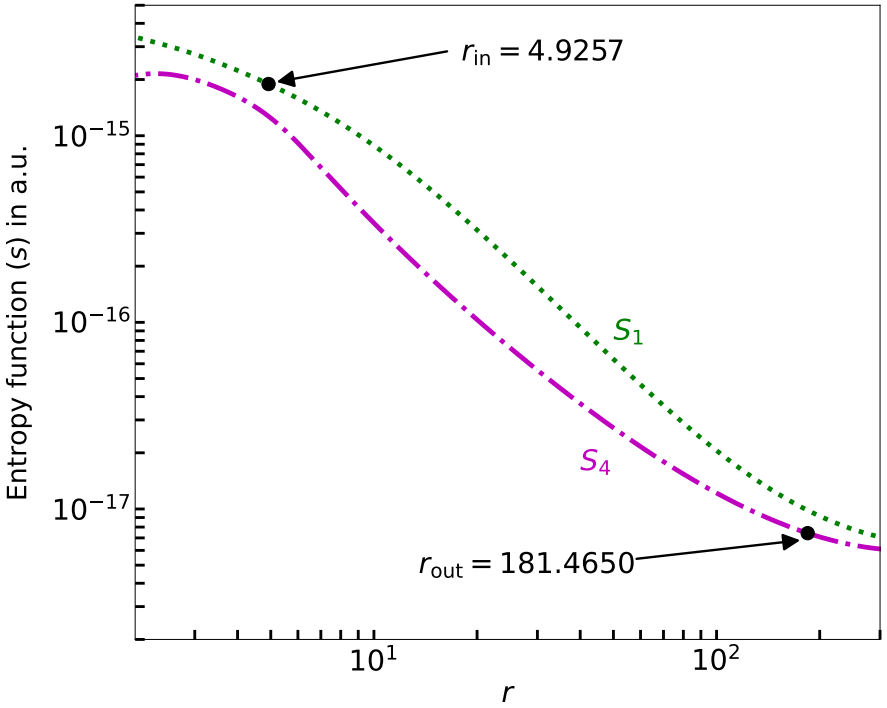

FIGURE 2.12: Variation of the specific entropy function (s) as a function of radial distance (r). Dotted and dot-dashed curves denote the results corresponding to the accretion solutions marked 'S_1' and 'S_4' in Fig. 2.3. In the figure, inner critical point (r_{in}) and outer critical point (r_{out}) are marked. See the text for details.

flow around the black hole. What is more is that s is seen to remain higher at all radii for solution passing through r_{in} compared to the solution possessing r_{out}. A point worth mentioning here is that the global GRMHD accretion solution that changes its sonic character at r_{in} instead of r_{out} to become transonic is perhaps thermodynamically favourable as it possesses high entropy content, although their outer boundary conditions differ only by means of b^r_{edge} values.

2.4 Chapter Conclusions

In this chapter, we investigate the global structure of a steady, magnetized, advective accretion flow around a Schwarzschild black hole. Towards this, we self-consistently solve a set of governing equations (Anile, 1990; Porth et al., 2017, and references therein) that regulate the dynamical structure of the MHD flow under the general relativistic framework. With this, we obtain the global trans-magnetosonic accretion solutions for the first time, to the best of our knowledge, using the relativistic EoS. Subsequently,

we examine the properties of the accretion flow in terms of input parameters, namely, energy ($\mathcal{E}$) and angular momentum ($\mathcal{L}$) flux, and radial magnetic field (b^r), respectively. The findings of this work are summarized as follows:

- We obtain a complete set of global GRMHD accretion solutions around a non-rotating black hole and find that accretion flow passes through either inner critical point ($r_{\rm in}$) or outer critical point ($r_{\rm out}$) before entering into the black hole. We further notice that for a given $(\mathcal{E}, \mathcal{L})$, when radial magnetic field at the outer edge of the disk is below a minimum value ($b^{r,\rm min}_{\rm edge}$), accretion flow possessing $r_{\rm in}$ changes its character and moves through $r_{\rm out}$ instead of $r_{\rm in}$ while approaching the black hole (see Fig. 2.3). Similar findings are also observed when $\mathcal{L}$ or $\mathcal{E}$ are varied, keeping other input parameters unchanged (see Figs. 2.4 and 2.5). Such inner and outer critical point-passing accretion solutions have not been studied before in the GRMHD framework.

- We observe that accretion flow remains mostly gas pressure dominated throughout the disk ($\beta > 10$) except at the near horizon limit $\lesssim 10r_g$, where magnetic fields are seen to become considerably active ($\beta \sim 1$) (see Fig. 2.6b). We also notice that the magnetic field strength is largely dominated by the toroidal field ($b^\phi b_\phi$) at all radii over the radial field ($b^r b_r$) except at the inner edge $r \lesssim 3r_g$ (see Fig. 2.6c). We obtain the robust estimate of magnetic field strength over the entire length scale of the disk and observe that B monotonically increases with the decrease of radial distance. For a solar mass ($M_{\rm BH} = M_\odot$) black hole, the magnetic field strength becomes very strong ($\sim 10^6$ Gauss) in the region close to the horizon (see Fig. 2.6a). We also compute the viscosity parameter (α) that governs the transport of specific angular momentum (λ) by means of Maxwell stress ($T^{\rm MAX}_{r\phi}$). We observe that unlike in standard disk (Shakura & Sunyaev, 1973), α varies with r (see Fig. 2.6f) and its profile agrees with the results from magnetically arrested disk (MAD) simulations (Avara et al., 2016).

- We attempt to elucidate the radial profile of ρ, $p_{\rm gas}$, $p_{\rm mag}$, b^r and b^ϕ by means of best fit power-law distribution. We find that all these flow variables can be ascertained satisfactorily as $\rho \propto r^{-(n+1/2)}$, $p_{\rm gas} \propto r^{-(n+7/6)}$, $p_{\rm mag} \propto r^{-(n+5/2)}$, $b^r \propto r^{-(n+1)}$,

and $b^{\phi} \propto r^{-(n+9/5)}$, where $n \sim 1$. For pure accretion (no outflow), the density profile appears to be consistent with the results of Narayan & Yi (1995a); Blandford & Begelman (2004) (see Fig. 2.7). We further examine the correlation between α and plasma-β that generally assumes the form of power law as $\alpha \propto \beta^{-q}$. For $6r_g \lesssim r < 50r_g$, we obtain $\alpha \propto \beta^{-2/5}$ which are in close agreement with results of the local shearing box simulation (Salvesen et al., 2016). Interestingly, to the best of our knowledge, we find a new scaling relation yielding $\alpha \propto \beta^{-7/5}$ in the region $(2r_g < r \lesssim 6r_g)$, where the disk is magnetically active (see Fig. 2.8).

- It may be noted that depending on the input parameters, the accretion solution passing through $r_{\rm in}$ may not extend up to $r_{\rm edge}$ as it becomes closed at $r < r_{\rm edge}$ (see Fig. 2.9). In reality, solutions of this kind are potentially promising as they can be a part of the global shocked accretion flow. Considering this, we identify the effective domain of three-dimensional parameter space in $(\mathcal{L}, \mathcal{E}, r_{\rm in})$ for a given set of $(b^r_{\rm in}, b^{\phi}_{\rm in})$ that admits closed GRMHD accretion solutions possessing $r_{\rm in}$. Generally, it appears that for smaller $\mathcal{L}$, one requires higher $r_{\rm in}$ to obtain the closed solution and vice versa (see Fig. 2.10).

With the above findings, we wish to emphasize that magnetic fields play a pivotal role in regulating the structure as well as the dynamics of the GRMHD accretion flow around black holes. Overall, it is intriguing that the present formalism provides insight into GRMHD accretion solution in the steady state limit, and it would be useful in carrying out state-of-the-art GRMHD simulation studies in higher dimensions. So far, we have discussed the magnetized accretion around a Schwarzschild BH, but in reality, astrophysical objects are expected to be rotating (Reynolds, 2021). Therefore, in the next Chapter, we focus on studying the magnetized accretion flows around Kerr BHs.

Chapter 3

Low angular momentum general relativistic magnetohydrodynamic accretion flow around rotating black holes with shocks

The content of this chapter has been published in Mitra S., Das S., ApJ, 971, 1, 2024.

THIS chapter outlines the low angular momentum, advection dominated GRMHD accretion flows around rotating BHs in the steady state. Such choice of angular momentum (λ) distribution of matter ($\lambda \ll \lambda_{\rm Kep}$ *i.e.,* sub-Keplerian in nature) is important as the circularization radius comes out to be of the order of a few hundreds of $r_{\rm g}$, where $r_{\rm g}$ is the gravitational radius of the accretor (Frank et al., 2002; Moscibrodzka et al., 2007). In a similar context, Proga & Begelman (2003) numerically showed that very low angular momentum matter is important in determining the total mass supply and the accretion rate onto the BHs. Needless to mention that the observed spectrum of black hole partly comes from a Keplerian disk as a multi-color black body emission (Shakura & Sunyaev, 1973) and a power-law component mainly from the quasi-spherical, low angular momentum flow component (Abramowicz et al., 1988; Chakrabarti & Mandal, 2006). Therefore, exploring the low angular momentum flows in the GRMHD framework is necessary to explain the astrophysical observations. In doing so, we observe that the low

angular momentum accretion flows often possess multiple critical points ($r_{\rm in}$ and $r_{\rm out}$) depending on the model parameters. These multi-transonic flows are potentially viable to harbour the dynamically important shock waves (Fukue, 1987; Chakrabarti, 1989) (Lichnerowicz, 1970; Appl & Camenzind, 1988; Takahashi et al., 2006; Fukumura et al., 2007). Accretion solutions containing shocks are thermodynamically preferred due to their high entropy content (Becker & Kazanas, 2001) over the shock-free solutions. The presence of shock waves often facilitates in explaining the spectro-temporal signatures of BH-XRBs (Chakrabarti & Titarchuk, 1995; Mandal & Chakrabarti, 2005; Nandi et al., 2012; Iyer et al., 2015; Das et al., 2021; Majumder et al., 2022; Nandi et al., 2024, and references therein). Realizing the astrophysical significance of shock-induced accretion solutions, these are widely studied both in hydrodynamics (Fukue, 1987; Chakrabarti, 1989; Yang & Kafatos, 1995; Ryu et al., 1997; Lu et al., 1999; Das et al., 2001a; Becker & Kazanas, 2001; Chakrabarti & Das, 2004; Fukumura & Tsuruta, 2004; Das, 2007; Becker et al., 2008; Das et al., 2009; Kumar et al., 2013; Das et al., 2014; Suková & Janiuk, 2015; Suková et al., 2017; Aktar et al., 2017; Kim et al., 2019; Dihingia et al., 2019; Sen et al., 2022; Patra et al., 2022; Debnath et al., 2024; Singh & Das, 2024) as well as magneto-hydrodynamic (Nishikawa et al., 2005; Takahashi et al., 2006; Fukumura et al., 2007; Sarkar & Das, 2015, 2016; Fukumura et al., 2016; Das & Sarkar, 2018; Dihingia et al., 2020a) scenarios. However, efforts are pending to investigate the shock dynamics in steady GRMHD flow around rotating black holes with a REoS.

Therefore, in Chapter 3, we study the thin, standing, non-dissipative shock waves in the ideal GRMHD framework around weakly as well as rapidly rotating BHs. We characterize the shock-induced global GRMHD accretion solutions by a set of flow parameters, such as energy flux ($\mathcal{E}$), angular momentum flux ($\mathcal{L}$), radial magnetic flux (Φ), and iso-rotation parameter (F). Considering the highly conducting flows, the local magnetic fields (the radial (b^r) and toroidal (b^ϕ) component) threading the disk mid-plane can be expressed in terms of the conserved quantities Φ and F, respectively. With this, we notice that shock properties, namely shock location ($r_{\rm sh}$), compression ratio (R, the measure of density compression across the shock front), and shock strength (Ψ, measure of temperature jump across the shock front) strongly depend on $\mathcal{E}, \mathcal{L}$, and Φ. However, the effect of F on shock dynamics is found insignificant. Due to shock compression, a hot, dense,

and strongly magnetized post-shock corona (PSC) forms. The presence of such coronal structure significantly affects the emergent radiations from the disk (Poutanen, 1998; Nandi et al., 2012; Iyer et al., 2015; Majumder et al., 2022; Nandi et al., 2024). Moreover, we find that shock in GRMHD flow continues to exist for a wide range of flow parameters. This allows us to identify the effective domain of parameter space in the $\mathcal{L}-\mathcal{E}$ plane, where shock solutions are feasible. Further, we examine the modification of the shock parameter space and notice that it shifts towards the lower angular momentum values with increasing Φ and black hole spin ($a_{\rm k}$). Finally, we compute the critical radial magnetic flux ($\Phi^{\rm cri}$) that admits shocks in GRMHD flow and ascertain that $\Phi^{\rm cri}$ is higher (lower) for a black hole of spin $a_{\rm k}=0.99(0.0)$ and vice versa. Moreover, we indicate that the GRMHD shocked accretion flows are not consistent with the magnetically arrested disk (MAD) as $\Phi \ll \Phi_{\rm MAD}$ (Sądowski, 2016b).

3.1 Magnetized flow: Formalism and underlying assumptions

In this Section, we study the magnetized hot accretion flows around a stationary, axisymmetric rotating BH. In Boyer-Lindquist coordinates, the line element of rotating BH space-time takes the form (Kerr, 1963):

$$ds^2=-\left(1-\frac{2r}{\Sigma}\right)dt^2-\frac{4a_{\rm k}r}{\Sigma}\sin^2\theta dt\, d\phi+\frac{\Sigma}{\Delta}dr^2+\Sigma d\theta^2+\left[r^2+a_{\rm k}^2+\frac{2ra_{\rm k}^2}{\Sigma}\sin^2\theta\right]\sin^2\theta d\phi^2, \tag{3.1}$$

where $\Sigma=r^2+a_{\rm k}^2\cos^2\theta$, $\Delta=r^2+a_{\rm k}^2-2r$ and $a_{\rm k}$ is the BH spin. In this work, we express length r and time t in terms of $r_{\rm g}$ and $r_{\rm g}/c$, $r_{\rm g}\,(=GM_{\rm BH}/c^2)$ being gravitational radius, where G is the gravitational constant, c is the speed of light, and $M_{\rm BH}$ is the mass of BH. With this unit system, we write the governing GRMHD equations (Lichnerowicz, 1970; Anile, 1990, and references therein) as,

$$\nabla_\mu(\rho u^\mu)=0; \quad \nabla_\mu T^{\mu\nu}=0; \quad \nabla_\mu {}^*\mathcal{F}^{\mu\nu}=0, \tag{3.2}$$

where ρ is the mass density, u^μ is the four velocity, $T^{\mu\nu}$ is the energy-momentum tensor, and ${}^*\mathcal{F}^{\mu\nu}$ is the dual of Faraday's electromagnetic tensor. We consider the accretion flow with infinite conductivity that allows the magnetic field lines to remain frozen into the accreting plasma according to the ideal GRMHD conditions, *i.e.,* $u_\mu b^\mu = 0$. In a magnetized flow, the energy-momentum tensor is given by (Abramowicz & Fragile, 2013),

$$T^{\mu\nu} = (e + p_{\rm gas})u^\mu u^\nu + p_{\rm gas} g^{\mu\nu} + \frac{1}{2} g^{\mu\nu} b^2 + b^2 u^\mu u^\nu - b^\mu b^\nu. \tag{3.3}$$

Here, $p_{\rm gas}$ is the gas pressure, e is the internal energy, b^μ refers to the four magnetic fields in the comoving frame and $B^2 = b_\mu b^\mu = b^2$. Note that δ^μ_ν $(= g^{\mu\alpha} g_{\alpha\nu})$ is the contraction of the covariant and contravariant metric components.

3.1.1 Conserved quantities in the MHD flow

We consider the magnetized advective disk to be confined in the mid-plane ($\theta = \pi/2$) in the steady state, *i.e.,* $\partial_t \to 0$. With the background axisymmetry $\partial_\phi \to 0$, we impose the condition, $u^\theta \sim 0$ throughout the disk and neglect the motion along $\theta-$direction ($\partial_\theta \to 0$). Here, the disk is threaded by radial (b^r) and toroidal (b^ϕ) magnetic fields, and the respective field lines are frozen in the plasma following the ideal MHD condition. With these considerations, we calculate the following conserved quantities below:

The particle number conservation equation takes the form,

$$\sqrt{-g}\rho u^r = \text{constant} = C_{\mathcal{M}}. \tag{3.4}$$

Being stationary and axisymmetric, the Kerr metric is associated with two Killing vector fields. As the fluid is assumed to obey the symmetries of the chosen space-time, the energy-momentum conservation takes the form $\nabla_\mu (T^\mu_\nu \xi^\nu) = 0$, where ξ^ν refers to the generic killing vectors. Accordingly, we obtain the globally conserved specific energy flux ($\mathcal{E}$) for $\nu = t$ as,

$$-\frac{\sqrt{-g}T^r_t}{C_{\mathcal{M}}} = -h_{\rm tot} u_t + \frac{1}{\rho u^r} b^r (g_{tt} b^t + g_{t\phi} b^\phi) = \mathcal{E}, \tag{3.5}$$

and the conserved specific angular momentum flux ($\mathcal{L}$) is obtained for $\nu = \phi$ as,

$$\frac{\sqrt{-g}T^r_\phi}{C_\mathcal{M}} = h_{\rm tot}u_\phi - \frac{1}{\rho u^r}b^r\left(g_{\phi\phi}b^\phi + g_{t\phi}b^t\right) = \mathcal{L}. \tag{3.6}$$

Additionally, the t and $\phi-$components of Maxwell's equation imply,

$$-\sqrt{-g}\,{}^*\mathcal{F}^{rt} = \text{const} = \Phi, \tag{3.7}$$

and,

$$\sqrt{-g}{}^*\mathcal{F}^{r\phi} = \text{const} = F, \tag{3.8}$$

where ${}^*\mathcal{F}^{rt} = u^tb^r - u^rb^t$, and ${}^*\mathcal{F}^{r\phi} = u^rb^\phi - u^\phi b^r$. Here, the constants Φ and F refer to radial magnetic flux and the iso-rotation parameter, respectively. Finally, we obtain the r-component of the Navier-Stokes equation by projecting the energy-momentum conservation equation along the radial direction in the fluid frame, which is given by,

$$\gamma^r_\mu\nabla_\nu T^{\mu\nu} = (g^{r\nu} + u^ru^\nu)\nabla_\nu p_{\rm tot} + \rho h_{\rm tot}u^\nu\nabla_\nu u^\alpha - \nabla_\nu(b^rb^\nu) - u^ru_\mu\nabla_\nu(b^\mu b^\nu) = 0, \tag{3.9}$$

where γ^r_μ $(= \delta^r_\mu + u^ru_\mu)$ is the projection operator, $p_{\rm tot}$ $(= p_{\rm gas} + p_{\rm mag})$ is the total pressure, $p_{\rm mag}$ $(= b^2/2)$ is the magnetic pressure, and $h_{\rm tot}$ $[= (e + p_{\rm gas})/\rho + b^2/\rho]$ is the total enthalpy.

Following Riffert & Herold (1995); Peitz & Appl (1997), we calculate the local half-thickness (H) of the magnetized disk considering hydrostatic equilibrium in the vertical direction, which is given by,

$$H^2 = \frac{p_{\rm gas}r^3}{\rho\mathbb{F}}, \quad \mathbb{F} = \gamma^2_\phi\frac{(r^2 + a^2_{\rm k})^2 + 2\Delta a^2_{\rm k}}{(r^2 + a^2_{\rm k})^2 - 2\Delta a^2_{\rm k}}, \tag{3.10}$$

where γ_ϕ $(= 1/\sqrt{1 - v^2_\phi})$ is the Lorentz factor. We define the specific angular momentum of the flow as λ $(= -u_\phi/u_t)$ and the angular velocity of the flow is given by Ω $(= u^\phi/u^t)$ (Dihingia et al., 2018a). We follow Lu (1985) to describe the three components of fluid velocities in the corotating frame as $v^2_\phi = u^\phi u_\phi/(-u^tu_t)$, $v^2_r = u^ru_r/(-u^tu_t)$, and $v^2_\theta = u^\theta u_\theta/(-u^tu_t)$, where $v_\theta = 0$ as $u^\theta \sim 0$ in the disk mid-plane. Upon integrating equation (3.4), we obtain the globally conserved mass accretion rate in the comoving

frame, which is given by,

$$\dot{M} = -4\pi\rho v\gamma_v H\sqrt{\Delta}, \tag{3.11}$$

where v $(= \gamma_\phi v_r)$ is the flow velocity and $\gamma_v = 1/\sqrt{1-v^2}$. In this work, we express the accretion rate as $\dot{m} = \dot{M}/\dot{M}_{\rm Edd}$, where $\dot{M}_{\rm Edd}$ is the Eddington accretion rate ($\dot{M}_{\rm Edd} = 1.4\times10^{18}(\frac{M_{\rm BH}}{M_\odot})$ g s^{-1}, $M_\odot$ being the solar mass). In this work, we choose $\dot{m} = 0.001$. Using ideal MHD condition $u_\mu b^\mu = 0$ and equations (3.7-3.8), we express $b^{r,\phi}$ in terms of Φ and F as

$$b^r = -\frac{\gamma_\phi^2(\Phi + F\lambda)}{u^t\mathcal{P}}, \quad b^\phi = \frac{Fv^2 - \gamma_\phi^2(F+\Phi\Omega)}{u^r\mathcal{P}}, \tag{3.12}$$

where $\mathcal{P} = r^2(v^2-1)$. Adopting the transformations in equation (3.12), we analyze the magnetized accretion flow in terms of the global constants Φ and F, respectively.

3.1.2 Equation of state

In order to close the dynamical equations [*i.e.,* equations (3.5-3.9) and equation (3.11)], we use the relativistic equation of state (REoS; Chattopadhyay & Ryu, 2009), which is given by Eq. 2.20-2.21 in Chapter 2.

Notably, the characteristic wave speeds for magnetized flows are associated with the Alfvén and magneto-sonic waves, respectively. Following Gammie et al. (2003), we define the Alfvén speed as $C_{\rm a}^2 = b_\mu b^\mu/(\rho h_{\rm tot})$, and the fast-magnetosonic speed as $C_{\rm f}^2 = C_{\rm s}^2 + C_{\rm a}^2 - C_{\rm s}^2C_{\rm a}^2$, where the relativistic sound speed is given by $C_{\rm s}^2 = \Gamma p_{\rm gas}/(e+p_{\rm gas})$. Moreover, we define the magnetosonic Mach number as $M = v/C_{\rm f}$.

3.1.3 Critical point analysis

We combine equations (3.5-3.9, 3.11) and obtain three coupled non-linear differential equations as follows,

(a) the radial momentum equation:

$$\mathcal{R}_0 + \mathcal{R}_v\frac{dv}{dr} + \mathcal{R}_\Theta\frac{d\Theta}{dr} + \mathcal{R}_\lambda\frac{d\lambda}{dr} = 0, \tag{3.13}$$

(b) the azimuthal momentum equation:

$$L_0 + L_v \frac{dv}{dr} + L_\Theta \frac{d\Theta}{dr} + L_\lambda \frac{d\lambda}{dr} = 0, \tag{3.14}$$

(c) the energy equation:

$$E_0 + E_v \frac{dv}{dr} + E_\Theta \frac{d\Theta}{dr} + E_\lambda \frac{d\lambda}{dr} = 0. \tag{3.15}$$

The coefficients ($\mathcal{R}_j, L_j, E_j$; $j \rightarrow 0, v, \Theta$, and λ) in equations (3.13-3.15) are given in Appendix-A.

Using equations (3.13-3.15), we obtain the wind equation of the GRMHD flow after some simple algebra as,

$$\frac{dv}{dr} = \frac{\mathcal{N}(r, a_{\rm k}, v, \Theta, \lambda, \Phi, F)}{\mathcal{D}(r, a_{\rm k}, v, \Theta, \lambda, \Phi, F)}, \tag{3.16}$$

where the explicit expression of numerator $\mathcal{N}$ and denominator $\mathcal{D}$ are given in Appendix B.1. Moreover, we express the gradients of the angular momentum (λ) and temperature (Θ) in terms of dv/dr as

$$\frac{d\lambda}{dr} = \tilde{\lambda}_1 + \tilde{\lambda}_2 \frac{dv}{dr}, \tag{3.17}$$

and

$$\frac{d\Theta}{dr} = \tilde{\Theta}_1 + \tilde{\Theta}_2 \frac{dv}{dr}, \tag{3.18}$$

where the detailed expressions of the coefficients ($\tilde{\lambda}_1, \tilde{\lambda}_2, \tilde{\Theta}_1, \tilde{\Theta}_2$) are described in Appendix B.2. To obtain GRMHD accretion solutions around rotating BH, we simultaneously solve equations (3.16-3.18) for a set of model parameters, namely $\mathcal{E}$, $\mathcal{L}$, Φ, F and $a_{\rm k}$, respectively.

3.1.4 Solution Methodology

We follow the solution procedure as described in Section 2.2.1 to obtain the global GRMHD accretion solution. In this chapter, we are interested to examine the effect of the radial magnetic flux (Φ) and the iso-rotation parameter (F) on the accretion

dynamics instead of the local magnetic fields (b^r and b^ϕ). It is noteworthy that, the GRMHD accretion flow around BHs often possesses multiple critical points depending on the model parameters $(a_{\rm k}, \mathcal{E}, \mathcal{L}, \Phi, F)$. Such GRMHD flows are potentially viable to harbour shock waves (Fukue, 1987; Chakrabarti, 1989; Takahashi et al., 2006; Das & Chakrabarti, 2004; Das, 2007; Fukumura et al., 2007, 2016; Sarkar & Das, 2016, 2018; Sarkar et al., 2018; Dihingia et al., 2019, 2020a; Sarkar et al., 2020; Das et al., 2021, 2022; Sen et al., 2022; Patra et al., 2022; Singh & Das, 2024, and references therein). Accordingly, in the subsequent sections, we study the shock-induced magnetized accretion flows around rotating BH adopting the general relativistic framework.

3.2 Shock-induced GRMHD accretion flow

Depending on the model parameters $(a_{\rm k}, \mathcal{E}, \mathcal{L}, \Phi, F)$, subsonic GRMHD accretion flow becomes supersonic after passing through the outer critical point ($r_{\rm out}$), and continues to proceed towards the BH. Meanwhile, flow starts experiencing centrifugal repulsion, which momentarily slows down the accreting matter. Because of this, matter accumulates in the vicinity of the BH, and a barrier is formed in the form of an effective boundary layer around BH. Such a centrifugal barrier cannot hold the accumulation of matter indefinitely and beyond a critical limit, it eventually triggers the discontinuous transition of the flow variables in the form of shock waves (Fukue, 1987; Chakrabarti, 1989; Frank et al., 2002; Takahashi et al., 2002; Das & Chakrabarti, 2007; Fukumura et al., 2007; Sarkar & Das, 2016; Sarkar et al., 2018; Dihingia et al., 2019, 2020a; Sarkar et al., 2020; Sen et al., 2022; Patra et al., 2022; Singh & Das, 2024). Considering this, we describe the shock conditions for MHD flow in the GR framework, which eventually enables us to study shock properties, namely shock location ($r_{\rm sh}$), shock compression ratio (R), and shock strength (Ψ).

In order to execute discontinuous shock transition, magnetized accretion flow must satisfy the general relativistic shock conditions (Lichnerowicz, 1970; Appl & Camenzind, 1988; Takahashi et al., 2006; Fukumura et al., 2007), which are given by,

(a) Mass flux conservation, $\left[\rho u^r\right] = 0$,

(b) Energy flux conservation, $\left[T^{rt}\right] = 0$,

(c) Angular momentum flux conservation, $\left[T^{r\phi}\right] = 0$,

(d) Radial magnetic flux conservation, $\left[{}^{*}F^{rt}\right] = 0$,

(e) Iso-rotation conservation, $\left[{}^{*}F^{r\phi}\right] = 0$,

and,

(f) Pressure balance condition, $\left[T^{rr}\right] = 0$.

Here, the square bracket '[ ]' denotes the difference of a quantity across the shock front. Using these conditions, we obtain a shock-induced global GRMHD accretion solution around rotating BH. Note that, in this work, we assume the shocks to be thin and non-dissipative in nature for simplicity.

> **Note:** In this work, we consider the thickness of the shock front to be small (*i.e.,* much smaller than the lengthscales of gradients in the gas), as it allows us to assume the radiative losses are negligible across the shock front. This assumption yields the adiabatic shock conditions (Frank et al., 2002), and hence, the shocks under consideration remain non-dissipative in nature.

Across the shock front ($r_{\rm sh}$), supersonic pre-shock flow jumps into the subsonic branch, resulting a hot and dense post-shock flow (Aktar et al. (2015)). This happens because the kinetic energy of pre-shock flow is converted into thermal energy and post-shock flow becomes compressed due to shock compression. This yields the PSC to act as a perfect reservoir of hot electrons which eventually intercepts the soft photons from the cooler pre-shock flow and reprocesses them to produce high energy radiations via inverse Comptonization (Chakrabarti & Titarchuk, 1995; Mandal & Chakrabarti, 2005; Nandi et al., 2012; Iyer et al., 2015; Das et al., 2021; Majumder et al., 2022; Nandi et al., 2024). After the shock transition, the subsonic flow gradually gains its radial velocity and ultimately enters into BH supersonically after crossing the inner critical point ($r_{\rm in}$).

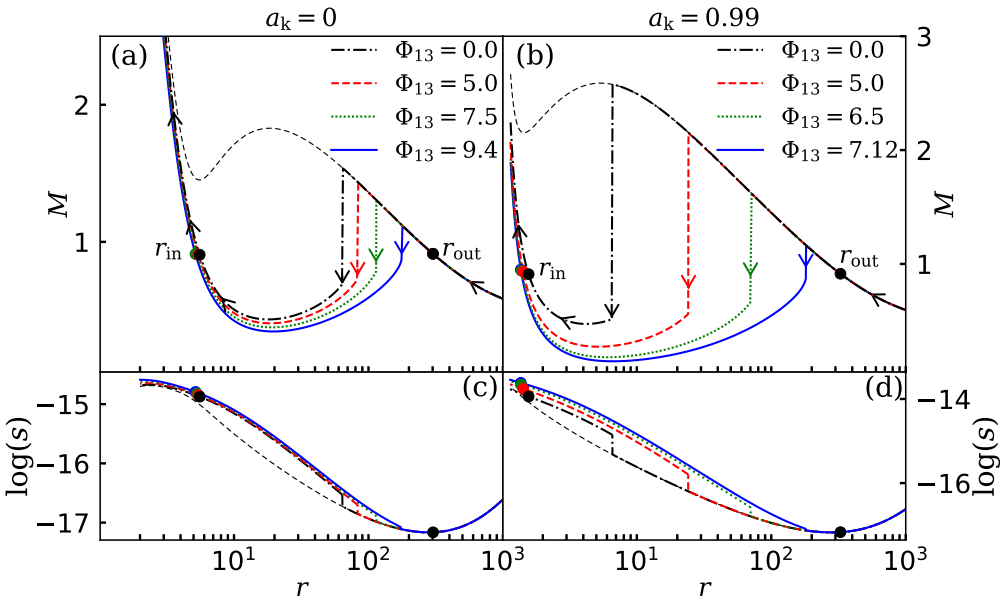

FIGURE 3.1: Plot of fast-magnetosonic Mach number ($M = v/C_f$) with radial coordinate (r) for shock-induced accretion solutions around BHs. The chosen model parameters are $(\mathcal{E}, F_{15})$=(1.001, 7.5). (a) Dot-dashed, dashed, dotted and solid curves denote the accretion solutions for $\Phi_{13} = 0.0$, 5.0, 7.5 and 9.4, respectively, where $\mathcal{L} = 3.15$ and $a_k = 0.0$. (b) Dot-dashed, dashed, dotted and solid curves denote the accretion solutions for $\Phi_{13} = 0.0$, 5.0, 6.5 and 7.12, respectively, where $\mathcal{L} = 1.95$ and $a_k = 0.99$. In both panels, vertical arrows indicate the shock transitions at radii (r_{sh}) and filled circles denote the critical points (r_{in} and r_{out}). Arrows indicate the overall direction of the flow motion towards BH. Entropy density (s) associated with the solutions presented in (a) and (b) are presented in (c) and (d), respectively. See the text for the details.

3.3 Results

We investigate the dynamical structure of shock-induced trans-magnetosonic accretion solutions around BH of spin a_k for a set of model parameters, namely $\mathcal{E}$, $\mathcal{L}$, Φ and F, respectively. In doing so, we examine the effects of the radial magnetic flux (Φ) and iso-rotation parameter (F) on the GRMHD solutions. Given the diminutive nature of the dimensionless radial magnetic flux and iso-rotation parameter, we denote them as $\Phi = \Phi_{13} \times 10^{-13}$ and $F = F_{15} \times 10^{-15}$, and use them ($\Phi_{13}$ and F_{15}) to signify magnetic flux values. Moreover, in this work, we choose $M_{BH} = 10 M_\odot$ and $\dot{m} = 0.001$ as fiducial values unless stated otherwise.

3.3.1 Shock-induced global GRMHD accretion solutions

To begin with, we consider an advective flow that accretes towards a non-rotating black hole starting from the outer edge of the disk at $r_{edge} = 1000$. The flow is characterized

with the model parameters as $\mathcal{E} = 1.001$, $\mathcal{L} = 3.15$, $F_{15} = 7.5$ and $a_{\rm k} = 0$. The obtained results are plotted in Fig. 3.1a, where fast-magnetosonic Mach number ($M = v/C_{\rm f}$) is plotted with radial coordinate (r) for accretion solutions containing shock waves. Here, we observe that for $\Phi_{13} = 0.0$, subsonic flow changes its sonic state after crossing the outer critical point at $r_{\rm out} = 302.235$ to become supersonic. While the supersonic flow can smoothly enter into the black hole (thin dashed curve), it undergoes a discontinuous shock transition at $r_{\rm sh} = 63.881$ (dot-dashed vertical arrow), as the entropy content of the post-shock branch is higher compared to the pre-shock flow (Das et al., 2001b). This is not surprising as it happens in accordance with the second law of thermodynamics due to the fact that shocked solution is thermodynamically preferred (Becker & Kazanas, 2001) over the shock free solution. After the shock, the subsonic flow gradually gains radial velocity as it moves inward and crosses the inner critical point at $r_{\rm in} = 5.556$ before entering the black hole supersonically. This result is presented using dot-dashed (black) curve. Next, we increase the radial magnetic flux as $\Phi_{13} = 5.0$, keeping the other model parameters fixed, that increases of magnetic pressure leading to the rise of total pressure ($p_{\rm tot}$). This eventually pushes the shock front outwards and shock settles down to a larger radius at $r_{\rm sh} = 83.088$. This result is shown using dashed (red) curve and dashed vertical arrow denotes the location of shock transition. For further increase of radial magnetic flux as $\Phi_{13} = 7.5$, the shock transition happens at $r_{\rm sh} = 113.975$ and shock-induced GRMHD solution is depicted using dotted (green) curve. Needless to mention that an indefinite increase of Φ_{13} is not possible, because beyond a critical limit of radial magnetic flux $\Phi_{13} = 9.4$, shock ceases to exist as the shock conditions (Sec. 3.2) are not satisfied. In the figure, we denote this solution using solid (blue) curve. Furthermore, following Das et al. (2009); Porth et al. (2017), we compute the specific entropy function ($s \propto p_{\rm tot}/\rho^{\Gamma-1}$) corresponding to the shocked accretion solutions delineated in Fig. 3.1a and plot it as function of r in panel Fig. 3.1c. We observe that in all cases, s jumps to higher value at the shock radius ($r_{\rm sh}$), which evidently confirms that shocked accretion solutions possess higher entropy than the shock free solution.

We continue to examine the effect of Φ_{13} on the flow solutions for rapidly rotating BH as well. Towards this, we choose $a_{\rm k} = 0.99$ and keep the remaining model parameters unchanged (*i.e.*, $\mathcal{E} = 1.001$ and $F_{15} = 7.5$) as in Fig. 3.1a, except $\mathcal{L} = 1.95$ to obtain the

shock-induced magnetized accretion solutions. The obtained results are shown in Fig. 3.1b. Note that we use lower $\mathcal{L}$ value for higher $a_{\rm k}$ simply because low angular momentum flow ($\mathcal{L}$) can only sustain shocks around rapidly rotating BHs (Das & Chakrabarti, 2008; Dihingia et al., 2019; Sen et al., 2022). We observe that for $\Phi_{13} = 0$, shock transition happens at a relatively smaller radius at $r_{\rm sh} = 6.525$ (black) compared to the non-spinning case. This possibly happens as the lower $\mathcal{L}$ resulted weak centrifugal repulsion and hence, shock front moves further inward. However, when Φ_{13} is increased to 5.0, 6.5 and 7.0, the shock front moves outward as expected, and we obtain $r_{\rm sh} = 24.25$ (dashed in red), 70.07 (dotted in green), and 180.74 (solid in blue), respectively. Note that beyond $\Phi_{13} = 7.12$, shock conditions are not favourable and hence, shock ceases to exist for the chosen set of model parameters. We further notice that Mach number (M) of the relativistic magnetized flow generally remain restricted within $M \leq 3$ around rapidly spinning BH mainly due to the rapid increase in sound speed close to the horizon ($r_{\rm h} = 1.14107$). This happens because of the frame-dragging effect (Fukumura & Kazanas, 2007) around a rotating BH. Here, the rotation of BH compels the matter to corotate with the BH along ϕ-direction before getting trapped by the strong gravitational pull. This essentially heats up the inner disk, and hence, sound speed increases. Indeed, a similar finding is observed for general relativistic hydrodynamic flows as well (Dihingia et al., 2018a). Next, in Fig. 3.1d, we present the plot of specific entropy function (s) with r for solutions presented in Fig. 3.1b, and find that for all cases, s increases at $r_{\rm sh}$. This provides clear evidence that shocked accretion solutions possess higher entropy compared to the solution without a shock.

3.3.2 Flow variables of shocked-induced GRMHD accretion solutions

In Fig. 3.2, we investigate the behavior of various flow variables corresponding to the shocked GRMHD solutions depicted in Fig. 3.1. In Fig. 3.2a, we present the radial velocity (v) variation as a function of r around a rapidly rotating BH of spin $a_{\rm k} = 0.99$. We observe that for a set of model parameters $\mathcal{E} = 1.001$, $\mathcal{L} = 1.95$, and $F_{15} = 7.5$, flow velocity monotonically increases in the pre-shock region and discontinuously drops down to the subsonic branch at the shock radius $r_{\rm sh}$. After the shock transition, flow momentarily slows down, although it gradually picks up radial velocity and ultimately

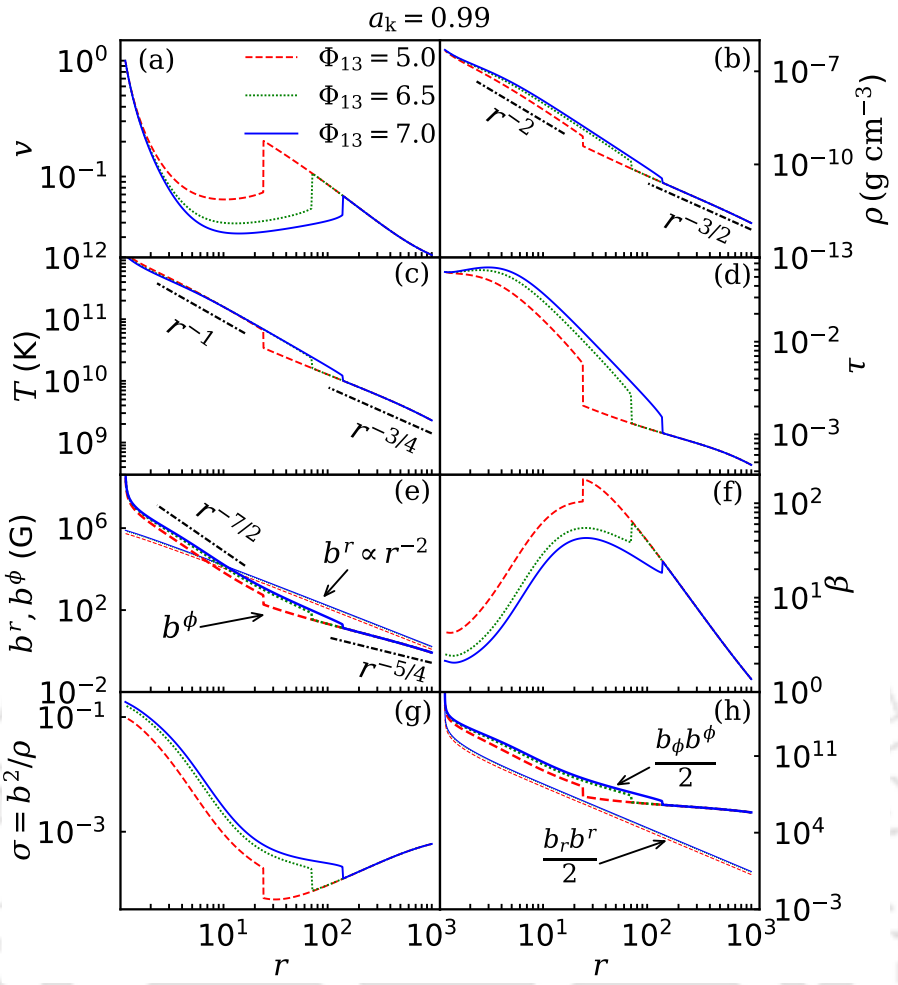

FIGURE 3.2: Radial variation of the primitive flow variables corresponding to shock-induced GRMHD accretion solutions presented in Fig. 3.1b. In panels (a-h), profiles of radial velocity (v), density (ρ), temperature (T), scattering optical depth (τ), radial (b^r) and toroidal (b^ϕ) magnetic fields, plasma-β, magnetization ($\sigma = b^2/\rho$), and radial and toroidal magnetic pressures are plotted for different Φ_{13}. Dashed (red), dotted (green) and solid (blue) curves denote results for $\Phi_{13} = 5.0$, 6.5 and 7.12, respectively. In panels (b), (c) and (e), dot-dashed lines represent best-fit power law profiles of pre- and post-shock flow variables. See the text for the details.

enters into the BH with a velocity comparable to speed of light (c). Results plotted using dashed (red), dotted (green) and solid (blue) are obtained for $\Phi_{13} = 5.0$, 6.5 and 7.12, respectively, which are marked in the figure, and vertical lines denote the shock transition radii. In Fig. 3.2b, we show the variation of mass density (ρ) with r, where sudden increase in ρ is observed just after the shock transition for all Φ_{13} values. This happens because the radial velocity decreases at shock and hence, ρ increases to higher value in order to preserve the conservation of mass flux across the shock front. We observe that post-shock density profile follows a steeper power-law as $\rho \propto r^{-2}$, whereas the pre-shock density follows $\rho \propto r^{-3/2}$. Note that the pre-shock density profile exactly matches with

the self-similar solutions for a pure inflow model in absence of outflows (Narayan & Yi, 1995a). In Fig. 3.2c, we depict the variation of flow temperature (T) with r. During the shock transition, the supersonic flow jumps into the subsonic branch and loses most of its kinetic energy that results in a hot post-shock flow. We notice that the temperature profile follows $T \propto r^{-1}$, which is commonly observed in Radiatively Inefficient Accretion Flow (RIAF) simulations (Olivares S. et al., 2023). However, in the pre-shock regime, flow maintains a relatively shallower profile as $T \propto r^{-3/4}$. Due to shock compression, the hot and dense post-shock flow becomes puffed up resulting in an effective boundary layer (PSC) surrounding the BH. The presence of such coronal structure significantly affects the emergent radiations from the disk (Chakrabarti & Titarchuk, 1995; Poutanen, 1998; Nandi et al., 2012, and references therein). Keeping this in mind, in Fig. 3.2d, we estimate the scattering optical depth $\tau = \kappa\rho H$, where κ ($= 0.38$ cm^2 g^{-1}) is the electron scattering opacity, and H is the disk half-thickness. We find that disk continues to remain optically thin ($\tau < 1$) in the post-shock regime, which eventually indicates that the emergent high energy radiations can easily escape from the PSC. Next, in Fig. 3.2e, we show the variation of radial (b^r; thin lines) and toroidal (b^ϕ; thick lines) magnetic fields as a function of r. We notice that b^r increases monotonically with decreasing r following $b^r \propto r^{-2}$ profile. We also observe that in the pre-shock regime, the toroidal field follows the self-similar profile as $b^\phi \propto r^{-5/4}$, and it is amplified at $r_{\rm sh}$ just to maintain the continuity of radial flux ($\Phi_- = \Phi_+$) across the shock front. Thereafter, b^ϕ continues to follow a steeper power-law as $b^\phi \propto r^{-7/2}$. With this, the toroidal magnetic field reaches up to $\sim 10^{7-9}$ Gauss near the horizon for the chosen accretion solutions, where magnetic activities are strongest. However, the radial magnetic field limits itself within $\sim 10^{5-6}$ Gauss. An equivalent assessment of magnetic activity is illustrated with the variation of plasma$-\beta$ ($= p_{\rm gas}/p_{\rm mag}$) in Fig. 3.2f. As the flow starts accreting towards the BH, gas pressure ($p_{\rm gas}$) initially dominates over the magnetic pressure ($p_{\rm mag}$), which enhances β values. Indeed, β decreases at PSC as b^ϕ jumps up higher and it yields magnetically stronger PSC, although flow remains thermal pressure dominated ($\beta > 1$). We further notice that the magnetization σ ($= b^2/\rho$) varies with r as shown in Fig. 3.2g and σ becomes roughly ~ 100 times higher near the horizon as compared to the outer edge value. Finally, we present the variation of magnetic pressure corresponding to the radial

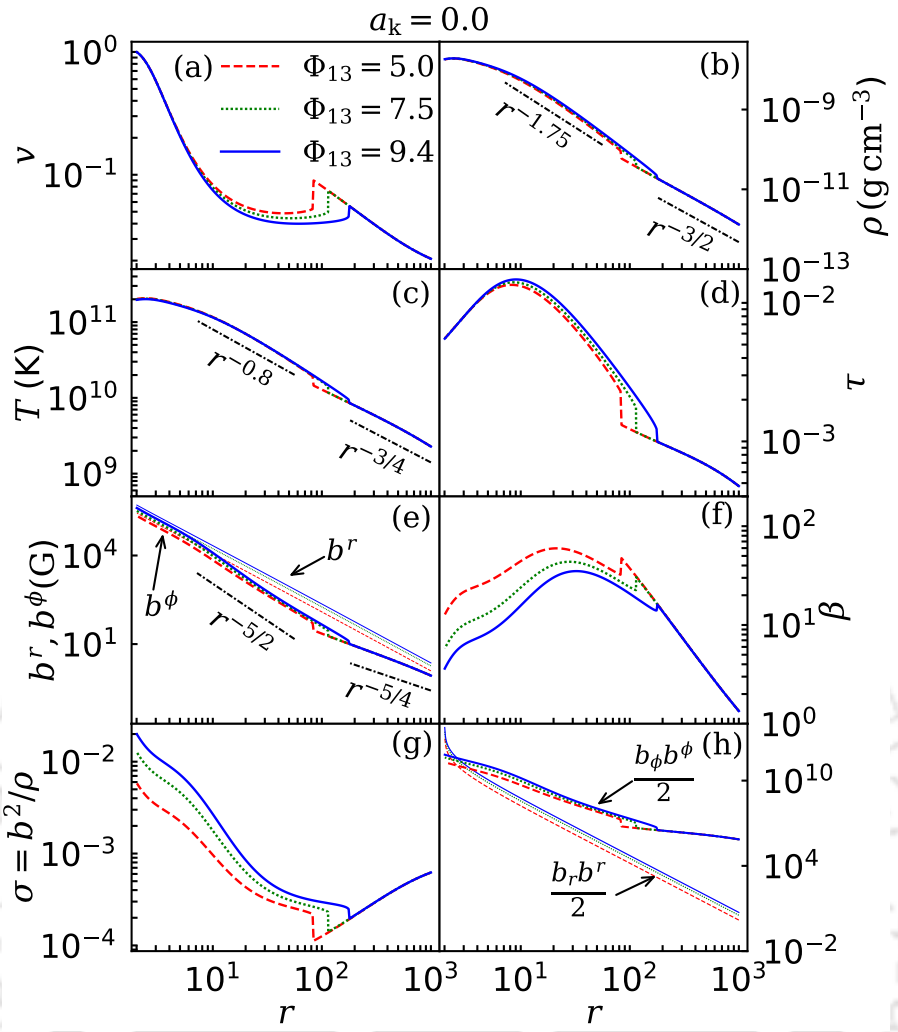

FIGURE 3.3: Same as Fig. 3.2, but flow variables correspond to shocked solutions presented in Fig. 3.1a. Here, dashed (red), dotted (green) and solid (blue) curves denote results for $\Phi_{13} = 5.0$, 7.0 and 9.4, respectively. See the text for the details.

and toroidal components, and find that toroidal magnetic pressure dominates the disk magneto-hydrodynamics as $b^\phi b_\phi > b_r b^r$ all throughout the disk including near horizon domain (see Fig. 3.2h).

It is useful to examine the properties of the primitive flow variables focusing on a non-rotating black hole ($a_k = 0.0$), as illustrated in Fig. 3.3. The model parameters remain consistent with those in Fig. 3.2, except for $\mathcal{L} = 3.15$. The radial variations of the flow variables exhibit qualitative similarity with the results obtained for solutions around rapidly rotating BH of spin $a_k = 0.99$. Nevertheless, as the shock transition tends to occur at relatively larger radii around a non-rotating BH ($a_k = 0.0$), the compression at the post-shock flow weakens. As a result, the density (ρ), temperature (T), and

magnetic fields near the black hole decrease. This results in shallower fitting profiles of the post-shock flow variables in panel (b) $\rho \propto r^{-1.75}$, (c) $T \propto r^{-0.8}$, and (e) $b^{\phi} \propto r^{-5/2}$, compared to the results obtained for $a_{\rm k} = 0.99$. Notably, the pre-shock variables exhibit the same radial dependency as observed in Fig. 3.2, regardless of the spin of BH. Finally, it is observed that the radial component of magnetic pressure ($b^r b_r/2$) exceeds the toroidal component ($b^{\phi} b_{\phi}/2$) near the horizon (see Fig. 3.3h), which contrasts with the rotating black hole case (see Fig. 3.2h).

3.3.3 Shock properties

It is intriguing to investigate the effect of magnetic fields on the shock properties, namely shock location ($r_{\rm sh}$), compression ratio (R), and shock strength (Ψ) as the spectral properties of BH often rely on these quantities (Chakrabarti & Titarchuk, 1995; Nandi et al., 2012, 2018). Towards this, we examine how shock properties change with radial magnetic flux (Φ_{13}) and iso-rotation parameter (F_{15}) for GRMHD flows accreting on to rapidly rotating BH of spin $a_{\rm k} = 0.99$.

In Fig. 3.4a, we depict the variation of shock location ($r_{\rm sh}$) as a function of radial magnetic flux (Φ_{13}) for different values of angular momentum ($\mathcal{L}$). Here, we choose $\mathcal{E} = 1.0015$ and $F_{15} = 5.0$. Solid, dotted and dashed curves represent results for $\mathcal{L} = 1.95$, 1.975 and 2.0, respectively. We observe that for the chosen set of model parameters $(\mathcal{E}, \mathcal{L}, F_{15})$, standing shocks form for minimum radial flux limit $\Phi_{13}^{\rm min} = 0$. Moreover, we find that for a fixed $\mathcal{L}$, standing shocks continue to form at larger radii as Φ_{13} is increased until it reaches a critical limit ($\Phi_{13}^{\rm cri}$). Beyond $\Phi_{13}^{\rm cri}$, shock disappears as shock conditions are not satisfied. Indeed, $\Phi_{13}^{\rm cri}$ does not possess universal value as it depends on the other model parameters. Further, we notice that for fixed Φ_{13}, shocks form at larger radii as $\mathcal{L}$ is increased. This evidently indicates that standing shocks in GRMHD flows seems to be centrifugally supported. Indeed, it is useful to study the density profile of the GRMHD flow as the emitted radiations directly depends on it. Meanwhile, we find that convergent GRMHD flow experiences density compression across the shock front $r_{\rm sh}$ (see Figs. 3.2b, 3.3b). Accordingly, we compute the compression ratio R defined as the ratio of surface mass density (ρH) of post-shock and pre-shock flow and depict it in

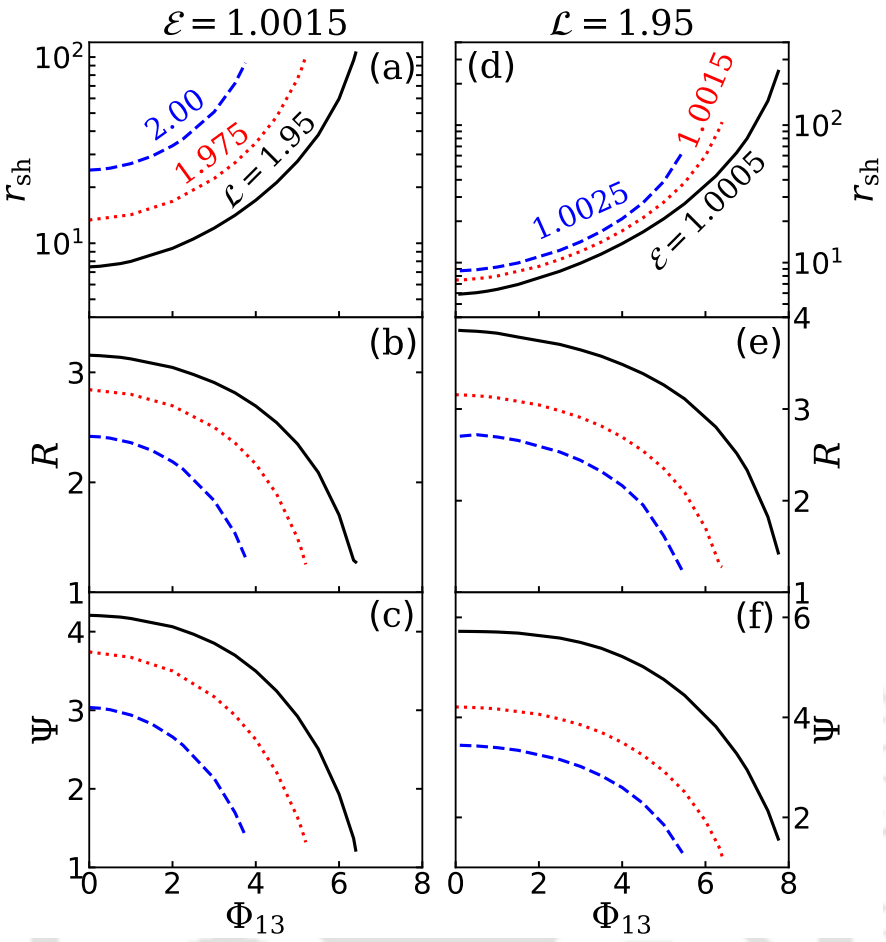

FIGURE 3.4: Variation of (a, d) shock location $r_{\rm sh}$, (b, e) compression ratio R, and (c, f) shock strength Ψ with Φ_{13}. In left panels, angular momentum fluxes is varied as $\mathcal{L} = 1.95$, 1.975 and 2.00, keeping $\mathcal{E} = 1.0015$ fixed. Similarly, in right panels, we vary energy as $\mathcal{E} = 1.0005$, 1.0015 and 1.0025 for fixed $\mathcal{L} = 1.95$. Remaining model parameters are set as $a_{\rm k} = 0.99$ and $F_{15} = 5.0$. See the text for the details.

Fig. 3.4b as function of Φ_{13} for the same set of model parameters as in Fig. 3.4a. For a fixed $\mathcal{L}$, R decreases with higher Φ_{13}. This happens because enhanced Φ_{13} increases the magnetic pressure inside the disk and hence, shock front is pushed outward resulting the weakening of density compression due to expansion of PSC size. Similarly, for a given Φ_{13}, GRMHD flow with higher $\mathcal{L}$ experiences less compression at the PSC as increased centrifugal pressure counteracts the inward motion of the flow. Overall, we observe that strong shock ($R \to 4$) exists for smaller Φ_{13}, whereas shock tends to become weak ($R \to 1$) for larger Φ_{13}. We further compute shock strength (Ψ) that accounts the temperature jump across the shock front. The shock strength is defined as the ratio of pre-shock to post-shock Mach numbers as $\Psi = \frac{v_-/C_{\rm s_-}}{v_+/C_{\rm s_+}}$, and we plot Ψ in Fig. 3.4c as a function of Φ_{13} for identical model parameters as in Fig. 3.4a. We find that for a

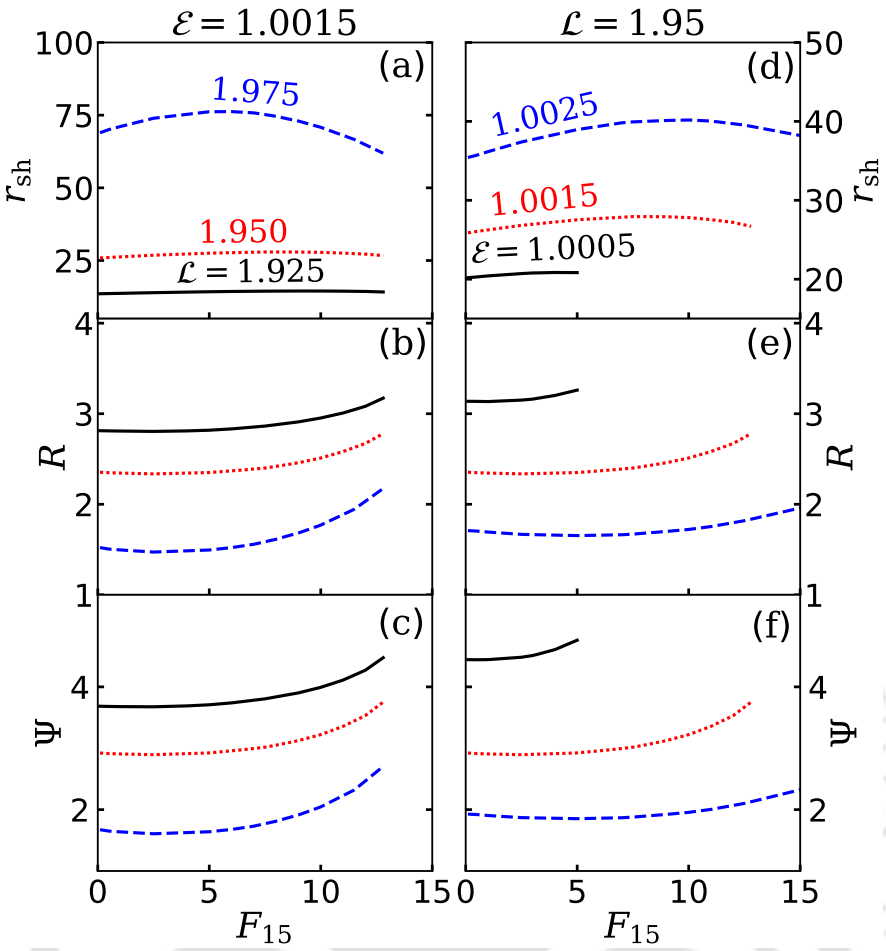

FIGURE 3.5: Variation of (a, d) shock location $r_{\rm sh}$, (b, e) compression ratio R, and (c, f) shock strength Ψ with F_{15}. In left panels, angular momentum fluxes is varied as $\mathcal{L} = 1.925$, 1.950 and 1.975, keeping $\mathcal{E} = 1.0015$ fixed. Similarly, in right panels, we vary energy as $\mathcal{E} = 1.0005$, 1.0015 and 1.0025 for fixed $\mathcal{L} = 1.95$. Remaining model parameters are set as $a_{\rm k} = 0.99$ and $\Phi_{13} = 5.0$. See the text for the details.

given $\mathcal{L}$, Ψ is stronger when Φ_{13} is smaller and vice versa. Moreover, we observe that Ψ exhibits a similar trend to that of the compression ratio (R).

In Fig. 3.4d, we show the variation $r_{\rm sh}$ with Φ_{13} for different values of flow energy ($\mathcal{E}$). Here, we choose $\mathcal{L} = 1.95$ and $F_{15} = 5.0$. Solid, dotted and dashed curves denote results corresponding to $\mathcal{E} = 1.0005$, 1.0015 and 1.0025, respectively. We find that for a fixed $\mathcal{E}$, shock settles down at larger radii as Φ_{13} is increased. Indefinite increase of radial magnetic flux is not possible as there exists a cut-off value of Φ_{13} for which shock conditions are not satisfied. Furthermore, we calculate R and S as in Fig. 3.4b-c and observe that both quantities are decreased when Φ_{13} is increased.

In Fig. 3.5, we depict the comparison of shock properties as a function of the iso-rotation

parameter (F_{15}). In panels (a-c) of Fig. 3.5, we plot $r_{\rm sh}$, R and Ψ for different values of $\mathcal{L}$. Here, we choose the model parameters as $\mathcal{E} = 1.0015$, $\Phi_{13} = 5.0$ and $a_{\rm k} = 0.99$. The solid, dotted and dashed curves denote results for $\mathcal{L} = 1.925$, 1.950 and 1.975, respectively. On the contrary, in Fig. 3.5d-f, we present the results of $r_{\rm sh}$, R and Ψ for different $\mathcal{E}$, where solid, dotted and dashed are for $\mathcal{E} = 1.0005$, 1.0015 and 1.0025, respectively. The model parameters are chosen as $\mathcal{L} = 1.95$, $\Phi_{13} = 5.0$ and $a_{\rm k} = 0.99$. In both scenarios, we notice that the shock location remains nearly unaffected due to the increase in F_{15}. Consequently, both compression ratio (R) and shock strength (Ψ) exhibit negligible variation with F_{15} as well. Because of this, now onwards, we refrain examining the influence of F_{15} on the shock properties unless stated otherwise.

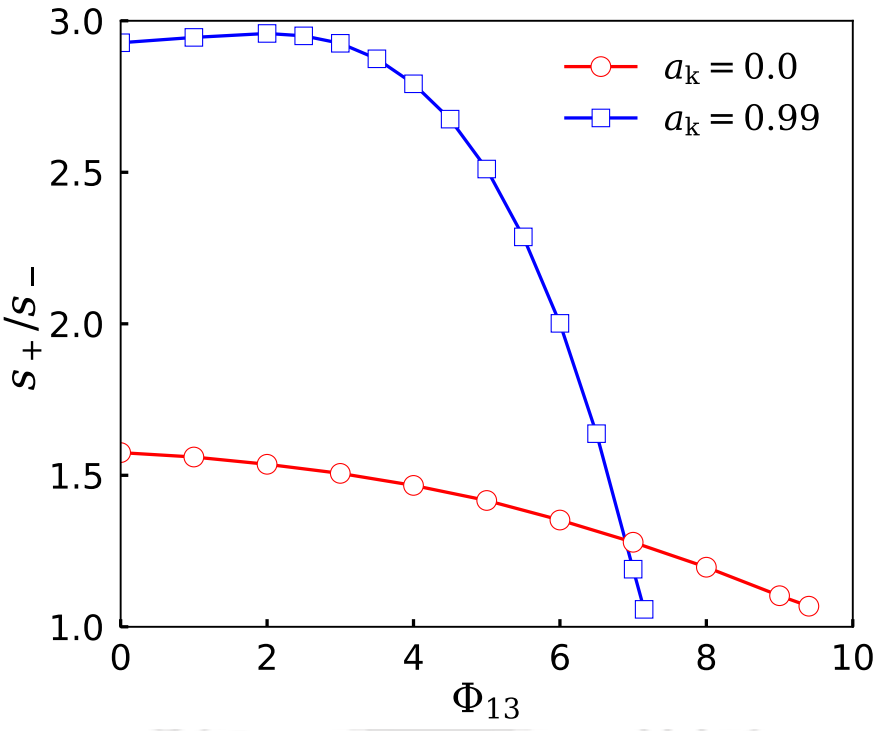

FIGURE 3.6: Plot of ratio of post-shock (s_+) to pre-shock (s_-) entropy functions across the shock front with Φ_{13}. Open circles and open squares joined with solid lines denote results obtained for non-rotating ($a_{\rm k} = 0.0$) and rapidly rotating ($a_{\rm k} = 0.99$) BHs. Here, we choose $\mathcal{L} = 3.15$ for $a_{\rm k} = 0.0$ and $\mathcal{L} = 1.95$ for $a_{\rm k} = 0.99$, while other model parameters are kept fixed as $\mathcal{E} = 1.001$ and $F_{15} = 7.5$. See the text for the details.

As previously noted, shock-induced global GRMHD solutions are favoured over shock-free solutions due to their elevated entropy content. However, the role of the magnetic fields in contributing to the flow entropy is not well understood. To address this, we calculate the ratio of entropy functions measured immediately after (s_+) and before (s_-) the shock transition. The obtained results are depicted in Fig. 3.6, where we plot

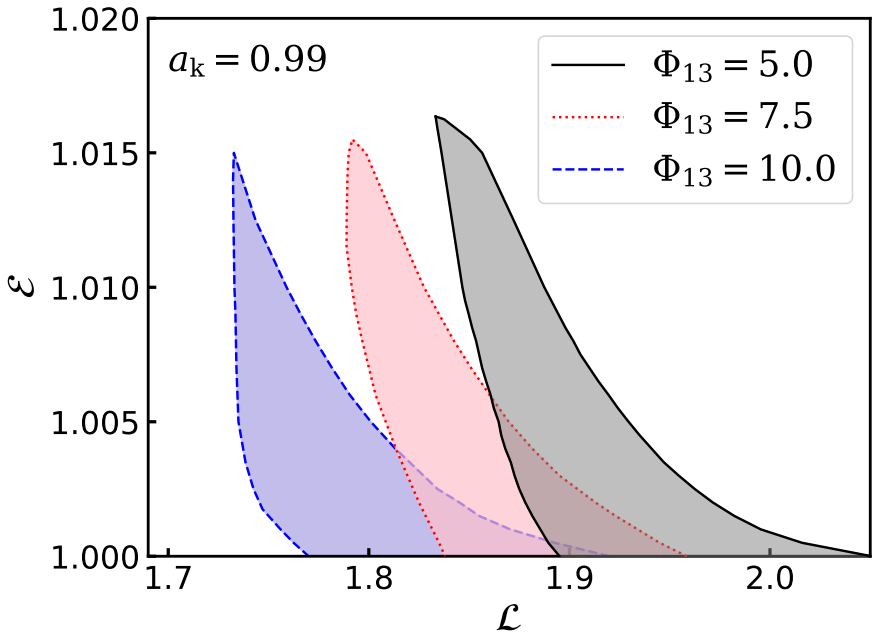

FIGURE 3.7: Plot of shock parameter space in $\mathcal{L} - \mathcal{E}$ plane for different radial magnetic fluxes (Φ_{13}) around a rotating BH. Here, we choose $a_k = 0.99$ and $F_{15} = 5.0$. Effective area bounded by solid (black), dotted (red) and dashed (blue) curves correspond to $\Phi_{13} = 5.0, 7.5$ and 10.0, respectively. See the text for the details.

the variation of s_+/s_- with Φ_{13} for flows with fixed energy $\mathcal{E} = 1.001$ and iso-rotation parameter $F_{15} = 7.5$. In the figure, open circles joined with solid lines represent results corresponding to the shocked accretion solutions around a non-rotating BH with $a_k = 0.0$ and $\mathcal{L} = 3.15$. Similarly, open squares joined with solid lines are for rapidly rotating BH with $a_k = 0.99$, and $\mathcal{L} = 1.95$. We observe that for a chosen set of model parameters, s_+/s_- is maximum for $\Phi_{13} = 0.0$ irrespective to a_k values, and it generally decreases with the increase of Φ_{13}. When Φ_{13} reaches a critical limit, the ratio s_+/s_- approaches unity, indicating that shock ceases to exist as shock conditions are not favourable. Indeed, it's worth noting that this critical limit of Φ_{13} isn't universal, as it varies depending on the other model parameters.

3.3.4 Parameter space for standing shock

It has already been indicated that shock-induced GRMHD accretion solutions are not isolated solutions, instead these solutions continue to exist for a wide range of model parameters, namely $\mathcal{E}$, $\mathcal{L}$, Φ_{13}, F_{15}, and a_k. Hence, it is useful to identify the ranges of model parameters that admit shocked accretion solutions. Towards this, in Fig. 3.7,

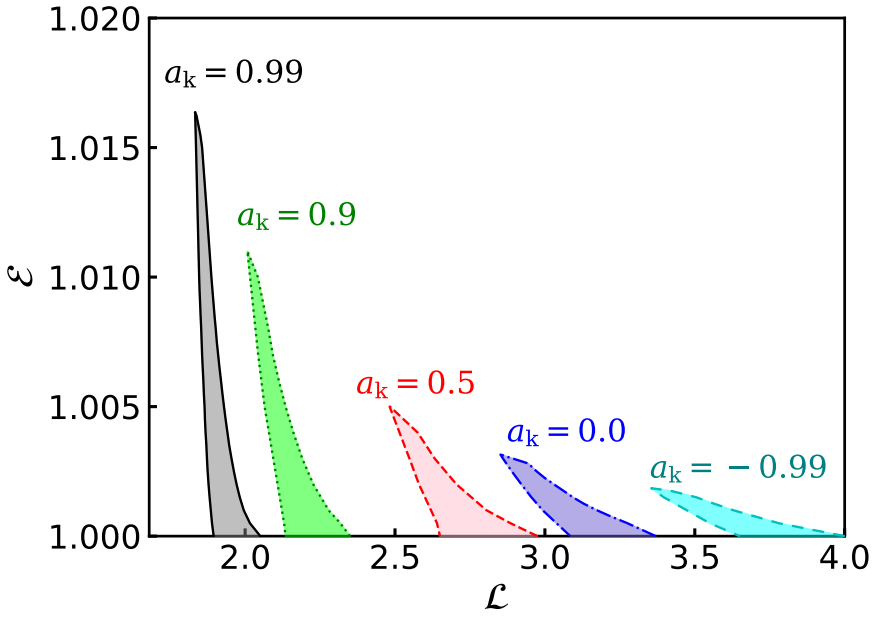

FIGURE 3.8: Modification of shock parameter space in $\mathcal{L} - \mathcal{E}$ plane with BH spin varied as $a_k = 0.99, 0.9, 0.5, 0.0$ and -0.99 (left to right). Here, we fix $\Phi_{13} = 5.0$ and $F_{15} = 5.0$. See the text for the details.

we separate the effective domain of the parameter space in $\mathcal{L} - \mathcal{E}$ plane and examine the modification of the parameter space for different Φ_{13}, where spin of the BH and F_{15} are kept fixed as $a_k = 0.99$ and 5.0. The region enclosed by solid (black), dotted (red), and dashed (blue) curves are for $\Phi_{13} = 5.0, 7.5$, and 10.0, respectively. We observe that parameter space shifts towards the lower angular momentum ($\mathcal{L}$) domain as Φ_{13} is increased. This happens because the increase of Φ_{13} effectively enhances the angular momentum transport outwards leading to the reduction of $\mathcal{L}$, which allows shock transition for higher Φ_{13}. Similarly, in Fig. 3.8, we present the modification of the parameter space for different a_k. Here, we choose $\Phi_{13} = 5.0$ and $F_{15} = 5.0$. We observe that the effective region bounded by different line style are obtained for $a_k = 0.99$, 0.9, 0.5, 0.0, and -0.99 (from left to right). We again observe that parameter space is shifted to the lower angular momentum side as the BH spin is increased (Aktar et al., 2015; Dihingia et al., 2019). This is not surprising because relatively low angular momentum flow experiences shock transition around BH of higher a_k (Das & Chakrabarti, 2008; Dihingia et al., 2019; Sen et al., 2022). Overall, we stress that both a_k and Φ_{13} play pivotal role in determining the shock parameter space of GRMHD flow.

Subsequently, we investigate the critical radial magnetic flux ($\Phi_{13}^{\rm cri}$) necessary to render

global GRMHD accretion solutions around BHs harbouring shocks. In doing so, we

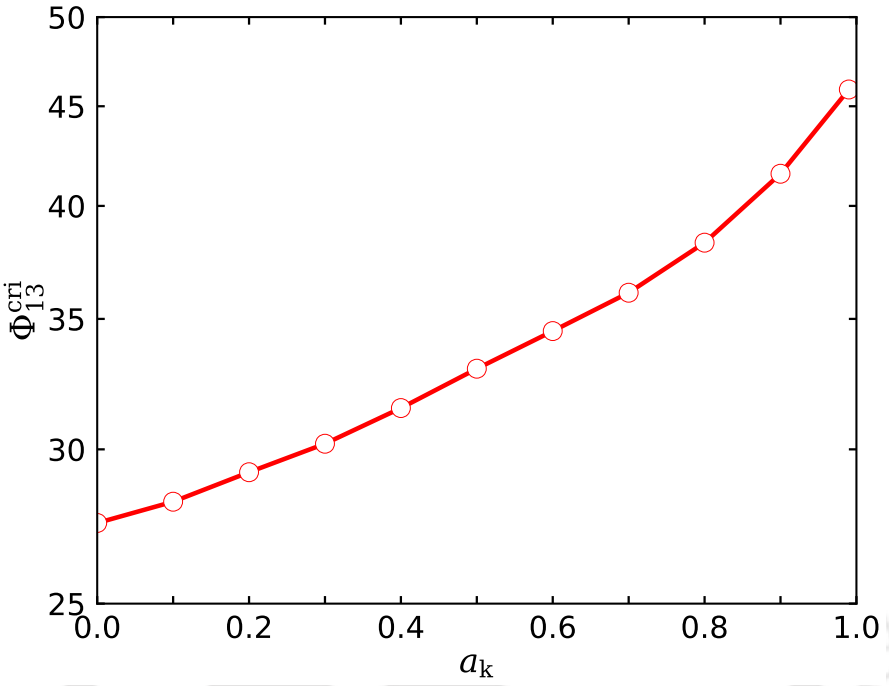

FIGURE 3.9: Variation of maximum radial magnetic flux ($\Phi_{13}^{\rm max}$ as a function of BH spin ($a_{\rm k}$) for shocked accretion solutions. Here, we choose $F_{15} = 5.0$, and $(\mathcal{E}, \mathcal{L})$ are chosen freely. See the text for details.

calculate $\Phi_{13}^{\rm cri}$ for various values of BH spin ($a_{\rm k}$), while keeping the iso-rotation parameter and accretion rate fixed at $F_{15} = 5.0$ and $\dot{m} = 0.001$, respectively, and the energy ($\mathcal{E}$) and angular momentum ($\mathcal{L}$) of flow are allowed to vary freely. The obtained results are depicted in Fig. 3.9, where open circles connected by solid lines represent the variation of $\Phi_{13}^{\rm cri}$ with $a_{\rm k}$. We observe that shock-induced GRMHD accretion solutions exist for a wide range of Φ_{13}. In particular, we find that for $a_{\rm k} = 0.0$, $\Phi_{13}^{\rm cri} = 27.5$, and $\Phi_{13}^{\rm cri}$ increases with the increase of $a_{\rm k}$, where $\Phi_{13}^{\rm cri} = 45.9$ for $a_{\rm k} = 0.99$. This finding evidently indicates that GRMHD accretion flow with stronger magnetic fields continues to sustain shocks around rapidly rotating black holes and vice versa. What is more is that by analysing the disk magnetic flux, one can speculate whether the magnetized accretion flow is consistent with the results of either Magnetically Arrested Disk (MAD, Igumenshchev et al., 2003; Narayan et al., 2003) or Standard and Normal Evolution (SANE) state (Narayan et al., 2012; Chatterjee & Narayan, 2022).

Note: MAD accretion disks have sufficiently strong magnetic fields to impact on the disk dynamics and produce stronger poloidal (or non-toroidal) magnetic fields. Whereas the weaker magnetic fields of a SANE disk are sheared out by the motion of the plasma into a toroidal configuration. Usually, SANE models are more turbulent and disordered, unlike the MAD models. Details can be found in Bisnovatyi-Kogan & Ruzmaikin, 1974; Tchekhovskoy et al., 2011; Yuan & Narayan, 2014.

To assess this, we calculate the upper limit of magnetic flux entering the ergosphere as $\int_0^{2\pi} -\sqrt{-g}\, {}^*F^{rt} d\phi = 3.23 \times 10^{18} \Phi_{13}^{\rm cri}$ G cm^2, and find that the GRMHD accretion flows under consideration remain significantly below the MAD limit $\sim 10^{21}$ G cm^2, as indicated by Sądowski (2016b), for a black hole of mass of $10 M_\odot$ and spin parameter within the range $0 \leq a_{\rm k} < 0.99$.

3.4 Chapter Conclusions

In this chapter, we study the global structure of shock-induced, magnetized, advective accretion flow around rotating BHs. In doing this, we solve the GRMHD equations that govern the flow motion in the steady state and obtain comprehensive solutions for global trans-magnetosonic accretion flow around weakly ($a_{\rm k} \to 0$) as well as rapidly ($a_{\rm k} = 0.99$) rotating BHs. We observe that depending on the model parameters, namely $\mathcal{E}$, $\mathcal{L}$, Φ_{13}, F_{15} and $a_{\rm k}$, GRMHD flow often possess multiple critical points ($r_{\rm in}$ and $r_{\rm out}$). It is noteworthy that the accretion solutions simultaneously passing through both $r_{\rm in}$ and $r_{\rm out}$ are of special importance as they may harbour shock waves and shock-induced accretion solutions are potentially promising in explaining the spectro-temporal properties of BH sources. With this, we summarize our present findings below.

- To the best of our knowledge, for the first time, we obtain the shock-induced global GRMHD accretion solutions around rotating BHs. We observe that irrespective of the BH spin ($a_{\rm k}$), shock forms further out as the radial magnetic flux (Φ_{13}) is increased for flows with fixed model parameters ($\mathcal{E}$, $\mathcal{L}$, F_{15}). We further notice

that the entropy of the shocked accretion solution always remains higher than the shock-free solution, confirming that shocked solutions are thermodynamically preferred (see Fig. 3.1).

- We observe that magnetic fields play an important role in regulating the structure of the shocked GRMHD accretion flow around BHs (see Fig. 3.2-3.3). In general, the accretion flow largely remains gas pressure dominated ($\beta > 10$) throughout the disk, except at the inner part of the disk ($r < 10r_g$). Moreover, we find that in the pre-shock regime, the toroidal field follows a self-similar radial profile as $b^\phi \propto r^{-5/4}$ (Yuan & Narayan, 2014). However, it becomes stepper in the post-shock flow (*i.e.*, $b^\phi \propto r^{-5/2}$ for $a_{\rm k} = 0$ and $b^\phi \propto r^{-7/2}$ for $a_{\rm k} = 0.99$) in order to maintain the continuity of radial flux balance across the shock front (see §3.2). The toroidal field becomes more intense around the rotating BHs due to the effect of frame-dragging, and for a $10M_\odot$ BH of spin $a_{\rm k} = 0.99$, it becomes very strong as $b^\phi \sim 10^{7-9}$ G near the horizon. On the contrary, we find $b^\phi \sim 10^{5-6}$ G in the region close to the horizon of a non-rotating ($a_{\rm k} = 0.0$) BH.

- We also examine the best-fitted power-law profiles of density (ρ) and temperature (T) in both pre- and post-shock regimes around weakly rotating ($a_{\rm k} \to 0.0$) as well as rapidly rotating ($a_{\rm k} = 0.99$) black holes. We ascertain that in the pre-shock regime, the density and temperature profiles of GRMHD flow remain unaffected due to BH spin and are obtained as $\rho \propto r^{-3/2}$ and $T \propto r^{-3/4}$, respectively. These findings are in agreement with the results of Narayan & Yi (1994); Yuan & Narayan (2014). However, due to shock compression, both ρ and T follow steeper power-law profile as $\rho \propto r^{-2}$ and $T \propto r^{-1}$ for $a_{\rm k} = 0.99$, and $\rho \propto r^{-1.75}$ and $T \propto r^{-0.8}$ for $a_{\rm k} = 0.00$ (see Fig. 3.2-3.3).

- Convergent GRMHD shocked accretion flow yields hot and dense post-shock flow (see Fig. 3.2-3.3) resembling a post-shock corona (PSC), containing hot electrons. When soft photons from the pre-shock flow interact with the PSC, they undergo inverse Comptonization, producing hard X-ray radiations commonly observed from black hole X-ray binaries (Chakrabarti & Titarchuk, 1995; Nandi et al., 2012; Iyer et al., 2015; Nandi et al., 2018). Since the PSC characteristics (*i.e.*, its size, density

and temperature) are determined by the shock properties, and magnetic fields (Φ_{13} and F_{15}) controls $r_{\rm sh}$, R and Ψ (see Figs. 3.4-3.5), it is therefore evident that magnetic fields play a crucial role in determining the spectral properties of black holes.

- Moreover, we find that the shock-induced GRMHD accretion solutions are not isolated solutions as solutions of this kind continue to exist for a wide range of model parameters, namely $\mathcal{E}$, $\mathcal{L}$, Φ_{13}, F_{15} and $a_{\rm k}$. To ascertain this, we separate the parameter space in $\mathcal{L}-\mathcal{E}$ plane for different Φ_{13} that admits GRMHD shock solutions around rapidly rotating ($a_{\rm k}=0.99$) BHs (see Fig. 3.7). Moreover, we examine the modification of the shock parameter space (in $\mathcal{L}-\mathcal{E}$ plane) for various BH spin ($a_{\rm k}$) values and observe that GRMHD accretion flows exhibit shocks within the spin range $-0.99 < a_{\rm k} < 0.99$ (see Fig. 3.8).

- We calculate the critical radial magnetic flux ($\Phi_{13}^{\rm cri}$), representing the threshold beyond which shocks cease to exist in GRMHD accretion flow around BHs. We observe a strong dependence of $\Phi_{13}^{\rm cri}$ on the spin of the black hole ($a_{\rm k}$), with $\Phi_{13}^{\rm cri}$ being higher for $a_{\rm k}=0.99$ compared to $a_{\rm k}=0.0$ (see Fig. 3.9). We also observe that shock-induced GRMHD accretion flow under consideration remains restricted below the MAD threshold.

It is worth mentioning that the low angular momentum, advective accretion flow remains gravitationally unbound as the flow energy exceeds the rest mass energy ($\mathcal{E}>1$). Thus, a hot, advective disk usually plays an important role in launching thermal outflows. Several numerical studies in hot accretion flows reported that in the presence of thermal conduction, the efficiency of launching outflows is enhanced (Khajenabi & Shadmehri, 2013; Bu et al., 2011, 2016). With this, in Chapter 4, we investigate the low angular momentum transonic accretion flows in the presence of thermal conduction.

Chapter 4

Global Transonic Solution of Hot Accretion Flow with Thermal Conduction

The content of this chapter has been published in Mitra S., Ghoreyshi S. M., Mosallanezhad A., Abbassi S., Das S., 2022, MNRAS, 523, 2023, 4431.

Hot accretion flow (HAF) models are useful in explaining the observational features of supermassive BHs, Sgr A* (Manmoto et al., 1997; Yuan et al., 2002; Yuan & Narayan, 2014; Dexter et al., 2020; Ressler et al., 2020a; Event Horizon Telescope Collaboration et al., 2022; Satapathy et al., 2023; Lin & Yuan, 2024; Zhao et al., 2024), M87 (Reynolds et al., 1996; Event Horizon Telescope Collaboration et al., 2019a; Park et al., 2019; Xie et al., 2023), the low-luminosity AGNs (Lasota et al., 1996; Nemmen et al., 2006, 2014; Younes et al., 2019; Szanecki et al., 2023), and BH-XRBs (Esin et al., 1997; Hameury et al., 1997; Yuan & Cui, 2005; Liu et al., 2011; Dexter et al., 2021; Niedźwiecki et al., 2022; You et al., 2023, 2024; Jiang et al., 2024) in hard/quiescence states. For systems with very low mass accretion rate, hot accreting plasmas surrounding the BH happens to be collisionless. This eventually results in a significant influence of thermal conduction on the disk dynamics, which helps in energy transport from the inner to outer regions (Tanaka & Menou, 2006; Johnson & Quataert, 2007; Quataert, 2008). Keeping this in mind, in this Chapter, we examine the effect of thermal conduction on the low angular

momentum hot accretion flow (HAF) around non-rotating black holes accreting mass at a very low rate. While doing so, we adopt the conductive heat flux in the saturated form (Cowie & McKee, 1977) and solve the set of dynamical equations corresponding to a steady, axisymmetric, viscous, advective accretion flow around a non-rotating BH using numerical methods. In order to describe the space-time around a non-rotating BH, we choose the pseudo-Newtonian potential (Paczyński & Wiita, 1980), and for simplicity, we ignore magnetic fields. We study the dynamical and thermodynamical properties of accreting matter in terms of the input parameters, namely energy (ε_0) and angular momentum at the horizon (λ_0), viscosity parameter (α), and saturation constant ($\Phi_{\rm s}$) regulating the effect of thermal conduction. We find that $\Phi_{\rm s}$ plays a pivotal role in deciding the transonic properties of the global accretion solutions. In general, when $\Phi_{\rm s}$ is increased, the critical point ($r_{\rm c}$) is receded away from the black hole, and flow variables are altered, particularly at the outer part of the disk. To quantify the physically acceptable range of $\Phi_{\rm s}$, we compare the global transonic solutions with the self-similar solutions and observe that the maximum saturation constant ($\Phi_{\rm s}^{\rm max}$) estimated from the global solutions exceeds the saturated thermal conduction limit ($\Phi_{\rm sc}$) derived from the self-similar formalism (Narayan & Yi, 1995a). Moreover, we calculate the correlation between α and $\Phi_{\rm s}^{\rm max}$ and find ample disagreement between global transonic solutions and self-similar solutions. Further, using the input parameters, we compute the Bernoulli parameter (Be), which remains positive all throughout the disk, although flow becomes loosely unbound for higher $\Phi_{\rm s}$. Finally, we indicate the relevance of this work in the astrophysical context in explaining the possibility of mass loss from the unbound disk.

4.1 Governing equations

We begin with a low angular momentum, steady, axisymmetric, viscous, advective hot accretion flow around a non-rotating black hole. In order to deal with the HAF, we employ the same set of height integrated governing equations as delineated in Narayan et al. (1997) except the energy equation, where we include the effect of thermal conduction. In addition, we consider the hydrostatic equilibrium in the vertical direction, and hence, the flow variables are vertically averaged. Accordingly, in this formulation, the flow variables

are expressed as functions of radius r only. Under these assumptions, the governing equations are given by,

$$\dot{M} = -4\pi r H \rho v, \tag{4.1}$$

$$v\frac{dv}{dr} = (\Omega^2 - \Omega_{\rm K}^2)r - \frac{1}{\rho}\frac{d(\rho C_{\rm s}^2)}{dr}, \tag{4.2}$$

$$\rho r H v \frac{d(\Omega r^2)}{dr} = \frac{d}{dr}\left(\nu \rho H r^3 \frac{d\Omega}{dr}\right), \tag{4.3}$$

$$\frac{\rho v}{(\Gamma - 1)}\frac{dC_{\rm s}^2}{dr} - C_{\rm s}^2 v \frac{d\rho}{dr} = f\nu\rho r^2\left(\frac{d\Omega}{dr}\right)^2 - \frac{1}{r}\frac{d(rF_{\rm s})}{dr}. \tag{4.4}$$

In the above equations, ρ and Ω are the mass density and the angular velocity of the gas, respectively. The radial velocity of the flow v is assumed to be negative for an inward flow of gas. Here, $H \equiv C_{\rm s}/\Omega_{\rm K}$ is the vertical half-thickness of the flow, where $C_{\rm s}$ is the isothermal sound speed and $\Omega_{\rm K}$ is the Keplerian angular velocity. Adopting pseudo-Newtonian potential $\Phi_{\rm PW} = -GM_{\rm BH}/(r - r_{\rm s})$ (Paczyński & Wiita, 1980), the Keplerian angular velocity is given by,

$$\Omega_{\rm K}^2 = \frac{GM_{\rm BH}}{r(r - r_{\rm s})^2}, \tag{4.5}$$

where $r_{\rm s}\,(= 2GM_{\rm BH}/c^2)$ is the Schwarzschild radius for a BH with mass $M_{\rm BH}$. In obtaining the accretion solutions, we employ a unit system as $G = M_{\rm BH} = c = 1$. This allows us to simplify our calculations and obtain results that are seamlessly compared with previous studies. The last term on the right hand side of equation (4.2) is the acceleration due to the pressure gradient. Here, the pressure is defined by the isothermal sound speed $C_{\rm s}$ and the density ρ as $p_{\rm gas} = \rho C_{\rm s}^2$. The Shakura-Sunyaev prescription (Shakura & Sunyaev, 1973) is adopted for the kinematic coefficient of viscosity (ν) as,

$$\nu = \alpha C_{\rm s} H, \tag{4.6}$$

where α is the viscosity parameter. We assume that the viscosity parameter is a constant, and independent of r. By substituting equation (4.6) into equation (4.3), and using equation (4.1), we have,

$$\frac{d}{dr}\left(\rho H v r^3 \Omega\right) = \frac{d}{dr}\left(\frac{\alpha C_{\rm s}^2 \rho H r^3}{\Omega_{\rm K}}\frac{d\Omega}{dr}\right), \tag{4.7}$$

which on integration gives

$$\frac{d\Omega}{dr} = \frac{v\Omega_{\rm K}(\lambda - \lambda_0)}{\alpha r^2 C_{\rm s}^2}, \tag{4.8}$$

where $\lambda\,(=\Omega r^2)$ is the angular momentum per unit mass (hereafter specific angular momentum) for the accreting gas at radius r. The integration constant λ_0 represents the specific angular momentum eventually swallowed by the black hole. In the energy equation (4.4), Γ is the ratio of specific heat of the gas. The advection parameter $f\ (=1-Q_{\rm rad}/Q_{\rm vis})$ is assumed to be a constant which lies in the range $0 \leq f \leq 1$. Here, $Q_{\rm vis}$ and $Q_{\rm rad}$ denote viscous heating and radiative cooling rates. Since the collisional mean free paths of the charged particles in HAFs are much larger than the typical lengthscale of the accretion flows, one may no longer apply the classical theory for thermal conduction. Under these conditions, the heat flux is described as the saturated form of conduction. The last term on the right hand side of the equation (4.4) represents the transfer of energy due to the saturated thermal conduction. Following Cowie & McKee (1977), the saturated conduction flux $F_{\rm s}$ is obtained as,

$$F_{\rm s} = 5\Phi_{\rm s}\rho C_{\rm s}^3, \tag{4.9}$$

where $\Phi_{\rm s}$ is the dimensionless saturation constant with $0 \leq \Phi_{\rm s} < 1$. For the detailed derivation of the saturated flux, see Appendix C.

4.1.1 Critical point analysis and boundary conditions

Using equations (4.1), (4.4), (4.8), and (4.9), we get the radial gradient of the sound speed as,

$$\left(\frac{\Gamma+1}{\Gamma-1}+10\,\Phi_{\rm s}\frac{C_{\rm s}}{v}\right)\frac{d\ln C_{\rm s}}{dr}=-\left(1-5\Phi_{\rm s}\frac{C_{\rm s}}{v}\right)\frac{d\ln|v|}{dr}+\left(1-5\Phi_{\rm s}\frac{C_{\rm s}}{v}\right)\frac{d\ln\Omega_{\rm K}}{dr}-\frac{1}{r}+\frac{fv\Omega_K}{\alpha r^2C_{\rm s}^4}(\lambda-\lambda_0)^2. \quad (4.10)$$

We next use equations (4.1) and (4.10) to eliminate $d\rho/dr$ and $dC_{\rm s}/dr$ in equation (4.2) and thereby express the wind equation as,

$$\left[\frac{2\Gamma+5\,\Phi_{\rm s}(\Gamma-1)C_{\rm s}/v}{(\Gamma+1)+10\,\Phi_{\rm s}(\Gamma-1)C_{\rm s}/v}-\frac{v^2}{C_{\rm s}^2}\right]\frac{d\ln|v|}{dr}=\frac{r\left(\Omega_{\rm K}^2-\Omega^2\right)}{C_{\rm s}^2}-\left[\frac{2\Gamma+10\,\Phi_{\rm s}(\Gamma-1)C_{\rm s}/v}{(\Gamma+1)+10\,\Phi_{\rm s}(\Gamma-1)C_{\rm s}/v}\right]\frac{1}{r}+\left[\frac{2\Gamma+5\,\Phi_{\rm s}(\Gamma-1)C_{\rm s}/v}{(\Gamma+1)+10\,\Phi_{\rm s}(\Gamma-1)C_{\rm s}/v}\right]\frac{d\ln\Omega_{\rm K}}{dr}+\frac{f\Omega_{\rm K}v}{\alpha r^2C_{\rm s}^4}\times\left[\frac{\Gamma-1}{(\Gamma+1)+10\,\Phi_{\rm s}(\Gamma-1)C_{\rm s}/v}\right](\lambda-\lambda_0)^2\,. \quad (4.11)$$

We numerically solve the differential equations (4.8), (4.10), and (4.11) to obtain the radial profile of v, $C_{\rm s}$ and λ. In doing so, one is required to supply the boundary conditions. We begin with the critical point conditions $\mathcal{N}_{\rm c}=\mathcal{D}_{\rm c}=0$ following section 2.2.1, which are explicitly yielded as,

$$\mathcal{D}_{\rm c}\equiv\frac{2\Gamma+5\,\Phi_{\rm s}(\Gamma-1)C_{\rm sc}/v_{\rm c}}{(\Gamma+1)+10\,\Phi_{\rm s}(\Gamma-1)C_{\rm sc}/v_{\rm c}}-\frac{v_{\rm c}^2}{C_{\rm sc}^2}=0, \quad (4.12)$$

$$\mathcal{N}_{\rm c}\equiv\frac{r_{\rm c}\left(\Omega_{\rm K}^2-\Omega_{\rm c}^2\right)}{C_{\rm sc}^2}-\left[\frac{2\Gamma+10\,\Phi_{\rm s}(\Gamma-1)C_{\rm sc}/v_{\rm c}}{(\Gamma+1)+10\,\Phi_{\rm s}(\Gamma-1)C_{\rm sc}/v_{\rm c}}\right]\frac{1}{r_{\rm c}}+\left[\frac{2\Gamma+5\,\Phi_{\rm s}(\Gamma-1)C_{\rm sc}/v_{\rm c}}{(\Gamma+1)+10\,\Phi_{\rm s}(\Gamma-1)C_{\rm sc}/v_{\rm c}}\right]\frac{d\ln\Omega_{\rm K}}{dr}+\frac{f\Omega_{\rm K}v_{\rm c}}{\alpha r_{\rm c}^2C_{\rm sc}^4}\times\left[\frac{\Gamma-1}{(\Gamma+1)+10\,\Phi_{\rm s}(\Gamma-1)C_{\rm sc}/v_{\rm c}}\right](\lambda_{\rm c}-\lambda_0)^2=0. \quad (4.13)$$

where $v_{\rm c}$, $\Omega_{\rm c}$, $C_{\rm sc}$, and $\lambda_{\rm c}$ denote the radial velocity, angular velocity, sound speed and angular momentum at the critical point ($r_{\rm c}$), respectively. Since the flow remains smooth

along the streamline, dv/dr must be real and finite all throughout. Hence, we calculate $dv/dr|_{\rm c}$ by applying the l'Hôpital's rule, leading to

$$\left(\frac{dv}{dr}\right)_{\rm c} = \left(\frac{d\mathcal{N}/dr}{d\mathcal{D}/dr}\right)_{r=r_{\rm c}}. \tag{4.14}$$

In addition to this, we use another boundary condition, which implies the vanishing of the viscous shear stress at the horizon (Becker & Le, 2003; Das et al., 2009). Hence, considering $d\Omega/dr = 0$, we obtain,

$$\lim_{r\to r_{\rm s}} \Omega(r) \equiv \Omega_0 = \frac{\lambda_0}{r_{\rm s}^2}. \tag{4.15}$$

4.1.2 Globally conserved energy equation

In order to obtain the energy transport rate per unit mass of a viscous advective flow in the presence of thermal conduction, we rewrite equation (4.4) as

$$E = \frac{v^2}{2} - \frac{\lambda^2}{2r^2} + \Phi_{\rm PW} + h + \frac{\lambda\lambda_0}{r^2} + \frac{5\Phi_{\rm s}C_{\rm s}^3}{v} - \int\left(\frac{5\Phi_{\rm s}C_{\rm s}^3}{vH}\frac{dH}{dr}\right)dr, \tag{4.16}$$

where h $[= \Gamma p/\rho(\Gamma-1)]$ is the specific enthalpy. We note that the saturated conduction flux decreases in regions of the accreting flow where the electrons become relativistic (Tanaka & Menou, 2006). Therefore, the effect of thermal conduction can be negligible in the innermost regions ($r_{\rm inner}$) of the disk, where $r_{\rm inner} = r_{\rm s} + 0.001$. Accordingly, we set $\Phi_{\rm s} \sim 0$ at $r_{\rm inner}$, and redefine the energy transport rate per unit mass (ε_0) at $r_{\rm inner}$ as,

$$\varepsilon_0 = \frac{v^2}{2} - \frac{\lambda^2}{2r^2} + \Phi_{\rm PW} + h + \frac{\lambda\lambda_0}{r^2}. \tag{4.17}$$

It is worth mentioning that ε_0 is conserved for a viscous, advective accretion flow. Moreover, we express the Bernoulli parameter (Be) (Nakamura et al., 1997) that contains the local information of radial motion, azimuthal motion, gravity, and thermodynamic terms and is given by,

$$Be = \frac{v^2}{2} + \frac{\lambda^2}{2r^2} + \Phi_{\rm PW} + h. \tag{4.18}$$

Needless to mention that in the absence of any viscosity, $\lambda = \lambda_0$, and hence, we have $\varepsilon_0 = Be$.

4.2 Solution Methodology

We obtain the global transonic solutions using an iteration method as described in Becker & Le (2003); Das et al. (2009); Kumar & Gu (2018). In this method, we begin the numerical integration of the flow equations from a location just outside the black hole horizon at $r_{\rm inner}$. For a given set of input parameters $(\varepsilon_0, \lambda_0, \alpha, \Phi_{\rm s})$, we compute three flow variables, namely velocity $v_{\rm in}$, sound speed $C_{\rm s_{in}}$, and angular momentum $\lambda_{\rm in}$ at $r_{\rm inner}$. Needless to mention that the flow angular momentum at the horizon has to be in the range $0 \leq \lambda_0 < \lambda_{\rm ms}$, where $\lambda_{\rm ms}\,(= 2\sqrt{3})$ is the innermost stable angular momentum around a Schwarzschild BH. Considering this, we pursue the following chronology for obtaining the global solutions.

- Close to horizon i.e., $r - r_{\rm s} \to 0$, the matter falls with free fall velocity $v_{\rm ff} = -\sqrt{2/(r - r_{\rm s})}$. Here, we consider a fractional constant $\delta < 1$, such that $v_{\rm in} = \delta \times v_{\rm ff}$, and accreting matter enters into the BH with this velocity $v_{\rm in}$.

- Next, we determine the asymptotic flow variables just outside the horizon at $r_{\rm inner}$. Using Frobenius expansion, we get the asymptotic behaviour of flow angular momentum as,

$$\lambda_{\rm in} = \lambda_0 + A(r - r_{\rm s})^p; \qquad r \to r_{\rm s}, \tag{4.19}$$

  where A and p are positive constants. We implement $\lambda_{\rm in}$ in equation (4.8) and we demand that,

$$\lim_{r \to r_{\rm s}} \frac{d\lambda_{\rm in}}{dr} = 0, \qquad \lim_{r \to r_{\rm s}} \frac{\delta\sqrt{2}A(r - r_{\rm s})^p}{\sqrt{r_{\rm s}}(r - r_{\rm s})^{\frac{3}{2}}\alpha C_{\rm s}^2} = \frac{2\lambda_0}{r_{\rm s}}. \tag{4.20}$$

  To eliminate all terms involving $(r - r_{\rm s})$ in equation (4.20), we require $p = 3/2$ and $A = \sqrt{2/r_{\rm s}}(\alpha C_{\rm s}^2 \lambda_0/\delta)$. Accordingly, we get the expression of angular momentum at $r_{\rm inner}$ for a suitable choice of $(\delta, \lambda_0, \alpha, \Phi_{\rm s})$.

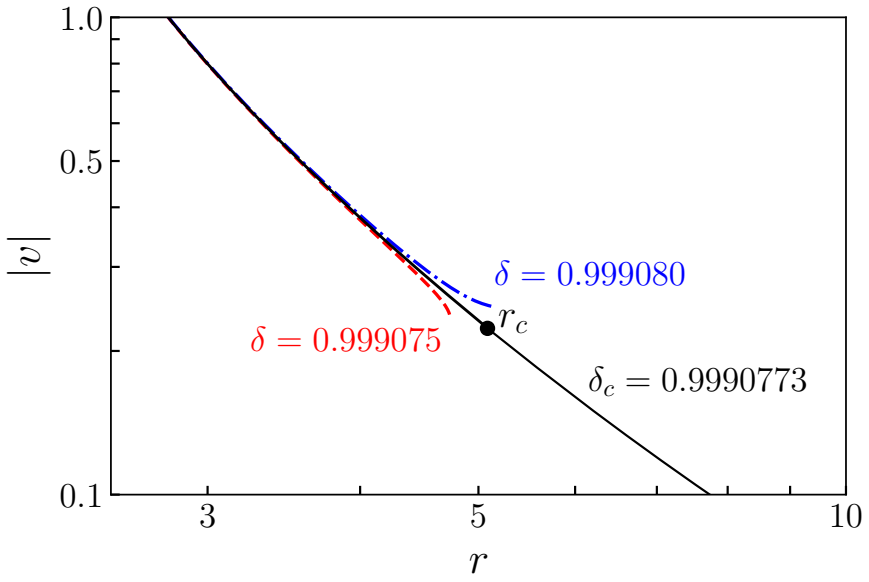

FIGURE 4.1: Variation of flow velocity $|v|$ as a function of radial coordinate r for three different iteration parameters. Dashed (red), solid (black) and dot-dashed (blue) curves denote results for $\delta = 0.999075, 0.9990773$, and 0.999080. Here, $\delta = \delta_c = 0.9990773$ corresponds to transonic solution where critical point is obtained at $r_c = 5.0286$ for the chosen input parameters $(\varepsilon_0, \lambda_0, \alpha, \Phi_s, \gamma) = (0.005, 3.05, 0.04, 0.0015, 1.5)$.

- We use $v_{\rm in}$ and $\lambda_{\rm in}$ in equation (4.16), where we consider that the effect of conduction is negligible (Tanaka & Menou, 2006), and determine the sound speed $C_{s_{\rm in}}$ by solving equation (4.17) for a given energy ε_0.

- Using $v_{\rm in}$, $C_{\rm s_{in}}$, and $\lambda_{\rm in}$, we integrate equations (4.8, 4.10, 4.11) from $r_{\rm inner}$ outwards, and check the critical point conditions described in equations (4.12) and (4.13). We keep tuning the iteration parameter δ until the critical point conditions are satisfied for $\delta = \delta_{\rm c}$, and thereafter, we obtain the critical point $r_{\rm c}$ (see Fig. 4.1).

- At $r_{\rm c}$, we calculate $dv/dr|_{\rm c}$ by applying the l'Hôpital's rule. Since the transonic accretion solutions are able to pass through the saddle type critical points, we focus only on these points. Moreover, the real and negative radial velocity gradient corresponds to accretion solution, and hence, for $dv/dr|_c < 0$, we further integrate equations (4.8, 4.10, 4.11) starting from $r_{\rm c}$ upto to the outer edge of the disk $r_{\rm edge} = 1000$. Finally, we join both parts of the solutions (from $r_{\rm inner}$ to $r_{\rm c}$ and $r_{\rm c}$ to $r_{\rm edge}$) to obtain the global transonic accretion solution for a HAF around non-rotating BH.

Applying the aforementioned conditions and adopting the methodology outlined in section 4.2, we obtain comprehensive global transonic accretion solutions around black holes in the presence of thermal conduction. With careful adherence to this approach, we can model the behavior and characteristics of the hot accretion flow, which provides precious insights into the underlying physical processes under consideration.

4.3 Results

The structure of HAFs is influenced by a variety of factors, including the energy transport rate ε_0 at $r_{\rm inner}$, angular momentum transport rate λ_0 at the horizon, the viscosity parameter α, the saturation constant $\Phi_{\rm s}$, and the ratio of specific heats Γ. In this study, we choose $\Gamma = 1.5$ unless stated otherwise and set $f = 1$ for the purpose of representation. To find the critical point location, we utilize the iteration methodology discussed in Sec. 4.2. We then solve the coupled differential equations (4.8), (4.10), and (4.11) simultaneously for a given set of input parameters $(\varepsilon_0, \lambda_0, \alpha, \Phi_{\rm s})$ to obtain the global solution for HAFs in the presence of thermal conduction.

4.3.1 Global transonic solutions

We choose a set of input parameters, $(\varepsilon_0, \lambda_0, \alpha) = (0.001, 2.75, 0.05)$, and integrate the flow equations (4.8, 4.10, 4.11) towards the outer edge ($r_{\rm edge}$) of the disk starting from $r_{\rm inner} = 2.001$ considering $\Phi_{\rm s} = 0$. The obtained results are depicted in Fig. 4.2, where the solid (black) curve smoothly connects the horizon with $r_{\rm edge} = 1000$ via a critical point at $r_{\rm c} = 6.233$. Next, we increase the saturation constant to $\Phi_{\rm s} = 0.00025$, and notice that the obtained global solution (dashed curve in red) deviates from the accretion solution with $\Phi_{\rm s} = 0$. It is interesting to note that the global accretion solutions obtained for different $\Phi_{\rm s}$ remain quite insensitive, particularly in the inner regions of the disk. However, the effect of thermal conduction on the accretion solutions is prominently visible in the region far from the black hole horizon. We keep increasing the saturation constant upto a critical value $\Phi_{\rm s} = 0.000425$ (dot-dashed curve in green), beyond that the flow fails to connect the outer edge as the solution becomes closed (Sarkar & Das,

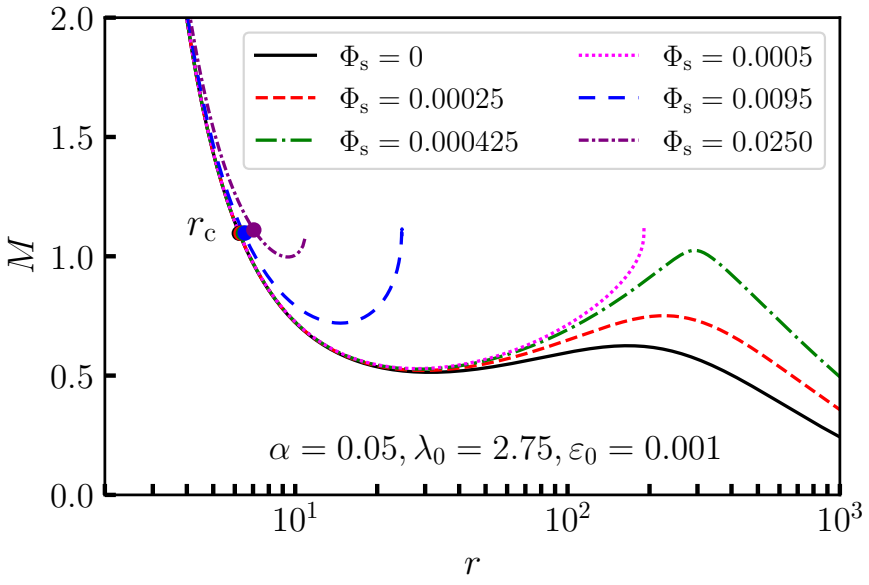

FIGURE 4.2: Variation of Mach number ($M = |v|/C_s$) as a function of radial coordinate (r) for different Φ_s values starting from 0 to 0.0250 which are marked. Here, the input parameters are chosen as $(\varepsilon_0, \lambda_0, \alpha) = (0.001, 2.75, 0.05)$. The filled circles represent the critical points. See the text for the details.

2018), shown using a dotted (magenta) curve. If we keep increasing Φ_s, we continue to obtain closed solutions depicted in long-dashed (blue) and dot-dashed (purple) curves. Note that these solutions are apparently of less importance as they fail to connect $r_{\rm inner}$ to the outer edge of the disk. Depending on the flow parameters, these solutions are often joined via shock with supersonic solutions passing through an outer critical point, which is usually located far away from the horizon (Fukue, 1987; Chakrabarti, 1989, 1996; Das et al., 2001b; Chakrabarti & Das, 2004; Das, 2007; Das et al., 2009, 2022, and references therein). Finally, we find an upper limit of the saturation constant, $\Phi_s = 0.025$, above which accretion solutions cease to exist. We observe that the critical point shifts outwards with the increase of the saturation constant (see § 4.3.2). This finding contradicts the previously reported results (Faghei, 2012) and hence, we intend to analyse this in detail in the subsection § 4.3.2.

4.3.2 Dependency of critical point on input parameters

In Fig. 4.3, we find a unique correspondence between the critical point location and the saturation constant (Φ_s) for different combinations of $(\varepsilon_0, \lambda_0, \alpha)$. In Fig. 4.3a, we choose $(\varepsilon_0, \lambda_0, \alpha) = (0.001, 2.75, 0.05)$, and start with $\Phi_s = 0$. For this configuration, we

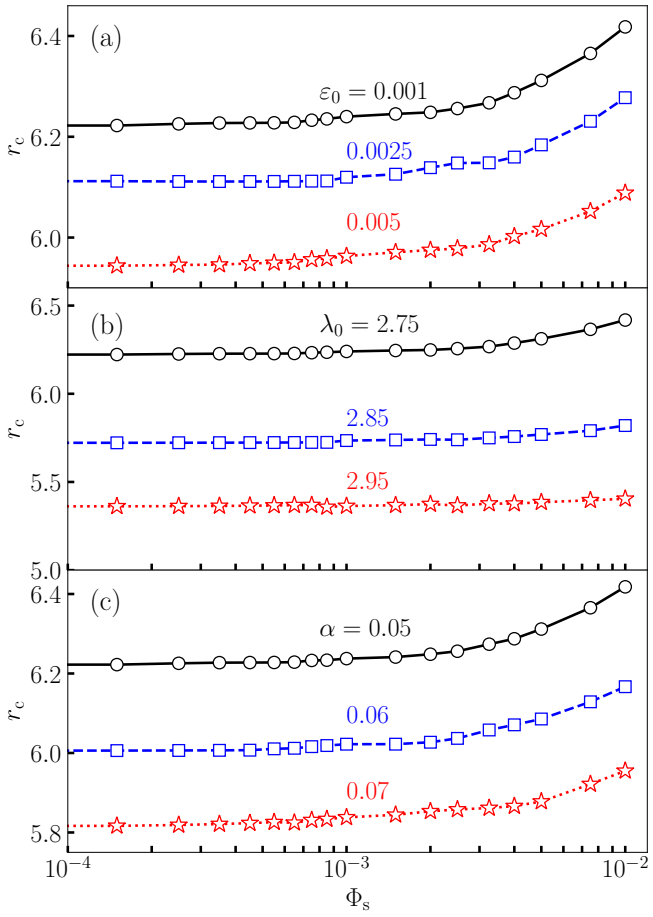

FIGURE 4.3: Variation of the critical point location (r_c) as a function of Φ_s. In panel (a), we fix $(\alpha, \lambda_0) = (0.05, 2.75)$, and show r_c for $\varepsilon_0 = 0.001, 0.0025$, and 0.005. In panel (b), we choose $(\varepsilon_0, \alpha) = (0.001, 0.05)$, and obtain results for different angular momentum at the horizon as $\lambda_0 = 2.75, 2.85$, and 2.95. In panel (c), we set $(\varepsilon_0, \lambda_0) = (0.001, 2.75)$, and vary the viscosity parameter as $\alpha = 0.05, 0.06$, 0.07. In each panel, open circles, squares and asterisks represent the location of critical points r_c. See the text for the details.

obtain the critical point at $r_c = 6.233$, and as Φ_s is increased, the critical point shifts outwards. In reality, as Φ_s is increased, flow temperature at a given radial coordinate is decreased (see Fig. 4.4b), and hence, C_s is also decreased there. Further, since Mach number M_{r_c} $[= (v/C_s)_{r_c}]$ at r_c remains largely insensitive to Φ_s, r_c shifts outward with the increase of Φ_s to restore M_{r_c}. Next, we keep λ_0 and α fixed and increase energy as $\varepsilon_0 = 0.0025$ and 0.005 that causes the critical point location to settle at a smaller radius. Indeed, as energy is increased, the temperature of the disk also increases, which causes the critical points to move inwards to maintain the higher temperature. In Fig. 4.3b, we fix $(\varepsilon_0, \alpha) = (0.001, 0.05)$ and vary angular momentum as $\lambda_0 = 2.75, 2.85$, and 2.95, respectively. Finally, in Fig. 4.3c, we vary the viscosity parameter as $\alpha = 0.05, 0.06$, and 0.07, keeping other parameters fixed as $(\varepsilon_0, \lambda_0) = (0.001, 2.75)$. When λ_0 or α is

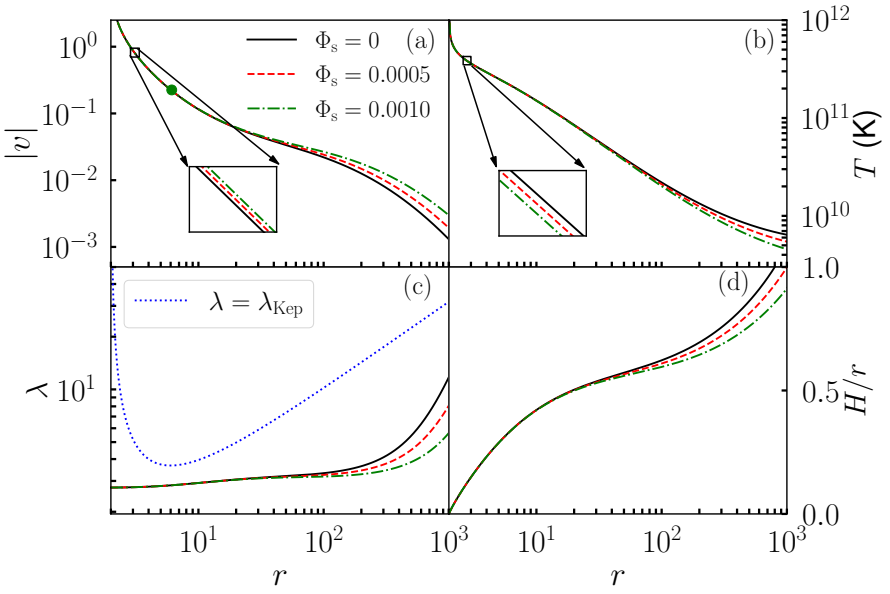

FIGURE 4.4: The profiles of velocity v, temperature T, angular momentum λ, and aspect ratio H/r are plotted as a function of radial distance r for different values of $\Phi_s = 0$ (solid), 0.0005 (dashed), and 0.0010 (dot-dashed), respectively. Here, the input parameters are chosen as $(\varepsilon_0, \lambda_0, \alpha) = (0.0025, 2.75, 0.05)$. See the text for the details.

increased, the viscous dissipation increases within the flow, eventually yielding enhanced viscous heating. Hence, the critical points move inwards with the increase of λ_0 or α, although we observe an opposite behaviour with the variation of Φ_s. However, the overall variation of the critical point location (r_c) for $(\varepsilon_0, \lambda_0)$, and α appears to remain similar as was reported earlier (Chakrabarti & Das, 2004; Das et al., 2009, 2022).

4.3.3 Effect of thermal conduction on the flow variables

In Fig. 4.4, we depict the behaviour of flow variables corresponding to global transonic solution in the presence of thermal conduction. Here, we set the input parameters as $(\varepsilon_0, \lambda_0, \alpha) = (0.0025, 2.75, 0.05)$. The solutions are illustrated for different values of the saturation constant as $\Phi_s = 0.0, 0.0005$, and 0.0010, which are plotted using solid (black), dashed (red), and dot-dashed (green) curves, respectively. In panel (a), the subsonic accretion flow from $r_{edge} = 1000$ starts accreting with negligible velocity and gradually gains radial velocity as it proceeds towards the black hole. At r_c, flow becomes supersonic and ultimately crosses the horizon supersonically. Note that flow velocity exceeds the speed of light just outside the horizon. This happens due to the limitation of the pseudo-Newtonian potential which deviates to mimic the space-time geometry of the black hole

there. For $\Phi_s = 0.0, 0.0005$, and 0.0010, the critical points are obtained at $r_c = 6.0924$, 6.1113, and 6.1219, respectively. We find that radial velocity is increased marginally with Φ_s at the inner part of the disk as shown at the inset, however, noticeable deviation is observed towards the outer part of the disk. In a convergent flow, the temperature (T) is increased with the decrease of r mainly due to the geometrical compression. However, the presence of thermal conduction generally leads to the reduction of temperature, because the heat generated by the viscous dissipation is transferred away due to the thermal conduction. As expected, the reduction of temperature at the outer edge of the disk is observed (see panel (b) of Fig. 4.4), which is in agreement with the results of the numerical simulation (Wu et al., 2010). In panel (c), we display the variation of the angular momentum λ with r corresponding to the solutions presented in panel (a). We find that the angular momentum transport is very inefficient particularly at the inner part of the disk, although the increase of λ is seen at higher radial coordinates. Meanwhile, Faghei (2012) argued that for enhanced Φ_s, viscous turbulence is reduced that weakens the efficiency of angular momentum transport inside the disk. We further compare the flow angular momentum profile with the Keplerian angular momentum ($\lambda_{\rm Kep}$) distribution (dotted curve in blue) and observe that λ of HAFs remains sub-Keplerian all throughout. In panel (d), we demonstrate the relative thickness of the disk H/r at all radii. From the figure, it is clear that $H/r \ll 1$ is generally maintained at the inner region, however, flow is intended to become quasi-spherical $H/r \sim 1$ towards the outer regions. Moreover, we find that the disk thickness is reduced at the outer regions as the influence of thermal conduction is increased. This is naturally expected, as the increased Φ_s generally reduces the disk temperature (T) at the outer part of the disk that eventually resulted the reduction of the disk height.

4.3.4 Self-similar solutions

In this Chapter, one of our main objectives is to conduct a comparative analysis of HAFs by means of the self-similar solutions (Narayan & Yi, 1994) with the global transonic HAFs. These analyses provide valuable insights into the similarities and differences between the two kinds of solutions. Indeed, the self-similar solutions satisfactorily describe the structure of an accretion flow far from boundaries (both inner and outer),

and hence, such solutions are obtained for $r \gg r_{\rm s}$, which allows us to replace the pseudo-Newtonian potential by the Newtonian one. Following Narayan & Yi (1994), we choose the self-similar treatment in the following forms:

$$v(r) = -\alpha C_1 v_{\rm K}, \tag{4.21}$$

$$\Omega(r) = C_2 \Omega_{\rm K}, \tag{4.22}$$

$$C_{\rm s}^2(r) = C_3 v_{\rm K}^2, \tag{4.23}$$

where $v_{\rm K}$ $(= \sqrt{GM_{\rm BH}/r})$ is the Keplerian velocity, and C_1, C_2 and C_3 are constants. By substituting the self-similar solutions (equations (4.21), (4.22), (4.23)) into the equations (4.2)-(4.4), we obtain a closed set of dimensionless equations that allow us to determine the constants C_1, C_2, and C_3. The closed set of dimensionless equations are given by,

$$-\frac{1}{2}\alpha^2 {C_1}^2 = {C_2}^2 - 1 + \frac{5}{2}C_3, \tag{4.24}$$

$$C_1 = \frac{3}{2}C_3, \tag{4.25}$$

$$\Big[\frac{1}{\Gamma - 1} - \frac{3}{2}\Big] C_1 = \frac{9}{4} f {C_2}^2 + 10\frac{\Phi_{\rm s}}{\alpha}\sqrt{C_3}. \tag{4.26}$$

After some algebraic manipulations, an equation for C_1 is obtained as

$$\frac{9f\alpha^2}{8}{C_1}^2 + \Big[\frac{1}{\Gamma - 1} - \frac{3}{2} + \frac{15f}{4}\Big] C_1 - \frac{10\sqrt{6}\Phi_{\rm s}}{3\alpha}\sqrt{C_1} - \frac{9f}{4} = 0. \tag{4.27}$$

As reported in Tanaka & Menou (2006), that the solution of equation (4.27) yields the significant changes in the radial and rotational velocity profiles when thermal conduction is active inside the flow. In particular, they pointed out that in the presence of thermal conduction, the accreting flow rotates with lower rate, while its inward motion becomes faster. Meanwhile, in the self-similar solutions, when $\Phi_{\rm s}$ reaches a specific saturation constant $\Phi_{\rm sc}$, the accreting flow reaches a non-rotating limit[1] (Shadmehri, 2008; Ghasemnezhad et al., 2012; Faghei, 2012; Ghoreyshi & Shadmehri, 2020). Accordingly, we calculate $\Phi_{\rm sc}$ using equations (4.24)-(4.26) subject to the condition $C_2 = 0$. With this,

[1]Accordingly, the physically acceptable accretion solutions around a black hole are given by the remaining allowed range of the saturation constant, $0 \leq \Phi_{\rm s} \leq \Phi_{\rm sc}$.

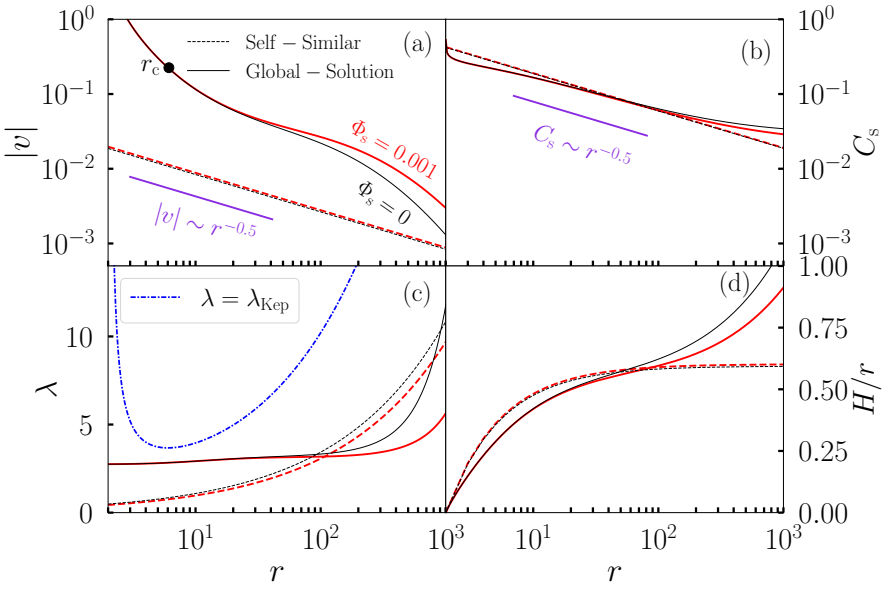

FIGURE 4.5: Comparison of global (solid curves) and self-similar (dashed curves) solutions in presence and absence of thermal conduction. In panels (a), (b), (c) and (d), radial velocity ($|v|$), sound speed ($C_{\rm s}$), angular momentum (λ) and local disk thickness (H/r) are plotted. Here, we choose the input parameters for global solutions as $(\varepsilon_0, \lambda_0, \alpha) = (0.0025, 2.75, 0.05)$ (same as in Fig. 4.4). The thin and thick curves represent results for $\Phi_{\rm s} = 0$ and $\Phi_{\rm s} = 0.001$, respectively. For self-similar solution, we choose $f = 1$ and $\Gamma = 1.5$. See the text for the details.

we have

$$\Phi_{\rm sc} = \sqrt{-10 + 2\sqrt{18\alpha^2 + 25}}\,\frac{5 - 3\Gamma}{40(\Gamma - 1)}. \tag{4.28}$$

Equation (4.28) clearly indicates that $\Phi_{\rm sc}$ strictly depends on both viscosity parameter α and ratio of specific heats Γ, when self-similar solutions are adopted. What is more is that for $\Phi_{\rm s} > \Phi_{\rm sc}$, ${C_2}^2$ in equation (4.26) becomes negative resulting unphysical solutions as it leads to $\Omega^2 < 0$.

In Fig. 4.5, we compare the global transonic solutions with the self-similar solutions. While doing so, we choose the same set of input parameters for global solutions as used in Fig. 4.4, *i.e.*, $(\varepsilon_0, \lambda_0, \alpha) = (0.0025, 2.75, 0.05)$. And, for self-similar solutions, we need to specify $\alpha = 0.05$, $f = 1$, and $\Gamma = 1.5$, respectively. In panel (a), the profile of the radial velocity $|v|$ is presented, and in panel (b), we show the variation of sound speed $C_{\rm s}$. For the self-similar solutions, the effects of thermal conduction in $|v|$, and $C_{\rm s}$ appear to be insignificant even for high saturation constant $\Phi_{\rm s} = 0.001$. This happens because both radial velocity and sound speed follow simple power law as $|v|,\ C_{\rm s} \sim r^{-1/2}$ having an ignorable impact of thermal conduction. On the contrary, the impact of $\Phi_{\rm s}$ is seen to be prominent in the global solutions. In addition, the Mach number M $(= |v|/C_{\rm s})$

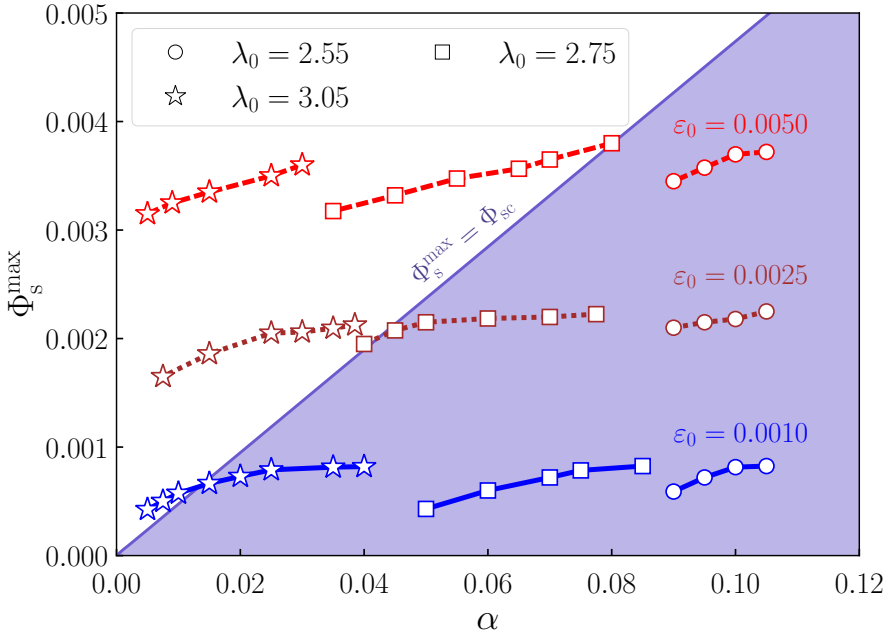

FIGURE 4.6: Correlation between α and maximum value of saturation constant Φ_s^{max} that renders the global transonic accretion solutions around black holes. Here, circles, squares, and asterisks are for $\lambda_0 = 2.55, 2.75$ and 3.05 and these points connected with solid (blue), dotted (maroon), and dashed (red) lines represent the results for $\varepsilon_0 = 0.0010, 0.0025$, and 0.0050, respectively. The shaded (violet) region corresponds to the self-similar solutions (see Eq. (4.28)) where slanting solid line refers the limiting value of saturation constant ($\Phi_s^{max} = \Phi_{sc}$). See the text for the details.

in global solutions generally decreases with radius, whereas it remains independent on r for self-similar solutions (Faghei, 2012). In fact, self-similar solutions do not possess critical points as they remain subsonic across the lengthscale of the disk. In panel (c), we illustrate the variation of angular momentum λ for the same solutions presented in Fig. 4.5(a). We find that λ is reduced with the increase of saturation constant Φ_s particularly towards the outer part of the disk, which is in agreement with the results of Tanaka & Menou (2006). Moreover, λ steeply rises at larger radii as $\lambda \propto r^{1/2}$ in a self-similar approach, although HAFs remain sub-Keplerian all throughout provided α do not assume highend values. In panel (d), we present the variation of the local disk thickness H/r as a function of r. In the self-similar model, H/r remains almost constant ($H/r \sim 0.6$) at the outer regions of the disk, whereas flow geometry becomes quasi-spherical ($H/r \sim 1$) for global solutions.

4.3.5 Parameter space for global and self-similar solutions

In this section, we put effort to determine the Φ_s that admits global accretion solutions for a given set of input parameters $(\varepsilon_0, \lambda_0, \alpha)$. Upon tuning $(\varepsilon_0, \lambda_0)$, we compute the maximum value of saturation constant Φ_s^{max} for a given α and present the obtained results in Fig. 4.6. Here, circles, squares, and asterisks are for $\lambda_0 = 2.55, 2.75$ and 3.05, and these points are joined using solid (blue), dotted (maroon), and dashed (red) lines corresponding to $\varepsilon_0 = 0.0010, 0.0025$, and 0.0050, respectively. We observe that for a set of $(\varepsilon_0, \lambda_0)$, Φ_s^{max} increases with the increase of α, which is in agreement with the results obtained from the self-similar solutions (Ghasemnezhad et al., 2012; Faghei, 2012). Further, we notice that for a given ε_0, when λ_0 is small (high), flow with relatively higher (lower) viscosity admits global transonic solution. On the other hand, for a given α, when ε_0 is increased (decreased), the acceptable range of Φ_{sc}^{max} is also increased (decreased), irrespective to the choice of λ_0 values. The shaded (violet) region corresponds to the self-similar solutions (see Eq. (4.28)), where slanting solid line refers the limiting value of saturation constant ($\Phi_s^{max} = \Phi_s$). Here, we choose $f = 1$ and $\Gamma = 1.5$. When $\Phi_s > \Phi_s^{max}$, global solutions become infeasible and cease to exist (see §4.3.4). It is noteworthy that for lower λ_0, Φ_{sc} agrees well with Φ_s^{max} obtained from the global solutions. When λ_0 is higher, a coarse agreement is observed for flows with lower ε_0 values. With this, we argue that the physically motivated global accretion solutions are prevalent than the simplistic self-similar solutions.

Next, we compare the limiting range of $\Phi_s^{max} = \Phi_{sc}$ as a function of viscosity parameter α for different Γ values. The obtained results are shown in Fig. 4.7, where Φ_s^{max} is plotted as a function of α. In the figure, the effective domain shaded in violet is for $\Gamma = 1.5$, whereas the same in red is obtained for $\Gamma = 1.6$. It is evident that the acceptable range of the saturation constant Φ_s decreases as Γ is increased (see also Tanaka & Menou, 2006). Based on this findings, we infer that self-similar solutions obtained using relatively lower Γ seems to be potentially more viable in articulating the features of global accretion solutions of HAFs (see Fig. 4.6).

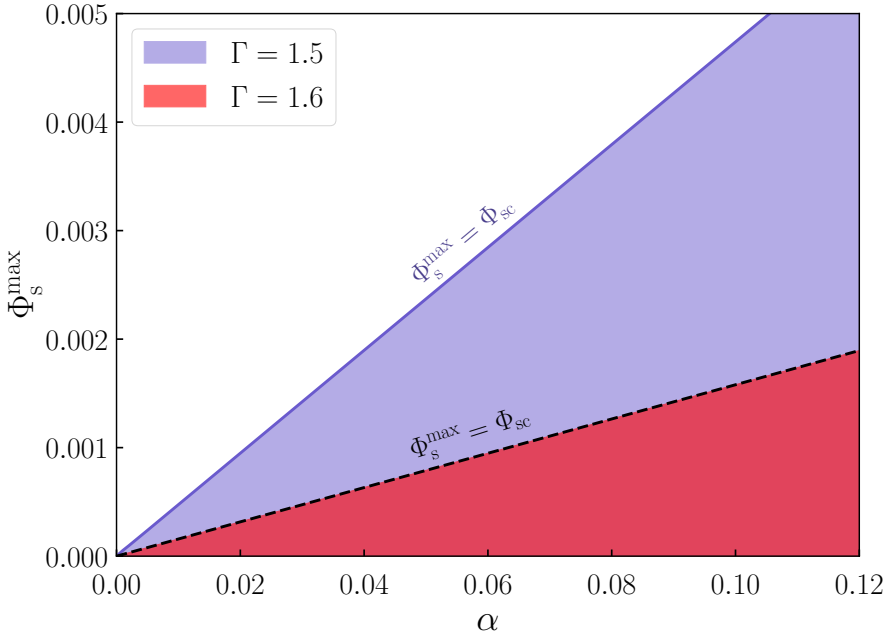

FIGURE 4.7: Correlation between α and Φ_s^{max} based on self-similar solutions (see equation (4.28)) for different adiabatic index Γ. The shaded region in violet and red are for $\Gamma = 1.5$ and 1.6, respectively. See the text for the details.

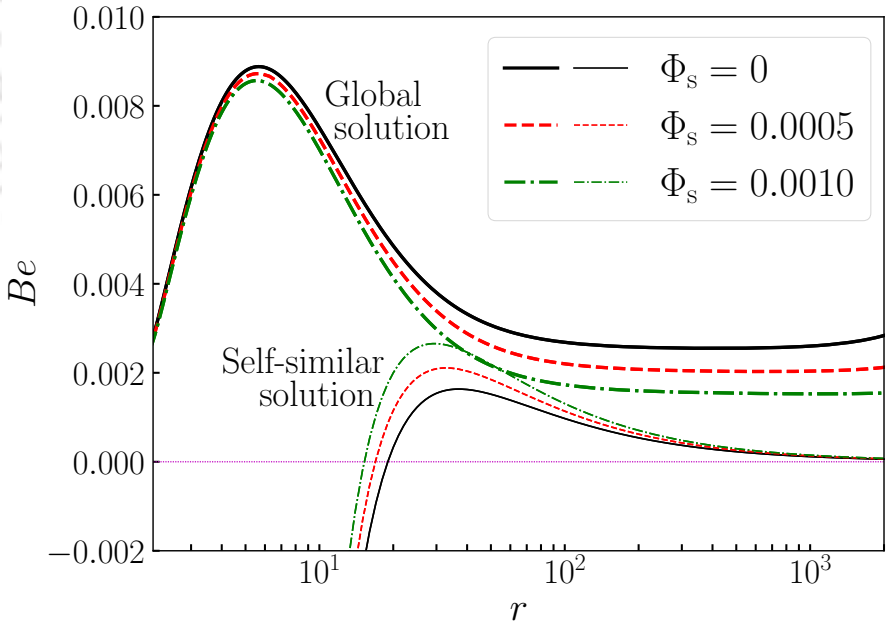

FIGURE 4.8: Plot of Bernoulli parameter (Be) as a function of logarithmic radial coordinate for different saturation constants Φ_s. Here, we choose the input parameters as $\Gamma = 1.5$, $f = 1.0$, and $\alpha = 0.05$, respectively. Thick curves represent results obtained from the global solutions using $\varepsilon_0 = 0.0025$, and $\lambda_0 = 2.75$, whereas thin curves are for self-similar solutions. The solid (black), dashed (red), and dot-dashed (green) curves denote results for $\Phi_s = 0, 0.0005$, and 0.0010, respectively. The dotted (magenta) horizontal line corresponds to $Be = 0$. See the text for the details.

4.3.6 Bernoulli parameter

In this section, we study the Bernoulli parameter Be (see equation (4.18)), which coarsely accounts for the evidence of outflow likely to be originated from the accretion disk. Accordingly, in Fig. 4.8, we display the typical variation of the Bernoulli parameter Be as a function of radial coordinate (r). In the figure, thick curves correspond to the results obtained from the global accretion solutions, where input parameters are chosen as $\Gamma = 1.5$, $f = 1.0$, $\alpha = 0.05$, $\varepsilon_0 = 0.0025$, and $\lambda_0 = 2.75$, respectively. Here, thick solid (black), dashed (red), and dot-dashed (green) curves represent results corresponding to $\Phi_s = 0.0, 0.0005$, and 0.0010. Note that the overall profile of Be is in agreement with the smooth solutions reported in Das et al. (2009) (see also Kumar & Gu, 2018). We find that the Bernoulli parameter Be of global transonic solutions remains positive throughout the disk, which is in agreement with Narayan et al. (1997). The positive Bernoulli parameter suggests that the accreting gas is unbound, and therefore, a part of the accreting gas may escape (equivalently mass loss) in the form of the outflow with a net positive (kinetic) energy avoiding the strong gravitational pull of BH. With this, accreting gas tends to become energetically bound. However, these outflows are expected to be quite weak as the terminal Lorentz factor ranges $\gamma = Be + 1 \sim 1.01$ (Das et al., 2009).

It is worthy to compare the Bernoulli parameter obtained from global and self-similar solutions. Although the Bernoulli parameter of global transonic solution always remain positive, however, in self-similar approach, it often alters its sign from positive to negative as the accreting flow moves towards the black hole from the outer edge. In Fig. 4.8, we present the profile of Be obtained from self-similar solutions using thin curves, where $\Gamma = 1.5$, $f = 1.0$, $\alpha = 0.05$ are used as input parameters. As before, the results plotted using thin solid (black), dashed (red) and dot-dashed (green) curves are for $\Phi_s = 0.0, 0.0005$, and 0.0010, respectively. We observe that Be becomes negative only at the inner part of the disk, where potential energy overcomes the remaining terms in equation (4.18) yielding strongly bound flow. This happens because the radial and rotational velocities close to BH in the self-similar solutions are smaller than those in the global solutions. Further, we notice that the effect of thermal conduction on the Bernoulli parameter Be is seen to be opposite. We infer that this finding possibly arises

as the radial dependence of the disk variables in self-similar solutions (see equation (4.21)−(4.23)) differs considerably from the global solutions when the thermal conduction is active inside the HAFs.

4.4 Chapter Conclusions

In this Chapter, we present a comprehensive study of a low angular momentum, steady, axisymmetric, viscous, and advective accretion flow around a non-rotating BH in the presence of thermal conduction. Here, the conductive heat flux is described in the saturated form. This is observed in the case of low-mass accreting systems because the hot plasmas in such systems become weakly collisional (Quataert, 2004; Tanaka & Menou, 2006). We adopt the pseudo-Newtonian potential introduced by Paczyński & Wiita (1980) that satisfactorily mimics the space-time geometry around the non-rotating BHs. With this, we examine the effect of thermal conduction on the properties of the global transonic hot accretion flows around BHs. In this regard, the conservation equations augmented by the inner boundary conditions permit us to carry out the analysis from the location just outside the BH horizon $r_{\rm inner} = 2.001$. Using the model input parameters, namely energy (ε_0), angular momentum (λ_0), viscosity parameter (α), adiabatic index (Γ), and saturation constant ($\Phi_{\rm s}$) and following the solution methodology presented in section 4.2, we obtain the complete set of global transonic solutions for the first time to the best of our knowledge in presence of thermal conduction. We summarize our findings below.

We find that the effect of thermal conduction on global accretion solutions is significant, particularly on the outer part of the disk. When the saturation constant $\Phi_{\rm s}$ exceeds its limiting value, the nature of the global solution is altered and it becomes closed failing to connect the BH horizon with the outer edge of the disk (see Fig. 4.2). When $\Phi_{\rm s}$ is increased for flows with fixed input parameters $(\varepsilon_0, \lambda_0, \alpha)$, critical points recede away from the BH horizon (see Fig. 4.3). We also examine the role of thermal conduction on the flow variables. We see that the increase of $\Phi_{\rm s}$ reduces the flow temperature and disk height at the outer region (see Fig. 4.4). This possibly happens due to the fact that high thermal conduction generally weakens the viscous turbulence (Faghei, 2012) that

lowers the disk temperature. Indeed, these findings are in agreement with the results reported in Tanaka & Menou (2006); Wu et al. (2010). Further, we compare the flow variables obtained by means of global and self-similar solutions, and ample disagreement is noticed (see Fig. 4.5). In fact, we observe that radial velocity and sound speed are not noticeably affected by thermal conduction for self-similar solutions. Notice that global accretion solutions remain sub-Keperian all throughout, however, self-similar solutions may become super-Keplerian near the critical radius provided α assumes lower value (Narayan et al., 1997; Chen et al., 1997; Kumar & Gu, 2018).

One of the important results of this work is to identify the correlation between viscosity α and maximum saturation constant $\Phi_{\rm s}^{\rm max}$ that renders the global transonic solutions of HAFs. We find a positive correlation where $\Phi_{\rm s}^{\rm max}$ increases with α irrespective to the choice of $(\varepsilon_0, \lambda_0)$. We also observe that the flow with higher ε_0 can sustain higher $\Phi_{\rm s}^{\rm max}$ for global solutions. However, such dependencies are non-existent, indicating the limitation of the self-similar approach (see Fig. 4.6).

In addition, we calculate the Bernoulli parameter Be in the presence of thermal conduction to explore the possible existence of outflows in HAFs. Global solutions display a positive Bernoulli parameter at all radii, whereas self-similar solutions yield a negative Bernoulli parameter at the inner part of the disk (see Fig. 4.8). Evidently, an accretion flow with a positive Bernoulli parameter is unbound, and therefore, matter is likely to escape from such an unbound disk, avoiding the strong gravity of BH in the form of outflow. Overall, the present model is a potential candidate for addressing the two-dimensional inflow-outflow solutions around BHs.

The pseudo-Newtonian approach is quite simple and useful for describing the accretion flows around compact objects. However, due to its over-simplified form of equations, many interesting physics near the compact objects might lost, which comes directly from the GR effects. On the contrary, solving the exact GR hydrodynamics or GRMHD equations by undertaking all the physical processes (radiative cooling, dissipation, thermal conduction, etc.) is tricky and non-trivial. We, therefore, look for an alternative approach where post-Newtonian theory could help, as it deals with the Newtonian hydrodynamic equations with gravity but incorporates relativistic correction terms from GR with

different orders in $1/c^2$ (c is the speed of light). The final working Chapter solely focuses on this aspect.

Chapter 5

Accretion flows around spinning compact objects in the post-Newtonian regime

The content of this chapter has been published in Nazari E., Mitra S., Abbassi S., Das S., 2024, JCAP05, 117, 2024.

One of the most successful approximations to general relativity based on the slow motion condition[1] and the weak field limit[2] is the post-Newtonian (PN) theory. With this theoretical formalism, one can find the missing link between the Newtonian and GR descriptions of accretion flows. This theory consists of Newtonian hydrodynamics and gravity (0PN), and includes higher order relativistic corrections. Motivating with this, in the present Chapter, we discuss the structure of a low angular momentum accretion flows around rotating compact objects incorporating relativistic corrections up to the leading post-Newtonian order, *i.e.,* 1PN. The weak field limit suggests that the effect of PN theory is valid upto a certain radius known as the post-Newtonian radius, $r_{\rm PN} \sim 10$ (Will, 2011). To begin with, we formulate the governing post-Newtonian hydrodynamic equations (Poisson & Will, 2014) for the mass and energy-momentum flux without imposing any symmetries. However, for the sake of simplicity, we consider the flow to be stationary,

[1]Motion in physical systems are slow compared to the speed of light (c), *i.e.,* $v/c \ll 1$.

[2]Locally the metric can be written as the Minkowskian along with small perturbations, *i.e.,* $g_{\mu\nu} \simeq \eta_{\mu\nu} + h_{\mu\nu}$, with $h_{\mu\nu} << 1$.

axisymmetric, and inviscid in nature. Next, we identify an effective potential $\Phi_{\rm eff}^{\rm PN}$ around a general axisymmetric PN background from the radial and the azimuthal component of the Navier-Stokes equation. Further, we compare the PN potential with the effective potential around a Kerr black hole (Dihingia et al., 2018a, $\Phi_{\rm eff}^{\rm GR}$) and the Newtonian one ($\Phi_{\rm eff}^{\rm N}$). Indeed the $\Phi_{\rm eff}^{\rm PN}$ is sandwiched between $\Phi_{\rm eff}^{\rm N}$ and $\Phi_{\rm eff}^{\rm GR}$. As the realm of PN theory is beyond $r > 10$ gravitational radius, the polytropic equation of state (EoS) is suitable to describe the thermodynamics of a vertically integrated accretion flow confined to the disk mid-plane. With this, we solve the governing equations and obtain the global accretion solutions for the first time in the PN background. It is noteworthy that the spin-orbit coupling effects manifest themselves in the PN accretion dynamics, which was absent in the Newtonian hydrodynamics.

5.1 Post-Newtonian space-time

We first need to be armed with an appropriate metric that correctly describes the space-time around a spinning body in the post-Newtonian regime. In this work, we consider an accretion disk with negligible self-gravity. So, the curvature of the space-time is only affected by the central spinning body. The metric of the space-time outside a single spinning body up to the 1PN order is given by (Poisson & Will, 2014),

$$g_{00} = -1 + \frac{2}{c^2}\frac{GM_*}{r} - \frac{2}{c^4}\Big(\frac{GM_*}{r}\Big)^2 + O(c^{-6}), \tag{5.1a}$$

$$g_{0j} = \frac{2}{c^3}\frac{G(\boldsymbol{x}\times\boldsymbol{S})^j}{r^3} + O(c^{-5}), \tag{5.1b}$$

$$g_{jk} = \Big(1 + \frac{2}{c^2}\frac{GM_*}{r}\Big)\delta_{jk} + O(c^{-4}), \tag{5.1c}$$

where M_* and $\boldsymbol{S}$ are the mass and spin vector of the compact body, respectively. Also, $\boldsymbol{x}$ is the position vector of the field point outside the body. Its component notation is $x^j := (x, y, z)$. Here, $r := |\boldsymbol{x}|$ and δ_{jk} is the Kronecker delta. In this space-time, the metric determinant is given by,

$$-g = 1 + \frac{4}{c^2}\frac{GM_*}{r} + O(c^{-4}). \tag{5.2}$$

As seen in Eqs. (5.1a)-(5.1c), the post-Newtonian expansion of the time-time, time-space, and space-space components is truncated to $O(c^{-4})$, $O(c^{-3})$, and $O(c^{-2})$, respectively.

5.1.1 Validity of post-Newtonian Approximation

An important question may be raised as to what radius this approximation works and in what region around the central object it can be applied. In fact, in the accretion disk system, there is a radius where the velocity of the fluid element, as well as the gravitational fields can be large so that the post-Newtonian gravity is no longer valid. On the other hand, due to our lack of knowledge of the convergence properties of this approximation, this radius is not known a priori Will (2011). However, to answer this question and obtain the post-Newtonian validity domain, we apply the following scheme.

We analyze the aforementioned post-Newtonian metric and compare the post-Newtonian terms with the Newtonian one. We know that the second term in Eq. (5.1a) is a Newtonian term. Also, as mentioned earlier, the third term in this relation is the first post-Newtonian correction. It is then obvious that the ratio of the third term to the second is small enough (the weak field limit $\frac{GM_*}{r\,c^2} \ll 1$). Therefore, from this comparison, the constraint $r \gg r_{\rm g}$ is deduced, where $r_{\rm g} = GM_*/c^2$. In a similar fashion, comparing the post-Newtonian term in the time-space component of the metric with the Newtonian term in the time-time component also reveals that $r \gg \frac{\boldsymbol{S}}{cM_*}$. This limit indeed demands a weaker constraint on r. From the dimensions of the spin, we can write $\boldsymbol{S} \equiv \frac{GM_*^2}{c}$. Inserting this value into the condition $r \gg \frac{\boldsymbol{S}}{cM_*}$, we arrive at $r \gg r_{\rm g}$ as obtained before. So, the condition resulting from the comparison of the post-Newtonian and Newtonian terms of the time-time component places a tighter bound on r and automatically fulfills the condition $r \gg \frac{\boldsymbol{S}}{cM_*}$. From the aforementioned discussions, it is obvious that the post-Newtonian metric introduced here can describe the space-time in regions $r \gg r_{\rm g}$. Therefore, we assume this limiting radius to be at least an order of magnitude larger than $r_{\rm g}$, which is called the post-Newtonian radius, $r_{\rm PN} \simeq 10\, r_{\rm g}$. Hence, the 1PN corrections are reliable from very far radii, $r_{\rm PN} \leqslant r \leqslant r_\infty$. To investigate a system at inner radii, *i.e.,* $r < r_{\rm PN}$, one needs to take into account the exact relativistic corrections and apply

the Kerr metric as discussed in Chapter 3. This is indeed one of the shortcomings of the post-Newtonian approximation.

5.2 Governing hydrodynamic equations up to 1PN order

In this section, we present the hydrodynamic equations governing the behavior of a perfect fluid in post-Newtonian space-time. To proceed further, we introduce the contravariant components of the metric (5.1a)-(5.1c) as well as the corresponding Christoffel symbols in Appendix D.1.

5.2.1 Relativistic perfect fluid

The energy-momentum tensor of the perfect fluid is given by[3],

$$T^{\alpha\beta} = \left(\rho + \frac{\epsilon_0}{c^2} + \frac{p_{\rm gas}}{c^2}\right) u^\alpha u^\beta + p_{\rm gas} g^{\alpha\beta} \tag{5.3}$$

where ρ is the proper rest-mass density, ϵ_0 is the proper internal energy density, $p_{\rm gas}$ is thermal pressure, and $u^\alpha = \gamma(c, V^j)$ is the four-velocity field. Here, $\gamma = u^0/c$. Following the slow motion condition and weak field ($\frac{GM_*}{c^2 r} \ll 1$) limit, we express the mass and energy-momentum conservation equations as

$$\nabla_\mu (\rho u^\mu) = \partial_t \rho^* + \partial_j (\rho^* V^j) = 0, \tag{5.4}$$

and

$$\nabla_\beta T^{\alpha\beta} = \partial_\beta (\sqrt{-g} T^{\alpha\beta}) + \Gamma^\alpha_{\beta\mu} (\sqrt{-g} T^{\beta\mu}) = 0. \tag{5.5}$$

To obtain Eq. (5.5), we use the relation $\Gamma^\mu_{\mu\beta} = (-g)^{-1/2} \partial_\beta (-g)^{1/2}$. Here, ρ^* is the rescaled mass density defined as

$$\rho^* = \sqrt{-g}\gamma\rho. \tag{5.6}$$

[3]The Greek indices (α, β) run from $(0 \to 3)$ and Roman indices (i, j) run from $(1 \to 3)$.

Hereafter, we use ρ^* in the context of the post-Newtonian gravity unless otherwise specified. Eqs. (5.4) and (5.5) are, in fact, the equations governing the behavior of a generic fluid in a general curved space-time. To find the lorentz factor γ, we use the normalization condition $g_{\alpha\beta}u^\alpha u^\beta = -c^2$. After inserting the definition of the four-velocity and applying the slow motion condition, one can arrive at the following equation,

$$\gamma = 1 + \frac{1}{c^2}\frac{GM_*}{r} + \frac{1}{2c^2}V^2 + O(c^{-4}). \tag{5.7}$$

With Eqs. (5.2) and (5.7), we return to the definition (5.6) and find

$$\rho^* = \rho\Big(1 + \frac{1}{c^2}\frac{3\,GM_*}{r} + \frac{1}{2c^2}V^2\Big) + O(c^{-4}), \tag{5.8}$$

after expanding the result in powers of c and truncating it to $O(c^{-2})$.

We begin with the time component of the energy-momentum conservation (5.5), which provides us the conservation of energy. By expanding the time component, we have

$$\frac{1}{c}\partial_t(\sqrt{-g}T^{00}) + \partial_j(\sqrt{-g}T^{0j}) + \Gamma^0_{00}(\sqrt{-g}T^{00}) + 2\Gamma^0_{0j}(\sqrt{-g}T^{0j}) + \Gamma^0_{jk}(\sqrt{-g}T^{jk}) = 0. \tag{5.9}$$

Notably, each term of Eq. (5.9) must be computed upto 1PN order and the relevant calculations are summarized in Appendix D.1. Using Eqs. (D.3)-(D.4d), we arrive at

$$\partial_t\rho^* + \partial_j(\rho^* V^j) + \frac{1}{c^2}\Big\{\partial_t\Big[\rho^*\big(\frac{GM_*}{r} + \frac{V^2}{2} + \Pi\big)\Big] + \partial_j\Big[\rho^*\,V^j\big(\frac{GM_*}{r} + \frac{V^2}{2} + \Pi\big)\Big] + \partial_j(p_{\rm gas}\,V^j) + \frac{GM_*}{r^2}\rho^*\Big[\partial_t r + 2\partial_j r\,V^j\Big]\Big\} + O(c^{-4}) = 0. \tag{5.10}$$

Here, $\Pi\,(=\epsilon_0/\rho^*)$ is the specific internal energy of the fluid. Moreover, using Eq. (5.4), one can simplify Eq. (5.10) and obtain the following equation:

$$\rho^*\partial_t\Big(\frac{V^2}{2} + \Pi\Big) + \rho^* V^j\partial_j\Big(\frac{V^2}{2} + \Pi\Big) + \partial_j(p_{\rm gas}\,V^j) + \frac{GM_*}{r^2}\partial_j r\,\rho^* V^j = 0. \tag{5.11}$$

It is the local conservation of the energy within the fluid. To simplify Eq. (5.11), we use the Newtonian Euler equation as

$$\rho^* \frac{dV^j}{dt} = -\partial_j p_{\rm gas} - \frac{GM_*}{r^2}\partial_j r\,\rho^*, \tag{5.12}$$

where $d/dt = \partial_t + V^k\partial_k$. Note that Eq. (5.12) is obtained from the spatial component of Eq. (5.5) in the Newtonian order (0PN order). Using Eqs. (5.11-5.12), we finally get

$$\frac{d\Pi}{dt} = \frac{p_{\rm gas}}{\rho^{*2}}\frac{d\rho^*}{dt} + O(c^{-2}). \tag{5.13}$$

Eq. (5.13) is in fact the first law of thermodynamics for perfect fluids. As expected, the spin effects do not appear in this equation Eq. (5.13) up to the order kept here. It is worth noting that it is sufficient to know the energy equation to the 0PN order as written in Eq. (5.13). This is because the terms including the internal energy will eventually appear with the coefficient $\frac{1}{c^2}$ in the hydrodynamic equations. Therefore, the $O(c^{-2})$ terms in Eq. (5.13) play a role in the 2PN corrections, namely $O(c^{-4})$. We clarify this point in the next paragraphs.

Similarly, we attempt to obtain the spatial components of Eq. (5.5) that yields momentum conservation. By expanding this component, we obtain

$$\frac{1}{c}\partial_t(\sqrt{-g}T^{0j}) + \partial_k(\sqrt{-g}T^{jk}) + \Gamma^j_{00}(\sqrt{-g}T^{00}) + 2\Gamma^j_{0k}(\sqrt{-g}T^{0k}) + \Gamma^j_{kn}(\sqrt{-g}T^{kn}) = 0. \tag{5.14}$$

The five terms in Eq. (5.14) are given in Eqs. (D.5)-(D.6d) to the required order. Further, substituting Eqs. (D.5)-(D.6d) into Eq. (5.14), we get

$$\begin{aligned}
&\partial_t(\mu\rho^* V^j) + \partial_k(\mu\rho^* V^j V^k) + \partial_j p_{\rm gas} + \frac{GM_*\,\rho^*}{r^2}\partial_j r + \frac{GM_*\,\rho^*}{c^2 r^2}\partial_j r\Big[\Pi + \frac{p_{\rm gas}}{\rho^*} - \frac{3\,GM_*}{r} + \frac{3}{2}V^2\Big] \\
&+ \frac{G\rho^*}{c^2 r^2}\Big\{\frac{2}{r}\Big[(\boldsymbol{x}\times\partial_t\boldsymbol{S})_j + (\partial_t\boldsymbol{x}\times\boldsymbol{S})_j\Big] - \frac{6}{r^2}\partial_t r(\boldsymbol{x}\times\boldsymbol{S})_j - 2M_*\,V^j(\partial_t r + V^k\partial_k r) \\
&+ 2V^k\Big[\frac{3}{r^2}\Big(\partial_j r(\boldsymbol{x}\times\boldsymbol{S})_k - \partial_k r(\boldsymbol{x}\times\boldsymbol{S})_j\Big) - \frac{1}{r}\Big((\partial_j\boldsymbol{x}\times\boldsymbol{S})_k - (\partial_k\boldsymbol{x}\times\boldsymbol{S})_j\Big)\Big]\Big\} + O(c^{-4}) = 0,
\end{aligned} \tag{5.15}$$

where $\mu \coloneqq 1+\frac{1}{c^2}(\Pi+\frac{p_{\rm gas}}{\rho^*}+\frac{GM_*}{r}+\frac{V^2}{2})$. Using Eq. (5.4), the sum of the first two terms in this relation are written as follows:

$$\partial_t(\mu\rho^* V^j)+\partial_k(\mu\rho^* V^j V^k)=\rho^* V^j\frac{d\mu}{dt}+\mu\,\rho^*\frac{dV^j}{dt}. \tag{5.16}$$

With the definition of μ, we have,

$$\frac{d\mu}{dt}=\frac{1}{c^2}\Big[\frac{1}{\rho^*}\partial_t p_{\rm gas}-\frac{2\,GM_*}{r^2}V^k\partial_k r-\frac{GM_*}{r^2}\partial_t r\Big]. \tag{5.17}$$

Using Eq. (5.17) and carrying out some manipulations, we finally arrive at,

$$\begin{aligned}\rho^*\frac{dV^j}{dt}&=-\partial_j p_{\rm gas}-\frac{GM_*\,\rho^*}{r^2}\partial_j r+\frac{1}{c^2}\Big\{\Big(\Pi+\frac{p_{\rm gas}}{\rho^*}+\frac{GM_*}{r}+\frac{V^2}{2}\Big)\times\partial_j p_{\rm gas}-V^j\partial_t p_{\rm gas}\Big\}\\&-\frac{G\,\rho^*}{c^2r^2}\Big\{M\Big(V^2-\frac{4\,GM_*}{r}\Big)\partial_j r-M_*\,V^j(3\,\partial_t r+4\,V^k\partial_k r)+\frac{2}{r}\Big[(\boldsymbol{x}\times\partial_t\boldsymbol{S})_j+(\partial_t\boldsymbol{x}\times\boldsymbol{S})_j\Big]\\&-\frac{6}{r^2}\partial_t r(\boldsymbol{x}\times\boldsymbol{S})_j+2V^k\Big[\frac{3}{r^2}\Big(\partial_j r(\boldsymbol{x}\times\boldsymbol{S})_k-\partial_k r(\boldsymbol{x}\times\boldsymbol{S})_j\Big)-\frac{1}{r}\Big((\partial_j\boldsymbol{x}\times\boldsymbol{S})_k-(\partial_k\boldsymbol{x}\times\boldsymbol{S})_j\Big)\Big]\Big\}\\&+O(c^{-4}).\end{aligned} \tag{5.18}$$

This relation is the Euler equation of a post-Newtonian fluid embedded in the post-Newtonian field of a spinning compact body. The terms within the braces are the relativistic corrections to the Newtonian Euler equation.

So far, five hydrodynamic equations, *i.e.,* three equations from Eq. (5.18) and two equations from Eqs. (5.13) and (5.4), are introduced to describe a perfect fluid with six unknowns $(\rho^*, p_{\rm gas}, \Pi, V^j)$. As usual, the last equation complementing this set of hydrodynamic equations is the EoS. In hydrodynamics, a class of the equations of state is considered as barotropic, which states that pressure is only a function of the density ρ (see Rezzolla & Zanotti (2013) and references therein). On the other hand, in the context of post-Newtonian gravity, ρ^* has been applied as the rescaled mass density. Following this scheme, we consider that pressure is a function of ρ^* to define a barotropic fluid in the post-Newtonian framework (Poisson & Will, 2014; Nazari et al., 2017; Kazemi et al., 2018). So, we have the EoS given by

$$p_{\rm gas}=p_{\rm gas}(\rho^*). \tag{5.19}$$

Using Eq. (5.19), we define the post-Newtonian sound speed as

$$(C_{\rm s}^2)_{\rm PN} := \Big(\frac{\partial p_{\rm gas}}{\partial \rho^*}\Big)_{s_0}, \tag{5.20}$$

where s_0 is the specific entropy. In the following, after specifying the form of Eq. (5.19), we derive the relation between post-Newtonian and Newtonian sound speeds.

5.3 Accretion flow structure and the underlying assumptions

We choose the spherical polar coordinates (r, θ, ϕ) to express the flow structure, and the thin disk is assumed to be confined in the mid-plane, *i.e.,* $\theta = \pi/2$. In this coordinate system, $\boldsymbol{x} = r\hat{r}$ and $\boldsymbol{V} = V_r\hat{r} + V_\theta\hat{\theta} + V_\phi\hat{\phi}$. Eventually, we refrain from any motion above the mid-plane ($V_\theta \sim 0$) and the flow remains in vertical equilibrium. Furthermore, we assume that the spin vector of the body remains constant with respect to time, and consequently, we set $d\boldsymbol{S}/dt = 0$. Applying the above assumptions, we obtain the post-Newtonian hydrodynamic equations governing the accretion dynamics around the spinning compact body. After some algebraic manipulations, we arrive at the radial momentum equation as,

$$\partial_t V_r + V_r\partial_r V_r + \frac{V_\phi}{r}\partial_\phi V_r - \frac{V_\phi^2}{r} = -\frac{1}{\rho^*}\partial_r p_{\rm gas} - \frac{GM_*}{r^2} + \frac{1}{c^2}\Bigg\{\frac{1}{\rho^*}\partial_r p_{\rm gas}\Big(\Pi + \frac{p_{\rm gas}}{\rho^*} + \frac{GM_*}{r} + \frac{1}{2}V^2\Big)$$
$$- \frac{1}{\rho^*}V_r\partial_t p_{\rm gas} + \frac{GM_*}{r^2}\Big(\frac{4\,GM_*}{r} + 3\,V_r^2 - V_\phi^2 + \frac{2\,s_{\rm J}\,V_\phi}{r}\Big)\Bigg\} + O(c^{-4}), \tag{5.21}$$

and azimuthal momentum equation,

$$\partial_t V_\phi + V_r\partial_r V_\phi + \frac{V_\phi}{r}\partial_\phi V_\phi + \frac{V_r\,V_\phi}{r} = -\frac{1}{\rho^*\,r}\partial_\phi p_{\rm gas} + \frac{1}{c^2}\Bigg\{\frac{1}{\rho^*\,r}\partial_\phi p_{\rm gas}\Big(\Pi + \frac{p_{\rm gas}}{\rho^*} + \frac{GM_*}{r} + \frac{1}{2}V^2\Big)$$
$$- \frac{1}{\rho^*}V_\phi\partial_t p_{\rm gas} + \frac{2\,GM_*\,V_r}{r^2}\Big(2\,V_\phi - \frac{s_{\rm J}}{r}\Big)\Bigg\} + O(c^{-4}). \tag{5.22}$$

Here, $V_r\,(=\dot{r})$ is the radial *drift* velocity, $V_\phi\,(=r\dot{\phi})$ is the azimuthal velocity, and $s_{\rm J}\,(=\frac{\boldsymbol{S}}{M_*})$ is the spin of the body per unit mass.

Overall, the equations (5.21) and (5.22) capture the basic characteristics of fluid motion confined to the mid-plane around a spinning compact body in the post-Newtonian gravity. It may be noted that the terms within the braces in equations (5.21)-(5.22) are the post-Newtonian corrections to the Newtonian equations.

5.3.1 Accretion flows in steady state

In this section, we focus on a special case of advective, axisymmetric ($\partial/\partial\phi \to 0$) accretion flows in the steady state ($\partial/\partial t \to 0$). To analyze the physical processes, we derive the dynamical equations in the local rest frame (LRF) of the fluid. In order to transform from the global frame (*i.e.,* the Boyer-Lindquist frame) to LRF and vice versa, we follow the standard procedure applied by Popham & Gammie (1998); Gammie & Popham (1998). In a similar fashion, we introduce two important frames: 1 – locally nonrotating frame (LNRF) and 2 – corotating frame (CRF). The LNRF is attached to an observer whose worldline is $\theta =$ const., $r =$ const., and $\phi = \omega\, t +$ const., where ω is the rate of frame dragging by the central spinning body and is obtained in terms of the spin ($s_{\rm J}$) as described in in Eq. (D.9). When the observer is attached to a frame that corotates with the fluid, the frame is called CRF. This corotating frame moves relative to the LNRF with a constant velocity v_ϕ confined to the ϕ-direction. Hence, with an azimuthal Lorentz boost ($\gamma_\phi = \left(1 - v_\phi^2/c^2\right)^{-1/2}$), it is possible to transform from LNRF to CRF. On the other hand, LRF has a constant radial velocity (v), with respect to CRF. Due to the accretion of the material onto the central body, v is indeed negative. Therefore, we get the LRF of the fluid, using radial Lorentz boost ($\gamma_r = \left(1 - v^2/c^2\right)^{-1/2}$) from CRF. Moreover, using two auxiliary frames, *i.e.,* LNRF and CRF, with an appropriate combination of coordinate transformations, one can reach the LRF from the global frame. All the relevant calculations are summarized in Appendix D.2. By imposing the aforementioned assumptions, in the subsequent sections, the post-Newtonian hydrodynamic equations are expressed in LRF of the fluid.

5.3.2 Particle number conservation

In the case of the steady, axisymmetric model, Eq. (5.4) reduces to

$$-\dot{M} = 4\pi H r \rho u^r \Big(1 + \frac{2\,GM_*}{c^2\,r}\Big). \tag{5.23}$$

Here, $\dot{M}$ is a constant interpreted as the mass accretion rate and H is the local half-thickness of the disk. Next, using Eq. (D.14) and writing u^r in terms of v, we arrive at

$$-\dot{M} = 4\pi H r \rho v \Big[1 + \frac{1}{c^2}\Big(\frac{GM_*}{r} + \frac{1}{2}v^2\Big)\Big]. \tag{5.24}$$

Eq. (5.24) renders a constant inflow of the rest mass passing through each radius of the post-Newtonian accretion disk [4]. By removing these 1PN corrections, one reaches the standard form of the accretion rate $\dot{M} = 4\pi H r \rho v$ in the non-relativistic regime.

5.3.3 Radial momentum equation

Using Eq. (5.21), we deduce the radial component of the Euler equation as

$$V_r \partial_r V_r = \frac{V_\phi^2}{r} - \frac{1}{\rho^*}\partial_r p_{\rm gas} - \frac{GM_*}{r^2} + \frac{1}{c^2}\Big\{\frac{1}{\rho^*}\partial_r p_{\rm gas}\Big(\Pi + \frac{p_{\rm gas}}{\rho^*} + \frac{GM_*}{r} + \frac{1}{2}V^2\Big) + \frac{GM_*}{r^2}\Big(\frac{4\,GM_*}{r} + 3\,V_r^2 - V_\phi^2 + \frac{2\,s_{\rm J}\,V_\phi}{r}\Big)\Big\}. \tag{5.25}$$

Next, we simplify Eq. (5.25) to express it in terms of the preferred variables v and v_ϕ. For that, we derive the required quantities γ, V_ϕ, and V_r. First, using Eq. (D.14), we get,

$$\gamma = \gamma_{\rm tot}\Big(1 + \frac{1}{c^2}\frac{GM_*}{r} - \frac{1}{c^4}\frac{G^2M_*^2}{r^2}\Big), \tag{5.26}$$

[4] Of course, this statement is reliable only in the interval $r_{\rm PN} \leqslant r \leqslant r_{\rm infty}$ which is the realm of validity of this study.

where $\gamma_{\rm tot}$ $(=\gamma_r\gamma_\phi)$ is the total Lorentz factor. After substituting the definition of $\gamma_{\rm tot}$ and truncating the result to the 1PN order, we have

$$\gamma = 1+\frac{1}{c^2}\Big(\frac{GM_*}{r}+\frac{1}{2}v^2+\frac{1}{2}v_\phi^2\Big), \tag{5.27}$$

Comparing Eq. (5.7) with Eq. (5.27) reveals that $V^2 \simeq v^2+v_\phi^2$. We use this relation to determine ρ^* in terms of v and v_ϕ. In our notation, the radial component of the four-velocity is defined as $u^r=\gamma\dot{r}=\gamma V_r$. Therefore, considering Eq. (D.14) for u^r as well as Eq. (5.27) for γ, we obtain

$$V_r = v\Big[1-\frac{1}{c^2}\Big(\frac{2\,GM_*}{r}+\frac{1}{2}v_\phi^2\Big)\Big]. \tag{5.28}$$

Similarly, using $u^\phi=\gamma\dot{\phi}$, we obtain

$$V_\phi = \frac{\lambda}{r}\Big[1-\frac{1}{c^2}\Big(\frac{3\,GM_*}{r}+\frac{1}{2}v^2+\frac{1}{2}v_\phi\Big)\Big]+\frac{GM_*\,s_{\rm J}}{c^2r^2}, \tag{5.29}$$

where λ is the angular momentum per unit mass of the fluid element. The last term in Eq. (5.29) corresponds to the drag of the fluid element along the rotation of the central body, which eventually contains information about the Coriolis force. Meanwhile, using Eqs. (5.8), (5.27)-(5.29), and (D.13), the radial component of the post-Newtonian Euler equation (5.25) reduces to,

$$\begin{aligned} v\partial_r v\Big[1-\frac{1}{c^2}\Big(\frac{4\,GM_*}{r}+\frac{\lambda^2}{r^2}\Big)\Big] &= \frac{\lambda^2}{r^3}-\frac{1}{\rho}\partial_r p_{\rm gas}-\frac{GM_*}{r^2}-\frac{1}{c^2}\Big\{\frac{\lambda^2}{r^3}\Big(3\,v^2+\frac{\lambda^2}{r^2}\Big)-2\frac{\lambda\,v^2}{r^2}\partial_r\lambda \\ &-\frac{1}{\rho}\partial_r p_{\rm gas}\Big(\Pi+\frac{p_{\rm gas}}{\rho}+\frac{4\,GM_*}{r}+v^2+\frac{\lambda^2}{r^2}\Big)-\frac{GM_*}{r^2}\Big(\frac{4\,GM_*}{r}+v^2-\frac{7\,\lambda^2}{r^2}+\frac{4\,s_{\rm J}\,\lambda}{r^2}\Big)\Big\}. \end{aligned} \tag{5.30}$$

It is noteworthy that the spin-orbit interaction manifests itself in the leading PN corrections. However, the spin-spin interaction remains hidden in the first and last terms on the right hand side of Eq. (5.25). Note that this effect would be like a *self*-spin interaction and is bilinear in the body spin (*i.e.,* $\mathcal{O}(s_{\rm J}^2)$). Clearly, it can exist in the 2PN order, but definitely not in the 1PN order. We keep in mind that in order to have a complete description of spin-spin effects, in addition to the aforementioned terms, the

rest of the $O(c^{-4})$ terms that were omitted from Eq. (5.25) at the beginning, must be brought back into play. A full investigation of these effects is beyond the scope of the present study.

5.3.4 Azimuthal angular momentum equation

Considering Eq. (5.29) and expanding the result to $O(c^{-2})$, the azimuthal component of the Euler equation (Eq. 5.22) is rewritten as

$$\partial_r V_\phi + \frac{V_\phi}{r} = -\frac{1}{c^2}\frac{GM_*}{r^2}\Big(\frac{2\,s_{\rm J}}{r} - 4\,V_\phi\Big), \tag{5.31}$$

which finally reduces to

$$\partial_r \lambda = -\frac{1}{c^2}\Big[\frac{GM_*}{r^2}(s_{\rm J} - \lambda) + \frac{\lambda^3}{r^3} - \lambda\, v\partial_r v\Big]. \tag{5.32}$$

Eq. (5.32) indicates that the relativistic angular momentum λ is complicated and the post-Newtonian corrections prevent it from being a constant. In other words, unlike the Newtonian case, the angular momentum of the rotating fluid can change with respect to the radius. We emphasize that this change is triggered due to the relativistic/post-Newtonian effects.

5.3.5 Internal energy and equation of state

For a steady and axisymmetric disk, the energy equation (5.13) reduces to

$$\partial_r \Pi = \frac{p_{\rm gas}}{\rho^{*2}}\partial_r \rho^*. \tag{5.33}$$

As already mentioned, Π appears in the equations of motion as a post-Newtonian term. Keeping this in mind, we simply convert ρ^* to ρ in Eq. (5.33) and neglect the $O(c^{-2})$ terms. Therefore, the energy equation boils down to

$$\partial_r \Pi = \frac{p_{\rm gas}}{\rho^2}\partial_r \rho. \tag{5.34}$$

To obtain accretion solutions, one requires to use the EoS, which describes a relation among the thermodynamical variables, namely density (ρ), pressure ($p_{\rm gas}$), and internal energy (Π). Since the effect of PN corrections is valid only in regions outside $\sim 10\,r_{\rm g}$ where general relativistic effects are less significant. Therefore, we consider an ideal EoS (IEoS) and assume that the fluid element undergoes reversible adiabatic changes. Accordingly, we have:

$$p_{\rm gas} = K\rho^{\Gamma}, \tag{5.35}$$

where K is a constant and a measure of entropy, and Γ is the adiabatic index. In this work, we choose $\Gamma = 13/9$ throughout to maintain the trans-relativistic nature (see Fig. 2.2f) of the flow unless stated otherwise. For the ideal fluid, the internal energy per unit mass is given by (Das et al., 2009),

$$\Pi = \frac{1}{(\Gamma-1)}\frac{p_{\rm gas}}{\rho}. \tag{5.36}$$

Next, we define the post-Newtonian sound speed and examine its relation with the Newtonian one. Towards this, we use Eq. (5.8), (5.19) and (5.35) and after some algebraic simplifications, we get

$$(C_{\rm s}^2)_{\rm PN} = (C_{\rm s}^2)_{\rm N}\Big[1+\frac{\Gamma-1}{c^2}\big(\frac{3\,GM_*}{r}+\frac{1}{2}v^2\big)\Big], \tag{5.37}$$

where $(C_{\rm s}^2)_{\rm N}\,(=K\,\Gamma\,\rho^{\Gamma-1})$ is the Newtonian sound speed.

5.3.6 Vertical equilibrium in thin accretion disks

We consider that the hydrostatic balance holds in the thin accretion disk around a spinning body in the z direction (Novikov & Thorne, 1973; Riffert & Herold, 1995; Peitz & Appl, 1997). So, the vertical momentum equation is expressed as

$$\partial_z p_{\rm gas}\Big[1-\frac{1}{c^2}\Big(\Pi+\frac{p_{\rm gas}}{\rho^*}+\frac{GM_*}{r}+\frac{1}{2}V^2\Big)\Big] = -\frac{GM_*\,\rho^*}{r^3}z\Big[1-\frac{1}{c^2}\Big(\frac{4\,GM_*}{r}-V^2+\frac{6\,s_{\rm J}\,V_\phi}{r}\Big)\Big].$$

Using Eqs. (5.8), (5.28), and (5.29), we arrive at the post-Newtonian version of the hydrostatic equilibrium

$$\partial_z p_{\rm gas}\Big[1-\frac{1}{c^2}\Big(\Pi+\frac{p_{\rm gas}}{\rho}+\frac{4\,GM_*}{r}+v^2+\frac{\lambda^2}{r^2}\Big)\Big]=\rho g_z^{\rm PN}, \tag{5.38}$$

where $g_z^{\rm PN}$ is the vertical component of the gravitational acceleration at the height z

$$g_z^{\rm PN}=-\frac{GM_*}{r^3}z\Big[1-\frac{1}{c^2}\Big(\frac{4\,GM_*}{r}-v^2-\frac{\lambda^2}{r^2}+\frac{6\,s_{\rm J}\,\lambda}{r^2}\Big)\Big]. \tag{5.39}$$

Eq. (5.38) governs the balance between the vertical gradient of pressure and the vertical gravitational force with the relevant post-Newtonian corrections. To sum up, in the reference frame comoving with the fluid element, Eqs. (5.24), (5.30), (5.32), (5.36), and (5.38) together with the EoS (Eq. 5.35) construct a complete set of differential equations that describe the behavior of a relativistic, steady thin, accretion disk in the post-Newtonian space-time of a spinning compact body.

5.4 Transonic accretion solutions in Post-Newtonian space-time

To examine the importance of the gravitational relativistic effects and to evaluate the physics behind them, we classify the post-Newtonian equations in three specific cases: (a) semi-relativistic (SR) flow, (b) semi-Newtonian (SN) flow, (c) non-relativistic (NR) flow, and evaluate the critical point conditions for them.

5.4.1 Semi-relativistic fluid

It is shown that in the region $r>8\,r_{\rm g}$, the ratio of the radial velocity of the fluid element to the speed of light is of the order $v/c\leq 10^{-1}$, (Sarkar et al., 2018, and references therein). Since the PN theory is based on successive approximations in $1/c^2$, we consider that

$$\frac{v^2}{c^2}\sim\epsilon, \tag{5.40}$$

where $\epsilon \to 0$ and $\gamma_r \to 1$. Based on the condition (5.40), the radial momentum equation becomes,

$$v\partial_r v = \frac{\lambda^2}{r^3} - \frac{1}{\rho}\partial_r p_{\rm gas} - \frac{GM_*}{r^2} + \frac{1}{c^2}\Big\{\frac{1}{\rho}\partial_r p_{\rm gas}\Big(\Pi + \frac{p_{\rm gas}}{\rho}\Big) - \frac{4\,GM_*}{r^2}\Big(\frac{\lambda^2}{r^2} - \frac{s_{\rm J}\,\lambda}{r^2}\Big)\Big\}. \quad (5.41)$$

From the above Eq. (5.41), we identify an effective force term (*i.e.,* the gravitational and centrifugal force) apart from the pressure forces. Upon integrating this term under a constant λ provides us with the post-Newtonian effective potential in SR limit as follows,

$$\Phi_{\rm SR} = \frac{\lambda^2}{2\,r^2} - \frac{GM_*}{r}\Big[1 + \frac{4}{3\,c^2}\Big(\frac{\lambda^2}{r^2} - \frac{s_{\rm J}\,\lambda}{r^2}\Big)\Big]. \quad (5.42)$$

Next, the azimuthal momentum Eq. (5.32) boils down to

$$\partial_r \lambda = -\frac{1}{c^2}\Big[\frac{GM_*}{r^2}(s_{\rm J} - \lambda) + \frac{\lambda^3}{r^3}\Big]. \quad (5.43)$$

Finally, in the SR limit vertical component of the Euler equation becomes

$$\partial_z p_{\rm gas} = -\frac{GM_*\rho}{r^3} z\Big[1 + \frac{1}{c^2}\Big(\Pi + \frac{p_{\rm gas}}{\rho} + \frac{2\,\lambda^2}{r^2} - \frac{6\,s_{\rm J}\,\lambda}{r^2}\Big)\Big]. \quad (5.44)$$

To derive the above relation, we follow the scheme introduced by Kato et al. (2008) and use the fact that pressure is zero on the surface of the disk. Hence, using Eq. (5.44), the half-thickness of the SR disk is given by

$$H_{\rm SR} = \frac{1}{\Omega_{\rm K}}\sqrt{\frac{p_{\rm gas}}{\rho}}\Big[1 - \frac{1}{2\,c^2}\Big(\Pi + \frac{p_{\rm gas}}{\rho} + \frac{2\,\lambda^2}{r^2} - \frac{6\,s_{\rm J}\,\lambda}{r^2}\Big)\Big], \quad (5.45)$$

where $\Omega_{\rm K}$ $(= \sqrt{\frac{GM_*}{r^3}})$ is the Keplerian angular velocity. Imposing the condition (5.40) on Eq. (5.24), we have

$$4\pi H_{\rm SR}\, r\rho v\Big[1 + \frac{1}{c^2}\frac{GM_*}{r}\Big] = -\dot{M}_{\rm SR}. \quad (5.46)$$

Meanwhile, in the SR limit, the post-Newtonian EoS (5.35) reduces to

$$p_{\rm gas} = C_{\rm s}^2\frac{\rho}{\Gamma}\Big[1 + \frac{\Gamma}{c^2}\Big(\frac{3\,GM_*}{r} + \frac{\lambda^2}{2\,r^2}\Big)\Big]. \quad (5.47)$$

To obtain an accretion solution, we need to evaluate the dynamical equations corresponding to the flow velocity v, sound speed $C_{\rm s}$, and specific angular momentum of the flow λ, respectively. After some simplifications, we obtain the radial velocity gradient (or wind equation) as

$$\frac{dv}{dr}|_{\rm SR} = \frac{N_{\rm SR}(r, v, C_{\rm s}, \lambda, s_{\rm J})}{D_{\rm SR}(r, v, C_{\rm s}, \lambda, s_{\rm J})}, \tag{5.48}$$

and the temperature gradient equation as

$$\frac{dC_{\rm s}}{dr} = C_{0_{\rm SR}} + C_{v_{\rm SR}} \frac{dv}{dr}. \tag{5.49}$$

The explicit form of $N_{\rm SR}$, $D_{\rm SR}$, $C_{0_{\rm SR}}$, and $C_{v_{\rm SR}}$ are given in Appendix D.3.1. In Sec. 5.4.4, we present the global accretion solutions obtained from these equations.

5.4.2 Semi-Newtonian fluid

In this case, it is assumed that the pressure and internal energy of the fluid are not relativistic. Hence, in addition to the radial velocity, these quantities do not exceed the non-relativistic limit. We then impose the following conditions

$$\frac{p_{\rm gas}}{\rho c^2} \sim \frac{\Pi}{c^2} \sim \frac{v^2}{c^2} \sim \epsilon, \tag{5.50}$$

where $\epsilon \to 0$. This is the semi-Newtonian (SN) regime. Under this approximation, the matter distribution is allowed to move rapidly in the ϕ direction. The hydrodynamic equations governing the SN fluid are given below.

The radial structure is given by

$$v\partial_r v = \frac{\lambda^2}{r^3} - \frac{1}{\rho}\partial_r p_{\rm gas} - \frac{GM_*}{r^2}\Big[1 + \frac{4}{c^2}\Big(\frac{\lambda^2}{r^2} - \frac{s_{\rm J}\,\lambda}{r^2}\Big)\Big]. \tag{5.51}$$

We find that the azimuthal Euler equation is not affected by the SN conditions (5.50) and remains the same as in Eq. (5.43). Moreover, for the vertical structure, we have

$$\partial_z p_{\rm gas} = -\frac{GM_*\rho}{r^3} z\Big[1 + \frac{2}{c^2}\Big(\frac{\lambda^2}{r^2} - \frac{3\,s_{\rm J}\,\lambda}{r^2}\Big)\Big]. \tag{5.52}$$

So, the half-thickness of the SN disk is given by

$$H_{\rm SN} = \frac{1}{\Omega_{\rm K}}\sqrt{\frac{p_{\rm gas}}{\rho}}\Big[1-\frac{1}{c^2}\Big(\frac{\lambda^2}{r^2}-\frac{3\,s_{\rm J}\,\lambda}{r^2}\Big)\Big]. \tag{5.53}$$

Also, for this system, the mass conservation is obtained as,

$$4\pi H_{\rm SN}\, r\rho v\Big[1+\frac{1}{c^2}\frac{GM_*}{r}\Big] = -\dot{M}_{\rm SN}. \tag{5.54}$$

In the semi-Newtonian limit, the EoS is the same as in the SR case. Further, comparing Eqs. (5.41) and (5.51), we have, $\Phi_{\rm SN} \equiv \Phi_{\rm SR}$ (Eq. 5.42). Moreover, using Eqs. (5.34), (5.35), (5.43), (5.51), and (5.54), we obtain the wind equation and the temperature gradient as,

$$\frac{dv}{dr}|_{\rm SN} = \frac{N_{\rm SN}(r,v,C_{\rm s},\lambda,s_{\rm J})}{D_{\rm SN}(r,v,C_{\rm s},\lambda,s_{\rm J})}, \tag{5.55}$$

and

$$\frac{dC_{\rm s}}{dr} = C_{0_{\rm SN}} + C_{V_{\rm SN}}\frac{dV}{dr}. \tag{5.56}$$

The explicit form of $N_{\rm SN}, D_{\rm SN}, C_{0_{\rm SN}}, C_{V_{\rm SN}}$ are given in Appendix D.3.2.

5.4.3 Non-relativistic fluid

For this case, we ignore the following post-Newtonian corrections (setting $\epsilon \to 0$) as

$$\frac{p_{\rm gas}}{\rho c^2} \sim \frac{\Pi}{c^2} \sim \frac{v^2}{c^2} \sim \frac{v_\phi^2}{c^2} \sim \epsilon. \tag{5.57}$$

With this assumption, we consider that the fluid system is non-relativistic (NR). However, we keep post-Newtonian corrections associated with the metric of the spinning body. So, this NR system is indeed embedded in the background post-Newtonian space-time.

In the classical picture of the standard accretion disk (Shakura & Sunyaev, 1973), in the absence of pressure as well as friction (viscosity), the centrifugal force is balanced by the

gravitational force. So, for a Keplerian fluid around a body with mass M_*, we have

$$\lambda_{\rm Kep}^2 = GM_* r. \tag{5.58}$$

On the other hand, we choose the leading order post-Newtonian corrections related to the central body and keep terms like $\frac{GM_*}{c^2 r}$ in the equations of motion. Since we assume a low angular momentum ($\lambda \ll \lambda_{\rm Kep}$) accretion flow, the ratio $\frac{\lambda^2}{r^2 c^2}$ remains small throughout the disk.

Furthermore, in the post-Newtonian description, we consider that the space-time deviates from the flat space-time and apply $\frac{GM_*}{c^2 r} \ll 1$. For an extreme Kerr black hole with $s_{\rm J} = \frac{GM_*}{c}$, the post-Newtonian term $\frac{s_{\rm J}\lambda}{c^2 r^2}$ related to the general relativistic effect of the black hole spin, is much smaller than the term $\frac{GM_*}{c^2 r}$ related the general relativistic effect of the black hole mass. Therefore, in the following calculations, in addition to the mentioned terms, we consider that

$$\frac{s_{\rm J}\,\lambda}{c^2 r^2} \sim \epsilon, \tag{5.59}$$

where $\epsilon \to 0$.

Applying the above restrictions, we obtain the NR equations of motion. The first one is the radial structure which reduces to the Newtonian case

$$v\partial_r v = \frac{\lambda^2}{r^3} - \frac{1}{\rho}\partial_r p_{\rm gas} - \frac{GM_*}{r^2}. \tag{5.60}$$

From the above Eq. (5.60), we can easily identify the Newtonian effective potential as $\Phi_{\rm eff}^{\rm N} = -\frac{GM_*}{r} + \frac{\lambda^2}{2r^2}$.

By imposing the conditions (5.57) and (5.59), the angular momentum equation (5.32) boils down $\partial_r \lambda = 0$, *i.e.,* the constant λ case. Moreover, the vertical structure and the mass conservation are described by

$$\partial_z p_{\rm gas} = -\rho \frac{GM_*}{r^3} z, \tag{5.61}$$

and

$$4\pi H_{\rm NR}\rho r V\Big(1+\frac{GM_*}{c^2\,r}\Big)=-\dot{M}_{\rm NR}, \tag{5.62}$$

respectively. Here, $H_{\rm NR}$ is the half-thickness of the NR disk, which is obtained from Eq. (5.61) as follows:

$$H_{\rm NR}=\frac{1}{\Omega_{\rm K}}\sqrt{\frac{p_{\rm gas}}{\rho}}. \tag{5.63}$$

Further, the EoS is expressed as

$$p_{\rm gas}=C_{\rm s}^2\frac{\rho}{\Gamma}\Big[1+\frac{\Gamma}{c^2}\frac{3\,GM_*}{r}\Big]. \tag{5.64}$$

Finally, we evaluate the wind equation as

$$\frac{dV}{dr}|_{\rm NR}=\frac{N_{\rm NR}(r,V,C_{\rm s},\lambda,s_{\rm J})}{D_{\rm NR}(r,V,C_{\rm s},\lambda,s_{\rm J})}, \tag{5.65}$$

and

$$\frac{dC_{\rm s}}{dr}=C_{0_{\rm NR}}+C_{V_{\rm NR}}\frac{dV}{dr}, \tag{5.66}$$

where the coefficients $N_{\rm NR}, D_{\rm NR}, C_{0_{\rm NR}}, C_{V_{\rm NR}}$ are mentioned in detail in Appendix D.3.3.

In order to express the flow variables, we use a unit system as $G=M_*=c=1$. Hence, the units of the radial coordinate, velocity, angular momentum, and effective potential are measured in units of $r_{\rm g}$, c, $r_{\rm g}\,c$, and c^2, respectively. Before introducing the accretion solutions in the post-Newtonian framework, we discuss the effective potentials.

Using the above choice of the unit system, we rewrite the post-Newtonian effective potential (5.42) as follows,

$$\Phi_{\rm eff}^{\rm PN}=\frac{\lambda^2}{2\,r^2}-\frac{1}{r}\Big[1+\frac{4}{3}\Big(\frac{\lambda^2}{r^2}-\frac{s_{\rm J}\lambda}{r^2}\Big)\Big]. \tag{5.67}$$

This relation indicates that the relativistic part of the effective potential is a function of r^{-3}, while the standard one is a function of r^{-1} and r^{-2}. As the radius decreases, this correction grows faster. However, at each radius, the value of this correction should not

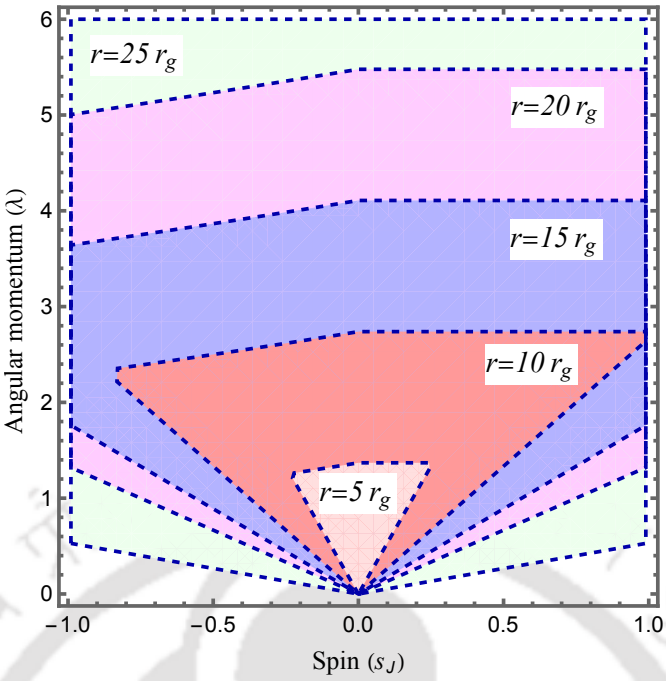

FIGURE 5.1: The $s_{\rm J} - \lambda$ parameter space in the post-Newtonian framework. Each region shows the allowed values of the spin parameter and the dimensionless angular momentum at a specific radius. For the values beyond the specified boundaries, the post-Newtonian approximation is not reliable for that specific radius, while it still works at outer radii. For instance, for $\lambda \gtrsim 4$, one can study the accretion disk at $r \gtrsim 15\, r_{\rm g}$ in the post-Newtonian gravity.

exceed the Newtonian term, and the ratio of corrections to the standard term should be very small. We assume this ratio is at most of the order 10^{-1}. The allowed $s_{\rm J} - \lambda$ parameter space in which the above condition is satisfied is shown in Fig. 5.1. As the inner radius is reduced, the allowed region shrinks. Here, we consider $-1 \leq s_{\rm J} \leq 1$ for the spin parameter. The lower (upper) limit corresponds to the maximally rotating retrograde (prograde) black hole with an accretion disk.

Given this parameter space, we examine the behavior of $\Phi_{\rm eff}^{\rm PN} (\equiv \Phi_{\rm SR} = \Phi_{\rm SN})$ and compare it with the exact GR and the Newtonian cases (see Fig. 5.2). The Newtonian effective potential is

$$\Phi_{\rm eff}^{\rm N} = \frac{\lambda^2}{2\, r^2} - \frac{1}{r}, \tag{5.68}$$

and the effective potential around Kerr BH (Dihingia et al., 2018a) is given as

$$\Phi_{\rm eff}^{\rm GR} = \frac{1}{2} \ln \left[\frac{r(r^2 + a_{\rm k}^2 - 2r)}{a_{\rm k}^2 (r+2) - 4 a_{\rm k} \lambda + r^3 - \lambda^2 (r-2)} \right]. \tag{5.69}$$

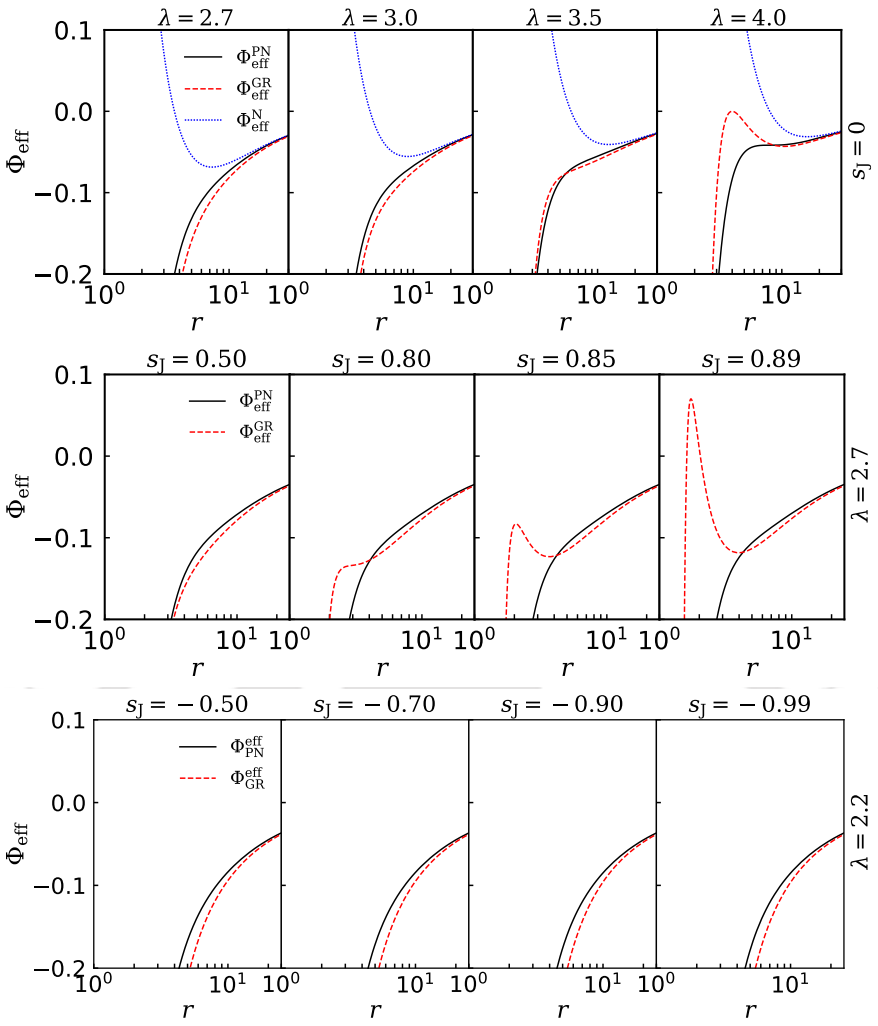

FIGURE 5.2: Comparison of effective potentials ($\Phi_{\rm eff}$): Post-Newtonian ($\Phi^{\rm PN}_{\rm eff}$), general-relativistic ($\Phi^{\rm GR}_{\rm eff}$) and Newtonian ($\Phi^{\rm N}_{\rm eff}$), as a function of logarithmic radial distance (r) for different λ and $s_{\rm J}$ is presented here. In the upper panel, we fix spin parameter $s_{\rm J} = 0$ and vary the constant angular momentum as $\lambda = 2.7, 3.0, 3.5, 4.0$, respectively. Here, solid, dashed, and dotted curves correspond to post-Newtonian, GR, and Newtonian cases. In the middle panel, $\Phi^{\rm PN}_{\rm eff}$ and $\Phi^{\rm GR}_{\rm eff}$ are plotted for a fixed $\lambda = 2.7$, and the spin parameter is only varied here $s_{\rm J} = 0.50, 0.80, 0.85$, and 0.89. Finally, in the lower panel, we repeat the above exercise for the retrograde spin as the middle panel, only the spin orientation is taken as opposite as, $s_{\rm J} = -0.50, -0.70, -0.90, -0.99$ and $\lambda = 2.2$.

Note that, the spin parameter $a_{\rm k}$ introduced in Chapters 2 and 3 is equivalent to $s_{\rm J}$.

In the next, we plot the effective potentials corresponding to the Newtonian ($\Phi^{\rm N}_{\rm eff}$), post-Newtonian ($\Phi^{\rm PN}_{\rm eff}$), and general relativistic ($\Phi^{\rm GR}_{\rm eff}$) regimes around a compact object. To begin with, in the upper panels of Fig. 5.2, we fix the spin $s_{\rm J} = 0$ and vary the angular momentum λ as 2.7, 3.0, 3.5 and 4.0, respectively. In all these cases, we notice that $\Phi^{\rm PN}_{\rm eff}$ remains sandwiched between $\Phi^{\rm N}_{\rm eff}$ and $\Phi^{\rm GR}_{\rm eff}$. Note that these three potentials converge beyond $r \geq 30 r_{\rm g}$. However, as we approach inwards, the Newtonian potential

starts to deviate from the GR one, although the PN potential continues to mimic the general relativistic potential even beyond the post-Newtonian radius, $r \leq r_{\rm PN}$. This is reminiscent of the "unreasonable" effectiveness of post-Newtonian approximation reported in gravitational wave physics (Will, 2011). Furthermore, we repeat the analysis for the spinning compact object (see middle panels of Fig. 5.2) with $s_{\rm J} = 0.50, 0.80, 0.85$ and 0.89, respectively. Here, we choose $\lambda = 2.7$. For all the spin values, we observe that $\Phi_{\rm eff}^{\rm PN}$ mimics the GR potential even at $r \sim 5r_{\rm g}$. Finally, in the lower panels of Fig. 5.2, we examine the behaviour of effective potentials around a compact object with spin angular momentum opposite to the direction of the flow angular momentum ($s_{\rm J} < 0$). Here, we choose $\lambda = 2.2$ and vary the spin as $s_{\rm J} = -0.50, -0.70, -0.90$ and -0.99, respectively. Overall, we point out that the post-Newtonian potential closely approximates the general relativity potential even beyond the post-Newtonian zone ($r_{\rm PN} \leqslant r \leqslant r_{\infty}$).

5.4.4 Global accretion solutions

In order to determine a global transonic solution for the steady, thin, axisymmetric, low angular momentum accretion flow in the post-Newtonian space-time near a spinning compact object, we solve a set of coupled differential equations (such as the wind equation, angular momentum equation, and temperature gradient equation). In doing so, we follow the critical point analysis from the section 2.2.1. It is worth mentioning that we are interested in the accretion solutions passing through the outer saddle type critical point, as the present post-Newtonian regime is valid outside $10\,r_{\rm g}$ (see Sec. 5.1 for details).

In Fig. 5.3, we present a family of global accretion solutions in SR regime, where Mach number ($M = v/C_{\rm s}$) is plotted as a function of logarithmic radial distance (r) for various input parameters ($r_{\rm c}, s_{\rm J}, \lambda_c$). To begin with, we choose the input flow parameters as $(r_{\rm c}, s_{\rm J}, \lambda_{\rm c}) = (200, 0, 0)$ and solve equations describing the critical point conditions $N_{\rm SR} = D_{\rm SR} = 0$. Thereafter, we calculate the dv/dr at $r_{\rm c}$ and integrate Eqs. (5.43), (5.48), and (5.49) for the flow variables $(v, C_{\rm s}, \lambda)$ both towards the compact object and away ($r_{\rm c} \leq r \leq r_{\rm edge}$[5]) from the compact object. For the given set of input parameters, the flow smoothly connects the post-Newtonian radius ($r_{\rm PN}$) with the $r_{\rm edge}$. This particular

[5]Here, $r_{\rm edge}(= 1000r_{\rm g})$ is the outer edge of the accretion disk.

case, where $\lambda = 0$, is known as the 'Bondi-type' solution (Bondi, 1952; Michel, 1972; Patra et al., 2022). A recent study also showcased the spherically symmetric accretion in the post-Newtonian limit (Kremer & Mehret, 2021).

As pointed out in Fig. 5.2, the effective post-Newtonian potential mimics the GR potential even beyond the post-Newtonian radius ($r < r_{\rm PN}$), encouraging us to explore the accretion solutions in this region. We find that Mach number monotonically increases in this regime, which is similar to the GR case (see Fig. 2.2a). Next, we increase $\lambda_{\rm c} = 2.50$ and find an open type global accretion solution like the previous one (see Fig. 5.3b). As we increase $\lambda_{\rm c}$ to 3.00, the inflowing matter entering from the outer edge just touches the $r_{\rm PN}$ but becomes the closed type solution. Further, at a higher $\lambda_{\rm c} = 3.50$, the solution fails to reach the post-Newtonian radius (Fig. 5.3c,d). These closed solutions are of limited physical importance as they fail to reach near to the compact object.

In the middle panels, we plot the radial profile of Mach number (M) for the maximally spinning case, $s_{\rm J} = 0.99$, and keep $\lambda_{\rm c} = 1.90$ in all the panels (e-h). Here, we vary the location of the outer critical point as $r_{\rm c} = 80, 100, 150$ and 200, respectively. For first two cases, we obtain accretion solutions that are closed in nature, however, the flow reaches up to $r_{\rm PN}$. Although the accretion solutions remain closed type, we find that the wind branch reaches smoothly up to the inner edge, and these kinds of solutions are reported earlier by Das & Chakrabarti (2004) for the case of black holes. Interestingly, as we increase $r_{\rm c}$ beyond 150, we get open type global transonic solutions that connect the inner edge of the disk with the $r_{\rm edge}$. Finally, in the lower panels (i-l), we plot the accretion solutions for the retrograde case, *i.e.*, $s_{\rm J} = -0.99$. In all cases, we fix $\lambda_{\rm c} = 1.90$, and the critical point location is varied as in the middle panels. For each of the panels, we get open type global transonic accretion solutions.

In the next, we compare the accretion solutions among the SR, SN, and NR cases in Fig. 5.4. Note that, for NR approximation, λ is a constant and the spin ($s_{\rm J}$) vanishes. We therefore choose $(r_{\rm c}, s_{\rm J}, \lambda_{\rm c}) = (200, 0, 1.90)$ in the left panel. We find that SR and SN results match closely all over the radius, but the NR one deviates from the other two around $r \sim 30$. In the right panel, we include the maximally spinning case $s_{\rm J} = 0.99$, keeping other parameters fixed. We notice similar behavior in SR and SN

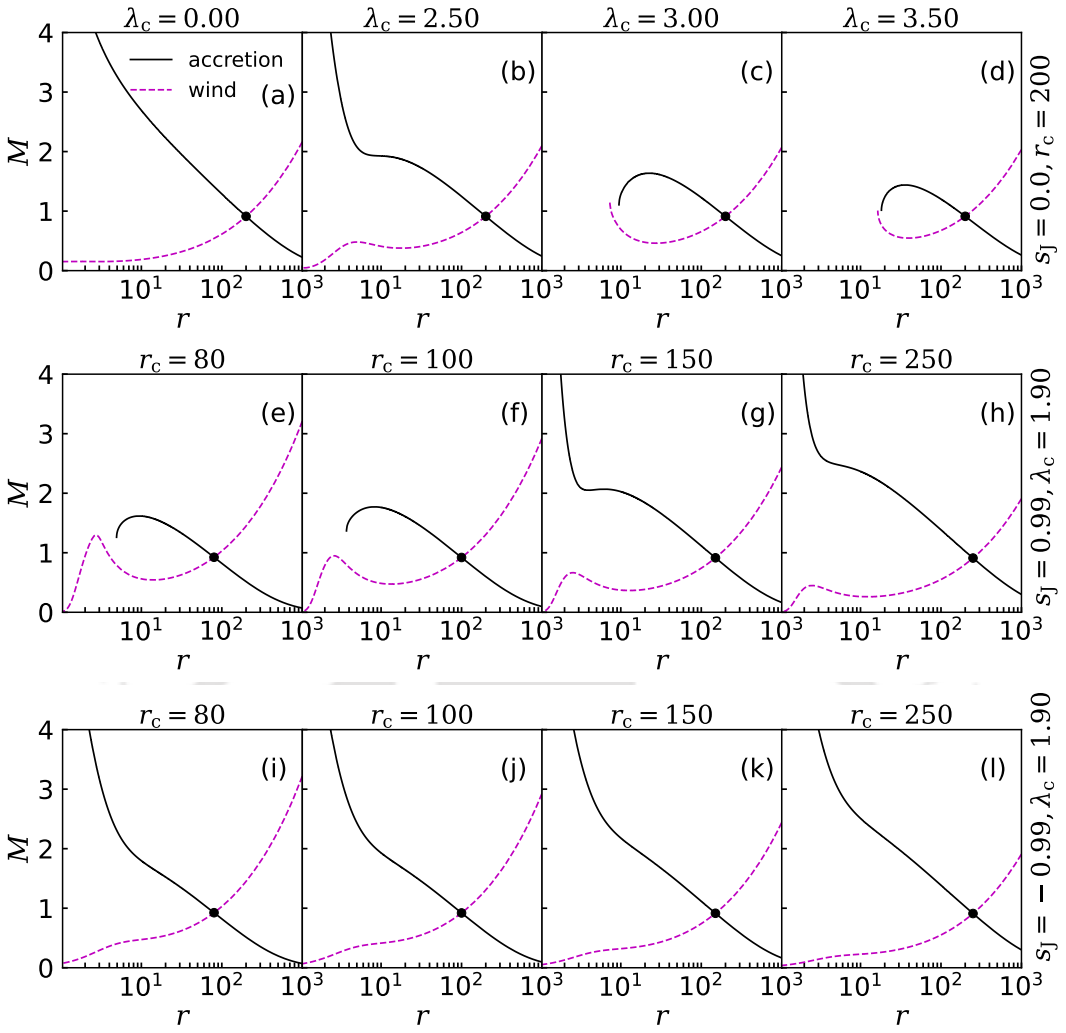

FIGURE 5.3: Upper panel: Mach number ($M = v/C_s$) for the semi-relativistic (SR) fluid is plotted as a function of radial distance for $s_J = 0$ in the post-Newtonian framework. Here, we fix the outer critical point (r_c) at 200, and the angular momentum at the critical point (λ_c) is only varied as $\lambda_c = 0$ (Bondi-type), 2.50, 3.00, and 3.50, respectively. Lower panel: Here, we fix the spin of the compact object as $s_J = 0.99$ and vary the critical point location as $r_c = 80, 100, 150,$ and 250. Note the solid curve corresponds to accretion solutions, whereas the dashed curves represent wind solutions, and the filled circle corresponds to the critical point location.

results. Interestingly, we find the low angular momentum accretion solutions in the NR limit fail to provide an open type solution for any choice of input parameters. This fact also illustrates the importance of the post-Newtonian corrections. Further, in Fig. 5.5, we explore the variation of the flow variables, namely (a) flow velocity v, (b) the mass-density ρ, (c) temperature $T\,(= \frac{2m_p C_s^2}{k_B} c^2)$ [6], and (d) flow angular momentum λ, for the SR and SN cases. In doing so, we choose the spin of the compact body as $s_J = 0.99$ and angular momentum at critical point as $\lambda_c = 1.90$. Here, r_c is kept at 200 (same

[6]Here, m_p is the proton mass and k_B is the Boltzmann's constant.

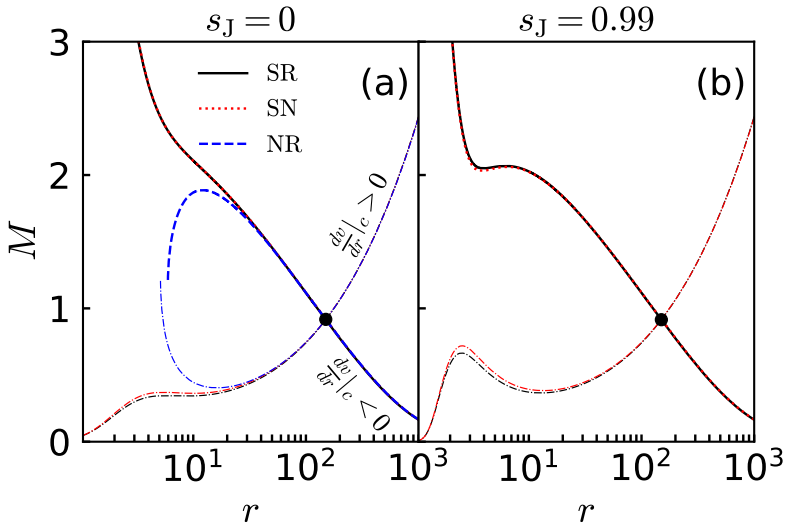

FIGURE 5.4: Comparison of accretion for SR (solid), SN (dotted), and NR (dashed) cases, respectively. We fix the spin $s_J = 0$ in the left panel, whereas the right panel corresponds to $s_J = 0.99$. In both panels, $r_c = 200$ and $\lambda_c = 1.90$ are kept fixed. Here, $\frac{dv}{dr}|_c < 0$ branch refers to the accretion solution (solid curves), whereas $\frac{dv}{dr}|_c > 0$ (dot-dashed curves) represents the wind branch. The gray-shaded region represents $r < r_{PN}$.

as in the right panel of Fig. 5.4). We observe that the subsonic accretion flow from the outer edge of the disk ($r_{edge} = 1000$) eventually gains its radial velocity as it moves inwards and makes a smooth transition to become supersonic at the outer critical point ($r_c = 200$) before falling into the central body. Next, we depict the density profile of the converging flow in Fig. 5.5b, where a gradual increase of density is observed with decreasing r. This happens mainly due to the geometric compression of infalling matter, and as a consequence, the temperature of the flow is increased with the decrease of radial distance, as shown in panel (c).

We notice the disk temperature reaches $T \gtrsim 6.5 \times 10^{11}$ K within the post-Newtonian regime, r_{PN}. It is noteworthy that the density profile follows the same power-law distribution $\rho \propto r^{-3/2}$ as in the self-similar limit, whereas the temperature profile follows a shallower one $T \propto r^{-1/3}$. However, for the global accretion solutions in GR, flow temperature varies as $T \propto r^{-3/4}$. Further, in panel (d), we depict the radial profile of flow angular momentum. It shows a slowly decreasing behavior up to r_{PN}. This can be due to the presence of the spin-orbit coupling in the governing post-Newtonian equations. This feature was not reported earlier in the post-Newtonian accretion.

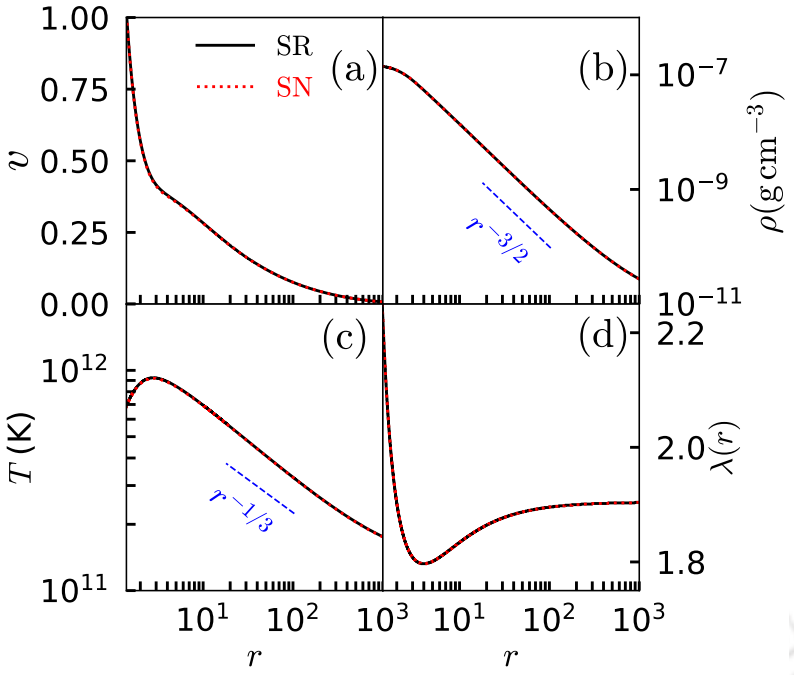

FIGURE 5.5: A comparative study of the flow variables, namely the velocity (v), mass-density (ρ), temperature (T), and the angular momentum (λ) for the set of solutions obtained in Fig. 5.4b are plotted as a function of radial coordinate (r). Here, the gray-shaded region ($r < r_{\rm PN}$) is beyond the scope of the post-Newtonian framework. Note that we depict only the accretion solutions, not the wind, as per the point of interest.

5.5 Astrophysical Importance

The inflowing matter not only loses its angular momentum while falling onto the compact object but also releases a significant amount of flow energy to reach the compact body. In order to examine the contribution of 1PN , we retain the terms comprising with c and G, M_*. In doing so, we consider the local potential energy released during the accretion from r to $r-\Delta r$ in the vicinity of the central object following $\Phi^{\rm PN} = -\frac{GM_*}{r}\Big[1+\frac{4}{3\,c^2}\Big(\frac{\lambda^2}{r^2}-\frac{s_{\rm J}\,\lambda}{r^2}\Big)\Big]$ (Eq. 5.42). Following Kato et al. (2008), we have

$$\begin{aligned}\Delta L^{\rm PN}_{\rm pot} &= \Big(\Phi^{\rm PN}(r)-\Phi^{\rm PN}(r-\Delta r)\Big)\dot{M}\\ &\simeq \frac{GM_*\,\dot{M}}{r^2}\Big[1+\frac{4}{c^2}\Big(\frac{\lambda^2}{r^2}-\frac{s_{\rm J}\,\lambda}{r^2}\Big)\Big]\Delta r. \end{aligned} \tag{5.70}$$

Crudely, half of the potential energy $\Delta L^{\rm PN}_{\rm pot}$ is expected to be radiated away. Therefore, the local radiation energy is obtained as

$$\Delta L^{\rm PN}_{\rm rad} \simeq \frac{GM_*\,\dot{M}}{2\,r^2}\Big[1+\frac{4}{c^2}\Big(\frac{\lambda^2}{r^2}-\frac{s_{\rm J}\,\lambda}{r^2}\Big)\Big]\Delta r. \tag{5.71}$$

Consequently, the disk luminosity is computed for a fixed λ is expressed as

$$L_{\rm d} = \int_{r_{\rm PN}}^{\infty} \frac{GM_* \dot{M}}{2\,r^2}\Big[1+\frac{4}{c^2}\Big(\frac{\lambda^2}{r^2}-\frac{s_{\rm J}\,\lambda}{r^2}\Big)\Big]dr$$
$$= \frac{GM_* \dot{M}}{2\,r_{\rm PN}}\Big[1+\frac{4}{3\,c^2\,r_{\rm PN}^2}\Big(\lambda^2-s_{\rm J}\,\lambda\Big)\Big]. \tag{5.72}$$

It is obvious that the post-Newtonian corrections that depend on $s_{\rm J}$ and λ, affect the luminosity of the disk. The negative (positive) term $(\lambda^2 - s_{\rm J}\,\lambda)$ results in a dimmer (brighter) disk.

Considering $\Delta L_{\rm rad}^{\rm PN} = 2\,\pi\,r\,\Delta r(2\,F_0)$, the flux F_0 is obtained from Eq. (5.71) in the leading order post-Newtonian correction as,

$$F_0 = \frac{GM_* \dot{M}}{8\,\pi\,r^3}\Big[1+\frac{4}{c^2\,r^2}\Big(\lambda^2-s_{\rm J}\,\lambda\Big)\Big]. \tag{5.73}$$

Note that the local flux from standard disks varies as $1/r^3$ (Page & Thorne, 1974; Kato et al., 2008), while the 1PN correction contributes as $1/r^5$.

5.6 Chapter Conclusions

In this Chapter, we have shown the behavior of global transonic accretion solutions in the post-Newtonian framework up to the first post-Newtonian (1PN) order around a spinning compact body. We have obtained the explicit relativistic hydrodynamic equations that allow us to study accretion disks around rotating objects without imposing any symmetries up to the 1PN order. The aim is to bridge the gap between the Newtonian framework to exact GR solutions around rotating space-time. Indeed, this is important as the Newtonian or pseudo-Newtonian approach works well around the non-rotating compact bodies. In doing so, we have considered the disk to be confined on the mid-plane (*i.e.,* $\theta = \pi/2$), and axisymmetry has been taken into account. The equations (5.21) and (5.22) describe the fluid motion around a spinning compact body in the post-Newtonian gravity where several relativistic corrections to the Newtonian equations play a crucial role. Among them, an interesting relativistic correction to the hydrodynamic equations has been obtained here, such as the spin-orbit interaction. This effect is not present

in Newtonian gravity. Further, we have explored the transonic accretion solutions by analyzing three case studies: Semi-relativistic (SR), Semi-Newtonian (SN) and Non-relativistic (NR) regimes in the steady state limit ($\partial/\partial t \to 0$). Our findings are as follows:

- We compute the range of flow angular momentum (λ) for the allowed range of spin ($s_{\rm J}$) values (see Fig. 5.1), which bounds us to choose the appropriate λ from the region of interest, *i.e.,* $r > r_{\rm PN}$. With the suitable choice of λ, we compare the effective potentials among the Newtonian, post-Newtonian, and GR cases. We notice from Fig. 5.2 that the post-Newtonian potential tends to follow the exact GR from infinity up to $r_{\rm PN}$ while the Newtonian potential starts to deviate from the relativistic cases around $r \sim 30 r_{\rm g}$. This indicates that compared to the Newtonian analysis, the relativistic corrections considered in the post-Newtonian gravity provide a more realistic description. To investigate a system at inner radii, *i.e.,* $r < r_{\rm PN}$, one needs to take into account the exact relativistic corrections and apply the Kerr metric. This is indeed one of the main shortcomings of the post-Newtonian approximation. Furthermore, to improve the measurements in the post-Newtonian zone, *i.e.,* $r_{\rm PN} \leqslant r \leqslant r_{\infty}$, we need to consider higher order corrections and utilize the post-Newtonian expansion of the metric containing at least the $2_{\rm PN}$ corrections which is non-trivial.

- We obtain a complete set of global transonic accretion solutions for the first time for a rotating compact object in the post-Newtonian framework (see Fig. 5.3). Excellent agreement is noticed from both SR and SN limits (see Fig. 5.4). However, the NR (Newtonian) limit fails to provide an open type solution. This fact illustrates the importance of the post-Newtonian corrections. It may be noticed that as indicated in Fig. 5.4, these global transonic accretion solutions obtained in the post-Newtonian gravity are not reliable at the inner radii, and the exact GR needs to be applied. In fact, the post-Newtonian framework fails to harbor shock waves, which are commonly observed in the GR context.

- We observe that the density profile follows the self-similar ADAF limit, *i.e.,* $\rho \propto r^{-3/2}$ (Narayan & Yi, 1994). However, the temperature profile is shallower ($T \propto$

$r^{-1/3}$) than the general relativistic (GR) profiles $T \propto r^{-3/4}$. Fig. 5.5a exhibits the radial velocity v of a fluid element in terms of radius. As shown, it grows with decreasing r and reaches relativistic values close to the compact body. This is where the post-Newtonian approximation fails. We also notice the radial variation in the angular momentum profile (see Fig. 5.5d) even in the absence of any viscosity and magnetic fields. This effect appears purely due to the 1PN corrections.

With all the above findings, we wish to emphasize that the post-Newtonian hydrodynamics successfully mimic the exact solutions up to $r \sim r_{\rm PN}$. Indeed, it was expected that the post-Newtonian accretion solutions closely obey the relativistic one where Newtonian result fails. This indicates that post-Newtonian formalism is a potential alternative to the GR solutions in regions away from the central object over the Newtonian or pseudo-Newtonian descriptions.

Chapter 6

Thesis Conclusions & Future Directions

6.1 Summary of the Thesis

Semi-analytical modelling of transonic accretion flows is the backbone for understanding the plasma dynamics around compact objects due to its ability to connect distant matter to the central object, adopting several physical processes. Considering this, the present thesis aims to explore the low angular momentum advective accretion flows around BHs, addressing various astrophysical scenarios. In the first half of the thesis, we formulate the steady, trans-magnetosonic accretion flows using the general relativistic treatment. Eventually, we reveal the existence of shock waves in the global GRMHD accretion solutions and investigate the shock properties. However, the second part of the thesis is focused on the hydrodynamical narrative of fluid incorporating thermal conduction to explain the energy transport within the disk. Finally, we implement the advective accretion flow model in the post-Newtonian (PN) background and discuss the influence of PN corrections (upto 1PN order) on the global transonic accretion solutions. In the following, we broadly describe the conclusions of the work carried out in the thesis.

In Chapter 2, we begin with the magnetized advective accretion flow around a Schwarzschild BH using complete GR treatment. In such relativistic flows, the polytropic equation

of state is not suitable enough for describing the thermodynamics of the disk. Hence, we incorporate the REoS. The disk is assumed to be in vertical equilibrium and remains confined in the mid-plane. Further, we consider that radial (b^r) and toroidal (b^ϕ) magnetic fields are threading the disk mid-plane, and the field lines are *frozen in* the plasmas following ideal MHD condition. With this, we extensively study the transonic properties of GRMHD accretion flows in the steady state. The present study reveals that depending on the model parameters, *i.e.,* energy flux ($\mathcal{E}$), angular momentum flux ($\mathcal{L}$), and magnetic field strengths, the accretion solutions pass either through inner ($r_{\rm in}$) or outer ($r_{\rm out}$) critical points. We obtain, for the first time, a range of global trans-magnetosonic accretion solutions in the GRMHD flows. In this study, the interplay between b^r and b^ϕ is responsible for producing sufficient torque (*i.e.,* Maxwell's stress) that transports the angular momentum outwards. We notice that the toroidal magnetic field remains dominant over the disk and it determines the disk dynamics. Overall, the flow remains gas pressure dominated ($\beta > 1$) except in regions near the BH, where the growth of magnetic pressure ($p_{\rm mag}$) is faster relative to the gas pressure ($p_{\rm gas}$). For a non-rotating stellar-mass BH, the magnetic field strength reaches upto 10^6 G near the horizon. Notably, the accretion solutions passing through $r_{\rm in}$ are magnetically more active than the solution passing through the outer critical point. However, it is observed that accretion solutions passing through $r_{\rm in}$ often become closed type before reaching to the outer edge ($r_{\rm edge}$) of the disk. Solutions of these kinds are potentially important as they can jump to the supersonic branch via shock transition and eventually connect r_h and $r_{\rm edge}$.

With this idea, Chapter 3 demonstrates the standing, non-dissipative shock waves in GRMHD flows around a Kerr BH. In an accretion flow, shock solutions are of utmost importance due to their higher entropy content, and the post-shock corona (PSC) is responsible for producing high energy X-ray radiations. To obtain shocked GRMHD solutions, we employ relativistic MHD shock conditions (Appl & Camenzind, 1988; Takahashi et al., 2006, and references therein) and self-consistently solve the governing GRMHD equations. Here, the shock dynamics are being controlled via the radial magnetic flux (Φ), iso-rotation parameter (F), $\mathcal{E}, \mathcal{L}$, and BH spin $a_{\rm k}$. We notice that the shock properties, namely the shock location $r_{\rm sh}$, compression ratio R, and shock strength Ψ

largely depend on Φ. However, they feebly depend on F. Previously, Chakrabarti & Titarchuk (1995); Chakrabarti & Mandal (2006) revealed that $(r_{\rm sh}, R, \Psi)$ control the characteristics of the PSC, which eventually determines the different spectral states in BH-XRBs. Since Φ and F determine the shock properties, it is obvious that magnetic fields (or flux) play a major role in governing the spectral properties of BHs. Towards this, we compare flow variables (ρ, T, b^r, b^ϕ) in the pre-and-post-shock regime by means of power-law fittings around weakly as well as rapidly rotating BHs. We find that the pre-shock flow variables remain unaffected by the spin of the central BH and follow the self-similar profiles (Narayan & Yi, 1995a). However, the flow variables in the post-shock regime obey a steeper power-law index due to shock compression. Most interestingly, the toroidal field becomes more intense $b^\phi \sim 10^{7-9}$ G, near the maximally rotating BH $(M_{\rm BH} = 10 M_\odot)$ with $a_{\rm k} = 0.99$, whereas b^ϕ ranges within $\sim 10^{5-6}$ G close to the horizon of a non-rotating BH. This is purely due to the frame-dragging effect around the spinning BHs.

Furthermore, the present shock-induced GRMHD model is centrifugally supported as the shock front is pushed away from the BH when $\mathcal{L}$ is increased. We identify the shock parameter space in the $\mathcal{L} - \mathcal{E}$ plane and observe that the area under the bounded space (shock parameter space) shifts towards lower $\mathcal{L}$ with increasing $a_{\rm k}$ and Φ. Notably, the strength of magnetic flux may lead the accretion flow into two distinct astrophysical scenarios: MAD (strong magnetic flux) and SANE (weak magnetic flux). With this, we attempt to find the critical magnetic flux $\Phi^{\rm cri}$ corresponding to the shock solutions, where we observe a positive correlation between $\Phi^{\rm cri}$ and $a_{\rm k}$. However, the critical flux for shock solutions always remains within the SANE regime. This is quite obvious since MAD flows definitely need a strong poloidal magnetic field, which we ignore in this calculation.

In Chapter 4, we address the energy transport within the hot accretion flow (HAF) around a non-rotating BH. While studying, we ignore the magnetic fields and neglect the complicated general relativistic equations. Hence, we focus on the governing hydrodynamic equations (Narayan et al., 1997) using the pseudo-Newtonian potential (Paczyński & Wiita, 1980), which successfully mimics the space-time around a non-rotating BH. Moving on, the HAF models are useful in low-mass accreting systems, where the hot plasma surrounding the BH is collisionless. In such scenarios, thermal conduction shows

a significant influence on disk dynamics, resulting in energy transport within the disk. For simplicity, we choose the saturated form of thermal conduction following Cowie & McKee (1977) and obtain the global transonic accretion solutions. The present analysis suggests that the effect of thermal conduction is noticeable in the outer regions of the disk. We further estimate the physically acceptable range of $\Phi_{\rm s}$ and find that it largely depends on the model parameters, $(\varepsilon_0, \lambda_0, \alpha)$. However, the maximum value of saturated constant $\Phi_{\rm s}^{\rm max}$ obtained from the transonic solutions exceeds the $\Phi_{\rm s}^{\rm max}$ received from the self-similar approach. Thermal conduction allows the gas to become gravitationally unbound. Hence, thermal outflows are naturally produced from the unbound disk (Tanaka & Menou, 2006). In this regard, we self-consistently calculate the Bernoulli parameter (Be) for the transonic solutions and it remains positive all over the radial extent of the disk. Therefore, the present transonic model seems to be useful for studying thermal outflows as well.

It is worth mentioning that the pseudo-Newtonian approach has obvious limitations in describing the accretion process around rotating compact objects (Dihingia et al., 2018a). On the contrary, the GR hydrodynamic equations involving all physical processes are complicated to solve numerically. One of the best alternatives is, therefore, the slow motion condition and weak field limit of GR, *i.e.,* the post-Newtonian (PN) theory. With this idea, in our final working Chapter 5, we formulate the PN hydrodynamics equations upto the leading order corrections ($1_{\rm PN}$) around a spinning compact body. Considering an advective, axisymmetric, vertically integrated flow, we obtain the global transonic accretion solutions in the PN background for the first time ever. We compare the effective potentials in GR, PN and Newtonian theory, where $\Phi_{\rm eff}^{\rm PN}$ successfully mimics the GR potential even upto $r \simeq 5$. However, Newtonian gravity ($\Phi_{\rm eff}^{\rm N}$) fails to describe the spacetime inside $r \leq 30$ and for rotating spacetime, the Newtonian description may not hold. Overall, this study could bridge the gap between the Newtonian and GR descriptions of accretion flows.

Finally, Chapter 6 discusses the overall conclusions of the thesis and sheds light on the future prospects of these works.

6.2 Future prospects

Our research emphasizes the most general framework of accretion flows in a steady state, incorporating general relativity, magnetic fields, thermal conduction, and viscosity, and extending the analysis to the post-Newtonian domain. With this, we have identified numerous avenues and horizons for future exploration stemming from this thesis work.

As a starting point, we consider the flow to be threaded by the radial and toroidal magnetic fields. However, in reality, the existence of the polar component b^{θ} is essential to launch jets/outflows. This additionally requires the off-equatorial ($\theta \neq \pi/2$) study, which eventually will provide us with the complete picture of the dynamics of magnetic fields in the accretion disks. Further, to explain the dynamical evolution of the accretion disks, state-of-the-art numerical simulations are necessary (Porth et al., 2019; Davis & Tchekhovskoy, 2020; Mizuno, 2022; Dihingia & Fendt, 2024). In this regard, the semi-analytic formalism could be useful in providing a family of background seed solutions that possibly lead to more realistic outcomes. Few attempts have already been made in this direction (Olivares S. et al., 2023; Dihingia & Mizuno, 2024), which we are also going to take up soon.

In this thesis, we have shown that magnetic fields (Φ, F) determine the shock properties that eventually control the spectral states of the BH-XRBs. Based on the model parameters, we can uniquely determine various combinations of $(r_{\rm sh}, R, \Psi)$, which could be useful in studying the spectral state transitions in the XRBs. To explore the spectral states in detail, we need to self-consistently study radiative GRMHD (GRRMHD) flows with Bremsstrahlung, synchrotron, and Compton cooling mechanisms. Furthermore, we assume a strong coupling between electron and ion that allows the flow to maintain a single temperature, which is not valid near the BHs. Since in the inner parts of an advective flow, the infall time scale is much shorter than the electron-ion collision time scale. Hence, we will formulate a two-temperature accretion flow model to study the radiative GRMHD flows and study the influence of magnetic fields, shocks, and spin on the spectral signatures.

Apart from the spectral states, the modulation of PSC plays an important role in explaining the temporal properties, *i.e.,* high frequency quasi-periodic oscillations (HFQPOs) in XRBs. Several attempts have been made in the hydrodynamics framework with the shock oscillation model to constrain the BH parameters from the HFQPO data (Dihingia et al., 2019). This approach could also be implemented in the GRMHD framework to constrain the BH parameters and the magnetic fields.

Notably, there exists a temperature gradient across the shock front (*i.e.,* cool pre-shock flow and hot post-shock flow), which allows a fraction of available thermal energy to dissipate away along the disk surface. Therefore, the energy dissipated across the shock is fully accessible at the post-shock flow. A series of studies by Das et al. (2010); Sarkar & Das (2016); Sarkar et al. (2018); Das et al. (2022) showed that a part of this dissipated energy could be utilized to produce high-energy radiations in the form of gamma-rays and X-rays, whereas the rest can be used to power jets/outflows. Not only energy but also magnetic flux needs to be dissipated away from the shock front when outflows are being produced (Jacquemin-Ide et al., 2021; Scepi et al., 2024). We will be including these modifications in the shocked GRMHD calculations soon. Overall, in Chapters 2 and 3, we adopt the ideal MHD approximation as an introductory approach, although the works involving complex nonideal MHD approximations *i.e.,* resistive MHD, are more suitable, which we plan to consider for future endeavours.

In Chapter 4, we proposed a model of saturated thermal conduction, which can account for energy transport mechanisms within accretion disks. However, the inclusion of thermal conduction introduces an additional degree of freedom to the system, which is necessary for the launching of thermal outflows. As discussed previously, the presence of magnetic fields plays a crucial role in enabling such outflows. Therefore, the next step is to investigate the coupling between thermal conduction and magnetized accretion disks. Prior to this undertaking, a comprehensive two-dimensional analysis incorporating thermal conduction is required, which we intend to pursue as part of our future research agenda.

In the final part of the thesis, we introduce the post-Newtonian hydrodynamic equations upto the 1PN order and obtain the global transonic accretion solutions based on certain

assumptions. However, a detailed comparison between the GR and PN accretion solutions remains to be explored. Moreover, we plan to solve the transonic accretion solutions in the PN magnetohydrodynamics framework. Furthermore, to improve the measurements in the post-Newtonian zone, *i.e.,* $r_{\rm PN} \leqslant r \leqslant r_{\infty}$, one needs to consider higher corrections and utilize the post-Newtonian expansion of the metric containing at least the $2_{\rm PN}$ corrections.

In each of the works of our thesis, we have computed the flow variables in terms of the best-fitted power law profiles. These power-law distributions of (v, ρ, B, T) could be supplied directly into the general relativistic radiative transfer codes Dexter, 2016, (`grtrans`), Mościbrodzka & Gammie, 2018, (`ipole`), White, 2022, (`blacklight`) as inputs, and the intensity distribution of the disk, the polarization patterns can be generated. Although the existing GRMHD codes support this integration/pipeline, incorporating our semi-analytic solutions into these ray-tracing codes remains a promising direction for further research.

Appendix A

Appendix A

A.1 Calculation of Wind Equation

Using equation (2.18) in equations (2.11-2.14), and (2.16), we obtain,

$$R_0 + R_v\frac{dv}{dr} + R_\Theta\frac{d\Theta}{dr} + R_\lambda\frac{d\lambda}{dr} + R_{b_r}\frac{db^r}{dr} + R_{b_\phi}\frac{db^\phi}{dr} = 0, \tag{A.1}$$

$$\mathcal{L}_0 + \mathcal{L}_v\frac{dv}{dr} + \mathcal{L}_\Theta\frac{d\Theta}{dr} + \mathcal{L}_\lambda\frac{d\lambda}{dr} + \mathcal{L}_{b_r}\frac{db^r}{dr} + \mathcal{L}_{b_\phi}\frac{db^\phi}{dr} = 0, \tag{A.2}$$

$$\mathcal{E}_0 + \mathcal{E}_v\frac{dv}{dr} + \mathcal{E}_\Theta\frac{d\Theta}{dr} + \mathcal{E}_\lambda\frac{d\lambda}{dr} + \mathcal{E}_{b_r}\frac{db^r}{dr} + \mathcal{E}_{b_\phi}\frac{db^\phi}{dr} = 0, \tag{A.3}$$

$$\mathcal{B}_{r_0} + \mathcal{B}_{r_v}\frac{dv}{dr} + \mathcal{B}_{r_\Theta}\frac{d\Theta}{dr} + \mathcal{B}_{r_\lambda}\frac{d\lambda}{dr} + \mathcal{B}_{r_{b_r}}\frac{db^r}{dr} + \mathcal{B}_{r_{b_\phi}}\frac{db^\phi}{dr} = 0, \tag{A.4}$$

$$\mathcal{B}_{\phi_0} + \mathcal{B}_{\phi_v}\frac{dv}{dr} + \mathcal{B}_{\phi_\Theta}\frac{d\Theta}{dr} + \mathcal{B}_{\phi_\lambda}\frac{d\lambda}{dr} + \mathcal{B}_{\phi_{b_r}}\frac{db^r}{dr} + \mathcal{B}_{\phi_{b_\phi}}\frac{db^\phi}{dr} = 0. \tag{A.5}$$

The coefficients of the equations (A.1-A.5) take the form,

$$R_0 = (R_d + \mathcal{A}R_2)/\rho h_{\rm tot}\mathcal{A}, \mathcal{A} = (g^{rr} + u^r u^r), R_2 = \frac{\mathbb{F}_1\Theta\rho}{\mathbb{F}(1+m_p/m_e)} - \frac{3\Theta\rho}{r(1+m_p/m_e)} + h_{\rm tot}\rho u^r u^r{}_0 + R_1,$$

$$R_1 = \frac{g_{tt}u_r u_{t0}b^r b^t}{u_t^2} - \frac{g_{tt}u_{r0}b^r b^t}{u_t} - \frac{\Theta\rho\Delta'}{\Delta(1+m_p/m_e)} + \frac{1}{2}b^{\phi^2}g'_{\phi\phi} + \frac{1}{2}b^{t^2}g'_{tt}, \Delta' = \frac{\partial\Delta}{\partial r}$$

$$\mathbb{F}' = \frac{d\mathbb{F}}{dr} = \mathbb{F}_1 + \mathbb{F}_2\frac{d\lambda}{dr}, \mathbb{F}_1 = \frac{\partial\mathbb{F}}{\partial r}, \mathbb{F}_2 = \frac{\partial\mathbb{F}}{\partial\lambda}, u'_\mu = u_{\mu_0} + u_{\mu_v}v' + u_{\mu_\lambda}\lambda', u^{\mu'} = u^\mu_0 + u^\mu_v v' + u^\mu_\lambda\lambda',$$

$$\mu \equiv (t, r, 0, \phi), u^\mu_0 = \frac{\partial u^\mu}{\partial r}, u^\mu_v = \frac{\partial u^\mu}{\partial v}, u^\mu_\lambda = \frac{\partial u^\mu}{\partial \lambda}, u_{\mu_0} = \frac{\partial u_\mu}{\partial r}, u_{\mu_v} = \frac{\partial u_\mu}{\partial v}, u_{\mu_\lambda} = \frac{\partial u_\mu}{\partial \lambda}.$$

$$R_d = \frac{1}{2} g'_{\phi\phi} u^\phi - {b^r}^2 \frac{1}{2} g^{\phi\phi} g'_{\phi\phi} - \rho h_{\rm tot} \frac{1}{2} g^{rr} (u^\phi)^2 g'_{\phi\phi} + (u^r)^2 \frac{1}{2} (b^\phi)^2 g'_{\phi\phi} + R_c,$$

$$R_c = \frac{1}{2} {b^\phi}^2 g^{rr} g'_{\phi\phi} - \frac{1}{2} {b^r}^2 g^{\theta\theta} g'_{\theta\theta} - \rho h_{\rm tot} u^t \frac{1}{2} g^{rr} u^t g'_{tt} + b^t {u^r}^2 \frac{1}{2} b^t g'_{tt} + R_b,$$

$$R_b = -2 u^r b^r b^t u^t \frac{1}{2} g'_{tt} - \frac{(b^r)^2}{2} + \frac{1}{2} {b^t}^2 g^{rr} g'_{tt} + \frac{1}{2} \rho h_{\rm tot} g^{rr} (u^r)^2 g'_{rr} - \frac{{b^r}^2 u^r u_r u_{t_0} g_{tt} u^t}{u_t^2} + R_a,$$

$$R_a = h_{\rm tot} \rho u^r {u^r}_0 + \frac{{b^r}^2 u^r u_{r_0} g_{tt} u^t}{u_t} - {b^r}^2 g^{rr} g'_{rr} - \frac{1}{2} {b^r}^2 g^{rr} g_{rr} {u^r}^2 g'_{rr},$$

$$R_v = \frac{R_{v0} + \mathcal{A} R_{v1}}{\mathcal{A} \rho h_{\rm tot}}, R_{v0} = \frac{{b^r}^2 u^r u_{rv} g_{tt} u^t}{u_t} - \frac{{b^r}^2 u^r u_r u_{tv} g_{tt} u^t}{u_t^2},$$

$$R_{v1} = \frac{g_{tt} u_r u_{t_\lambda} b^r b^t}{u_t^2} + \frac{\mathbb{F}_2 \Theta \rho}{\mathbb{F}(1 + m_p/m_e)} + g_{tt} b^t b^\phi, R_\Theta = \frac{1}{h_{\rm tot}(1 + m_p/m_e)},$$

$$R_\lambda = \frac{R_{\lambda 0} + R_{\lambda 1} - u^r b^r b^\phi g_{tt} u^t}{\mathcal{A} \rho h_{\rm tot}},$$

$$R_{\lambda 0} = \mathcal{A}\left(\frac{\mathbb{F}_2 \Theta \rho}{\mathbb{F}(1 + m_p/m_e)} + \frac{g_{tt} u_r u_{t\lambda} b^r b^t}{u_t^2}\right), R_{\lambda 1} = \mathcal{A} g_{tt} b^t b^\phi - \frac{{b^r}^2 u^r u_r u_{t\lambda} g_{tt} u^t}{u_t^2},$$

$$R_{b_r} = \left(R_{b_{r0}} + \frac{b^r u^r u_r g_{tt} u^t}{u_t}\right) / \rho h_{\rm tot} \mathcal{A}, R_{b_{r0}} = \mathcal{A}(g_{rr} b^r - \frac{g_{tt} u_r b^t}{u_t}) - 2 b^r - g_{rr} b^r {u^r}^2,$$

$$R_{b_\phi} = \left(R_{b_{\phi 0}} - b^r u^r \lambda g_{tt} u^t - b^r u^r g_{\phi\phi} u^\phi\right) / \rho h_{\rm tot} \mathcal{A}, R_{b_{\phi 0}} = \mathcal{A}(g_{\phi\phi} b^\phi + g_{tt} \lambda b^t),$$

$$\mathcal{L}_0 = \frac{B^2 \Delta' u_\phi}{2 \Delta \rho} - \frac{b^r \Delta' b^\phi g_{\phi\phi}}{2 \Delta \rho u^r} - \frac{2 g_{tt} u_{r_0} u_\phi b^r b^t}{\rho u_t} + \mathcal{L}_{01},$$

$$\mathcal{L}_{01} = \frac{2 g_{tt} u_r u_{t_0} u_\phi b^r b^t}{\rho u_t^2} + \frac{{b^\phi}^2 u_\phi g'_{\phi\phi}}{\rho} - \frac{3 b^r b^\phi g_{\phi\phi}}{2 \rho u^r r} + \frac{3 B^2 u_\phi}{2 \rho r} - \frac{B^2 \mathbb{F}_1 u_\phi}{2 \mathbb{F} \rho} + \mathcal{L}_{02},$$

$$\mathcal{L}_{02} = \frac{\mathbb{F}_1 b^r b^\phi g_{\phi\phi}}{2 \mathbb{F} \rho u^r} + \frac{b^r u^r {}_0 b^\phi g_{\phi\phi}}{\rho {u^r}^2} + \frac{{b^r}^2 u_\phi g'_{rr}}{\rho} + u_{\phi 0} h_{\rm tot} - \frac{b^r b^\phi g'_{\phi\phi}}{\rho u^r} + \frac{{b^t}^2 u_\phi g'_{tt}}{\rho},$$

$$\mathcal{L}_v = -\frac{2 g_{tt} u_{rv} u_\phi b^r b^t}{\rho u_t} + \mathcal{L}_{v1} + \frac{b^r u^r {}_v b^\phi g_{\phi\phi}}{\rho {u^r}^2} - \frac{b^r \left(v^2 \gamma_v^2 + 1\right) b^\phi g_{\phi\phi}}{\rho u^r v} + u_{\phi v} h_{\rm tot} + \frac{B^2 u_\phi \left(v^2 \gamma_v^2 + 1\right)}{\rho v},$$

$$\mathcal{L}_\Theta = -\frac{b^r b^\phi g_{\phi\phi}}{2 \Theta \rho u^r} + \frac{u_\phi}{(1 + m_p/m_e)} \frac{df}{d\Theta} + \frac{2 u_\phi}{(1 + m_p/m_e)} + \frac{B^2 u_\phi}{2 \Theta \rho},$$

$$\mathcal{L}_\lambda = \frac{2 g_{tt} u_\phi b^t b^\phi}{\rho} + \frac{\mathbb{F}_2 b^r b^\phi g_{\phi\phi}}{2 \mathbb{F} \rho u^r} - \frac{B^2 \mathbb{F}_2 u_\phi}{2 \mathbb{F} \rho} + \mathcal{L}_{\lambda 1} + \frac{2 g_{tt} u_r u_{t\lambda} u_\phi b^r b^t}{\rho u_t^2} + u_{\phi\lambda} h_{\rm tot},$$

$$\mathcal{L}_{b_r} = \frac{2b^r g_{rr}u_\phi}{\rho} - \frac{2b^t g_{tt}u_r u_\phi}{\rho u_t} - \frac{b^\phi g_{\phi\phi}}{\rho u^r}, \mathcal{L}_{b_\phi} = \frac{2b^\phi g_{\phi\phi}u_\phi}{\rho} - \frac{b^r g_{\phi\phi}}{\rho u^r} + \frac{2\lambda b^t g_{tt}u_\phi}{\rho},$$

$$\mathcal{E}_0 = \frac{b^r \Delta' b^t g_{tt}}{2\Delta\rho u^r} - \frac{\Delta' u_t B^2}{2\Delta\rho} - \frac{{b^t}^2 u_t g'_{tt}}{\rho} - \frac{{b^r}^2 g_{tt}u_{r_0}}{\rho u_t u^r} + \frac{{b^r}^2 g_{tt}u_r u_{t_0}}{\rho u_t^2 u^r} + \mathcal{E}_{01},$$

$$\mathcal{E}_{01} = \frac{2g_{tt}u_{r_0}b^r b^t}{\rho} - \frac{2g_{tt}u_r u_{t_0}b^r b^t}{\rho u_t} + \frac{3b^r b^t g_{tt}}{2u^r \rho r} - \frac{{b^\phi}^2 u_t g'_{\phi\phi}}{\rho} - \frac{\mathbb{F}_1 b^r b^t g_{tt}}{2u^r \mathbb{F}\rho} + \mathcal{E}_{02},$$

$$\mathcal{E}_{02} = -\frac{3u_t B^2}{2\rho r} + \frac{B^2 \mathbb{F}_1 u_t}{2\mathbb{F}\rho} - h_{\rm tot}u_{t_0} + \frac{b^r b^t g'_{tt}}{u^r \rho} - \frac{{b^r}^2 u_t g'_{rr}}{\rho} + \frac{\mathbb{F}_1 u_t\left({b^r}^2 g_{rr} + {b^t}^2 g_{tt} + {b^\phi}^2 g_{\phi\phi}\right)}{2\mathbb{F}\rho} - \frac{b^r {u^r}_0 b^t g_{tt}}{{u^r}^2 \rho},$$

$$\mathcal{E}_v = -\frac{{b^r}^2 g_{tt}u_{rv}}{\rho u^r u_t} + \frac{{b^r}^2 g_{tt}u_r u_{tv}}{\rho u^r u_t^2} + \frac{2g_{tt}u_{rv}b^r b^t}{\rho} - \frac{2g_{tt}u_r u_{tv}b^r b^t}{\rho u_t} + \mathcal{E}_{v1},$$

$$\mathcal{E}_{v1} = \frac{b^r\left(v^2\gamma_v^2+1\right)b^t g_{tt}}{\rho u^r v} - \frac{B^2 u_t\left(v^2\gamma_v^2+1\right)}{\rho v} - h_{\rm tot}u_{tv} - \frac{b^r {u^r}_v b^t g_{tt}}{\rho {u^r}^2},$$

$$\mathcal{E}_\Theta = \frac{b^r b^t g_{tt}}{2\rho\Theta u^r} - \frac{B^2 u_t}{2\rho\Theta} - \frac{u_t}{(1+m_p/m_e)}\frac{df}{d\Theta} - \frac{2u_t}{(1+m_p/m_e)},$$

$$\mathcal{E}_\lambda = \frac{g_{tt}b^r b^\phi}{\rho u^r} + \frac{{b^r}^2 g_{tt}u_r u_{t\lambda}}{\rho u^r u_t^2} - \frac{2g_{tt}u_r u_{t\lambda}b^r b^t}{\rho u_t} - \frac{2g_{tt}u_t b^t b^\phi}{\rho} + \mathcal{E}_{\lambda 1},$$

$$\mathcal{E}_{\lambda 1} = -\frac{\mathbb{F}_2 b^r b^t g_{tt}}{2\mathbb{F}u^r\rho} + \frac{B^2\mathbb{F}_2 u_t}{2\mathbb{F}\rho} - h_{\rm tot}u_{t\lambda}, \mathcal{E}_{b_r} = \frac{2b^t g_{tt}u_r}{\rho} - \frac{2b^r g_{rr}u_t}{\rho} - \frac{b^r g_{tt}u_r}{\rho u^r u_t} + \frac{b^t g_{tt}}{\rho u^r},$$

$$\mathcal{E}_{b_\phi} = \left(2b^\phi g_{\phi\phi}u_t + 2\lambda b^t g_{tt}u_t + \frac{\lambda b^r g_{tt}}{u^r}\right)/\rho,$$

$$B_{r_0} = r\left(B_{r00} - B_{r01} - B_{r02}\right), \mathcal{B}_{r00} = 2\lambda b^\phi u^r + \lambda r b^\phi {u^r}_0 - \frac{r b^r u^r u_{r_0}}{u_t} + \frac{r b^r u^r u_r u_{t_0}}{u_t^2}, B_{r_{01}} = 2b^r u^t - r b^r {u^t}_0,$$

$$B_{r_{02}} = \frac{r b^r u_r {u^r}_0}{u_t} - \frac{2b^r u^r u_r}{u_t}, \mathcal{B}_{r_v} = r\left(\lambda r b^\phi {u^r}_v - \frac{r b^r u^r u_{rv}}{u_t} + \frac{r b^r u^r u_r u_{tv}}{u_t^2} - r b^r {u^t}_v - \frac{r b^r u_r {u^r}_v}{u_t}\right),$$

$$\mathcal{B}_{r_{b_\phi}} = \lambda r^2 u^r, \mathcal{B}_{r_{b_r}} = r\left(-r u^t - \frac{r u_r u^r}{u_t}\right), \ \mathcal{B}_{r_\Theta} = 0, \ \mathcal{B}_{r_\lambda} = r\left(r b^\phi u^r + \frac{r b^r u^r u_r u_{t\lambda}}{u_t^2} - r b^r {u^t}_\lambda\right),$$

$$\mathcal{B}_{\phi_0} = r^2 b^\phi {u^r}_0 - r^2 b^r {u^\phi}_0 + 2r\left(b^\phi u^r - b^r u^\phi\right), \ \mathcal{B}_{\phi_v} = r^2 b^\phi {u^r}_v - r^2 b^r {u^\phi}_v, \ \mathcal{B}_{\phi_\Theta} = 0,$$

$$\mathcal{B}_{\phi_\lambda} = -r^2 - b^r {u^\phi}_\lambda, \ \mathcal{B}_{\phi_{b_r}} = -r^2 u^\phi, \ \mathcal{B}_{\phi_{b_\phi}} = r^2 u^r.$$

With the help of equations (A.1)-(A.5), the wind equations is expressed as,

$$\frac{dv}{dr} = \frac{\mathcal{N}(r, v, \Theta, \lambda, b^r, b^\phi)}{\mathcal{D}(r, v, \Theta, \lambda, b^r, b^\phi)} \tag{A.6}$$

where,

$$\mathcal{N}(r,v,\Theta,\lambda,b^r,b^\phi) = -\Big(R_0 + b^r_{11}R_{b_r} + R_\Theta\Theta_{11} + R_\lambda\lambda_{11} + R_{b_\phi}b^\phi_{11}\Big) \tag{A.7}$$

and

$$\mathcal{D}(r,v,\Theta,\lambda,b^r,b^\phi) = R_v + b^r_{12}R_{b_r} + R_\Theta\Theta_{12} + R_\lambda\lambda_{12} + R_{b_\phi}b^\phi_{12}. \tag{A.8}$$

Here, are the remaining coefficients of the above equations (A.7, A.8) as follows,

$$\Theta_1 = -\frac{\Theta_{c0}}{\mathbb{D}}, \Theta_2 = -\frac{\Theta_{v0}}{\mathbb{D}}, \lambda_1 = \frac{\lambda_{c0}}{\mathbb{D}}, \lambda_2 = \frac{\lambda_{v0}}{\mathbb{D}}, b^r_1 = -\frac{b^r_{c0}}{\mathbb{D}}, b^r_2 = -\frac{b^r_{v0}}{\mathbb{D}}, b^\phi_1 = -\frac{b^\phi_{c0}}{\mathbb{D}}, b^\phi_2 = -\frac{b^\phi_{v0}}{\mathbb{D}},$$

where,

$$\begin{aligned}
\mathbb{D} &= \mathcal{B}_{r_{b_\phi}}\Big(\mathcal{L}_\lambda\mathcal{E}_{b_r}\mathcal{B}_{\phi_\Theta} - \mathcal{E}_\lambda\mathcal{L}_{b_r}\mathcal{B}_{\phi_\Theta} + \mathcal{B}_{\phi_\lambda}\left(\mathcal{E}_\Theta\mathcal{L}_{b_r} - \mathcal{L}_\Theta\mathcal{E}_{b_r}\right) + \mathcal{E}_\lambda\mathcal{L}_\Theta\mathcal{B}_{\phi_{b_r}} - \mathcal{E}_\Theta\mathcal{L}_\lambda\mathcal{B}_{\phi_{b_r}}\Big)\\
&+ \mathcal{E}_\Theta\mathcal{L}_\lambda\mathcal{B}_{r_{b_r}}\mathcal{B}_{\phi_{b_\phi}} + \mathcal{L}_{b_\phi}\Big(\mathcal{E}_{b_r}\mathcal{B}_{r_\Theta}\mathcal{B}_{\phi_\lambda} - \mathcal{E}_\Theta\mathcal{B}_{r_{b_r}}\mathcal{B}_{\phi_\lambda} + \mathcal{E}_\lambda\mathcal{B}_{r_{b_r}}\mathcal{B}_{\phi_\Theta} - \mathcal{E}_\lambda\mathcal{B}_{r_\Theta}\mathcal{B}_{\phi_{b_r}}\Big)\\
&+ \mathcal{L}_\Theta\mathcal{E}_{b_\phi}\mathcal{B}_{r_{b_r}}\mathcal{B}_{\phi_\lambda} - \mathcal{L}_\lambda\mathcal{E}_{b_\phi}\mathcal{B}_{r_{b_r}}\mathcal{B}_{\phi_\Theta} - \mathcal{L}_\lambda\mathcal{E}_{b_r}\mathcal{B}_{r_\Theta}\mathcal{B}_{\phi_{b_\phi}} + \mathcal{L}_\lambda\mathcal{E}_{b_\phi}\mathcal{B}_{r_\Theta}\mathcal{B}_{\phi b_r} + \mathcal{E}_\lambda\mathcal{L}_{b_r}\mathcal{B}_{r_\Theta}\mathcal{B}_{\phi_{b_\phi}}\\
&+ \mathcal{B}_{r_\lambda}\Big(\mathcal{L}_\Theta\mathcal{E}_{b_r}\mathcal{B}_{\phi_{b_\phi}} - \mathcal{L}_\Theta\mathcal{E}_{b_\phi}\mathcal{B}_{\phi_{b_r}} - \mathcal{E}_\Theta\mathcal{L}_{b_r}\mathcal{B}_{\phi_{b_\phi}} + \mathcal{E}_\Theta\mathcal{L}_{b_\phi}\mathcal{B}_{\phi_{b_r}} + \mathcal{L}_{b_r}\mathcal{E}_{b_\phi}\mathcal{B}_{\phi_\Theta} - \mathcal{E}_{b_r}\mathcal{L}_{b_\phi}\mathcal{B}_{\phi_\Theta}\Big)\\
&- \mathcal{L}_{b_r}\mathcal{E}_{b_\phi}\mathcal{B}_{r_\Theta}\mathcal{B}_{\phi_\lambda} - \mathcal{E}_\lambda\mathcal{L}_\Theta\mathcal{B}_{r_{b_r}}\mathcal{B}_{\phi_{b_\phi}},
\end{aligned}$$

$$\begin{aligned}
\Theta_{c0} &= \mathcal{B}_{r_{b_\phi}}\Big(\mathcal{B}_{\phi_0}\mathcal{L}_\lambda\mathcal{E}_{b_r} - \mathcal{B}_{\phi_0}\mathcal{E}_\lambda\mathcal{L}_{b_r} + \mathcal{B}_{\phi_\lambda}\left(\mathcal{E}_0\mathcal{L}_{b_r} - \mathcal{L}_0\mathcal{E}_{b_r}\right) + \mathcal{L}_0\mathcal{E}_\lambda\mathcal{B}_{\phi_{b_r}} - \mathcal{E}_0\mathcal{L}_\lambda\mathcal{B}_{\phi_{b_r}}\Big)\\
&+ \mathcal{L}_{b_\phi}\Big(\mathcal{B}_{r_0}\mathcal{E}_{b_r}\mathcal{B}_{\phi_\lambda} - \mathcal{E}_0\mathcal{B}_{r_{b_r}}\mathcal{B}_{\phi_\lambda} + \mathcal{B}_{\phi_0}\mathcal{E}_\lambda\mathcal{B}_{r_{b_r}} - \mathcal{B}_{r_0}\mathcal{E}_\lambda\mathcal{B}_{\phi b_r}\Big) + \mathcal{L}_0\mathcal{E}_{b_\phi}\mathcal{B}_{r_{b_r}}\mathcal{B}_{\phi_\lambda}\\
&- \mathcal{B}_{\phi_0}\mathcal{L}_\lambda\mathcal{E}_{b_\phi}\mathcal{B}_{r_{b_r}} - \mathcal{B}_{r_0}\mathcal{L}_\lambda\mathcal{E}_{b_r}\mathcal{B}_{\phi b_\phi} - \mathcal{L}_0\mathcal{E}_\lambda\mathcal{B}_{r_{b_r}}\mathcal{B}_{\phi_{b_\phi}} + \mathcal{E}_0\mathcal{L}_\lambda\mathcal{B}_{r_{b_r}}\mathcal{B}_{\phi_{b_\phi}} + \mathcal{B}_{r_0}\mathcal{L}_\lambda\mathcal{E}_{b_\phi}\mathcal{B}_{\phi_{b_r}}\\
&+ \mathcal{B}_{r_\lambda}\Big(\mathcal{L}_0\mathcal{E}_{b_r}\mathcal{B}_{\phi b_\phi} - \mathcal{L}_0\mathcal{E}_{b_\phi}\mathcal{B}_{\phi b_r} - \mathcal{E}_0\mathcal{L}_{b_r}\mathcal{B}_{\phi b_\phi} + \mathcal{E}_0\mathcal{L}_{b_\phi}\mathcal{B}_{\phi_{b_r}} + \mathcal{B}_{\phi_0}\mathcal{L}_{b_r}\mathcal{E}_{b_\phi} - \mathcal{B}_{\phi_0}\mathcal{E}_{b_r}\mathcal{L}_{b_\phi}\Big)\\
&+ \mathcal{B}_{r_0}\mathcal{E}_\lambda\mathcal{L}_{b_r}\mathcal{B}_{\phi b_\phi} - \mathcal{B}_{r_0}\mathcal{L}_{b_r}\mathcal{E}_{b_\phi}\mathcal{B}_{\phi_\lambda},
\end{aligned}$$

$$\begin{aligned}
\Theta_{v0} &= \mathcal{B}_{r_{b_\phi}}\Big(\mathcal{L}_\lambda\mathcal{E}_{b_r}\mathcal{B}_{\phi_v} - \mathcal{E}_\lambda\mathcal{L}_{b_r}\mathcal{B}_{\phi_v} + \mathcal{B}_{\phi_\lambda}\left(\mathcal{E}_v\mathcal{L}_{b_r} - \mathcal{L}_v\mathcal{E}_{b_r}\right) + \mathcal{L}_v\mathcal{E}_\lambda\mathcal{B}_{\phi_{b_r}} - \mathcal{E}_v\mathcal{L}_\lambda\mathcal{B}_{\phi_{b_r}}\Big)\\
&+ \mathcal{L}_{b_\phi}\Big(\mathcal{E}_{b_r}\mathcal{B}_{r_v}\mathcal{B}_{\phi_\lambda} - \mathcal{E}_v\mathcal{B}_{r_{b_r}}\mathcal{B}_{\phi_\lambda} + \mathcal{E}_\lambda\mathcal{B}_{r_{b_r}}\mathcal{B}_{\phi_v} - \mathcal{E}_\lambda\mathcal{B}_{r_v}\mathcal{B}_{\phi_{b_r}}\Big)\\
&+ \mathcal{L}_v\mathcal{E}_{b_\phi}\mathcal{B}_{r_{b_r}}\mathcal{B}_{\phi_\lambda} - \mathcal{L}_\lambda\mathcal{E}_{b_\phi}\mathcal{B}_{r_{b_r}}\mathcal{B}_{\phi_v} - \mathcal{L}_v\mathcal{E}_\lambda\mathcal{B}_{r_{b_r}}\mathcal{B}_{\phi_{b_\phi}} + \mathcal{E}_v\mathcal{L}_\lambda\mathcal{B}_{r_{b_r}}\mathcal{B}_{\phi_{b_\phi}} - \mathcal{L}_\lambda\mathcal{E}_{b_r}\mathcal{B}_{r_v}\mathcal{B}_{\phi b_\phi}\\
&+ \mathcal{B}_{r_\lambda}\Big(\mathcal{L}_v\mathcal{E}_{b_r}\mathcal{B}_{\phi b_\phi} - \mathcal{L}_v\mathcal{E}_{b_\phi}\mathcal{B}_{\phi_{b_r}} - \mathcal{E}_v\mathcal{L}_{b_r}\mathcal{B}_{\phi_{b_\phi}} + \mathcal{E}_v\mathcal{L}_{b_\phi}\mathcal{B}_{\phi b_r} + \mathcal{L}_{b_r}\mathcal{E}_{b_\phi}\mathcal{B}_{\phi_v} - \mathcal{E}_{b_r}\mathcal{L}_{b_\phi}\mathcal{B}_{\phi_v}\Big)\\
&+ \mathcal{L}_\lambda\mathcal{E}_{b_\phi}\mathcal{B}_{r_v}\mathcal{B}_{\phi b_r} + \mathcal{E}_\lambda\mathcal{L}_{b_r}\mathcal{B}_{r_v}\mathcal{B}_{\phi_{b_\phi}} - \mathcal{L}_{b_r}\mathcal{E}_{b_\phi}\mathcal{B}_{r_v}\mathcal{B}_{\phi_\lambda},
\end{aligned}$$

$$\lambda_{c0} = \mathcal{L}_0\mathcal{E}_{b_r}\mathcal{B}_{r_{b_\phi}}\mathcal{B}_{\phi_\Theta} - \mathcal{L}_0\mathcal{E}_{b_\phi}\mathcal{B}_{r_{b_r}}\mathcal{B}_{\phi_\Theta} - \mathcal{B}_{\phi_0}\mathcal{L}_\Theta\mathcal{E}_{b_r}\mathcal{B}_{r_{b_\phi}} + \mathcal{B}_{\phi_0}\mathcal{L}_\Theta\mathcal{E}_{b_\phi}\mathcal{B}_{r_{b_r}} - \mathcal{E}_0\mathcal{L}_{b_r}\mathcal{B}_{r_{b_\phi}}\mathcal{B}_{\phi_\Theta}$$
$$+ \mathcal{B}_{\phi_0}\mathcal{E}_\Theta\mathcal{L}_{b_r}\mathcal{B}_{r_{b_\phi}} + \mathcal{E}_0\mathcal{L}_{b_\phi}\mathcal{B}_{r_{b_r}}\mathcal{B}_{\phi_\Theta} - \mathcal{B}_{\phi_0}\mathcal{E}_\Theta\mathcal{L}_{b_\phi}\mathcal{B}_{r_{b_r}} - \mathcal{L}_0\mathcal{E}_{b_r}\mathcal{B}_{r_\Theta}\mathcal{B}_{\phi_{b_\phi}} + \mathcal{L}_0\mathcal{E}_{b_\phi}\mathcal{B}_{r_\Theta}\mathcal{B}_{\phi_{b_r}}$$
$$+ \mathcal{B}_{r_0}\mathcal{L}_\Theta\mathcal{E}_{b_r}\mathcal{B}_{\phi b_\phi} - \mathcal{B}_{r_0}\mathcal{L}_\Theta\mathcal{E}_{b_\phi}\mathcal{B}_{\phi b_r} + \mathcal{E}_0\mathcal{L}_{b_r}\mathcal{B}_{r_\Theta}\mathcal{B}_{\phi_{b_\phi}} - \mathcal{B}_{r_0}\mathcal{E}_\Theta\mathcal{L}_{b_r}\mathcal{B}_{\phi b_\phi} - \mathcal{E}_0\mathcal{L}_{b_\phi}\mathcal{B}_{r_\Theta}\mathcal{B}_{\phi b_r}$$
$$+ \mathcal{B}_{r_0}\mathcal{E}_\Theta\mathcal{L}_{b_\phi}\mathcal{B}_{\phi b_r} - \mathcal{B}_{\phi_0}\mathcal{L}_{b_r}\mathcal{E}_{b_\phi}\mathcal{B}_{r_\Theta} + \mathcal{B}_{r_0}\mathcal{L}_{b_r}\mathcal{E}_{b_\phi}\mathcal{B}_{\phi_\Theta} + \mathcal{B}_{\phi_0}\mathcal{E}_{b_r}\mathcal{L}_{b_\phi}\mathcal{B}_{r_\Theta} - \mathcal{B}_{r_0}\mathcal{E}_{b_r}\mathcal{L}_{b_\phi}\mathcal{B}_{\phi_\Theta}$$
$$- \mathcal{L}_0\mathcal{E}_\Theta\mathcal{B}_{\phi_{b_r}}\mathcal{B}_{r_{b_\phi}} + \mathcal{L}_0\mathcal{E}_\Theta\mathcal{B}_{r_{b_r}}\mathcal{B}_{\phi_{b_\phi}} + \mathcal{E}_0\mathcal{L}_\Theta\mathcal{B}_{\phi_{b_r}}\mathcal{B}_{r_{b_\phi}} - \mathcal{E}_0\mathcal{L}_\Theta\mathcal{B}_{r_{b_r}}\mathcal{B}_{\phi_{b_\phi}},$$

$$\lambda_{v0} = \mathcal{L}_v\mathcal{E}_{b_r}\mathcal{B}_{r_{b_\phi}}\mathcal{B}_{\phi_\Theta} - \mathcal{L}_v\mathcal{E}_{b_\phi}\mathcal{B}_{r_{b_r}}\mathcal{B}_{\phi_\Theta} - \mathcal{L}_\Theta\mathcal{E}_{b_r}\mathcal{B}_{r_{b_\phi}}\mathcal{B}_{\phi_v} + \mathcal{L}_\Theta\mathcal{E}_{b_\phi}\mathcal{B}_{r_{b_r}}\mathcal{B}_{\phi_v} - \mathcal{E}_v\mathcal{L}_{b_r}\mathcal{B}_{r_{b_\phi}}\mathcal{B}_{\phi_\Theta}$$
$$+ \mathcal{E}_\Theta\mathcal{L}_{b_r}\mathcal{B}_{r_{b_\phi}}\mathcal{B}_{\phi_v} + \mathcal{E}_v\mathcal{L}_{b_\phi}\mathcal{B}_{r_{b_r}}\mathcal{B}_{\phi_\Theta} - \mathcal{E}_\Theta\mathcal{L}_{b_\phi}\mathcal{B}_{r_{b_r}}\mathcal{B}_{\phi_v} - \mathcal{L}_v\mathcal{E}_{b_r}\mathcal{B}_{r_\Theta}\mathcal{B}_{\phi_{b_\phi}} + \mathcal{L}_v\mathcal{E}_{b_\phi}\mathcal{B}_{r_\Theta}\mathcal{B}_{\phi_{b_r}}$$
$$+ \mathcal{L}_\Theta\mathcal{E}_{b_r}\mathcal{B}_{r_v}\mathcal{B}_{\phi b_\phi} - \mathcal{L}_\Theta\mathcal{E}_{b_\phi}\mathcal{B}_{r_v}\mathcal{B}_{\phi_{b_r}} + \mathcal{E}_v\mathcal{L}_{b_r}\mathcal{B}_{r_\Theta}\mathcal{B}_{\phi_{b_\phi}} - \mathcal{E}_\Theta\mathcal{L}_{b_r}\mathcal{B}_{r_v}\mathcal{B}_{\phi b_\phi} - \mathcal{E}_v\mathcal{L}_{b_\phi}\mathcal{B}_{r_\Theta}\mathcal{B}_{\phi b_r}$$
$$+ \mathcal{E}_\Theta\mathcal{L}_{b_\phi}\mathcal{B}_{r_v}\mathcal{B}_{\phi b_r} - \mathcal{L}_{b_r}\mathcal{E}_{b_\phi}\mathcal{B}_{r_\Theta}\mathcal{B}_{\phi_v} + \mathcal{L}_{b_r}\mathcal{E}_{b_\phi}\mathcal{B}_{r_v}\mathcal{B}_{\phi_\Theta} + \mathcal{E}_{b_r}\mathcal{L}_{b_\phi}\mathcal{B}_{r_\Theta}\mathcal{B}_{\phi_v} - \mathcal{E}_{b_r}\mathcal{L}_{b_\phi}\mathcal{B}_{r_v}\mathcal{B}_{\phi_\Theta}$$
$$- \mathcal{L}_v\mathcal{E}_\Theta\mathcal{B}_{\phi_{b_r}}\mathcal{B}_{r_{b_\phi}} + \mathcal{L}_v\mathcal{E}_\Theta\mathcal{B}_{r_{b_r}}\mathcal{B}_{\phi_{b_\phi}} + \mathcal{E}_v\mathcal{L}_\Theta\mathcal{B}_{\phi_{b_r}}\mathcal{B}_{r_{b_\phi}} - \mathcal{E}_v\mathcal{L}_\Theta\mathcal{B}_{r_{b_r}}\mathcal{B}_{\phi_{b_\phi}},$$

$$b^r_{c0} = -\mathcal{L}_0\mathcal{E}_{b_\phi}\mathcal{B}_{r_\lambda}\mathcal{B}_{\phi_\Theta} + \mathcal{L}_0\mathcal{E}_{b_\phi}\mathcal{B}_{r_\Theta}\mathcal{B}_{\phi_\lambda} + \mathcal{B}_{\phi_0}\mathcal{L}_\Theta\mathcal{E}_{b_\phi}\mathcal{B}_{r_\lambda} - \mathcal{B}_{r_0}\mathcal{L}_\Theta\mathcal{E}_{b_\phi}\mathcal{B}_{\phi_\lambda} - \mathcal{B}_{\phi_0}\mathcal{L}_\lambda\mathcal{E}_{b_\phi}\mathcal{B}_{r_\Theta}$$
$$+ \mathcal{B}_{r_0}\mathcal{L}_\lambda\mathcal{E}_{b_\phi}\mathcal{B}_{\phi_\Theta} + \mathcal{E}_0\mathcal{L}_{b_\phi}\mathcal{B}_{r_\lambda}\mathcal{B}_{\phi_\Theta} - \mathcal{E}_0\mathcal{L}_{b_\phi}\mathcal{B}_{r_\Theta}\mathcal{B}_{\phi_\lambda} - \mathcal{B}_{\phi_0}\mathcal{E}_\Theta\mathcal{L}_{b_\phi}\mathcal{B}_{r_\lambda} + \mathcal{B}_{r_0}\mathcal{E}_\Theta\mathcal{L}_{b_\phi}\mathcal{B}_{\phi_\lambda}$$
$$+ \mathcal{B}_{\phi_0}\mathcal{E}_\lambda\mathcal{L}_{b_\phi}\mathcal{B}_{r_\Theta} - \mathcal{B}_{r_0}\mathcal{E}_\lambda\mathcal{L}_{b_\phi}\mathcal{B}_{\phi_\Theta} + \mathcal{L}_0\mathcal{E}_\Theta\mathcal{B}_{r_\lambda}\mathcal{B}_{\phi b_\phi} - \mathcal{L}_0\mathcal{E}_\lambda\mathcal{B}_{r_\Theta}\mathcal{B}_{\phi_{b_\phi}} - \mathcal{E}_0\mathcal{L}_\Theta\mathcal{B}_{r_\lambda}\mathcal{B}_{\phi_{b_\phi}}$$
$$+ \mathcal{B}_{r_0}\mathcal{E}_\lambda\mathcal{L}_\Theta\mathcal{B}_{\phi_{b_\phi}} + \mathcal{E}_0\mathcal{L}_\lambda\mathcal{B}_{r_\Theta}\mathcal{B}_{\phi_{b_\phi}} - \mathcal{B}_{r_0}\mathcal{E}_\Theta\mathcal{L}_\lambda\mathcal{B}_{\phi_{b_\phi}} - \mathcal{L}_0\mathcal{E}_\Theta\mathcal{B}_{r_{b_\phi}}\mathcal{B}_{\phi_\lambda} + \mathcal{L}_0\mathcal{E}_\lambda\mathcal{B}_{r_{b_\phi}}\mathcal{B}_{\phi_\Theta}$$
$$+ \mathcal{E}_0\mathcal{L}_\Theta\mathcal{B}_{r_{b_\phi}}\mathcal{B}_{\phi_\lambda} - \mathcal{B}_{\phi_0}\mathcal{E}_\lambda\mathcal{L}_\Theta\mathcal{B}_{r_{b_\phi}} - \mathcal{E}_0\mathcal{L}_\lambda\mathcal{B}_{r_{b_\phi}}\mathcal{B}_{\phi_\Theta} + \mathcal{B}_{\phi_0}\mathcal{E}_\Theta\mathcal{L}_\lambda\mathcal{B}_{r_{b_\phi}},$$

$$b^r_{v0} = -\mathcal{L}_v\mathcal{E}_{b_\phi}\mathcal{B}_{r_\lambda}\mathcal{B}_{\phi_\Theta} + \mathcal{L}_v\mathcal{E}_{b_\phi}\mathcal{B}_{r_\Theta}\mathcal{B}_{\phi_\lambda} + \mathcal{L}_\Theta\mathcal{E}_{b_\phi}\mathcal{B}_{r_\lambda}\mathcal{B}_{\phi_v} - \mathcal{L}_\Theta\mathcal{E}_{b_\phi}\mathcal{B}_{r_v}\mathcal{B}_{\phi_\lambda} - \mathcal{L}_\lambda\mathcal{E}_{b_\phi}\mathcal{B}_{r_\Theta}\mathcal{B}_{\phi_v}$$
$$+ \mathcal{L}_\lambda\mathcal{E}_{b_\phi}\mathcal{B}_{r_v}\mathcal{B}_{\phi_\Theta} + \mathcal{E}_v\mathcal{L}_{b_\phi}\mathcal{B}_{r_\lambda}\mathcal{B}_{\phi_\Theta} - \mathcal{E}_v\mathcal{L}_{b_\phi}\mathcal{B}_{r_\Theta}\mathcal{B}_{\phi_\lambda} - \mathcal{E}_\Theta\mathcal{L}_{b_\phi}\mathcal{B}_{r_\lambda}\mathcal{B}_{\phi_v} + \mathcal{E}_\Theta\mathcal{L}_{b_\phi}\mathcal{B}_{r_v}\mathcal{B}_{\phi_\lambda}$$
$$+ \mathcal{E}_\lambda\mathcal{L}_{b_\phi}\mathcal{B}_{r_\Theta}\mathcal{B}_{\phi_v} - \mathcal{E}_\lambda\mathcal{L}_{b_\phi}\mathcal{B}_{r_v}\mathcal{B}_{\phi_\Theta} + \mathcal{L}_v\mathcal{E}_\Theta\mathcal{B}_{r_\lambda}\mathcal{B}_{\phi_{b_\phi}} - \mathcal{L}_v\mathcal{E}_\lambda\mathcal{B}_{r_\Theta}\mathcal{B}_{\phi_{b_\phi}} - \mathcal{E}_v\mathcal{L}_\Theta\mathcal{B}_{r_\lambda}\mathcal{B}_{\phi_{b_\phi}}$$
$$+ \mathcal{E}_\lambda\mathcal{L}_\Theta\mathcal{B}_{r_v}\mathcal{B}_{\phi b_\phi} + \mathcal{E}_v\mathcal{L}_\lambda\mathcal{B}_{r_\Theta}\mathcal{B}_{\phi b_\phi} - \mathcal{E}_\Theta\mathcal{L}_\lambda\mathcal{B}_{r_v}\mathcal{B}_{\phi_{b_\phi}} - \mathcal{L}_v\mathcal{E}_\Theta\mathcal{B}_{rb_\phi}\mathcal{B}_{\phi_\lambda} + \mathcal{L}_v\mathcal{E}_\lambda\mathcal{B}_{r_{b_\phi}}\mathcal{B}_{\phi_\Theta}$$
$$+ \mathcal{E}_v\mathcal{L}_\Theta\mathcal{B}_{r_{b_\phi}}\mathcal{B}_{\phi_\lambda} - \mathcal{E}_\lambda\mathcal{L}_\Theta\mathcal{B}_{r_{b_\phi}}\mathcal{B}_{\phi_v} - \mathcal{E}_v\mathcal{L}_\lambda\mathcal{B}_{r_{b_\phi}}\mathcal{B}_{\phi_\Theta} + \mathcal{E}_\Theta\mathcal{L}_\lambda\mathcal{B}_{r_{b_\phi}}\mathcal{B}_{\phi_v},$$

$$b^\phi_{c0} = \mathcal{L}_0\mathcal{E}_{b_r}\mathcal{B}_{r_\lambda}\mathcal{B}_{\phi_\Theta} - \mathcal{L}_0\mathcal{E}_{b_r}\mathcal{B}_{r_\Theta}\mathcal{B}_{\phi_\lambda} - \mathcal{B}_{\phi_0}\mathcal{L}_\Theta\mathcal{E}_{b_r}\mathcal{B}_{r_\lambda} + \mathcal{B}_{r_0}\mathcal{L}_\Theta\mathcal{E}_{b_r}\mathcal{B}_{\phi_\lambda} + \mathcal{B}_{\phi_0}\mathcal{L}_\lambda\mathcal{E}_{b_r}\mathcal{B}_{r_\Theta}$$
$$- \mathcal{B}_{r_0}\mathcal{L}_\lambda\mathcal{E}_{b_r}\mathcal{B}_{\phi_\Theta} - \mathcal{E}_0\mathcal{L}_{b_r}\mathcal{B}_{r_\lambda}\mathcal{B}_{\phi_\Theta} + \mathcal{E}_0\mathcal{L}_{b_r}\mathcal{B}_{r_\Theta}\mathcal{B}_{\phi_\lambda} + \mathcal{B}_{\phi_0}\mathcal{E}_\Theta\mathcal{L}_{b_r}\mathcal{B}_{r_\lambda} - \mathcal{B}_{r_0}\mathcal{E}_\Theta\mathcal{L}_{b_r}\mathcal{B}_{\phi_\lambda}$$
$$- \mathcal{B}_{\phi_0}\mathcal{E}_\lambda\mathcal{L}_{b_r}\mathcal{B}_{r_\Theta} + \mathcal{B}_{r_0}\mathcal{E}_\lambda\mathcal{L}_{b_r}\mathcal{B}_{\phi_\Theta} + \mathcal{L}_0\mathcal{E}_\Theta\mathcal{B}_{r_{b_r}}\mathcal{B}_{\phi_\lambda} - \mathcal{L}_0\mathcal{E}_\lambda\mathcal{B}_{r_{b_r}}\mathcal{B}_{\phi_\Theta} - \mathcal{E}_0\mathcal{L}_\Theta\mathcal{B}_{r_{b_r}}\mathcal{B}_{\phi_\lambda}$$
$$+ \mathcal{B}_{\phi_0}\mathcal{E}_\lambda\mathcal{L}_\Theta\mathcal{B}_{r_{b_r}} + \mathcal{E}_0\mathcal{L}_\lambda\mathcal{B}_{r_{b_r}}\mathcal{B}_{\phi_\Theta} - \mathcal{B}_{\phi_0}\mathcal{E}_\Theta\mathcal{L}_\lambda\mathcal{B}_{r_{b_r}} - \mathcal{L}_0\mathcal{E}_\Theta\mathcal{B}_{r_\lambda}\mathcal{B}_{\phi_{b_r}} + \mathcal{L}_0\mathcal{E}_\lambda\mathcal{B}_{r_\Theta}\mathcal{B}_{\phi b_r}$$
$$+ \mathcal{E}_0\mathcal{L}_\Theta\mathcal{B}_{r_\lambda}\mathcal{B}_{\phi_{b_r}} - \mathcal{B}_{r_0}\mathcal{E}_\lambda\mathcal{L}_\Theta\mathcal{B}_{\phi_{b_r}} - \mathcal{E}_0\mathcal{L}_\lambda\mathcal{B}_{r_\Theta}\mathcal{B}_{\phi b_r} + \mathcal{B}_{r_0}\mathcal{E}_\Theta\mathcal{L}_\lambda\mathcal{B}_{\phi_{b_r}},$$

$$b^\phi_{v0} = \mathcal{L}_v\mathcal{E}_{b_r}\mathcal{B}_{r_\lambda}\mathcal{B}_{\phi_\Theta} - \mathcal{L}_v\mathcal{E}_{b_r}\mathcal{B}_{r_\Theta}\mathcal{B}_{\phi_\lambda} - \mathcal{L}_\Theta\mathcal{E}_{b_r}\mathcal{B}_{r_\lambda}\mathcal{B}_{\phi_v} + \mathcal{L}_\Theta\mathcal{E}_{b_r}\mathcal{B}_{r_v}\mathcal{B}_{\phi_\lambda} + \mathcal{L}_\lambda\mathcal{E}_{b_r}\mathcal{B}_{r_\Theta}\mathcal{B}_{\phi_v}$$
$$- \mathcal{L}_\lambda\mathcal{E}_{b_r}\mathcal{B}_{r_v}\mathcal{B}_{\phi_\Theta} - \mathcal{E}_v\mathcal{L}_{b_r}\mathcal{B}_{r_\lambda}\mathcal{B}_{\phi_\Theta} + \mathcal{E}_v\mathcal{L}_{b_r}\mathcal{B}_{r_\Theta}\mathcal{B}_{\phi_\lambda} + \mathcal{E}_\Theta\mathcal{L}_{b_r}\mathcal{B}_{r_\lambda}\mathcal{B}_{\phi_v} - \mathcal{E}_\Theta\mathcal{L}_{b_r}\mathcal{B}_{r_v}\mathcal{B}_{\phi_\lambda}$$
$$- \mathcal{E}_\lambda\mathcal{L}_{b_r}\mathcal{B}_{r_\Theta}\mathcal{B}_{\phi_v} + \mathcal{E}_\lambda\mathcal{L}_{b_r}\mathcal{B}_{r_v}\mathcal{B}_{\phi_\Theta} + \mathcal{L}_v\mathcal{E}_\Theta\mathcal{B}_{r_{b_r}}\mathcal{B}_{\phi_\lambda} - \mathcal{L}_v\mathcal{E}_\lambda\mathcal{B}_{r_{b_r}}\mathcal{B}_{\phi_\Theta} - \mathcal{E}_v\mathcal{L}_\Theta\mathcal{B}_{r_{b_r}}\mathcal{B}_{\phi_\lambda}$$
$$+ \mathcal{E}_\lambda\mathcal{L}_\Theta\mathcal{B}_{r_{b_r}}\mathcal{B}_{\phi_v} + \mathcal{E}_v\mathcal{L}_\lambda\mathcal{B}_{r_{b_r}}\mathcal{B}_{\phi_\Theta} - \mathcal{E}_\Theta\mathcal{L}_\lambda\mathcal{B}_{r_{b_r}}\mathcal{B}_{\phi_v} - \mathcal{L}_v\mathcal{E}_\Theta\mathcal{B}_{r_\lambda}\mathcal{B}_{\phi_{b_r}} + \mathcal{L}_v\mathcal{E}_\lambda\mathcal{B}_{r_\Theta}\mathcal{B}_{\phi_{b_r}}$$
$$+ \mathcal{E}_v\mathcal{L}_\Theta\mathcal{B}_{r_\lambda}\mathcal{B}_{\phi_{b_r}} - \mathcal{E}_\lambda\mathcal{L}_\Theta\mathcal{B}_{r_v}\mathcal{B}_{\phi b_r} - \mathcal{E}_v\mathcal{L}_\lambda\mathcal{B}_{r_\Theta}\mathcal{B}_{\phi_{b_r}} + \mathcal{E}_\Theta\mathcal{L}_\lambda\mathcal{B}_{r_v}\mathcal{B}_{\phi b_r}.$$

Appendix B

Appendix B

B.1 Derivation of Wind Equations

The radial momentum equation, angular momentum equation and energy equation are obtained as,

$$\mathcal{R}_0 + \mathcal{R}_v \frac{dv}{dr} + \mathcal{R}_\Theta \frac{d\Theta}{dr} + \mathcal{R}_\lambda \frac{d\lambda}{dr} = 0, \tag{B.1}$$

$$L_0 + L_v \frac{dv}{dr} + L_\Theta \frac{d\Theta}{dr} + L_\lambda \frac{d\lambda}{dr} = 0, \tag{B.2}$$

$$E_0 + E_v \frac{dv}{dr} + E_\Theta \frac{d\Theta}{dr} + E_\lambda \frac{d\lambda}{dr} = 0, \tag{B.3}$$

and the coefficients in equations (B.1-B.3) are given below. In order to express these coefficients, we begin with the derivative of the four-velocities $u'_\mu = \frac{du^\mu}{dr}$, where all the Greek symbols correspond to the following coordinates $\mu \equiv (t, r, \theta, \phi)$,

$$u'_\mu = u_{\mu_0} + u_{\mu_v} v' + u_{\mu_\lambda} \lambda', u^{\mu'} = u^\mu_0 + u^\mu_v v' + u^\mu_\lambda \lambda',$$

$$u^\mu_0 = \frac{\partial u^\mu}{\partial r}, u^\mu_v = \frac{\partial u^\mu}{\partial v}, u^\mu_\lambda = \frac{\partial u^\mu}{\partial \lambda}, u_{\mu_0} = \frac{\partial u_\mu}{\partial r}, u_{\mu_v} = \frac{\partial u_\mu}{\partial v}, u_{\mu_\lambda} = \frac{\partial u_\mu}{\partial \lambda}.$$

With the following definitions of b^r, b^ϕ (see Eq. 3.12) and b^t,

$$b^r = -\frac{\gamma^2_\phi(\Phi + F\lambda)}{u^t r^2(v^2-1)}, \quad b^\phi = \frac{Fv^2 - \gamma^2_\phi(F + \Phi\Omega)}{u^r r^2(v^2-1)}, \quad b^t = -\frac{u_r}{u_t} b^r + \lambda b^\phi,$$

we can write,

$$b^{\mu'} = b^\mu_0 + b^\mu_v v' + b^\mu_\lambda \lambda', \text{where } b^\mu_0 = \frac{\partial b^\mu}{\partial r}, b^\mu_v = \frac{\partial b^\mu}{\partial v}, b^\mu_\lambda = \frac{\partial b^\mu}{\partial \lambda}.$$

In this way, the derivative of the square of the magnetic field $\mathbb{B} = b_\mu b^\mu$ is expressed as,

$$\mathbb{B}' = \mathbb{B}_0 + \mathbb{B}_v v' + \mathbb{B}_\lambda \lambda', \;\; \mathbb{B}_0 = \frac{\partial \mathbb{B}}{\partial r}, \mathbb{B}_v = \frac{\partial \mathbb{B}}{\partial v}, \mathbb{B}_\lambda = \frac{\partial \mathbb{B}}{\partial \lambda}.$$

Similarly,

$$h'_{\rm tot} = h^0_{\rm t} + h^v_{\rm t} v' + h^\Theta_{\rm t} \Theta' + h^\lambda_{\rm t} \lambda', h^0_{\rm t} = \frac{\partial h_{\rm tot}}{\partial r}, h^v_{\rm t} = \frac{\partial h_{\rm tot}}{\partial v}, h^\Theta_{\rm t} = \frac{\partial h_{\rm tot}}{\partial \Theta}, h^\lambda_{\rm t} = \frac{\partial h_{\rm tot}}{\partial \lambda},$$

and

$$\mathbb{F}' = \frac{d\mathbb{F}}{dr} = \mathbb{F}_1 + \mathbb{F}_2 \frac{d\lambda}{dr}, \mathbb{F}_1 = \frac{\partial \mathbb{F}}{\partial r}, \mathbb{F}_2 = \frac{\partial \mathbb{F}}{\partial \lambda}, \Delta' = \frac{d\Delta}{dr}, \tau_0 = (1 + m_p/m_e).$$

With these definitions, we express the coefficients of the equations (B.1-B.3) as follows,

$$\mathcal{R}_0 = (\mathcal{R}_a + \mathcal{A}\mathcal{R}_1)/\rho h_{\rm tot}, \mathcal{A} = (g^{rr} + u^r u^r), \mathcal{R}_1 = \frac{\mathbb{B}_0}{2} - \frac{3\Theta\rho}{r\tau_0} + \frac{\mathbb{F}_1\Theta\rho}{\tau_0\mathbb{F}} - \frac{\Theta\rho\Delta'}{\tau_0\Delta},$$

$$\mathcal{R}_a = -b^r b^r_0 (2 + g_{rr} u^r u^r) + h_{\rm tot} u^r u^r_0 \rho - b^r u^r (u_t b^t_0 + u_\phi b^\phi_0) + \mathcal{R}_b,$$

$$\mathcal{R}_b = \frac{\rho h_{\rm tot}}{2} g^{rr} {u^r}^2 g'_{rr} + \frac{g^{rr} {b^t}^2}{2} g'_{tt} - g^{rr} {b^r}^2 (1 - \frac{1}{2} g_{rr} {u^r}^2) g'_{rr} + \mathcal{R}_c,$$

$$\mathcal{R}_c = g^{rr} g'_{t\phi} b^t b^\phi + \frac{g^{rr}}{2} {b^\phi}^2 g'_{\phi\phi} - \frac{g^{\theta\theta}}{2} {b^r}^2 g'_{\theta\theta} - \mathcal{S}_1({b^r}^2 + 2b^r u^r b^t u_t) - 2b^r u^r b^t u_\phi \mathcal{S}_2 + \mathcal{R}_d,$$

$$\mathcal{R}_d = -2b^r u^r b^\phi u_t \mathcal{S}_2 - \mathcal{S}_3 g_{rr} {u^r}^2 b^t + \mathcal{S}_4 h_{\rm tot} u^t \rho - g_{rr} {u^r}^2 b^\phi \mathcal{S}_5 + h_{\rm tot} \rho u^\phi \mathcal{S}_6 - \mathcal{S}_7({b^r}^2 + 2b^r u^r b^\phi u_\phi),$$

$$\mathcal{S}_1 = \frac{1}{2}(g^{tt} g'_{tt} + g^{t\phi} g'_{t\phi}), \mathcal{S}_2 = \frac{1}{2}(g^{tt} g'_{t\phi} + g^{t\phi} g'_{\phi\phi}), \mathcal{S}_3 = -\frac{g^{rr}}{2}(b^t g'_{tt} + b^\phi g'_{t\phi}), \mathcal{S}_4 = -\frac{g^{rr}}{2}(u^t g'_{tt} + u^\phi g'_{t\phi}),$$

$$\mathcal{S}_5 = -\frac{g^{rr}}{2}(b^t g'_{t\phi} + b^\phi g'_{\phi\phi}), \mathcal{S}_6 = -\frac{g^{rr}}{2}(u^t g'_{t\phi} + u^\phi g'_{\phi\phi}), \mathcal{S}_7 = \frac{1}{2}(g^{t\phi} g'_{t\phi} + g^{\phi\phi} g'_{\phi\phi}).$$

$$\mathcal{R}_v = (\mathcal{R}_e + \mathcal{A}\mathcal{R}_2)/\rho h_{\rm tot}, \mathcal{R}_2 = \frac{\mathbb{B}_v}{2} - \frac{2\Theta\rho(1 + v^2\gamma_v^2)}{\tau_0\mathbb{F}},$$

$$\mathcal{R}_e = -b^r b^r_v (2 + g_{rr} u^r u^r) + h_{\rm tot} u^r u^r_v \rho - b^r u^r (u_t b^t_v + u_\phi b^\phi_v),$$

$$\mathcal{R}_\Theta = \frac{1}{\tau_0 h_{\rm tot}}, \mathcal{R}_\lambda = (\mathcal{R}_f + \mathcal{A}\mathcal{R}_3)/\rho h_{\rm tot},$$

$$\mathcal{R}_3 = \frac{\mathbb{B}_\lambda}{2} + \frac{\mathbb{F}_2\Theta\rho}{\tau_0\mathbb{F}}, \mathcal{R}_f = -b^r b^r_\lambda (2 + g_{rr} u^r u^r) - b^r u^r (u_t b^t_\lambda + u_\phi b^\phi_\lambda).$$

$$L_0 = h^0_t u_\phi + h_{\rm tot} u_{\phi_0} - \frac{g_{t\phi} b^r b^t_0 + b^r_0 b_\phi + g_{\phi\phi} b^r b^\phi_0 - b^r b^t g'_{t\phi} + b^r b^\phi g'_{\phi\phi}}{u^r \rho} - \frac{3b^r b_\phi}{2ru^r\rho} + \frac{\mathbb{F}_1 b^r b_\phi}{2\mathbb{F}u^r\rho} - \frac{b^r b_\phi \Delta'}{2u^r\Delta\rho} + \frac{b^r u^r_0 b_\phi}{{u^r}^2\rho},$$

$$L_v = h_t^v u_\phi + h_{\rm tot} u_{\phi_v} - \frac{g_{t\phi} b^r b_v^t + b_v^r b_\phi + g_{\phi\phi} b^r b_v^\phi}{u^r \rho} + \frac{b^r u_v^r b_\phi}{u^{r^2} \rho} - \frac{b^r (1 + v^2 \gamma_v^2) b_\phi}{u^r v \rho},$$

$$L_\Theta = h_t^\Theta u_\phi - \frac{b^r b_\phi}{2 u^r \Theta \rho},\ L_\lambda = h_t^\lambda u_\phi + h_{\rm tot} u_{\phi_\lambda} - \frac{g_{t\phi} b^r b_\lambda^t}{u^r \rho} + \frac{\mathbb{F}_2 b^r b_\phi}{2\mathbb{F} u^r \rho} - \frac{b_\lambda^r b_\phi}{u^r \rho} - \frac{g_{\phi\phi} b^r b_\lambda^\phi}{u^r \rho}.$$

$$E_0 = -h_t^0 u_t - h_{\rm tot} u_{t_0} + \frac{g_{tt} b^r b_0^t + b_0^r b_t + g_{t\phi} b^r b_0^\phi - b^r b^\phi g'_{t\phi} + b^r b^t g'_{tt}}{u^r \rho} + \frac{3 b^r b_t}{2 r u^r \rho} - \frac{\mathbb{F}_1 b^r b_t}{2\mathbb{F} u^r \rho} - \frac{b^r b_t \Delta'}{2 u^r \Delta \rho} - \frac{b^r u_0^r b_t}{u^{r^2} \rho},$$

$$E_v = -h_t^v u_t - h_{\rm tot} u_{t_v} + \frac{g_{tt} b^r b_v^t + b_v^r b_t + g_{t\phi} b^r b_v^\phi}{u^r \rho} - \frac{b^r u_v^r b_t}{u^{r^2} \rho} + \frac{b^r (1 + v^2 \gamma_v^2) b_t}{u^r v \rho},$$

$$E_\Theta = -h_t^\Theta u_t + \frac{b^r b_t}{2 u^r \Theta \rho},\ E_\lambda = -h_t^\lambda u_t - h_{\rm tot} u_{t_\lambda} + \frac{g_{tt} b^r b_\lambda^t}{u^r \rho} - \frac{\mathbb{F}_2 b^r b_t}{2\mathbb{F} u^r \rho} + \frac{b_\lambda^r b_t}{u^r \rho} + \frac{g_{t\phi} b^r b_\lambda^\phi}{u^r \rho}.$$

B.2 Expressions of Numerator and Denominator

As mentioned previously, we express the wind equation (3.16) as,

$$\frac{dv}{dr} = \frac{\mathcal{N}(r, a_{\rm k}, v, \Theta, \lambda, \Phi, F)}{\mathcal{D}(r, a_{\rm k}, v, \Theta, \lambda, \Phi, F)}. \tag{B.4}$$

Here, the numerator ($\mathcal{N}$) is given by,

$$\mathcal{N} = -\mathcal{R}_0 - \mathcal{R}_\Theta \tilde{\Theta}_1 - \mathcal{R}_\lambda \tilde{\lambda}_1, \tag{B.5}$$

and the denominator ($\mathcal{D}$) is given by,

$$\mathcal{D} = \mathcal{R}_v + \mathcal{R}_\Theta \tilde{\Theta}_2 + \mathcal{R}_\lambda \tilde{\lambda}_2, \tag{B.6}$$

where

$$\tilde{\Theta}_1 = \frac{E_\lambda L_0 - E_0 L_\lambda}{-E_\lambda L_\Theta + E_\Theta L_\lambda},\ \tilde{\Theta}_2 = \frac{E_\lambda L_v - E_v L_\lambda}{-E_\lambda L_\Theta + E_\Theta L_\lambda},\ \tilde{\lambda}_1 = \frac{-E_\Theta L_0 + E_0 L_\Theta}{-E_\lambda L_\Theta + E_\Theta L_\lambda},\ \tilde{\lambda}_2 = \frac{-E_\Theta L_v + E_v L_\Theta}{-E_\lambda L_\Theta + E_\Theta L_\lambda}.$$

Appendix C

Appendix C

C.1 Classical theory of thermal conductivity

In collisional plasmas, thermal conduction is described by the heat flux equation:

$$F_{\rm cond} = -\kappa \nabla T, \tag{C.1}$$

where κ is the thermal conductivity coefficient. Here, the mean free path for electron energy exchange, $\tilde{\ell}$, is much shorter than the temperature lengthscale, $T/|\nabla T|$. In such dense, fully ionized gas, the thermal conductivity can be determined using the Spitzer (1962) formula as,

$$\kappa = \frac{1.84 \times 10^{-5}\, T_e^{5/2}}{\ln \Lambda}, \tag{C.2}$$

where T_e is the electron temperature, and $\ln \Lambda$ is the Coulomb logarithm. For temperatures $T > 4.2 \times 10^5$ K, the Coulomb logarithm is given by:

$$\ln \Lambda = 29.7 + \ln n^{-1/2} \left(\frac{T_e}{10^6\,\mathrm{K}} \right), \tag{C.3}$$

where n is the electron density. Typically, in this scenario, electrons are responsible for the heat conduction in the plasmas. It is worth mentioning that Eq. (C.2) contains the effect of the self-consistent electric field that is required to maintain zero electric current, and consequently, the value of κ reduces by a factor of approximately 0.4 from the value it would take otherwise (Cowie & McKee, 1977, hereby known as CM77).

C.1.1 Saturated thermal conduction

The classical thermal conductivity breaks down when the electron mean free path ($\tilde{\ell}$) due to Coulomb collision becomes comparable to or exceeds the temperature scale height *i.e.,*

$\tilde{\ell} \gtrsim T/|\nabla T|$. This phenomenon is described as *saturation effect* by CM77. Consequently, the heat flux Eq. (C.1) becomes invalid, and the maximum heat flux in such a plasma can be expressed as $(3/2)n_e kT_e v_{char}$. Here, v_{char} is a characteristic velocity, expected to be of the order of the electron thermal velocity. Assuming a Maxwellian distribution for the heat source, the characteristic velocity is given by (CM77):

$$v_{\rm char} = \left(\frac{8}{9\pi}\right)^{1/2} \left(\frac{kT}{m_e}\right)^{1/2}. \tag{C.4}$$

Following CM77, we assume that the heat flux in the saturated case is reduced by the same factor of 0.4 as in the classical case. Hence, the saturated flux is expressed as,

$$F_{\rm s} = 0.4\, n_e kT_e \sqrt{\frac{2kT_e}{\pi m_e}}. \tag{C.5}$$

CM77 demonstrated that this saturated heat flux is significantly lower than that proposed by (Parker, 1963; Morse & Nielson, 1973). To account for uncertainties in the estimate of $F_{\rm s}$, CM77 introduced a factor $\Phi_{\rm s}$, which is of the order of unity, modifying the equation to:

$$F_{\rm s} = 5\Phi_{\rm s}\rho C_{\rm s}^3, \tag{C.6}$$

where $C_{\rm s}$ is the sound speed, defined as $C_{\rm s}^2 = \frac{p_{\rm gas}}{\rho}$. The factor $\Phi_{\rm s}$, known as the saturation constant, allows for explicitly considering the uncertainty in estimating $F_{\rm s}$.

Appendix D

Appendix D

D.1 Contravariant components of metric and Christoffel symbols

This appendix is dedicated to introducing the essential quantities for performing the post-Newtonian calculations. The first are the contravariant components of the metric:

$$g^{00} = -1 - \frac{2}{c^2}\frac{GM_*}{r} - \frac{2}{c^4}\Big(\frac{GM_*}{r}\Big)^2 + O(c^{-6}), \tag{D.1a}$$

$$g^{0j} = \frac{2}{c^3}\frac{G(\boldsymbol{x}\times\boldsymbol{S})^j}{r^3} + O(c^{-5}), \tag{D.1b}$$

$$g^{jk} = \Big(1 - \frac{2}{c^2}\frac{GM_*}{r}\Big)\delta^{jk} + O(c^{-4}). \tag{D.1c}$$

In order to simplify the energy-momentum conservation Eq. (5.5) and study its zeroth and spatial components (5.9) and (5.14), we need to obtain the Christoffel symbols $\Gamma^{\mu}_{\alpha\beta}$ from Eq. (5.1a)-(5.1c). Using the relation $\Gamma^{\mu}_{\alpha\beta} = \frac{1}{2}g^{\mu\nu}\Big(\partial_\alpha g_{\nu\beta} + \partial_\beta g_{\nu\alpha} - \partial_\nu g_{\alpha\beta}\Big)$, after some manipulations, and truncating the results to the required post-Newtonian order,

we arrive at

$$\Gamma^0_{00} = \frac{1}{c^3}\frac{GM_*}{r^2}\partial_t r + O(c^{-5}), \tag{D.2a}$$

$$\Gamma^0_{0j} = \frac{1}{c^2}\frac{GM_*}{r^2}\partial_j r + O(c^{-4}), \tag{D.2b}$$

$$\Gamma^0_{jk} = -\frac{1}{c^3}\Big\{\frac{GM_*}{r^2}\partial_t r\delta_{jk} - \frac{G}{r^4}\Big[3\Big((\boldsymbol{x}\times\boldsymbol{S})_j\partial_k r + (\boldsymbol{x}\times\boldsymbol{S})_k\partial_j r\Big) - r\Big((\partial_j\boldsymbol{x}\times\boldsymbol{S})_k + (\partial_k\boldsymbol{x}\times\boldsymbol{S})_j\Big)\Big]\Big\} + O(c^{-5}), \tag{D.2c}$$

$$\Gamma^j_{00} = \frac{1}{c^2}\frac{GM_*}{r^2}\partial_j r + \frac{2}{c^4}\frac{G}{r^4}\Big\{r\Big[(\boldsymbol{x}\times\partial_t\boldsymbol{S})_j + (\partial_t\boldsymbol{x}\times\boldsymbol{S})_j\Big] - 3\partial_t r(\boldsymbol{x}\times\boldsymbol{S})_j\Big\} - \frac{4}{c^4}\frac{G^2M^2}{r^3}\partial_j r + O(c^{-6}), \tag{D.2d}$$

$$\Gamma^j_{0k} = -\frac{1}{c^3}\Big\{\frac{GM_*}{r^2}\partial_t r\delta_{jk} - \frac{G}{r^4}\Big[3\Big((\boldsymbol{x}\times\boldsymbol{S})_k\partial_j r - (\boldsymbol{x}\times\boldsymbol{S})_j\partial_k r\Big) - r\Big((\partial_j\boldsymbol{x}\times\boldsymbol{S})_k - (\partial_k\boldsymbol{x}\times\boldsymbol{S})_j\Big)\Big]\Big\} + O(c^{-5}), \tag{D.2e}$$

$$\Gamma^j_{kn} = -\frac{1}{c^2}\frac{GM_*}{r^2}\Big\{\delta_{jn}\partial_k r + \delta_{jk}\partial_n r - \delta_{kn}\partial_j r\Big\} + O(c^{-4}). \tag{D.2f}$$

In the following, we attempt to obtain each term of Eq. (5.9) separately. In this case, we examine each term to $O(c^{-1})$. This order is sufficient to provide local conservation of energy within the fluid. In this way, it would be clear why the above terms are shortened to these post-Newtonian orders. As mentioned, we assume a perfect fluid system whose energy-momentum tensor is given by Eq. (5.3). Regarding the definition (5.6) and relation (5.7), we have

$$\frac{1}{c}\partial_t(\sqrt{-g}T^{00}) = c\,\partial_t\rho^* + \frac{1}{c}\,\partial_t\Big[\rho^*\big(\frac{GM_*}{r} + \frac{1}{2}V^2 + \Pi\big)\Big] + O(c^{-3}), \tag{D.3}$$

for the first term of Eq. (5.9). Here, $\Pi = \epsilon_0/\rho^*$ is the fluid's internal energy per unit mass. In a similar manner, the rest of the terms are obtained as follows:

$$\partial_j(\sqrt{-g}T^{0j}) = c\,\partial_j(\rho^*V^j) + \frac{1}{c}\,\partial_j\Big[\rho^*V^j\big(\frac{GM_*}{r} + \frac{1}{2}V^2 + \Pi\big)\Big] + \frac{1}{c}\,\partial_j(p_{\rm gas}\,V^j) + O(c^{-3}), \tag{D.4a}$$

$$\Gamma^0_{00}(\sqrt{-g}T^{00}) = \frac{1}{c}\frac{GM_*}{r^2}\rho^*\partial_t r + O(c^{-3}), \tag{D.4b}$$

$$2\Gamma^0_{0j}(\sqrt{-g}T^{0j}) = \frac{2}{c}\frac{GM_*}{r^2}\,\rho^*V^j\partial_j r + O(c^{-3}), \tag{D.4c}$$

$$\Gamma^0_{jk}(\sqrt{-g}T^{jk}) = O(c^{-3}). \tag{D.4d}$$

Summing these terms gives Eq. (5.10).

To obtain the Euler equation including the leading relativistic corrections, we simplify each term of Eq. (5.14) to the order c^{-2}. For the first term in this equation, we get

$$\frac{1}{c}\partial_t(\sqrt{-g}T^{0j}) = \partial_t(\mu\rho^* V^j) + O(c^{-4}), \tag{D.5}$$

where $\mu = 1 + \frac{1}{c^2}(\Pi + \frac{p_{\rm gas}}{\rho^*} + \frac{GM_*}{r} + \frac{1}{2}V^2)$. After some manipulations, we find the rest of the terms as follows:

$$\partial_k(\sqrt{-g}T^{jk}) = \partial_k(\mu\rho^* V^j v^k) + \partial_j p_{\rm gas} + O(c^{-4}), \tag{D.6a}$$

$$\Gamma^j_{00}(\sqrt{-g}T^{00}) = \frac{GM_*}{r^2}\rho^*\partial_j r\Big\{\mu - \frac{1}{c^2}\Big(\frac{p_{\rm gas}}{\rho^*} + 4\frac{GM_*}{r}\Big)\Big\}$$
$$+ \frac{2}{c^2}\frac{G\,\rho^*}{r^4}\Big\{r\Big[(\boldsymbol{x}\times\partial_t\boldsymbol{S})_j + (\partial_t\boldsymbol{x}\times\boldsymbol{S})_j\Big] - 3\partial_t r(\boldsymbol{x}\times\boldsymbol{S})_j\Big\} + O(c^{-4}), \tag{D.6b}$$

$$2\Gamma^j_{0k}(\sqrt{-g}T^{0k}) = -\frac{2}{c^2}\frac{GM_*}{r^2}\rho^* V^j\,\partial_t r + \frac{2}{c^2}\frac{G}{r^4}\rho^* v^k\Big\{3\Big[\partial_j r(\boldsymbol{x}\times\boldsymbol{S})_k - \partial_k r(\boldsymbol{x}\times\boldsymbol{S})_j\Big]$$
$$- r\Big[(\partial_j\boldsymbol{x}\times\boldsymbol{S})_k - (\partial_k\boldsymbol{x}\times\boldsymbol{S})_j\Big]\Big\} + O(c^{-4}), \tag{D.6c}$$

$$\Gamma^j_{kn}(\sqrt{-g}T^{kn}) = -\frac{1}{c^2}\frac{GM_*}{r^2}\rho^*\Big\{\Big[2\partial_k r\,v^k V^j - \partial_j r\,v^2\Big] - \partial_j r\frac{p_{\rm gas}}{\rho^*}\Big\} + O(c^{-4}). \tag{D.6d}$$

D.2 Basis vectors of the local rest frame

In this appendix, we obtain the orthonormal tetrad basis vectors of the LRF. As mentioned earlier, instead of describing the equations of motion in the global frame, we obtain them in the LRF. In fact, we describe physical quantities by projecting them on the orthonormal tetrad basis carried by an observer who is locally at rest with respect to the fluid element. To do so, we use the method introduced by Bardeen et al. (1972).

The standard form of the metric which is valid for any stationary, axisymmetric, asymptotically flat spacetime is given by

$$ds^2 = -e^{2\nu}c^2dt^2 + e^{2\psi}(d\phi - \omega\,c\,dt)^2 + e^{2\mu_1}dr^2 + e^{2\mu_2}d\theta^2. \tag{D.7}$$

By rewriting the post-Newtonian metric (5.1a)-(5.1c) in the above standard form, one can deduce that

$$e^{2\nu} = 1 - \frac{2}{c^2}\frac{GM_*}{r} + \frac{2}{c^4}\Big(\frac{GM_*}{r}\Big)^2, \tag{D.8a}$$

$$e^{2\mu_1} = 1 + \frac{2}{c^2}\frac{GM_*}{r}, \tag{D.8b}$$

$$e^{2\mu_2} = r^2\Big(1 + \frac{2}{c^2}\frac{GM_*}{r}\Big), \tag{D.8c}$$

$$e^{2\psi} = r^2\sin^2\theta\Big(1 + \frac{2}{c^2}\frac{GM_*}{r}\Big), \tag{D.8d}$$

and

$$\omega = \frac{1}{c^3}\frac{GM_*\, s_{\rm J}}{r^3} + O(c^{-5}). \tag{D.9}$$

Here, it is assumed that the spin of the black hole is aligned with the z-axis. According to the general transformations between the LNRF and the standard one (D.7) introduced in Eqs. (3.1)-(3.2) by Bardeen et al. (1972), the Lorentz transformations between the LNRF and the CRF, and those between the CRF and the LRF, after doing straightforward calculations, we find

$$e_\mu^{(t)} = \Big\{\gamma_{\rm tot}\Big(1 - \frac{1}{c^2}\frac{GM_*}{r} + \frac{1}{c^4}(\frac{GM_*}{r})^2\Big) + \frac{1}{c}v_\phi\,\gamma_{\rm tot}\,\omega\, r,\ -\frac{1}{c}v\,\gamma_r\Big(1 + \frac{1}{c^2}\frac{GM_*}{r}\Big),\ 0,$$
$$-\frac{1}{c}v_\phi\gamma_{\rm tot}\, r\Big(1 + \frac{1}{c^2}\frac{GM_*}{r}\Big)\Big\}, \tag{D.10a}$$

$$e_\mu^{(r)} = \Big\{-\frac{1}{c}v\,\gamma_{\rm tot}\Big(1 - \frac{1}{c^2}\frac{GM_*}{r}\Big),\ \gamma_r\Big(1 + \frac{1}{c^2}\frac{GM_*}{r}\Big),\ 0,\ \frac{1}{c^2}v\,v_\phi\gamma_{\rm tot}\, r\Big(1 + \frac{1}{c^2}\frac{GM_*}{r}\Big)\Big\}, \tag{D.10b}$$

$$e_\mu^{(\theta)} = \Big\{0,\ 0,\ r\Big(1 + \frac{1}{c^2}\frac{GM_*}{r}\Big),\ 0\Big\}, \tag{D.10c}$$

$$e_\mu^{(\phi)} = \Big\{-\frac{1}{c}v_\phi\,\gamma_\phi\Big(1 - \frac{1}{c^2}\frac{GM_*}{r}\Big) - \gamma_\phi\,\omega\, r,\ 0,\ 0,\ \gamma_\phi\, r\Big(1 + \frac{1}{c^2}\frac{GM_*}{r}\Big)\Big\}, \tag{D.10d}$$

for the covariant LRF basis vectors. Here, $\gamma_{\rm tot} = \gamma_r \gamma_\phi$. In the above results, the case $\theta = \frac{\pi}{2}$ has been considered. For the contravariant basis vectors, we also arrive at

$$e^{\mu}_{\ (t)} = \Big\{\gamma_{\rm tot}\Big(1 + \frac{1}{c^2}\frac{GM_*}{r} - \frac{1}{c^4}(\frac{GM_*}{r})^2\Big),\ \frac{1}{c}v\gamma_r\Big(1 - \frac{1}{c^2}\frac{GM_*}{r}\Big),\ 0,\ \gamma_{\rm tot}\,\omega + \frac{1}{c\,r}v_\phi\,\gamma_{\rm tot}\Big(1 - \frac{1}{c^2}\frac{GM_*}{r}\Big)\Big\}, \tag{D.11a}$$

$$e^{\mu}_{\ (r)} = \Big\{\frac{1}{c}v\gamma_{\rm tot}\Big(1 + \frac{1}{c^2}\frac{GM_*}{r} - \frac{1}{c^4}(\frac{GM_*}{r})^2\Big),\ \gamma_r\Big(1 - \frac{1}{c^2}\frac{GM_*}{r}\Big),\ 0,\ \frac{1}{c}v\gamma_{\rm tot}\,\omega + \frac{1}{c^2 r}vv_\phi\gamma_{\rm tot}\Big(1 - \frac{1}{c^2}\frac{GM_*}{r}\Big)\Big\}, \tag{D.11b}$$

$$e^{\mu}_{\ (\theta)} = \Big\{0,\ 0,\ \frac{1}{r}\Big(1 - \frac{1}{c^2}\frac{GM_*}{r}\Big), 0\Big\}, \tag{D.11c}$$

$$e^{\mu}_{\ (\phi)} = \Big\{\frac{1}{c}v_\phi\gamma_\phi\Big(1 + \frac{1}{c^2}\frac{GM_*}{r}\Big),\ 0,\ 0,\ \frac{1}{c}v_\phi\gamma_\phi\omega + \frac{1}{r}\gamma_\phi\Big(1 - \frac{1}{c^2}\frac{GM_*}{r}\Big)\Big\}. \tag{D.11d}$$

Therefore, considering these vectors and the relations $u_\mu = e_\mu^{\ (\nu)} u_{(\nu)}$, we obtain that

$$\Big(u_t,\ u_r,\ u_\theta,\ u_\phi\Big) = \Big(-c\,\gamma_{\rm tot}\Big(1 - \frac{1}{c^2}\frac{GM_*}{r} + \frac{1}{c^4}(\frac{GM_*}{r})^2\Big) - \lambda\omega,\ v\Big(1 + \frac{1}{2}\frac{v^2}{c^2} + \frac{1}{c^2}\frac{GM_*}{r}\Big),\ 0,\ \lambda\Big). \tag{D.12}$$

Here, $u_\phi := \lambda$ is the angular momentum. Using the ϕ component of $u_\mu = e_\mu^{\ (\nu)} u_{(\nu)}$, expanding the result in powers of c and truncating it to $O(c^{-2})$, one can also show that

$$v_\phi = \frac{\lambda}{\gamma_{\rm tot}\,r}\Big(1 - \frac{1}{c^2}\frac{GM_*}{r}\Big). \tag{D.13}$$

Moreover, the contravariant components of the four-velocity field are obtained as follows:

$$\Big(u^t,\ u^r,\ u^\theta, u^\phi\Big) = \Big(c\,\gamma_{\rm tot}\Big(1 + \frac{1}{c^2}\frac{GM_*}{r} - \frac{1}{c^4}(\frac{GM_*}{r})^2\Big), v\Big(1 + \frac{1}{2}\frac{v^2}{c^2} - \frac{1}{c^2}\frac{GM_*}{r}\Big),\ 0,\ c\,\gamma_{\rm tot}\,\omega + \frac{\lambda}{r^2}\Big(1 - \frac{1}{c^2}\frac{2GM_*}{r}\Big)\Big). \tag{D.14}$$

D.3 Coefficients of Wind equation

As discussed in the paper, we use continuity equation, radial and azimuthal momentum equations along with the EoS to calculate the gradient of flow variables, namely the wind equation (dv/dr) and the temperature gradient ($dC_{\rm s}/dr$). In the following, we describe the explicit forms of these equations and their coefficients. Here, we use a unit system as $G = M_* = c = 1$.

D.3.1 Semi-Relativistic limit (SR)

$$\frac{dv_{\rm SR}}{dr} = \frac{N_{\rm SR}}{D_{\rm SR}},$$

where

$$N_{\rm SR} = N_{0_{\rm SR}} + \frac{C_{\rm s}^2}{2(\Gamma-1)\Gamma r^2}\Big[(\Gamma-1)\Big(5r-2(1-9\Gamma)\Big) - 5C_{\rm s}^2 r - \frac{\lambda}{2r}\Big(\Big(7\Gamma^2+\Gamma-8\Big)\lambda + 24(\Gamma+1)s_{\rm J}\Big) + \frac{(\Gamma-1)}{r^3}(\lambda^2-\lambda r+rs_{\rm J})\big((\Gamma+4)\lambda-6s_{\rm J}\big)\Big] - \frac{d\Phi_{\rm eff}^{\rm SR}}{dr}, \tag{D.15}$$

and

$$N_{0_{\rm SR}} = -\frac{C_{\rm s}^2(\Gamma-1)}{4\Gamma\left(-C_{\rm s}^2+\Gamma+1\right)r^7}\Big(\Gamma\lambda^2+2r(3\Gamma+r)\Big) \tag{D.16}$$
$$\times\Big(\lambda\Big[\lambda\big((\Gamma-4)\lambda+(\Gamma-4)r^2-(\Gamma-4)r+6s_{\rm J}\big)+rs_{\rm J}(\Gamma+12r-10)\Big]-5r^4+(3\Gamma+2)r^3+6rs_{\rm J}^2\Big).$$

Similarly, the denominator takes the form,

$$D_{\rm SR} = -\frac{C_{\rm s}^2}{\Gamma v} + \frac{C_{\rm s}^4}{(\Gamma-1)v} - \frac{C_{\rm s}^2}{v}\left(\frac{3}{r}+\frac{\lambda^2}{2r^2}\right) - \frac{(\Gamma-1)C_{\rm s}^2\Big(\Gamma\lambda^2+2r(3\Gamma+r)\Big)}{2\Gamma v(\Gamma-C_{\rm s}^2+1)r^2} + v. \tag{D.17}$$

Now, the coefficients for the temperature gradient equation are obtained as,

$$C_{0_{\rm SR}} = \frac{C_{\rm s}(\Gamma-1)}{2\left(-C_{\rm s}^2+\Gamma+1\right)r^5}\Big(\lambda\Big[\lambda\big((\Gamma-4)\lambda+(\Gamma-4)r^2 - (\Gamma-4)r+6s_{\rm J}\big)+s_{\rm J}\ r(\Gamma+12r-10)\Big]-5r^4+(3\Gamma+2)r^3+6rs_{\rm J}^2\Big). \tag{D.18}$$

$$C_{V_{\rm SR}} = -\frac{C_{\rm s}(\Gamma-1)}{v\left(-C_{\rm s}^2+\Gamma+1\right)}. \tag{D.19}$$

D.3.2 Semi-Newtonian limit (SN)

In a similar way, we write the coefficients for the Semi-Newtonian case.

$$N_{0_{\rm SN}} = -\frac{C_{\rm s}^2(\Gamma-1)}{\Gamma(\Gamma+1)r^7}\Big(\Gamma\lambda^2+2r(3\Gamma+r)\Big)\Big(\lambda[\lambda((\Gamma-4)\lambda(\Gamma-4)r^2-(\Gamma-4)r+6s_{\rm J}) + s_{\rm J}\ r(\Gamma+12r-10)]-5r^4+(3\Gamma+2)r^3+6rs_{\rm J}^2\Big). \tag{D.20}$$

$$N_{\rm SN} = \frac{C_{\rm s}^2}{4\Gamma r^5}\Big[\lambda r^2((7\Gamma+8)\lambda-24s_{\rm J})+2r^3(5r-2(1-9\Gamma))+2(\lambda^2-\lambda r+rs_{\rm J})((\Gamma+4)\lambda-6s_{\rm J})\Big] + \frac{1}{4}N_{0_{\rm SN}}-\frac{d\Phi_{\rm eff}^{\rm SN}}{dr}. \tag{D.21}$$

$$D_{\rm SN} = v-\frac{C_{\rm s}^2(\Gamma\lambda^2+2r(3\Gamma+r))}{(\Gamma+1)vr^2}. \tag{D.22}$$

$$C_{0_{\rm SN}} = \frac{C_{\rm s}(\Gamma-1)}{2(\Gamma+1)r^5}\Big(\lambda[\lambda((\Gamma-4)\lambda+(\Gamma-4)r^2-(\Gamma-4)r+6s_{\rm J})+s_{\rm J}\ r(\Gamma+12r-10)] - 5r^4+(3\Gamma+2)r^3+6rs_{\rm J}^2\Big). \tag{D.23}$$

$$C_{V_{\rm SN}} = \frac{C_{\rm s}}{v}\frac{(1-\Gamma)}{(1+\Gamma)}. \tag{D.24}$$

D.3.3 Non-relativistic limit (NR)

$$N_{\rm NR} = \frac{d\Phi_{\rm eff}^{\rm N}}{dr}+\frac{6+10r^2+3\Gamma(1-3\Gamma)+r(2+30\Gamma)}{2(1+\Gamma)r^3}, \tag{D.25}$$

$$D_{\rm NR} = \frac{-2(r+3\Gamma)C_{\rm s}^2}{(1+\Gamma)vr}+v. \tag{D.26}$$

$$C_{0_{\rm NR}} = \frac{(\Gamma-1)\,(2-5r+3\Gamma)C_{\rm s}}{2(1+\Gamma)r^2}, \tag{D.27}$$

$$C_{V_{\rm NR}} = \frac{C_{\rm s}(1-\Gamma)}{v(1+\Gamma)}. \tag{D.28}$$

Bibliography

Abbassi, S., Ghanbari, J., & Ghasemnezhad, M. 2010, mnras, 409, 1113, doi: 10.1111/j.1365-2966.2010.17364.x

Abbott, B. P., Abbott, R., & Abbott. 2017, 119, 161101, doi: 10.1103/PhysRevLett.119.161101

Abbott, B. P., Abbott, R., Abbott, T. D., et al. 2016, Physical Review X, 6, 041015, doi: 10.1103/PhysRevX.6.041015

Abramowicz, M. A., & Chakrabarti, S. K. 1990, apj, 350, 281, doi: 10.1086/168380

Abramowicz, M. A., Chen, X., Kato, S., Lasota, J.-P., & Regev, O. 1995, apjl, 438, L37, doi: 10.1086/187709

Abramowicz, M. A., Chen, X. M., Granath, M., & Lasota, J. P. 1996, apj, 471, 762, doi: 10.1086/178004

Abramowicz, M. A., Czerny, B., Lasota, J. P., & Szuszkiewicz, E. 1988, apj, 332, 646, doi: 10.1086/166683

Abramowicz, M. A., & Fragile, P. C. 2013, Living Reviews in Relativity, 16, 1, doi: 10.12942/lrr-2013-1

Abramowicz, M. A., Lanza, A., & Percival, M. J. 1997, apj, 479, 179, doi: 10.1086/303869

Abramowicz, M. A., & Zurek, W. H. 1981, apj, 246, 314, doi: 10.1086/158924

Aktar, R., Das, S., & Nandi, A. 2015, mnras, 453, 3414, doi: 10.1093/mnras/stv1874

Aktar, R., Das, S., Nandi, A., & Sreehari, H. 2017, mnras, 471, 4806, doi: 10.1093/mnras/stx1893

Aktar, R., Nandi, A., & Das, S. 2019, apss, 364, 22, doi: 10.1007/s10509-019-3509-0

Aktar, R., Pan, K.-C., & Okuda, T. 2024a, mnras, 527, 1745, doi: 10.1093/mnras/stad3287

—. 2024b, apj, 972, 18, doi: 10.3847/1538-4357/ad5a8a

Anile, A. M. 1990, Relativistic Fluids and Magneto-fluids

Appl, S., & Camenzind, M. 1988, aap, 206, 258

Armitage, P. J. 2020, Astrophysics of planet formation, Second Edition

Artemova, I. V., Bjoernsson, G., & Novikov, I. D. 1996, apj, 461, 565, doi: 10.1086/177084

Avara, M. J., McKinney, J. C., & Reynolds, C. S. 2016, mnras, 462, 636, doi: 10.1093/mnras/stw1643

Balbus, S. A., & Hawley, J. F. 1991, apj, 376, 214, doi: 10.1086/170270

—. 1998, Reviews of Modern Physics, 70, 1, doi: 10.1103/RevModPhys.70.1

Bardeen, J. M., Press, W. H., & Teukolsky, S. A. 1972, 178, 347, doi: 10.1086/151796

Baumgarte, T. W., & Shapiro, S. L. 2003, physrep, 376, 41, doi: 10.1016/S0370-1573(02)00537-9

Becker, P. A., Das, S., & Le, T. 2008, apjl, 677, L93, doi: 10.1086/588137

Becker, P. A., & Kazanas, D. 2001, apj, 546, 429, doi: 10.1086/318257

Becker, P. A., & Le, T. 2003, apj, 588, 408, doi: 10.1086/368377

Begelman, M. C., & Pringle, J. E. 2007, mnras, 375, 1070, doi: 10.1111/j.1365-2966.2006.11372.x

Begelman, M. C., Scepi, N., & Dexter, J. 2022, mnras, 511, 2040, doi: 10.1093/mnras/stab3790

Beloborodov, A. M. 1998, mnras, 297, 739, doi: 10.1046/j.1365-8711.1998.01530.x

Bisnovatyi-Kogan, G. S. 2019, Universe, 5, 146, doi: 10.3390/universe5060146

Bisnovatyi-Kogan, G. S., & Lovelace, R. V. E. 2000, apj, 529, 978, doi: 10.1086/308288

Bisnovatyi-Kogan, G. S., & Ruzmaikin, A. A. 1974, apss, 28, 45, doi: 10.1007/BF00642237

—. 1976, apss, 42, 401, doi: 10.1007/BF01225967

Blackman, E. G., Penna, R. F., & Varnière, P. 2008, na, 13, 244, doi: 10.1016/j.newast.2007.10.004

Blaes, O. M., Davis, S. W., Hirose, S., Krolik, J. H., & Stone, J. M. 2006, apj, 645, 1402, doi: 10.1086/503741

Blanchet, L., & Damour, T. 1989, 50, 377

Blanchet, L., Damour, T., & Iyer, B. R. 1995, 51, 5360, doi: 10.1103/PhysRevD.51.5360

Blandford, R. D., & Begelman, M. C. 2004, mnras, 349, 68, doi: 10.1111/j.1365-2966.2004.07425.x

Blandford, R. D., & Payne, D. G. 1982, mnras, 199, 883, doi: 10.1093/mnras/199.4.883

Blandford, R. D., & Znajek, R. L. 1977, mnras, 179, 433, doi: 10.1093/mnras/179.3.433

Bondi, H. 1952, mnras, 112, 195, doi: 10.1093/mnras/112.2.195

Bondi, H., & Hoyle, F. 1944, mnras, 104, 273, doi: 10.1093/mnras/104.5.273

Boyer, R. H., & Lindquist, R. W. 1967, Journal of Mathematical Physics, 8, 265, doi: 10.1063/1.1705193

Bu, D.-F., Wu, M.-C., & Yuan, Y.-F. 2016, mnras, 459, 746, doi: 10.1093/mnras/stw723

Bu, D.-F., Yuan, F., & Stone, J. M. 2011, mnras, 413, 2808, doi: 10.1111/j.1365-2966.2011.18354.x

Camenzind, M. 1986a, aap, 162, 32

—. 1986b, aap, 156, 137

—. 1987, aap, 184, 341

Camenzind, M. 1989, in Astrophysics and Space Science Library, Vol. 156, Accretion Disks and Magnetic Fields in Astrophysics, ed. G. Belvedere, 129, doi: 10.1007/978-94-009-2401-7_14

Chael, A., Narayan, R., & Johnson, M. D. 2019, mnras, 486, 2873, doi: 10.1093/mnras/stz988

Chakrabarti, S., & Titarchuk, L. G. 1995, apj, 455, 623, doi: 10.1086/176610

Chakrabarti, S. K. 1989, apj, 347, 365, doi: 10.1086/168125

—. 1990a, Theory of Transonic Astrophysical Flows, doi: 10.1142/1091

—. 1990b, mnras, 246, 134

—. 1996, apj, 464, 664, doi: 10.1086/177354

Chakrabarti, S. K., & Das, S. 2004, mnras, 349, 649, doi: 10.1111/j.1365-2966.2004.07536.x

Chakrabarti, S. K., & Mandal, S. 2006, apjl, 642, L49, doi: 10.1086/504319

Chakrabarti, S. K., & Manickam, S. G. 2000, apjl, 531, L41, doi: 10.1086/312512

Chakrabarti, S. K., & Mondal, S. 2006, mnras, 369, 976, doi: 10.1111/j.1365-2966.2006.10350.x

Chandrasekhar, S. 1965, 142, 1488, doi: 10.1086/148432

—. 1967, 148, 621, doi: 10.1086/149183

—. 1969, 158, 45, doi: 10.1086/150170

Chandrasekhar, S., & Esposito, F. P. 1970, 160, 153, doi: 10.1086/150414

Chandrasekhar, S., & Nutku, Y. 1969, 158, 55, doi: 10.1086/150171

Chatterjee, K., & Narayan, R. 2022, apj, 941, 30, doi: 10.3847/1538-4357/ac9d97

Chattopadhyay, I., & Chakrabarti, S. K. 2011, International Journal of Modern Physics D, 20, 1597, doi: 10.1142/S0218271811019487

Chattopadhyay, I., & Ryu, D. 2009, apj, 694, 492, doi: 10.1088/0004-637X/694/1/492

Chen, X. 1995, mnras, 275, 641, doi: 10.1093/mnras/275.3.641

Chen, X., Abramowicz, M. A., & Lasota, J.-P. 1997, apj, 476, 61, doi: 10.1086/303592

Chen, X., & Taam, R. E. 1994, apj, 431, 732, doi: 10.1086/174524

Cowie, L. L., & McKee, C. F. 1977, apj, 211, 135, doi: 10.1086/154911

Curd, B., & Narayan, R. 2019, mnras, 483, 565, doi: 10.1093/mnras/sty3134

Czerny, B. 2019, Universe, 5, 131, doi: 10.3390/universe5050131

Damour, T., & Taylor, J. H. 1991, 366, 501, doi: 10.1086/169585

Das, S. 2007, mnras, 376, 1659, doi: 10.1111/j.1365-2966.2007.11501.x

Das, S., Becker, P. A., & Le, T. 2009, apj, 702, 649, doi: 10.1088/0004-637X/702/1/649

Das, S., & Chakrabarti, S. K. 2004, International Journal of Modern Physics D, 13, 1955, doi: 10.1142/S0218271804005912

—. 2007, mnras, 374, 729, doi: 10.1111/j.1365-2966.2006.11185.x

—. 2008, mnras, 389, 371, doi: 10.1111/j.1365-2966.2008.13564.x

Das, S., Chakrabarti, S. K., & Mondal, S. 2010, mnras, 401, 2053, doi: 10.1111/j.1365-2966.2009.15793.x

Das, S., Chattopadhyay, I., & Chakrabarti, S. K. 2001a, apj, 557, 983, doi: 10.1086/321692

Das, S., Chattopadhyay, I., Nandi, A., & Chakrabarti, S. K. 2001b, aap, 379, 683, doi: 10.1051/0004-6361:20011307

Das, S., Chattopadhyay, I., Nandi, A., & Molteni, D. 2014, mnras, 442, 251, doi: 10.1093/mnras/stu864

Das, S., Nandi, A., Agrawal, V. K., Dihingia, I. K., & Majumder, S. 2021, mnras, 507, 2777, doi: 10.1093/mnras/stab2307

Das, S., Nandi, A., Stalin, C. S., et al. 2022, mnras, 514, 1940, doi: 10.1093/mnras/stac1398

Das, S., & Sarkar, B. 2018, mnras, 480, 3446, doi: 10.1093/mnras/sty2071

Davidson, P. A. 2001, An Introduction to Magnetohydrodynamics

Davis, S. W., & Tchekhovskoy, A. 2020, araa, 58, 407, doi: 10.1146/annurev-astro-081817-051905

De Villiers, J.-P., Hawley, J. F., & Krolik, J. H. 2003, apj, 599, 1238, doi: 10.1086/379509

De Villiers, J.-P., Hawley, J. F., Krolik, J. H., & Hirose, S. 2005, apj, 620, 878, doi: 10.1086/427142

Debnath, D., Chakrabarti, S. K., & Nandi, A. 2013, Advances in Space Research, 52, 2143, doi: 10.1016/j.asr.2013.09.002

Debnath, S., Chattopadhyay, I., & Joshi, R. K. 2024, mnras, 528, 3964, doi: 10.1093/mnras/stae181

Demianski, M., & Ivanov, P. B. 1997, aap, 324, 829

Dexter, J. 2016, mnras, 462, 115, doi: 10.1093/mnras/stw1526

Dexter, J., Scepi, N., & Begelman, M. C. 2021, apjl, 919, L20, doi: 10.3847/2041-8213/ac2608

Dexter, J., Tchekhovskoy, A., Jiménez-Rosales, A., et al. 2020, mnras, 497, 4999, doi: 10.1093/mnras/staa2288

Dihingia, I. K., Das, S., Maity, D., & Chakrabarti, S. 2018a, prd, 98, 083004, doi: 10.1103/PhysRevD.98.083004

Dihingia, I. K., Das, S., Maity, D., & Nandi, A. 2019, mnras, 488, 2412, doi: 10.1093/mnras/stz1933

Dihingia, I. K., Das, S., & Mandal, S. 2018b, mnras, 475, 2164, doi: 10.1093/mnras/stx3269

Dihingia, I. K., Das, S., Prabhakar, G., & Mandal, S. 2020a, mnras, 496, 3043, doi: 10.1093/mnras/staa1687

Dihingia, I. K., & Fendt, C. 2024, arXiv e-prints, arXiv:2404.06140, doi: 10.48550/arXiv.2404.06140

Dihingia, I. K., Maity, D., Chakrabarti, S., & Das, S. 2020b, prd, 102, 023012, doi: 10.1103/PhysRevD.102.023012

Dihingia, I. K., & Mizuno, Y. 2024, arXiv e-prints, arXiv:2403.18359, doi: 10.48550/arXiv.2403.18359

Dihingia, I. K., Vaidya, B., & Fendt, C. 2021, mnras, 505, 3596, doi: 10.1093/mnras/stab1512

Dullo, B. T., Gil de Paz, A., & Knapen, J. H. 2021, apj, 908, 134, doi: 10.3847/1538-4357/abceae

Eardley, D. M., & Lightman, A. P. 1975, apj, 200, 187, doi: 10.1086/153777

Eardley, D. M., Lightman, A. P., & Shapiro, S. L. 1975, apjl, 199, L153, doi: 10.1086/181871

Einstein, A., Infeld, L., & Hoffmann, B. 1938, Annals of Mathematics, 39, 65

Esin, A. A., McClintock, J. E., & Narayan, R. 1997, apj, 489, 865, doi: 10.1086/304829

Event Horizon Telescope Collaboration, Akiyama, K., Alberdi, A., et al. 2019a, apjl, 875, L1, doi: 10.3847/2041-8213/ab0ec7

—. 2019b, apjl, 875, L5, doi: 10.3847/2041-8213/ab0f43

Event Horizon Telescope Collaboration, Akiyama, K., Algaba, J. C., et al. 2021, apjl, 910, L13, doi: 10.3847/2041-8213/abe4de

Event Horizon Telescope Collaboration, Akiyama, K., Alberdi, A., et al. 2022, apjl, 930, L16, doi: 10.3847/2041-8213/ac6672

—. 2024, apjl, 964, L26, doi: 10.3847/2041-8213/ad2df1

Faber, J. A., & Rasio, F. A. 2000, 62, 064012, doi: 10.1103/PhysRevD.62.064012

Faghei, K. 2012, mnras, 420, 118, doi: 10.1111/j.1365-2966.2011.20006.x

Fock, V. A. 1964, The theory of space, time and gravitation (Macmillan)

Font, J. A. 2008, Living Reviews in Relativity, 11, 7, doi: 10.12942/lrr-2008-7

Frank, J., King, A., & Raine, D. J. 2002, Accretion Power in Astrophysics: Third Edition

Fukue, J. 1987, pasj, 39, 309

Fukumura, K., Hendry, D., Clark, P., Tombesi, F., & Takahashi, M. 2016, apj, 827, 31, doi: 10.3847/0004-637X/827/1/31

Fukumura, K., & Kazanas, D. 2007, apj, 669, 85, doi: 10.1086/521578

Fukumura, K., Takahashi, M., & Tsuruta, S. 2007, apj, 657, 415, doi: 10.1086/510660

Fukumura, K., & Tsuruta, S. 2004, apj, 611, 964, doi: 10.1086/422243

Gaia Collaboration, Panuzzo, P., Mazeh, T., et al. 2024, aap, 686, L2, doi: 10.1051/0004-6361/202449763

Gammie, C. F. 1999, apjl, 522, L57, doi: 10.1086/312207

Gammie, C. F., McKinney, J. C., & Tóth, G. 2003, apj, 589, 444, doi: 10.1086/374594

Gammie, C. F., & Popham, R. 1998, apj, 498, 313, doi: 10.1086/305521

Ghasemnezhad, M., Khajavi, M., & Abbassi, S. 2012, apj, 750, 57, doi: 10.1088/0004-637X/750/1/57

Ghoreyshi, S. M., & Shadmehri, M. 2020, mnras, 493, 5107, doi: 10.1093/mnras/staa599

Ghosh, P., & Abramowicz, M. A. 1997, mnras, 292, 887, doi: 10.1093/mnras/292.4.887

Giacconi, R., Gursky, H., Paolini, F. R., & Rossi, B. B. 1962, prl, 9, 439, doi: 10.1103/PhysRevLett.9.439

Giacconi, R., Kellogg, E., Gorenstein, P., Gursky, H., & Tananbaum, H. 1971, apjl, 165, L27, doi: 10.1086/180711

Gou, L., McClintock, J. E., Reid, M. J., et al. 2011, apj, 742, 85, doi: 10.1088/0004-637X/742/2/85

Gu, W.-M., & Lu, J.-F. 2004, Chinese Physics Letters, 21, 2551, doi: 10.1088/0256-307X/21/12/064

—. 2006, mnras, 365, 647, doi: 10.1111/j.1365-2966.2005.09750.x

Guilet, J., & Ogilvie, G. I. 2012, mnras, 424, 2097, doi: 10.1111/j.1365-2966.2012.21361.x

—. 2013, mnras, 430, 822, doi: 10.1093/mnras/sts551

Hameury, J. M., Lasota, J. P., McClintock, J. E., & Narayan, R. 1997, apj, 489, 234, doi: 10.1086/304780

Hawley, J. F. 2001, apj, 554, 534, doi: 10.1086/321348

Hawley, J. F., & Balbus, S. A. 1995, pasa, 12, 159, doi: 10.1017/S1323358000020208

Hawley, J. F., Gammie, C. F., & Balbus, S. A. 1995, apj, 440, 742, doi: 10.1086/175311

Hawley, J. F., & Krolik, J. H. 2001, apj, 548, 348, doi: 10.1086/318678

—. 2006, apj, 641, 103, doi: 10.1086/500385

Hirose, S., Krolik, J. H., De Villiers, J.-P., & Hawley, J. F. 2004, apj, 606, 1083, doi: 10.1086/383184

Hobson, M. P., Efstathiou, G. P., & Lasenby, A. N. 2006, General Relativity, doi: 10.2277/0521829518

Hoyle, F., & Lyttleton, R. A. 1939, Proceedings of the Cambridge Philosophical Society, 35, 405, doi: 10.1017/S0305004100021150

Huang, J., Jiang, Y.-F., Feng, H., et al. 2023, apj, 945, 57, doi: 10.3847/1538-4357/acb6fc

Ichimaru, S. 1976, apj, 208, 701, doi: 10.1086/154652

—. 1977, apj, 214, 840, doi: 10.1086/155314

Igumenshchev, I. V., Narayan, R., & Abramowicz, M. A. 2003, apj, 592, 1042, doi: 10.1086/375769

Ivanov, P. B., & Illarionov, A. F. 1997, mnras, 285, 394, doi: 10.1093/mnras/285.2.394

Iyer, N., Nandi, A., & Mandal, S. 2015, apj, 807, 108, doi: 10.1088/0004-637X/807/1/108

Jacquemin-Ide, J., Lesur, G., & Ferreira, J. 2021, aap, 647, A192, doi: 10.1051/0004-6361/202039322

Jana, C., & Das, S. 2024, jcap, 2024, 075, doi: 10.1088/1475-7516/2024/07/075

Jaranowski, P., Mach, P., Malec, E., & Piróg, M. 2015, prd, 91, 024039, doi: 10.1103/PhysRevD.91.024039

Jiang, Y., Li, S., Cao, X., et al. 2024, mnras, 532, 4524, doi: 10.1093/mnras/stae1777

Johnson, B. M., & Quataert, E. 2007, apj, 660, 1273, doi: 10.1086/513065

Kato, S., Fukue, J., & Mineshige, S. 2008, Black-Hole Accretion Disks — Towards a New Paradigm — (Kyoto University Press)

Kato, S., Wu, X.-B., Yang, L.-T., & Yang, Z.-L. 1993, mnras, 260, 317, doi: 10.1093/mnras/260.2.317

Kato, Y., Mineshige, S., & Shibata, K. 2004, apj, 605, 307, doi: 10.1086/381234

Kazemi, A., Roshan, M., & Nazari, E. 2018, 865, 71, doi: 10.3847/1538-4357/aadbaf

Kerr, R. P. 1963, Phys. Rev. Lett., 11, 237, doi: 10.1103/PhysRevLett.11.237

Khajenabi, F., & Shadmehri, M. 2013, mnras, 436, 2666, doi: 10.1093/mnras/stt1762

Kim, J., Garain, S. K., Balsara, D. S., & Chakrabarti, S. K. 2017, mnras, 472, 542, doi: 10.1093/mnras/stx1986

Kim, J., Garain, S. K., Chakrabarti, S. K., & Balsara, D. S. 2019, mnras, 482, 3636, doi: 10.1093/mnras/sty2953

Koide, S. 2004, apjl, 606, L45, doi: 10.1086/420976

Koide, S., Shibata, K., & Kudoh, T. 1998, apjl, 495, L63, doi: 10.1086/311204

—. 1999, apj, 522, 727, doi: 10.1086/307667

Kremer, G. M., & Mehret, L. C. 2021, 104, 024056, doi: 10.1103/PhysRevD.104.024056

Kumar, R., & Chattopadhyay, I. 2014, mnras, 443, 3444, doi: 10.1093/mnras/stu1389

Kumar, R., & Gu, W.-M. 2018, apj, 860, 114, doi: 10.3847/1538-4357/aac328

Kumar, R., Singh, C. B., Chattopadhyay, I., & Chakrabarti, S. K. 2013, mnras, 436, 2864, doi: 10.1093/mnras/stt1781

Kusunose, M., & Takahara, F. 1985, Progress of Theoretical Physics, 73, 41, doi: 10.1143/PTP.73.41

Kwan, T. M., Dai, L., & Tchekhovskoy, A. 2023, apjl, 946, L42, doi: 10.3847/2041-8213/acc334

Lai, D., & Wiseman, A. G. 1996, 54, 3958, doi: 10.1103/PhysRevD.54.3958

Landau, L. D., & Lifshitz, E. M. 1959, Fluid mechanics

Lančová, D., Abarca, D., Kluźniak, W., et al. 2019, apjl, 884, L37, doi: 10.3847/2041-8213/ab48f5

Lasota, J. P., Abramowicz, M. A., Chen, X., et al. 1996, apj, 462, 142, doi: 10.1086/177137

Le, T., & Becker, P. A. 2007, apj, 661, 416, doi: 10.1086/512851

Li, S.-L., & Begelman, M. C. 2014, apj, 786, 6, doi: 10.1088/0004-637X/786/1/6

Liang, E. P. T., & Thompson, K. A. 1980, apj, 240, 271, doi: 10.1086/158231

Lichnerowicz, A. 1970, Physica Scripta, 2, 221, doi: 10.1088/0031-8949/2/4-5/016

Lightman, A. P., & Eardley, D. M. 1974, apjl, 187, L1, doi: 10.1086/181377

Lin, X., & Yuan, F. 2024, mnras, 531, 3136, doi: 10.1093/mnras/stae1357

Liu, B. F., Done, C., & Taam, R. E. 2011, apj, 726, 10, doi: 10.1088/0004-637X/726/1/10

Liu, T., Gu, W.-M., & Zhang, B. 2017, nar, 79, 1, doi: 10.1016/j.newar.2017.07.001

Longair, M. S. 2011, High Energy Astrophysics

Lu, J. F. 1985, aap, 148, 176

Lu, J.-F., Gu, W.-M., & Yuan, F. 1999, apj, 523, 340, doi: 10.1086/307725

Lubow, S. H., Papaloizou, J. C. B., & Pringle, J. E. 1994, mnras, 267, 235, doi: 10.1093/mnras/267.2.235

Lynden-Bell, D. 1969, nat, 223, 690, doi: 10.1038/223690a0

Machida, M., Hayashi, M. R., & Matsumoto, R. 2000, apjl, 532, L67, doi: 10.1086/312553

Machida, M., Nakamura, K. E., & Matsumoto, R. 2006, pasj, 58, 193, doi: 10.1093/pasj/58.1.193

Mahadevan, R., & Quataert, E. 1997, apj, 490, 605, doi: 10.1086/304908

Majumder, S., Sreehari, H., Aftab, N., et al. 2022, mnras, 512, 2508, doi: 10.1093/mnras/stac615

Mandal, S., & Chakrabarti, S. K. 2005, aap, 434, 839, doi: 10.1051/0004-6361:20041235

—. 2008, apjl, 689, L17, doi: 10.1086/595782

Manmoto, T., Mineshige, S., & Kusunose, M. 1997, apj, 489, 791, doi: 10.1086/304817

Matsumoto, R., Kato, S., Fukue, J., & Okazaki, A. T. 1984, pasj, 36, 71

McKinney, J. C., & Gammie, C. F. 2004, apj, 611, 977, doi: 10.1086/422244

Melia, F., & Misra, R. 1993, apj, 411, 797, doi: 10.1086/172883

Menou, K. 2005, Hot Accretion with Saturated Conduction, Presented at the KITP Program: Physics of Astrophysical Outflows and Accretion Disks, Jul 7, 2005, Kavli Institute for Theoretical Physics, University of California, Santa Barbara, id.16, doi: 10.48550/arXiv.astro-ph/0507189

Mestel, L. 1968, mnras, 138, 359, doi: 10.1093/mnras/138.3.359

Michel, F. C. 1972, apss, 15, 153, doi: 10.1007/BF00649949

Mihalas, D., & Mihalas, B. W. 1984, Foundations of radiation hydrodynamics

Mineshige, S., Kusnose, M., & Matsumoto, R. 1995, apjl, 445, L43, doi: 10.1086/187885

Mishra, B., Begelman, M. C., Armitage, P. J., & Simon, J. B. 2020, mnras, 492, 1855, doi: 10.1093/mnras/stz3572

Mishra, B., Fragile, P. C., Anderson, J., et al. 2022, apj, 939, 31, doi: 10.3847/1538-4357/ac938b

Misner, C. W., Thorne, K. S., & Wheeler, J. A. 1973, Gravitation

Mitsuda, K., Inoue, H., Koyama, K., et al. 1984, pasj, 36, 741

Mizuno, Y. 2022, Universe, 8, 85, doi: 10.3390/universe8020085

Moffatt, H. K. 1978, Magnetic field generation in electrically conducting fluids

Molteni, D., Ryu, D., & Chakrabarti, S. K. 1996a, apj, 470, 460, doi: 10.1086/177877

Molteni, D., Sponholz, H., & Chakrabarti, S. K. 1996b, apj, 457, 805, doi: 10.1086/176775

Morse, R. L., & Nielson, C. W. 1973, Physics of Fluids, 16, 909, doi: 10.1063/1.1694445

Mosallanezhad, A., Zeraatgari, F. Z., Mei, L., & Bu, D.-F. 2021, apj, 909, 140, doi: 10.3847/1538-4357/abde49

Mościbrodzka, M., & Gammie, C. F. 2018, mnras, 475, 43, doi: 10.1093/mnras/stx3162

Moscibrodzka, M., Proga, D., Czerny, B., & Siemiginowska, A. 2007, aap, 474, 1, doi: 10.1051/0004-6361:20077703

Muchotrzeb, B., & Paczynski, B. 1982, actaa, 32, 1

Muchotrzeb-Czerny, B. 1986, actaa, 36, 1

Mukhopadhyay, B. 2002, apj, 581, 427, doi: 10.1086/344227

Mukhopadhyay, B., & Chatterjee, K. 2015, apj, 807, 43, doi: 10.1088/0004-637X/807/1/43

Nakamura, K. E., Kusunose, M., Matsumoto, R., & Kato, S. 1997, pasj, 49, 503, doi: 10.1093/pasj/49.4.503

Nandi, A., Chakrabarti, S. K., Vadawale, S. V., & Rao, A. R. 2001a, aap, 380, 245, doi: 10.1051/0004-6361:20011444

Nandi, A., Das, S., Majumder, S., et al. 2024, mnras, 531, 1149, doi: 10.1093/mnras/stae1208

Nandi, A., Debnath, D., Mandal, S., & Chakrabarti, S. K. 2012, aap, 542, A56, doi: 10.1051/0004-6361/201117844

Nandi, A., Manickam, S. G., Rao, A. R., & Chakrabarti, S. K. 2001b, mnras, 324, 267, doi: 10.1046/j.1365-8711.2001.04339.x

Nandi, A., Mandal, S., Sreehari, H., et al. 2018, apss, 363, 90, doi: 10.1007/s10509-018-3314-1

Narayan, R., Igumenshchev, I. V., & Abramowicz, M. A. 2003, pasj, 55, L69, doi: 10.1093/pasj/55.6.L69

Narayan, R., Kato, S., & Honma, F. 1997, apj, 476, 49, doi: 10.1086/303591

Narayan, R., & McClintock, J. E. 2008, nar, 51, 733, doi: 10.1016/j.newar.2008.03.002

Narayan, R., & Popham, R. 1993, nat, 362, 820, doi: 10.1038/362820a0

Narayan, R., SÄ dowski, A., Penna, R. F., & Kulkarni, A. K. 2012, mnras, 426, 3241, doi: 10.1111/j.1365-2966.2012.22002.x

Narayan, R., SaÌ§dowski, A., & Soria, R. 2017, mnras, 469, 2997, doi: 10.1093/mnras/stx1027

Narayan, R., & Yi, I. 1994, apjl, 428, L13, doi: 10.1086/187381

—. 1995a, apj, 452, 710, doi: 10.1086/176343

—. 1995b, apj, 444, 231, doi: 10.1086/175599

Nazari, E., Kazemi, A., Roshan, M., & Abbassi, S. 2017, apj, 839, 75, doi: 10.3847/1538-4357/aa68e0

Nemmen, R. S., Storchi-Bergmann, T., & Eracleous, M. 2014, mnras, 438, 2804, doi: 10.1093/mnras/stt2388

Nemmen, R. S., Storchi-Bergmann, T., Yuan, F., et al. 2006, apj, 643, 652, doi: 10.1086/500571

Niedźwiecki, A., Szanecki, M., Zdziarski, A. A., & Xie, F.-G. 2022, apj, 931, 167, doi: 10.3847/1538-4357/ac6c8b

Nishikawa, K. I., Richardson, G., Koide, S., et al. 2005, apj, 625, 60, doi: 10.1086/429360

Novikov, I. D., & Thorne, K. S. 1973, in Black Holes (Les Astres Occlus), 343–450

Oda, H., Machida, M., Nakamura, K. E., & Matsumoto, R. 2007, pasj, 59, 457, doi: 10.1093/pasj/59.2.457

—. 2009, apj, 697, 16, doi: 10.1088/0004-637X/697/1/16

—. 2010, apj, 712, 639, doi: 10.1088/0004-637X/712/1/639

Oda, H., Machida, M., Nakamura, K. E., Matsumoto, R., & Narayan, R. 2012, pasj, 64, 15, doi: 10.1093/pasj/64.1.15

Ohsuga, K., & Mineshige, S. 2011, apj, 736, 2, doi: 10.1088/0004-637X/736/1/2

Olivares S., H. R., Moscibrodzka, M. A., & Porth, O. 2023, arXiv e-prints, arXiv:2301.12020, doi: 10.48550/arXiv.2301.12020

Paczyński, B., & Wiita, P. J. 1980, aap, 88, 23

Page, D. N., & Thorne, K. S. 1974, apj, 191, 499, doi: 10.1086/152990

Pariev, V. I., Blackman, E. G., & Boldyrev, S. A. 2003, aap, 407, 403, doi: 10.1051/0004-6361:20030868

Park, J., Hada, K., Kino, M., et al. 2019, apj, 871, 257, doi: 10.3847/1538-4357/aaf9a9

Parker, E. N. 1963, Interplanetary dynamical processes.

—. 1966, apj, 145, 811, doi: 10.1086/148828

Patra, S., Majhi, B. R., & Das, S. 2022, Physics of the Dark Universe, 37, 101120, doi: 10.1016/j.dark.2022.101120

—. 2024, jcap, 2024, 060, doi: 10.1088/1475-7516/2024/01/060

Peitz, J., & Appl, S. 1997, mnras, 286, 681, doi: 10.1093/mnras/286.3.681

Penna, R. F., Kulkarni, A., & Narayan, R. 2013, aap, 559, A116, doi: 10.1051/0004-6361/201219666

Penna, R. F., McKinney, J. C., Narayan, R., et al. 2010, mnras, 408, 752, doi: 10.1111/j.1365-2966.2010.17170.x

Penna, R. F., Sądowski, A., & McKinney, J. C. 2012, mnras, 420, 684, doi: 10.1111/j.1365-2966.2011.20084.x

Pessah, M. E., Chan, C.-k., & Psaltis, D. 2007, apjl, 668, L51, doi: 10.1086/522585

Pessah, M. E., & Psaltis, D. 2005, apj, 628, 879, doi: 10.1086/430940

Piran, T. 1978, apj, 221, 652, doi: 10.1086/156069

Poisson, E., & Will, C. M. 2014, Gravity: Newtonian, Post-Newtonian, Relativistic (Cambridge University Press)

Popham, R., & Gammie, C. F. 1998, apj, 504, 419, doi: 10.1086/306054

Porth, O., Olivares, H., Mizuno, Y., et al. 2017, Computational Astrophysics and Cosmology, 4, 1, doi: 10.1186/s40668-017-0020-2

Porth, O., Chatterjee, K., Narayan, R., et al. 2019, apjs, 243, 26, doi: 10.3847/1538-4365/ab29fd

Poutanen, J. 1998, in Theory of Black Hole Accretion Disks, ed. M. A. Abramowicz, G. Björnsson, & J. E. Pringle, 100–122, doi: 10.48550/arXiv.astro-ph/9805025

Prendergast, K. H., & Burbidge, G. R. 1968, apjl, 151, L83, doi: 10.1086/180148

Pringle, J. E. 1976, mnras, 177, 65, doi: 10.1093/mnras/177.1.65

—. 1981, araa, 19, 137, doi: 10.1146/annurev.aa.19.090181.001033

Proga, D., & Begelman, M. C. 2003, apj, 592, 767, doi: 10.1086/375773

Pu, H.-Y., Nakamura, M., Hirotani, K., et al. 2015, apj, 801, 56, doi: 10.1088/0004-637X/801/1/56

Quataert, E. 2004, The Astrophysical Journal, 613, 322, doi: 10.1086/422973

Quataert, E. 2008, apj, 673, 758, doi: 10.1086/525248

Remillard, R. A., & McClintock, J. E. 2006, araa, 44, 49, doi: 10.1146/annurev.astro.44.051905.092532

Ressler, S. M., Quataert, E., & Stone, J. M. 2020a, mnras, 492, 3272, doi: 10.1093/mnras/stz3605

Ressler, S. M., White, C. J., Quataert, E., & Stone, J. M. 2020b, apjl, 896, L6, doi: 10.3847/2041-8213/ab9532

Reynolds, C. S. 2021, araa, 59, 117, doi: 10.1146/annurev-astro-112420-035022

Reynolds, C. S., Di Matteo, T., Fabian, A. C., Hwang, U., & Canizares, C. R. 1996, mnras, 283, L111, doi: 10.1093/mnras/283.4.L111

Rezzolla, L., & Zanotti, O. 2013, Relativistic Hydrodynamics (Oxford University Press)

Ricarte, A., Qiu, R., & Narayan, R. 2021, mnras, 505, 523, doi: 10.1093/mnras/stab1289

Riffert, H., & Herold, H. 1995, apj, 450, 508, doi: 10.1086/176161

Rilett, D. J. 2004, PhD thesis, Montana State University System

Ryan, B. R., Ressler, S. M., Dolence, J. C., Gammie, C., & Quataert, E. 2018, apj, 864, 126, doi: 10.3847/1538-4357/aad73a

Ryu, D., Chakrabarti, S. K., & Molteni, D. 1997, apj, 474, 378, doi: 10.1086/303461

Salpeter, E. E. 1964, apj, 140, 796, doi: 10.1086/147973

Salvesen, G., Armitage, P. J., Simon, J. B., & Begelman, M. C. 2016, mnras, 460, 3488, doi: 10.1093/mnras/stw1231

Sarkar, B., & Das, S. 2015, in Astronomical Society of India Conference Series, Vol. 12, Astronomical Society of India Conference Series, 91–92

Sarkar, B., & Das, S. 2016, mnras, 461, 190, doi: 10.1093/mnras/stw1327

—. 2018, Journal of Astrophysics and Astronomy, 39, 3, doi: 10.1007/s12036-017-9503-4

Sarkar, B., Das, S., & Mandal, S. 2018, mnras, 473, 2415, doi: 10.1093/mnras/stx2505

Sarkar, S., Chattopadhyay, I., & Laurent, P. 2020, aap, 642, A209, doi: 10.1051/0004-6361/202037520

Satapathy, K., Psaltis, D., & Özel, F. 2023, apj, 955, 47, doi: 10.3847/1538-4357/acef12

Scepi, N., Begelman, M. C., & Dexter, J. 2024, mnras, 527, 1424, doi: 10.1093/mnras/stad3299

Schekochihin, A. A., & Cowley, S. C. 2007, in Magnetohydrodynamics: Historical Evolution and Trends, ed. S. Molokov, R. Moreau, & H. K. Moffatt, 85, doi: 10.48550/arXiv.astro-ph/0507686

Sen, G., Maity, D., & Das, S. 2022, jcap, 2022, 048, doi: 10.1088/1475-7516/2022/08/048

Shadmehri, M. 2008, apss, 317, 201, doi: 10.1007/s10509-008-9882-8

Shakura, N. I. 1973, sovast, 16, 756

Shakura, N. I., & Sunyaev, R. A. 1973, aap, 24, 337

—. 1976, mnras, 175, 613, doi: 10.1093/mnras/175.3.613

Shapiro, S. L. 1973, apj, 185, 69, doi: 10.1086/152396

Shapiro, S. L., Lightman, A. P., & Eardley, D. M. 1976, apj, 204, 187, doi: 10.1086/154162

Shapiro, S. L., & Salpeter, E. E. 1975, apj, 198, 671, doi: 10.1086/153645

Shapiro, S. L., & Teukolsky, S. A. 1983, Black holes, white dwarfs and neutron stars. The physics of compact objects, doi: 10.1002/9783527617661

Shibata, K., Nozawa, S., Matsumoto, R., Sterling, A. C., & Tajima, T. 1990, apjl, 351, L25, doi: 10.1086/185671

Shibata, K., & Uchida, Y. 1985, pasj, 37, 31

Shukurov, A. M., & Subramanian, K. 2021, Astrophysical Magnetic Fields: From Galaxies to the Early Universe, doi: 10.1017/9781139046657

Shvartsman, V. F. 1971, sovast, 15, 377

Singh, M., & Das, S. 2024, Astrophysics and Space Science, 369, doi: https://doi.org/10.1007/s10509-023-04263-6

Sądowski, A. 2009, apjs, 183, 171, doi: 10.1088/0067-0049/183/2/171

—. 2016a, mnras, 459, 4397, doi: 10.1093/mnras/stw913

—. 2016b, mnras, 462, 960, doi: 10.1093/mnras/stw1852

Sądowski, A., Narayan, R., Penna, R., & Zhu, Y. 2013, mnras, 436, 3856, doi: 10.1093/mnras/stt1881

Sorathia, K. A., Reynolds, C. S., Stone, J. M., & Beckwith, K. 2012, apj, 749, 189, doi: 10.1088/0004-637X/749/2/189

Spitzer, L. 1962, Physics of Fully Ionized Gases

Sponholz, H., & Molteni, D. 1994, mnras, 271, 233, doi: 10.1093/mnras/271.1.233

Suková, P., Charzyński, S., & Janiuk, A. 2017, mnras, 472, 4327, doi: 10.1093/mnras/stx2254

Suková, P., & Janiuk, A. 2015, mnras, 447, 1565, doi: 10.1093/mnras/stu2544

Szanecki, M., Niedźwiecki, A., & Wojaczyński, R. 2023, mnras, 521, 2215, doi: 10.1093/mnras/stad699

Takahashi, M. 2002, apj, 570, 264, doi: 10.1086/339497

Takahashi, M., Goto, J., Fukumura, K., Rilett, D., & Tsuruta, S. 2006, apj, 645, 1408, doi: 10.1086/500107

Takahashi, M., Nitta, S., Tatematsu, Y., & Tomimatsu, A. 1990, apj, 363, 206, doi: 10.1086/169331

Takahashi, M., Rilett, D., Fukumura, K., & Tsuruta, S. 2002, apj, 572, 950, doi: 10.1086/340380

Tanaka, T., & Menou, K. 2006, apj, 649, 345, doi: 10.1086/506442

Tananbaum, H., Gursky, H., Kellogg, E., Giacconi, R., & Jones, C. 1972, apjl, 177, L5, doi: 10.1086/181042

Tchekhovskoy, A., Narayan, R., & McKinney, J. C. 2011, mnras, 418, L79, doi: 10.1111/j.1745-3933.2011.01147.x

Thorne, K. S., & Price, R. H. 1975, apjl, 195, L101, doi: 10.1086/181720

Wandel, A., & Liang, E. P. 1991, apj, 380, 84, doi: 10.1086/170564

Watarai, K.-y., Mizuno, T., & Mineshige, S. 2001, apjl, 549, L77, doi: 10.1086/319125

Weber, E. J., & Davis, Leverett, J. 1967, apj, 148, 217, doi: 10.1086/149138

Weinberg, S. 1972, Gravitation and Cosmology: Principles and Applications of the General Theory of Relativity

White, C. J. 2022, apjs, 262, 28, doi: 10.3847/1538-4365/ac77ef

Will, C. M. 1993, Theory and Experiment in Gravitational Physics (Cambridge University Press)

—. 2011, 108, 5938, doi: 10.1073/pnas.1103127108

Wu, M., Yuan, F., & Bu, D. 2010, Science China Physics, Mechanics, and Astronomy, 53, 168, doi: 10.1007/s11433-010-0037-x

Xie, F.-G., Narayan, R., & Yuan, F. 2023, apj, 942, 20, doi: 10.3847/1538-4357/aca534

Yang, R., & Kafatos, M. 1995, aap, 295, 238

You, B., Yang, S.-k., Yan, Z., Cao, X., & Zdziarski, A. A. 2024, apjl, 969, L33, doi: 10.3847/2041-8213/ad5b50

You, B., Cao, X., Yan, Z., et al. 2023, Science, 381, 961, doi: 10.1126/science.abo4504

Younes, G., Ptak, A., Ho, L. C., et al. 2019, apj, 870, 73, doi: 10.3847/1538-4357/aaf38b

Yuan, F., & Cui, W. 2005, apj, 629, 408, doi: 10.1086/431453

Yuan, F., Markoff, S., & Falcke, H. 2002, aap, 383, 854, doi: 10.1051/0004-6361:20011709

Yuan, F., & Narayan, R. 2014, araa, 52, 529, doi: 10.1146/annurev-astro-082812-141003

Zel'dovich, Y. B., & Novikov, I. D. 1964, Soviet Physics Doklady, 9, 246

Zhao, T.-L., Li, X.-F., Tang, Z.-Y., & Kumar, R. 2024, apj, 970, 157, doi: 10.3847/1538-4357/ad5d58

Zimmerman, E. R., Narayan, R., McClintock, J. E., & Miller, J. M. 2005, apj, 618, 832, doi: 10.1086/426071

VITA

Samik Mitra was born on 11th November 1994 in Chinsurah, Hooghly, West Bengal, India. He graduated with a Bachelor's degree (B.Sc.) in Physics in 2016 from the Raja Peary Mohan College, affiliated with the University of Calcutta, India. He completed his Master's in Physics and Astrophysics from the Department of Physics and Astrophysics, University of Delhi, back in 2018. He was enrolled in the doctoral program at the Department of Physics, Indian Institute of Technology Guwahati, India, in 2019. He received the prestigious *Prime Minister's Research Fellowship (PMRF)* in 2020 and served as a Prime Minister's fellow upto 2024. He is passionate about programming, art, and music. He is currently exploring the numerical modeling of accretion flows around BHs.

EXPERIENCES

- Visiting Lecturer at North Guwahati College, Guwahati, from 2021 to 2024.
- Teaching assistant at the Department of Physics, Indian Institute of Technology Guwahati from 2020 to 2024.

The best quotes that motivate me so far

"Do you know that the harder thing to do and the right thing to do are usually the same thing? Nothing that has meaning is easy. Easy doesn't enter into grown-up life." ∼ The Weather Man (2005).

"Be a warrior, not a worrier."

"Yesterday is history, tomorrow is a mystery, and today is a gift...that's why they call it the present!" — Master Oogway from Kung fu Panda.